Dynamics of the Jovian Magnetosphere: Combining Insights from Global MHD Simulations and In Situ Measurements from the Juno Spacecraft

by

Yash Sarkango

A dissertation submitted in partial fulfillment
of the requirements for the degree of
Doctor of Philosophy
(Climate and Space Sciences and Engineering)
in The University of Michigan
2021

Doctoral Committee:
Associate Professor Xianzhe Jia, Chair
Professor Mark J. Kushner
Professor James A. Slavin
Research Professor Gabor Toth

Yash Sarkango
sarkango@umich.edu
ORCID iD: 0000-0001-7812-7464

To my grandmothers, for their hard work and sacrifice;
without which none of this would have been possible.

Acknowledgements

I am very grateful to countless people who have assisted with and contributed to this dissertation in their own way.

Firstly, I want to thank my advisor, Prof. Xianzhe Jia, for giving me this opportunity to pursue scientific research as a career. His advice, professionalism, support and selfless assistance have been invaluable for the past six years. I could not have asked for a better role-model and mentor as an academic advisor. I have learned a lot working with him and have had the most positive experience as part of his research group.

I am very grateful to Prof. James Slavin for his mentorship, and for being so generous with his time. His encouragement and enthusiasm have made this journey much easier, and I have learned a lot from our interactions.

This work would not have been possible without the support of Prof. Gabor Toth, whose technical guidance and experience with the SWMF code has been crucial. I am very grateful for all his assistance and prompt response to any questions or issues.

I would like to thank Prof. Mark Kushner, who took time out of his busy schedule to serve as the cognate member of the committee. I especially thank him for his detailed reading of the dissertation draft and for making excellent suggestions that improved the text considerably.

This thesis and my graduate experience has greatly benefited from conversations and assistance from many colleagues. In particular I would like to thank Camilla Harris, Ryan Dewey, Sergio Vidal-Luengo, Abigail Azari, Jamie Jasinski and many other graduate students and postdocs for their kindness and interesting conversations. I'm also grateful to Yuxi Chen and Hongyang Zhou, who were always prompt and comprehensive in their help, whenever I

had any issues with the SWMF.

I am indebted to the CLASP IT group - Faye, Darren, Bryan, and Cameron. During the initial months of the pandemic, while the rest of us were sequestered at home, they would manually restart my office computer every few days while it suffered from unexplained crashes. They also tried their utmost to recover data which was lost due to a malfunctioning hard drive. I am truly grateful for their support. I would also like to thank Laura Hopkins, Claire Miller and Sandra Pytlinski for making every administration related task seem smooth.

I am grateful for the support of my friends from India and the US. In particular, I would like to thank Ayoub and Sergio for their friendship, frank yet constructive criticism, motivation and for many interesting discussions.

My experience in graduate school has been quite painless due to the constant support, honest feedback and patience of my partner, Bishakha. I am extremely grateful to my grandmothers, to whom this thesis is dedicated, for their support and commitment to learning and knowledge. Most of all, I thank my brother and my parents, who have been a constant source of support and strength, and who gave me the precious freedom and encouragement to pursue my interests; a risk not many people can afford to take.

Table of Contents

List of Tables

List of Figures

Abstract

Unlike the terrestrial magnetosphere, which responds strongly to changes in the solar wind and interplanetary magnetic field, Jupiter's magnetosphere depends largely on internal processes related to its strong planetary magnetic field, rapid rotation and presence of internal sources of plasma. The role of external factors, like the solar wind, is considered to be minimal and is not well understood. Observations of the Jovian UV aurora have hinted that it responds to changes in the upstream solar wind dynamic pressure, though the physical processes leading to this enhancement are poorly understood. Solar wind dynamic pressure is also considered to influence the oscillations of Jupiter's current sheet, particularly in the magnetotail. These questions are difficult to resolve using limited and sparse in situ observations.

In this work, we use a global magnetohydrodynamics model to study the dynamics of the Jovian magnetosphere. By performing systematic experiments in which we vary the solar wind dynamic pressure, we have analyzed the response of the Jovian magnetosphere and tracked the change in the intensity of corotation-enforcement currents, which are believed to be closely related to the Jovian aurora. Our model predicts that intensity of field-aligned currents in the dayside ionosphere would decrease after a dynamic pressure enhancement due to an increase in the corotation velocity of the plasma in the dayside magnetosphere, especially in the pre-noon sectors. Our model also predicts the release of plasmoids due to reconnection in the magnetotail, and we demonstrate that these plasmoids magnetically connect to the polar regions of the planet, which predominantly connect to open field lines in the solar wind.

We also study the response of Jupiter's oscillating magnetotail current sheet to changes

in the upstream solar wind dynamic pressure by incorporating a realistic internal field model into our simulations. It was previously thought that solar wind driven compression would reduce the amplitude of the current sheet oscillations and change the hinging distance of the current sheet. Using the MHD model, we find that increasing solar wind dynamic pressure also increases the density and temperature in the magnetotail lobes such that the Alfven and magnetosonic speeds in the magnetosphere may be reduced, which can decrease the wavelength of current sheet oscillations.

Lastly, our MHD model and other in situ observations have revealed that plasmoids produced in the Jovian magnetotail are large and infrequent. We have analyzed high temporal resolution magnetometer data from the Juno spacecraft and identified magnetic flux ropes and O-lines with durations lasting less than 300 seconds, which correspond to diameters comparable with the local ion-inertial length. These findings suggest that despite many differences, magnetic reconnection in the Jovian magnetotail can also operate via current sheet instabilities, similar to that seen at Earth, Mercury and in particle-in-cell simulations.

Our findings illustrate the complicated nature of dynamics in the Jovian magnetosphere, which is not well understood due to the sparse in situ data. We demonstrate that, in the absence of global empirical data, numerical experiments can serve to validate or invalidate theories of magnetospheric dynamics. Our results use and support data gathered by numerous in situ spacecraft such as Galileo and Juno, and can also support future missions to the Jupiter system. The Jovian magnetosphere is an extreme environment, and an excellent laboratory for plasma research, and additional observations and models are needed to understand its dynamics.

Chapter 1

Introduction

1.1 Motivation

Plasma refers to a collection of charged particles, either ions or electrons, which interact among themselves and the surrounding electromagnetic field. It is ubiquitous in the space environment, and can be found in the interior and surroundings of stars, planets and other planetary bodies. Space plasma physics is the study of plasma in these environments.

The study of space plasma in the regions near a planet is referred to as magnetospheric physics, named after the region of space surrounding the planetary body's interaction with the surrounding electromagnetic plasma medium, called the *magnetosphere*. The field of magnetospheric space plasma physics originated with the beginnings of the space age and was supported by the decades long ongoing investigation of the terrestrial magnetosphere by in situ spacecraft. The magnetosphere has various regions with different plasma characteristics, and each of these regions have been well studied using in situ measurements, theoretical analysis and through the development of numerical models. Especially in the last two decades, advancements in computing technology have allowed for complex, first-principle based, global models of the space environment, which can simultaneously solve for different magnetospheric regions and allow us to understand their interactions.

Magnetospheric physics has immediate practical applications in the study of 'space weather' - a term which refers to the electromagnetic response of the terrestrial magnetosphere to changes in the upstream plasma, composed of the solar wind and interplanetary

magnetic field which originates from the sun. The sun is a dynamic star, and produces various perturbations such as solar flares, coronal mass ejections and solar energetic particles (SEPs), which can be detrimental to society. For example, solar flares and SEPs increase the degree of radiation in outer space, which can directly harm satellite equipment and personnel. Changes in the solar wind can trigger geomagnetic storms, which are cause sudden changes in the geomagnetic field on the surface, leading to induced currents in power-grids and pipelines, which can result in serious economic damage.

Although the terrestrial magnetosphere has gained the most attention due to its proximity and direct influence on society, other magnetized bodies such as the planets Mercury, Jupiter, Saturn, Uranus and Neptune, all possess magnetospheres. Unmagnetized or weakly-magnetized bodies such as Venus, Mars, and comets also interact with the solar wind plasma as conducting obstacles, producing 'induced' magnetospheres. Many such regions have been visited by in situ spacecraft, with some dedicated orbiters such as the MESSENGER mission to Mercury, the Cassini mission to Saturn, and the Galileo and Juno spacecraft to Jupiter.

The magnetospheres of the gas giants, Jupiter and Saturn, are very different from that of the Earth due to their size, rotation and presence of heavy mass inside their magnetospheres. Although their magnetospheres have been visited by in situ spacecraft, the observations within these magnetospheres are sparse, which makes it difficult to understand local observations in the context of the global system, which span several million kilometers. One technique to complement in situ measurements is to use global models similar to those developed in the terrestrial context to solve for the plasma dynamics within the magnetosphere. Various global models have been developed for the gas giant magnetospheres over the past two decades.

Sparse measurements of plasma in the Jupiter system have largely confirmed that its magnetosphere is very different from the Earth. Plasma present within the Jovian magnetosphere co-rotates with the planet, and is highly energetic. The exact mechanism which accelerates the plasma to corotation and energizes particles to the observed energies, is not fully understood. Similar to what is observed at Earth, the magnetospheric processes at Jupiter also create an aurora, whose morphology is well studied through remote observations by the Hubble Space Telescope and the Hisaki spacecraft. The aurora is seen to brighten

during certain intervals, which may be a result of solar-wind-magnetosphere interaction, though this is difficult to reconcile without multi-spacecraft observations. Observations by the Juno spacecraft have also hinted that the Jovian aurora is not produced due to processes which produce the terrestrial aurora. All these questions are difficult to answer using limited, sparse in situ measurements.

In this work, we introduce a new model for Jupiter's magnetosphere and couple it with a simplified ionosphere. Jupiter's magnetosphere is large and dynamic, and a global model allows us to perform systematic experiments to understand its response to various inputs, such as the dynamic pressure of the solar wind. Using the model, we investigated long-standing questions about the Jovian magnetosphere -

1. How and to what extent does the solar wind influence Jupiter's magnetosphere and currents in the ionosphere?

2. How does magnetic reconnection occur in the Jovian magnetosphere and how are plasmoids released in the magnetotail? To which regions of the ionosphere and aurora do these plasmoids magnetically connect?

3. How does solar wind dynamic pressure influence the morphology of the magnetotail current sheet?

4. Where does magnetic reconnection occur in the Jovian magnetotail and are all Jovian plasmoids large and infrequent?

This dissertation is organized as follows. In the coming sections, a general description is provided to the reader unfamiliar with magnetospheric physics, where different terminologies used are explained briefly. In Chapter 2, a description of the global MHD model for the Jupiter's magnetosphere is provided. The questions mentioned previously are then investigated individually in the remaining chapters and summarized in Chapter 7.

1.2 Theoretical background

1.2.1 The MHD approximation

Plasmas comprise of innumerable charged particles which interact among themselves and the surrounding electromagnetic fields. In the space environment, they usually contain equal parts of positive and negative charges (i.e. are quasi-neutral), in the form of various ion species and electrons, and in most situations arising in magnetospheric physics, have low densities which makes collisions between particles rare and unimportant (Bruno & Carbone, 2013). For mathematical analysis, it is convenient to study the collective motion of particles instead of tracking them individually. One of the most fundamental ways to describe this collective behaviour is by assigning a distribution function $f(t, \mathbf{x}, \mathbf{v})$, which is used to estimate the likelihood of a particle having certain position $\mathbf{x}$ and $\mathbf{v}$ at time t. In the absence of collisions, the total change in f is assumed to be zero, i.e. phase space is conserved. This leads to the Vlasov equation, which is the fundamental conservation law of particle phase space (Chen, 1995; Gombosi, 1998).

$$\frac{df_\alpha}{dt} = \frac{\partial f_\alpha}{\partial t} + \mathbf{v}_\alpha \cdot \nabla f_\alpha + \mathbf{a}_\alpha \cdot \nabla_v f_\alpha = 0 \tag{1.1}$$

Where $\mathbf{a}_\alpha = (\mathbf{E} + \mathbf{v}_\alpha \times \mathbf{B}) e Z_\alpha / m_\alpha$ is the acceleration due to the Lorentz force on a particle species α with charge state Z_α. Apart from the assumption that the plasma is collision-less, the Vlasov equation is still relatively general and describes in a statistical way the evolution of a collection of charged particles. The analysis can be simplified by removing the dependence on the particles' velocity, which is done by integrating over the velocity space i.e. by multiplying Equation 1.1 by different powers of $\mathbf{v}$ in order to obtain its moments. The ideal MHD equations can be derived by considering three moments (zeroth, first and second) separately for the ions and electrons, and then combining them by defining a new variable $\mathbf{J}$, which is the density of the current generated due to the different ion and electron motions.

$$\mathbf{J} = en\left(\mathbf{v}_i - \mathbf{v}_e\right) \tag{1.2}$$

Where it is assumed that $n = Z_i n_i = n_e$ for charge-neutrality. This leads to the single-fluid ideal MHD equations (repeated below from Gombosi, 1998),

$$\frac{d\rho}{dt} = -\rho\,(\nabla \cdot \mathbf{v}) \tag{1.3}$$

$$\rho\frac{d\mathbf{v}}{dt} = -\nabla p + \mathbf{J} \times \mathbf{B} \tag{1.4}$$

$$\frac{3}{2}\frac{dp}{dt} = -\frac{5}{2}p\,(\nabla \cdot \mathbf{v}) \tag{1.5}$$

The above equations track the change in mass density ρ, velocity $\mathbf{v}$ and pressure p. The evolution of the magnetic field can be described using Faraday's law,

$$\frac{\partial \mathbf{B}}{\partial t} = -\nabla \times \mathbf{E} \tag{1.6}$$

Ampere's law provides the relationship between the magnetic field intensity $\mathbf{B}$ and the current density $\mathbf{J}$. The displacement current can be ignored if the timescales for the electric field fluctuations are much shorter than the timescales studied using the fluid approximation, which is usually the case in planetary magnetospheres, except in regions near the planet where the Alfven speeds approach the speed of light.

$$\nabla \times \mathbf{B} = \mu_0 \mathbf{J} \tag{1.7}$$

And finally, the equations are closed by using a form of Ohm's law, which can be derived by combining the ion and electron momentum equations (which are previously derived using their respective Vlasov equations). In the case of ideal MHD, we use a simplified form for the Ohm's law and neglect resistivity. This leads to the following expression for the motional electric field,

$$\mathbf{E} = -\mathbf{v} \times \mathbf{B} \tag{1.8}$$

The expression for the Ohm's law in ideal MHD implies that the electric field perceived by the moving plasma in the frame of reference moving with velocity $\mathbf{v}$ in a background

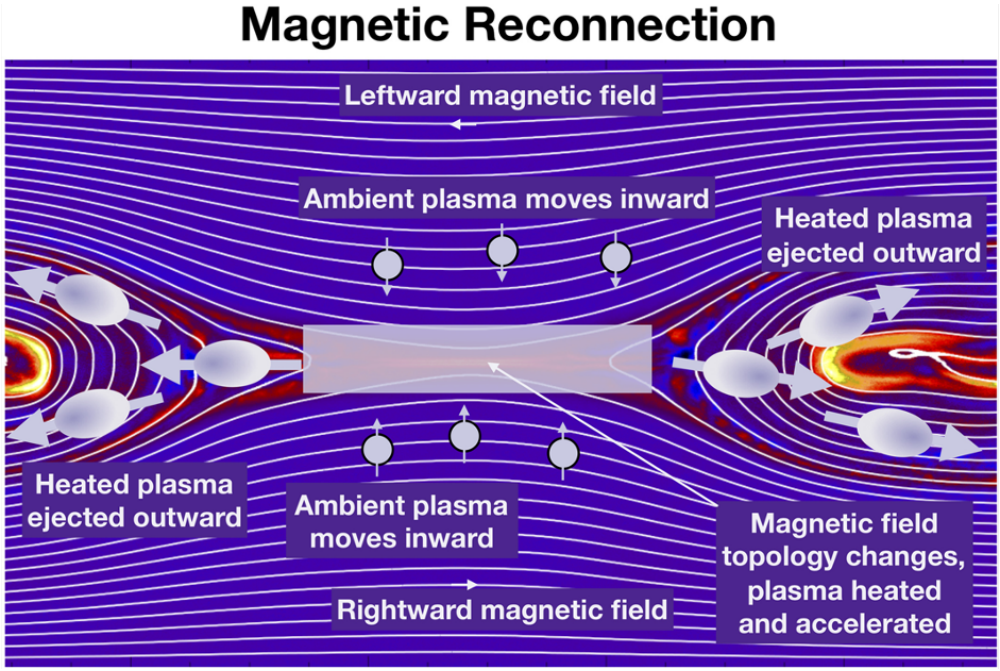

Figure 1.1: Schematic of magnetic reconnection adapted from Hesse and Cassak (2020) showing the different regions surrounding the X-line.

magnetic field **B** is zero. The Ohm's law in ideal MHD has one major implication: the plasma is "frozen-in" to the magnetic field. Diffusion across the magnetic field is not permitted.

1.2.2 Magnetic reconnection

Magnetic reconnection is a process by which two regions with sufficiently sheared magnetic fields merge and transfer the energy associated with magnetic stresses into the kinetic energy of the surrounding plasma (Priest & Forbes, 2000; Yamada, Kulsrud, & Ji, 2010). A simplistic analogy often used to describe magnetic reconnection is the 'disconnection' and *re*-connection of two magnetic field lines which are oppositely directed to each other (Gonzalez et al., 2016). Such breakage of magnetic field lines would violate the frozen-in flux condition, and thus, magnetic reconnection is a non-ideal phenomena which requires additional processes, such as finite resistivity, to occur in order to break the frozen-in flux condition.

Figure 1.1 shows a schematic where two regions with anti-parallel magnetic fields merge and reconnect. Magnetic field lines diffuse towards the center of the region, called the 'X-line', via the inflow region and are expelled at large velocities away from the X-line in the outflow

regions. Various theories have been put forward to explain and model the reconnection process, to explain the different rates of reconnection observed in different environments (see for e.g. Yamada et al., 2010 and references therein). In particular, we will discuss the two-fluid model of reconnection.

In the two-fluid model, the ions and electrons are presumed to demagnetize, i.e. stop following the magnetic field lines, in different regions near the X-line, where the magnetic field strength is at a minimum. The ions, being heavier, are demagnetized first as they enter the *ion diffusion region* and escape via the outflow, where they are accelerated. The electrons remain magnetized until they reach the *electron diffusion region*. The different motions of the electrons and ions generates a current system that in turn produces the quadrupolar Hall magnetic field. As the electron diffusion region is much smaller than that for the ions, it is much difficult to detect in in-situ measurements and remains an active topic for research. Studying the electron diffusion region is the primary objective of NASA's MMS spacecraft constellation, whose goal is to quantify the contribution of various terms in the generalized Ohm's law (e.g. Vasyliunas, 1975 and references therein) in breaking the frozen-in flux condition (Burch, Moore, Torbert, & Giles, 2016).

The model shown in Figure 1.1 represents a situation where magnetic reconnection is occurring in a steady manner. However, particle-in-cell and hybrid simulations of reconnecting fields have shown that this is not necessarily the case. Instead, the thin current sheet near the X-line was found to be unstable to the tearing instability, and breaks into individual closed magnetic loops separated by multiple X-lines (Drake, Swisdak, Che, & Shay, 2006; Drake, Swisdak, Schoeffler, et al., 2006). These magnetic loops, also called flux ropes or O-lines, are created within the ion-diffusion region and are transported away from the X-line through the outflow, where they can coalesce through repeated reconnection and enlarge or dissipate (Markidis et al., 2012; R. Wang et al., 2016).

The occurrence of magnetic reconnection depends strongly on the angle of magnetic shear between the reconnecting layers, and also on the plasma β, which is defined as the ratio of thermal pressure (p) to the magnetic pressure ($B^2/2\mu_0$) (Swisdak, Rogers, Drake, & Shay, 2003; Swisdak, Opher, Drake, & Alouani Bibi, 2010; Phan et al., 2010). In particular for asymmetric reconnection, where the two reconnecting layers had a large density gradient,

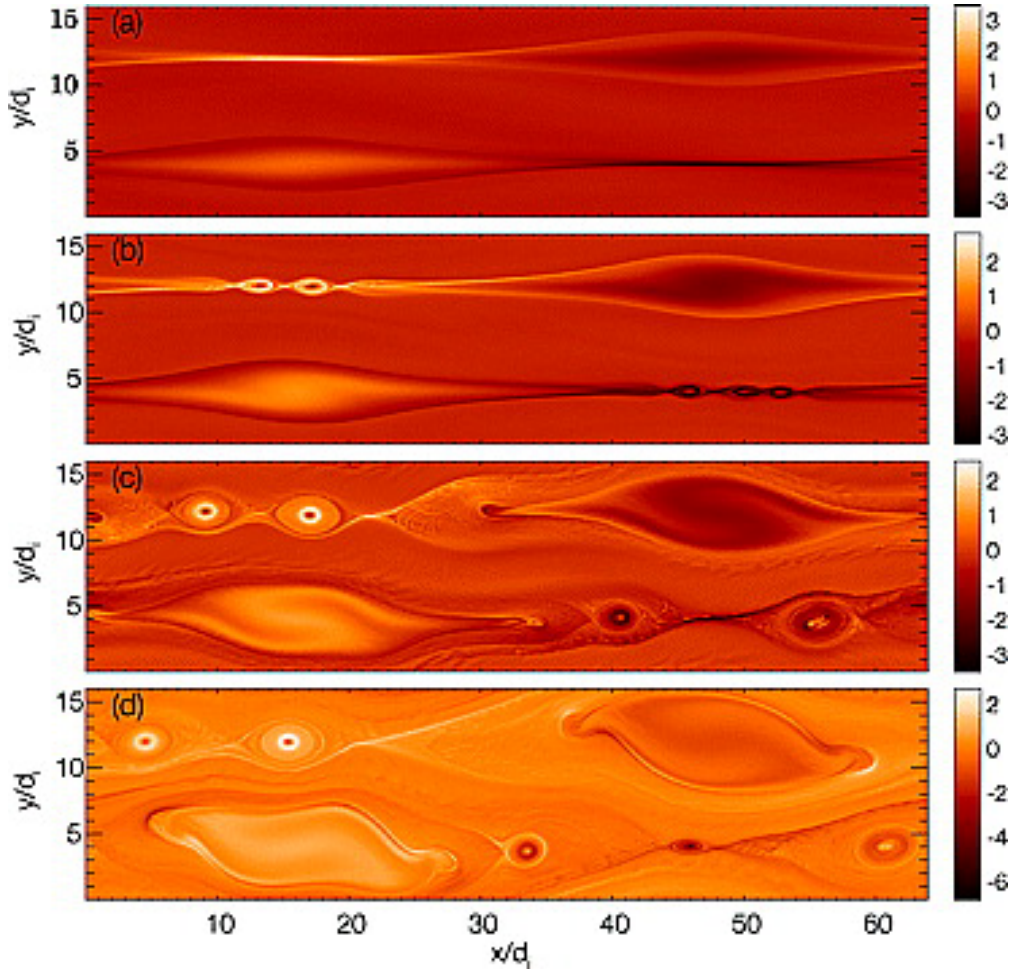

Figure 1.2: Example of multiple X-line reconnection adapted from Drake, Swisdak, Schoeffler, et al. (2006), who have used a particle-in-cell code to simulate anti-parallel magnetic fields. The contours show the out-of-plane component of the current density (J_z). Note the progression from steady reconnection to the generation of small magnetic islands at the thin current sheet, which coalesce and evolve to become large magnetic flux ropes or plasmoids.

greater differences in plasma β across the layers were found to suppress reconnection. This was argued to be the result of fast diamagnetic drifts, which prevented consistent presence of the x-line; which would be advected away with the electron flow, necessitating large magnetic shear angles. On the other hand, reconnection was also seen for small magnetic shear angles during cases when the change in plasma beta across the current sheet was relatively low. Swisdak et al. (2010) proposed a simple relation to gauge the possibility of magnetic reconnection being suppressed in a given setting based on the change in plasma beta $\Delta\beta$ and the magnetic shear angle $\Delta\theta$,

$$\Delta\beta > \frac{2L_p}{d_i} \tan\frac{\Delta\theta}{2} \tag{1.9}$$

Where L_p and d_i denote a characteristic pressure-based length scale near the X-line and the ion inertial length, respectively.

Magnetic reconnection is a fundamental and ubiquitous process in space plasmas and occurs in many different space environments, from the solar corona to the various planetary magnetospheres, to the heliopause. The consequences of magnetic reconnection on the magnetospheres of Earth and Jupiter, and the differences between the two, are discussed in subsequent sections.

1.3 Earth's magnetosphere

A brief description of the processes occurring in the terrestrial magnetosphere is provided in this section to better understand the similarities and differences between it and the Jovian magnetosphere.

1.3.1 The solar wind and interplanetary magnetic field

The solar wind is a stream of particles accompanied by the interplanetary magnetic field (IMF), which flows outward from the sun. It originates from the lower regions of the solar corona, expands and accelerates until it gains a speed roughly between 400 to 600 km/s, by which time it is usually supersonic and super-Alfvenic (Gombosi, 1998) i.e. its bulk motion

is faster than the local sound and Alfven speeds. It is composed primarily of protons with an average temperature on the order of 10^5 K and density of $\sim$7 cm^{-3} (at 1 AU = 1.49×10^8 km), though other species and charge states are also present.

It was hypothesized that the radial flow of solar wind plasma distorts the frozen-in interplanetary magnetic field into a spiral configuration with increasing distance from the sun (Parker, 1958; Ness & Wilcox, 1964) (see Figure 1.3). This may be a reasonable assumption during quiet intervals, but the solar wind and IMF can be highly dynamic, leading to the formation of corotating-interaction-regions (CIRs) and coronal-mass-ejections (CMEs). These can be associated with drastic changes in the solar wind dynamic pressure and orientation of the IMF, which perturb the terrestrial magnetosphere in various ways (Borovsky & Denton, 2006; Denton et al., 2006) e.g. by increasing the strength of the equatorial ring current, creating geomagnetically-induced currents on the planet's surface, and strengthening the terrestrial aurora, etc.

Figure 1.3 shows two interplanetary magnetic field lines which intersect the orbits of Earth and Jupiter at 1 AU and 5.2 AU, respectively. The Parker-spiral IMF at Earth typically possesses comparable radial and azimuthal components (where $\mathbf{r}$ is the Sun-Earth direction, also the direction of solar wind flow). On the other hand, the IMF becomes predominantly azimuthal by the time it reaches Jupiter's orbit. This would translate to a near 90-degree magnetic shear between the IMF and the internal field of the planet at the subsolar magnetopause, which has important implications on the magnetopause reconnection at Jupiter that will be discussed later.

Also associated with the radial outflow of the solar wind is the heliospheric current sheet. Since the solar magnetic axis is not aligned with its spin axis, the heliospheric current sheet undulates about a mean position at the Equator (Figure 1.4). At Earth, this can be seen in the North-South (Z) component of the IMF. Periods when the IMF is southward, and thus oppositely directed to the planetary field at the dayside boundaries of the magnetosphere, are considered to lead to increased geomagnetic activity due to magnetic reconnection (Boudouridis, 2005).

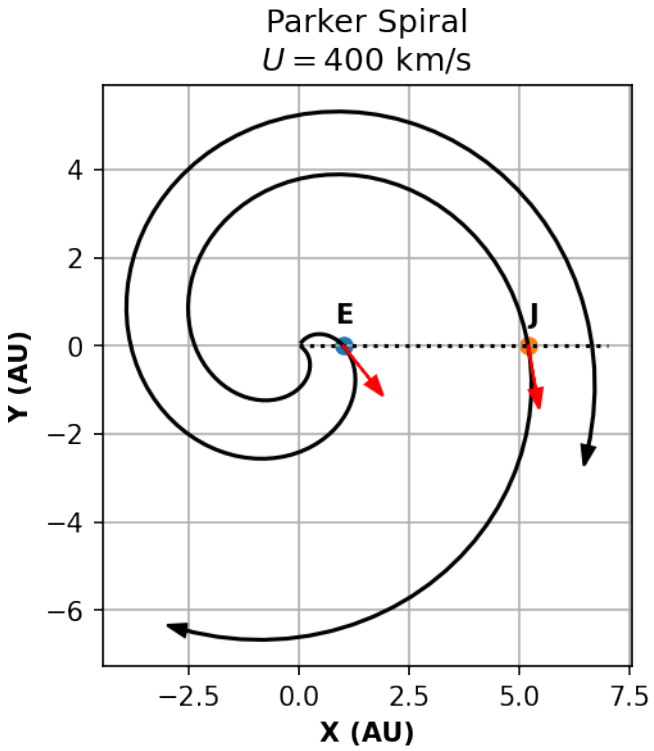

Figure 1.3: Interplanetary magnetic field lines showing the Parker-spiral in the ecliptic plane. The field lines intersect at the orbits of Earth and Jupiter at 1 AU and 5.2 AU respectively and the tangent to the curve is highlighted via arrows.

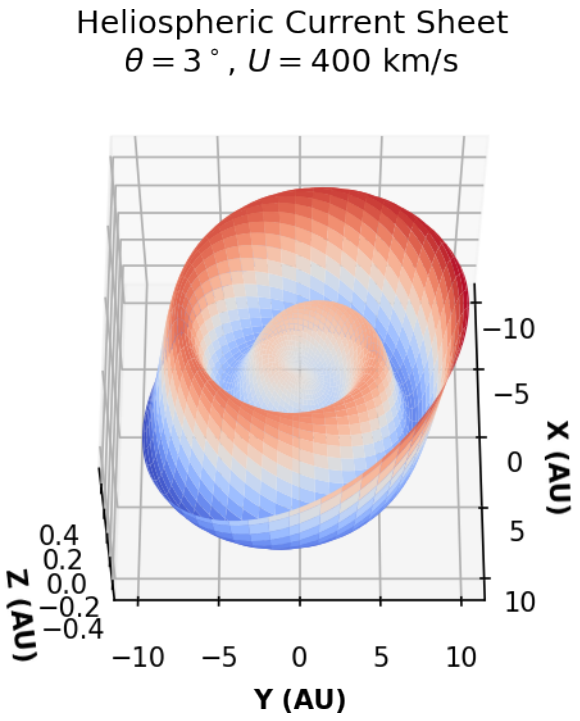

Figure 1.4: Wavy structure of the heliospheric current sheet assuming a constant 400 km/s solar wind flow and a dipole magnetic field.

1.3.2 Configuration of the terrestrial magnetosphere

The interaction between the solar wind and interplanetary magnetic field with the internal magnetic field of the Earth forms the magnetosphere. Since the incoming plasma is supersonic and super-Alfvenic, a bow shock is created at the interaction front (Spreiter, Summers, & Alksne, 1966). Downstream of the shock lies a region of shocked high-temperature solar wind called the magnetosheath (Lucek et al., 2005). The magnetic field strength in the magnetosheath is larger than in the solar wind, but the field lines are still 'open', i.e. they are connected at both ends to the interplanetary magnetic field. Separating the planetary field from the magnetosheath is a discontinuity called the magnetopause (Russell & Elphic, 1978; Sonnerup & Cahill, 1967). The magnetopause is a current-carrying layer that shields the magnetosphere from the external inputs.

On the nightside, the interaction of the tail magnetic field with the solar wind and IMF creates a magnetotail (Hones et al., 1984). Magnetic field lines in the magnetotail are considered to be primarily in the plane of the solar wind flow. Present between oppositely directed magnetic field lines in the northern and southern magnetotail lobes is the magnetospheric tail current sheet, which is surrounded by a region of high-density plasma called the plasmasheet.

In the inner regions of the magnetosphere are the planet's radiation belts; regions of trapped high-energy particles undergoing repeated bounce motions (Ripoll et al., 2020 and references therein). In these regions the current sheet is weak or non-existent and the magnetic field is close to being dipolar. Co-located with the radiation belts is the plasmasphere, composed of relatively low-energy particles (ions and electrons) which largely corotate with the Earth (Lemaire, Gringauz, Carpenter, & Bassolo, 1998).

1.3.3 Magnetic reconnection in the terrestrial magnetosphere

In the context of the terrestrial magnetosphere, magnetic reconnection is usually studied in two regions. The first region is the dayside magnetopause, where high density plasma of the magnetosheath associated with a shocked IMF interacts with the relatively low density plasma of the magnetosphere, associated with stronger magnetic fields. Magnetic reconnec-

tion has been observed to occur at all orientations of the IMF (clock angle), but is most prominent when the IMF is pointing southward (Swisdak et al., 2003), as in this situation the magnetic shear between it and the northward pointing magnetospheric field (at the magnetopause) is maximized. In such a case, IMF field lines in the solar wind reconnect with 'closed' field lines of the magnetosphere, and produce newly opened field lines which are transported away from the reconnection site by the reconnection outflow.

The second region where reconnection is studied widely is the terrestrial magnetotail (e.g. Nakamura et al., 2006). Magnetic field lines in the northern and southern magnetotail lobes which are separated by the magnetotail current sheet are often oppositely directed with respect to each other. Two such open field lines in the magnetotail may spontaneously reconnect and convert into a single closed field line. More often, magnetic reconnection is observed to occur near the planet, where field lines may still be closed, and is preceded by a thinning of the magnetotail current sheet, which results in an explosive reconnection event called a *substorm*.

Magnetic reconnection in both regions rarely occurs in a steady manner, but instead creates loop-like magnetic structures as seen in Figure 1.2. At the dayside magnetopause, these structures are referred to as flux-transfer events or FTEs. In the nightside magnetotail, they are referred to as plasmoids or flux ropes, depending on their internal properties.

1.3.4 Ionosphere

Neutral species in Earth's upper atmosphere can be ionized through photo-ionization and electron impact ionization, and the relatively low-densities at higher altitudes lead to longer collision time scales which supports a persistent region of charged particles called the ionosphere (Schunk & Nagy, 2009). The conducting ionosphere is intricately connected with the magnetosphere.

Ionospheric plasma at mid- to low-latitudes corotates with the planet due to collisions with the corotating thermospheric neutrals. The magnetic field lines associated with these regions are connected at both ends with the planet (i.e. they are *closed*) and have an equatorial footprint in the magnetosphere at a distance of a few Earth radii. Since the field lines in ideal MHD can be considered to possess the same electrostatic potential (Φ), the

corotation velocity of the ionospheric plasma is transmitted to the associated magnetic flux tube in the magnetosphere. This creates a corotating region of low-energy plasma called the plasmasphere. This is consistent with the picture that the plasmasphere is a result of $\mathbf{E} \times \mathbf{B}$ drift, where $\mathbf{E} = -\nabla\Phi$ can be considered to be the corotation electric field. Thus, the ionosphere plays a crucial role in maintaining the corotation of plasma at Earth.

At higher latitudes, magnetic field lines are typically open, i.e. they are connected at one end with the interplanetary magnetic field. In such a case, the ionosphere plays a more responsive role to changes in the solar wind and distant magnetosphere (discussed in the next section). Field aligned currents from the magnetosphere close through perpendicular (to $\mathbf{B}$) currents in the ionosphere. The precipitation of charged particles also modifies the conductivity in the ionosphere (Schunk & Nagy, 2009).

1.3.5 Magnetosphere-ionosphere coupling at Earth

The magnetosphere and ionosphere are intricately coupled at all latitudes. In the case of anti-parallel IMF, magnetic reconnection on the dayside magnetopause creates open field lines, which convect along with the solar wind. At the same time, one end of the field lines is connected to the polar regions of the planet. Eventually, open field lines, which are transported to the magnetotail by the solar wind, reconnect and re-create closed field lines. The newly closed magnetic flux returns to the dayside. This cycle of opening and closing of magnetic flux through magnetic reconnection is called the Dungey cycle and an illustration of this process is shown in Figure 1.5, which shows a simplified picture in two-dimensions of a field line which has reconnected on the dayside at stage 1, and eventually returns to the dayside (stage 9) after the motions described previously.

Effects of the Dungey cycle can be seen in the convection patterns of the high-latitude ionosphere (Figure 1.5, inset). In the anti-parallel IMF case, ionospheric plasma convects from the dayside to the nightside across the polar cap. After flux closure on the nightside, plasma returns to the dayside via flux tubes located at lower latitudes, on the dawn and dusk side of the magnetosphere; creating a two-cell convection pattern in the ionosphere. This overall convection of the magnetosphere and ionospheric plasma directly determines the location of upward field-aligned currents in the ionosphere, and hence the location of the

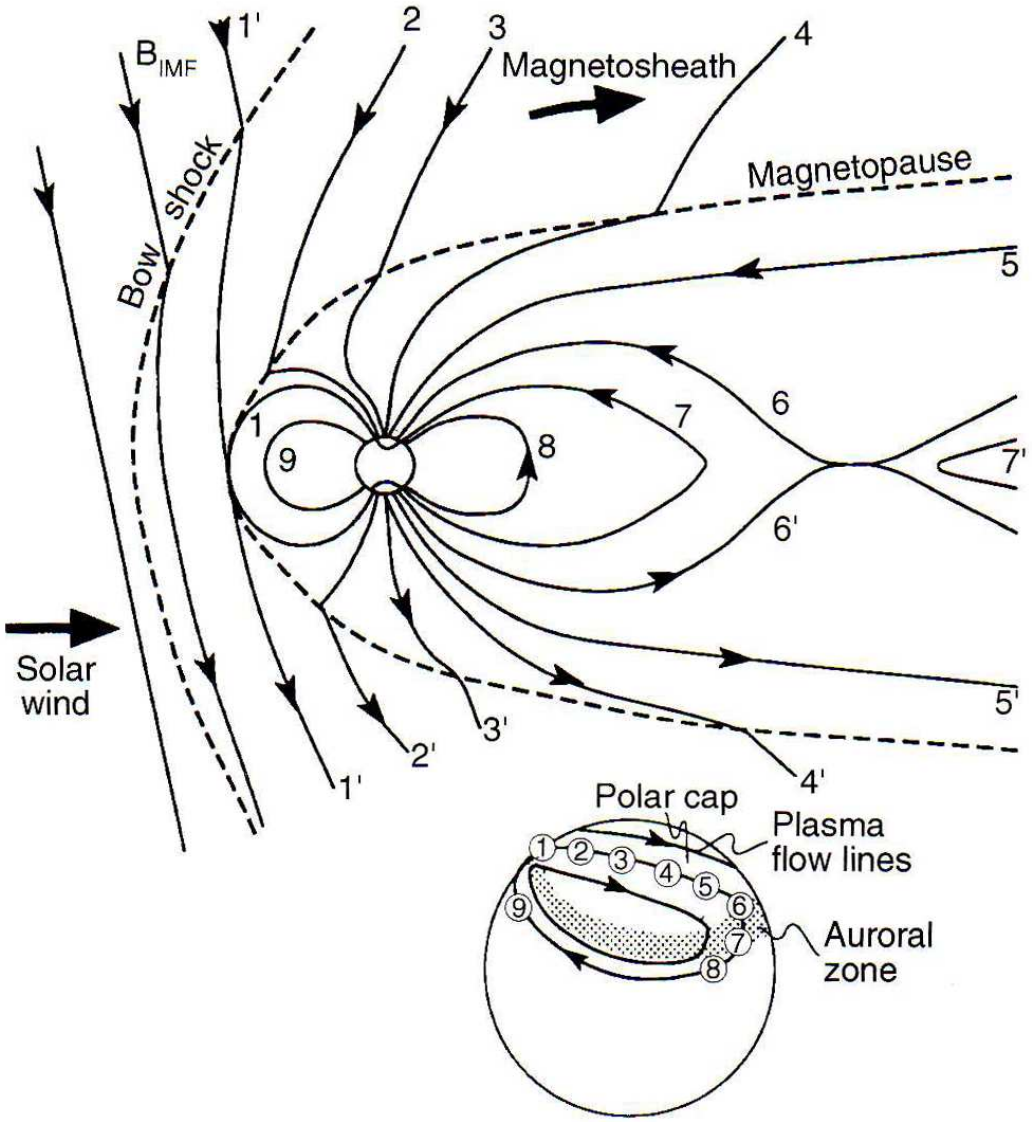

Figure 1.5: Schematic adapted from Hughes (2019) showing the different stages of the Dungey cycle in the terrestrial magnetosphere and the corresponding convection pattern in the ionosphere.

discrete terrestrial aurora.

In this way, the solar wind and interplanetary magnetic field directly influence convection in the terrestrial magnetosphere. Different IMF orientations and solar wind density and velocity change the convection patterns in the terrestrial magnetosphere and determine the size of the polar region of open flux, also referred to as the *polar cap* (Heelis, 1984; Milan, Boakes, & Hubert, 2008).

1.4 Jupiter's magnetosphere

Jupiter is a strongly magnetized planet, and the interaction of its planetary magnetic field with the solar wind and IMF creates its magnetosphere (Krupp et al., 2004). Much like at Earth, Jupiter's magnetosphere also consists of a bow-shock, magnetopause and magnetotail because of the supersonic and super-Alfvenic solar wind. However, there are crucial differences due to its large size, strong magnetic field and internal processes associated with its natural satellites. Some key differences between the two magnetospheres are highlighted in Table 1.1. Firstly, Jupiter's magnetosphere is much larger than that of the Earth in terms of the planets' respective radii. This is in part due to the strong magnetic field of Jupiter, along with the presence of energetic particles in the magnetosphere, which have a substantial contribution to the total pressure of the magnetospheric plasma (Bagenal & Delamere, 2011). Note that plasma β, which is defined as the ratio of thermal pressure p to the magnetic pressure ($B^2/2\mu_0$) is less than 1 for the plasma in most regions of the Earth's magnetosphere, but is between 10 to 100 for plasma in the Jovian magnetosphere.

The Jovian magnetosphere is usually divided into three regions for discussion (1 R_J = 71492 km is the equatorial radius of Jupiter at 1 bar pressure),

1. The inner magnetosphere, containing the Io and Europa plasma tori, which extends up to $r < 15\ R_J$.

2. The middle magnetosphere, containing the corotating regions, corotation-enforcement current systems, which ranges from $15R_J < r <\sim 30R_J$.

3. The outer magnetosphere, where corotation becomes weak and various dynamics such

	Earth	Jupiter
Equatorial Radius (km)	6378	71492
Surface field strength (nT)	∼30000	∼ 400000
Internal Source (kg/s)	5	250 to > 1000
Rotation Period (hours)	23.92	9.92
Dominant species	H^+, O^+	S^+, O^+, S^{++}, H^+
Plasma $\beta = p/(B^2/2\mu_0)$	<1	10 to 100
Magnetopause standoff distance (R_{planet})	8 to 11	62 to 111
Bow-shock standoff distance (R_{planet})	16 to 22	77 to 130
Auroral Power (GW)	20 to 100	200 to >1000
Dipole tilt (°)	∼ 11°	∼ 9.6°

Table 1.1: Comparison of various magnetospheric properties for Earth and Jupiter (Shue et al., 1998; Cairns & Lyon, 1996; Khurana et al., 2004; Krupp et al., 2004; Clarke et al., 2009; Krupp, 2016; Bagenal, 2013).

as magnetic reconnection, Kelvin-Helmholtz instabilities are observed; which lies beyond $r >\sim 30R_J$.

1.4.1 The inner magnetosphere

A key difference between the gas giant magnetospheres from that of the Earth is the presence of internal sources of plasma associated with their natural satellites (Bolton et al., 2015). In Jupiter's inner magnetosphere, the largest moons in increasing order of radial distance from the planet are Io (at 5.9 R_J), Europa (at 9.4 R_J) and Ganymede (at $\sim$ 15 R_J). Out of these, Io and Europa and considered to be un-magnetized, but interact with the surrounding magnetospheric plasma due to the conductive effects of sub-surface magma and saline oceans, respectively. Ganymede is the only known natural satellite in the solar system which possesses a strong internal magnetic field, which interacts with the Jovian magnetic field to create its own magnetosphere (Russell, 2005; Jia, Kivelson, Khurana, & Walker, 2010; Khurana et al., 2011; Kivelson et al., 1996, 2000).

Out of these satellites, Io and Europa are responsible for contributing substantial mass to the inner magnetosphere of Jupiter. Volcanism at Io creates SO_2, which is eventually ionized either electron-impact ionization or photo-ionization to produce S^+, S^{++}, O^+ and H^+ (Bagenal & Delamere, 2011 and references therein) etc. Meanwhile, plumes and/or sputtering of the atmosphere at Europa ejects water neutrals into the surroundings, which

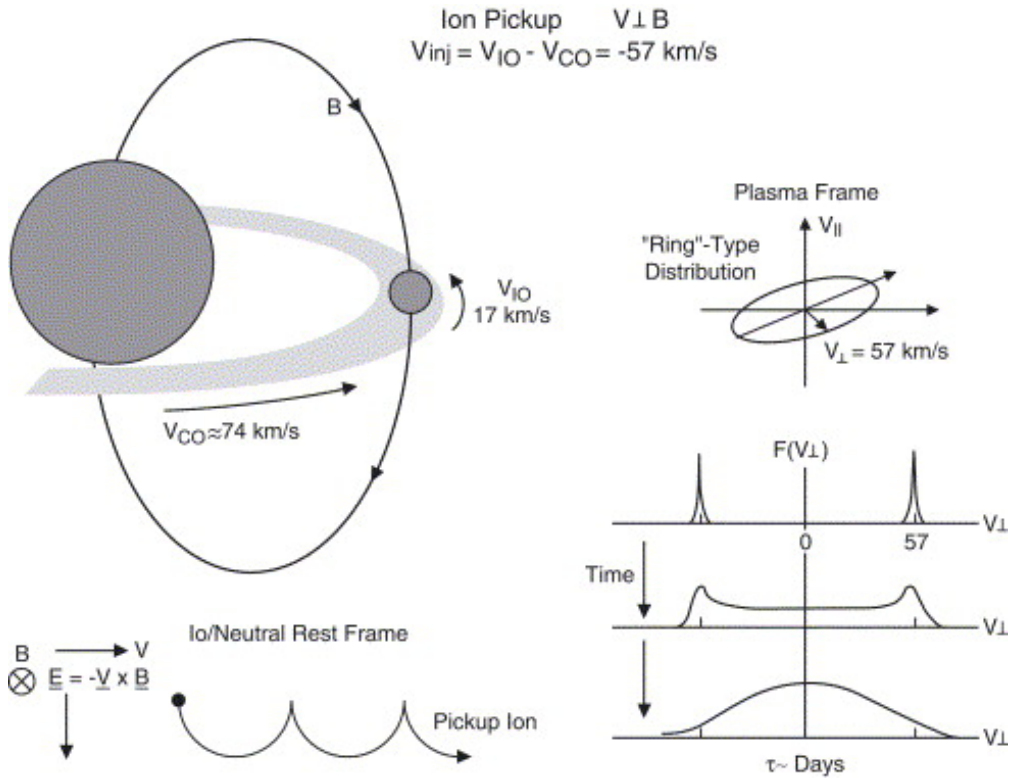

Figure 1.6: Schematic adapted from Russell (2005) showing features of mass loading at Io. The magnetospheric plasma is faster than Io's Keplerian velocity. The motional electric field of the corotating plasma "picks-up" the newly ionized particles, forming a ring-distribution that relaxes into a stable configuration over many days.

ionize to produce water group ions e.g. H^+, O^+. The typical lifetime for SO_2, S, O, H neutrals in the torus regions is between 1 to 20 hours, which implies that neutrals can diffuse away from the source and create a local neutral cloud that extends around a fraction of the natural satellite's orbit (Smyth, 1992; Smyth & Marconi, 2006). The net contribution of this ionization results in a mass addition of approximately 260-1400 kg/s for Io (Bagenal & Delamere, 2011) and ∼50 kg/s for Europa. A similar situation is seen at Saturn, where Enceladus adds ∼50 kg/s to its magnetosphere.

The newly ionized ions are "picked-up" by the surrounding magnetospheric plasma. These ions, which presumably still possess the Keplerian velocity of the neutrals (∼17 km/s at Io's orbit), perceive the motional electric field ($\mathbf{E} = -\mathbf{u} \times \mathbf{B}$) due to the faster magnetospheric flow ($u =\sim 74$ km/s) and undergo the $\mathbf{E} \times \mathbf{B}$ drift (Russell, 2005). Ion pickup increases particle velocity in the direction perpendicular to the magnetic field, increasing

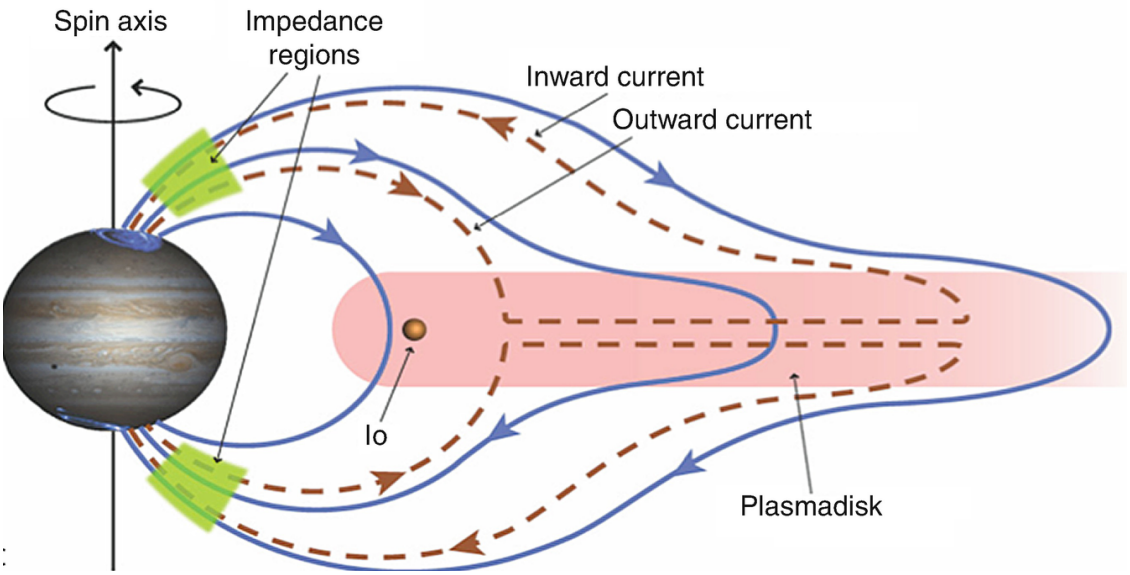

Figure 1.7: Figure adapted from Bagenal (2013) showing the extended magnetic field lines in the middle magnetosphere and the the radial currents corresponding to the out-of-plane bend back of the magnetic field. The radial corotation enforcement currents are presumed to be closed through the ionosphere.

anisotropy in the particle distribution.

The magnetospheric plasma in the inner magnetosphere co-rotates with the planet. Corotation at these distances is facilitated through ion-neutral collisions in the Jovian ionosphere, which prevents a velocity gradient from forming between the thermosphere and ionosphere; similar to the plasmasphere at Earth. The ionosphere then transmits the velocity to all regions in the magnetosphere with which it is connected via magnetic field lines. The corotation process in the inner magnetosphere does not require the presence of large-scale field aligned currents as in the case of the middle and outer magnetosphere (Vasyliunas, 1983), which we will discuss in the next section.

Also present in inner magnetosphere are trapped energetic particles comprising of Jupiter's radiation belts, which lie outside the scope of the present study.

1.4.2 The middle magnetosphere

The plasma created in the inner magnetosphere of Jupiter is believed to be lost through a series of instabilities. The large density in the inner magnetosphere leads to a decrease in flux tube content with radial distance, which, in the presence of the centrifugal force, creates

regions unstable to the interchange instability. Observations by in situ spacecraft have detected plasma and magnetic signatures containing pockets of high magnetic field strength or energetic plasma which is lower in density, within regions of lower energy high-density plasma (Thorne et al., 1997; Kivelson, Khurana, Russell, & Walker, 1997).

It is believed that as Iogenic plasma moves from the inner magnetosphere to further distances, angular momentum conservation results in the loss of some of its azimuthal velocity (S. W. Cowley & Bunce, 2001; Hill, 2001; Southwood & Kivelson, 2001), also referred to as 'breakdown of corotation'. The slowing down of magnetospheric plasma creates a "bend-back" of the frozen-in magnetic field lines in the equatorial plane, i.e. the equatorial portions of the magnetic field line begin to lag the regions located at higher-latitudes. The bending of these field lines, or more accurately, the production of magnetic curvature, creates radial currents in the equatorial region to counter the deceleration. The radial currents, together with the predominantly southward magnetic field, create a $\mathbf{J} \times \mathbf{B}$ force in the azimuthal direction, thereby enforcing corotation. These "corotation-enforcement" currents are closed via field-aligned currents and perpendicular currents in the Jovian ionosphere. The ionospheric location corresponding to the outward currents (and hence, precipitating electrons) is considered to be the location of the main oval of the Jovian ultraviolet aurora. Figure 1.7 shows a diagram of the magnetodisc configuration and the expected path of the corotation-enforcement current system.

The centrifugal force in Jupiter's magnetosphere also extends the magnetic field in the radial direction, leading to the formation of an equatorial current sheet at all longitudes, which creates a 'magnetodisc' configuration. Evidence for this process has been provided by in-situ spacecraft such as Galileo and Juno, which observed that field lines located at large distances departed greatly from the dipole expectation.

1.4.3 The outer magnetosphere

The mass added by Io and Europa thus corotates with the planet in the inner and middle magnetosphere, and in the process further stresses the magnetic field configuration. It is believed that eventually the stretching of magnetic field lines at large radial distances on the nightside thins the equatorial current sheet to an extent that allows magnetic reconnection

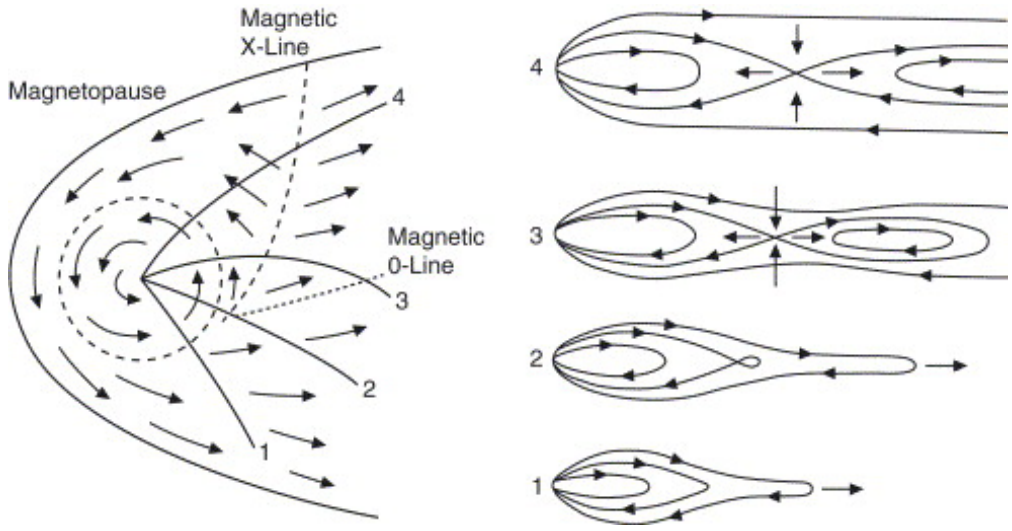

Figure 1.8: Schematic adapted from Vasyliunas (1983) and Russell (2005) showing how a plasmoid is released in the Jovian magnetotail. The image on the left shows the expected flow directions in the equatorial plane, while the different rows on the right correspond to different times during the evolution of a plasmoid.

to take place in the magnetotail, between two anti-parallel regions of the same field line.

Magnetic reconnection detaches a loop-like magnetic structures, called a plasmoid, which is disconnected from the other closed field lines and subsequently travels tail-ward to escape the magnetosphere. The newly reconnected closed field line, now devoid of heavy mass, returns to the planet and continues to corotate and re-loaded with mass from the inner magnetosphere. This cycle of mass loss through internal magnetic reconnection is called the "Vasyliunas" cycle (Vasyliunas, 1983). The Vasyliunas cycle is considered to be a crucial process that facilitates the loss of Iogenic plasma from the magnetosphere to the external solar wind. Figure 1.8 shows an illustration of this process in the equatorial and meridional plane.

Reconnection in Jupiter's magnetosphere occurs differently from the Dungey-cycle reconnection seen in the terrestrial magnetosphere, where open field lines in the magnetotail reconnect and produce a closed field line. At Jupiter, Vasyliunas cycle reconnection is believed to occur spontaneously due to the thinning of the magnetotail current sheet, with no input from the external solar wind and IMF.

In situ observations have largely confirmed that magnetic reconnection occurs in the Jovian magnetotail, either using magnetic field observations to identify rotations in the

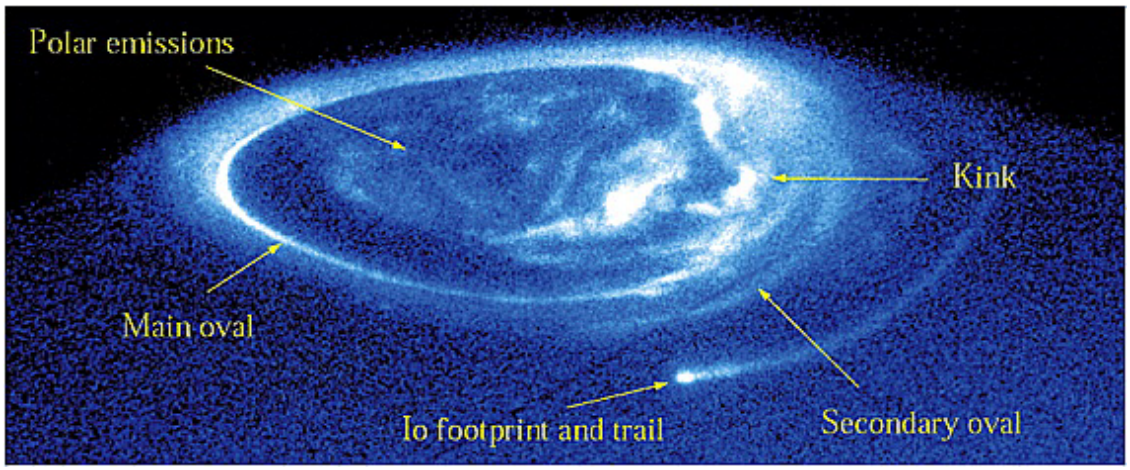

Figure 1.9: Hubble Space Telescope image of the Jovian UV aurora in the northern hemisphere adapted from Grodent, Clarke, Kim, et al. (2003), showing its different components. Dawn is roughly to the left of the image, while dusk is toward the right.

north-south component of the magnetic field (Vogt, Kivelson, Khurana, Joy, & Walker, 2010; Vogt et al., 2014), or by detecting bursts of energetic particles with a preference for travel in the radial direction (Woch, Krupp, & Lagg, 2002; Kronberg, Woch, Krupp, & Lagg, 2008; Kronberg et al., 2007). However, single-spacecraft observations do not provide information about the global context, and it is unclear whether these reconnection products result from Dungey or Vasyliunas cycle reconnection.

The relative influence of the solar wind and IMF on reconnection associated dynamics in the Jovian magnetosphere remains an open question. Some authors have argued that Jupiter's magnetosphere is largely closed, and magnetic reconnection on the dayside, if it did occur, could not lead to a persistent polar cap due to the large distances and long timescales involved (McComas & Bagenal, 2007). Others have disagreed (S. W. Cowley, Badman, Imber, & Milan, 2008), arguing that both Dungey and Vasyliunas cycle reconnection occur in the Jovian magnetotail, perhaps at different locations, on the dawn-side magnetotail and in the near-midnight region, respectively (S. W. Cowley & Bunce, 2003).

1.5 Jupiter's UV aurora

Jupiter produces bright aurora in the far ultraviolet (UV) spectrum with wavelengths usually between 70 to 180 nm in the polar regions of the planet with typical total power in the range

of 10^{12} W. The aurora are produced due to electrons of magnetospheric origin with energies typically between 30 and 200 keV (Gustin et al., 2006) precipitating into the ionosphere and causing excitation and subsequent de-excitation of H_2 or H, which releases photons in the Hydrogen Lyman and Werner bands (Grodent, 2015). Figure 1.9 shows an image from the Hubble Space Telescope of UV auroral emissions from the northern hemisphere of Jupiter. The Jovian UV auoral power is typically larger than 200 GW or even 1 TW (Clarke et al., 2009) with brightness of $\sim$ 1000 kR, which requires an electron flux of $\sim 40 - 90$ mW/m^2, corresponding to a parallel current density of approximately 0.1 or 0.2 μA/m^2 (Gustin et al., 2006). The field-aligned currents were generally assumed to be created due to the corotation enforcement current system (S. W. Cowley & Bunce, 2001).

The Jovian UV aurora has a well studied morphology and is typically divided into three components for discussion (and highlighted in Figure 1.9, with near equal intensities

1. The main emission, which maps to regions in the middle magnetosphere. The main auroral oval is present at all longitudes and is thought to be related to the corotation-enforcement current system. It corresponds to the ionospheric location where outward field-aligned currents are expected. Observations have shown that the main oval is thinner at dawn than at dusk, and is weakest in the pre-noon sector.

2. The polar aurorae, which occur pole-ward of the main oval and map to regions in the distant magnetosphere or solar wind. The polar aurorae are highly variable and show many repeating features such as 'arcs', 'swirls' and 'filaments'. Their origin cannot be determined without a clear understanding of the magnetic connectivity of the polar regions, and whether they correspond to closed or open field lines.

3. The equatorward emissions, which map to regions in the inner magnetosphere and are located equatorward of the main emission. These emissions may be a result of wave particle interactions, and could be the equivalent of 'diffuse' aurora. They have also been attributed to processes in the inner magnetosphere, such as the interchange instability.

Another set of features seen in the UV aurora are the footprints of Jupiter's natural satellites - Io, Europa, Ganymede and Callisto. These features are related to the satellites'

electromagnetic interaction with the Jovian magnetospheric plasma, and are outside the scope of the present work.

Observations made by the Cassini, HST and Juno spacecraft have hinted that the intensity of the main oval (and the overall aurora) varies according to solar wind dynamic pressure (Nichols et al., 2007, 2017), however this is not universally accepted, as most of the time there is no spacecraft to monitor the solar wind conditions upstream of Jupiter. Furthermore, by analyzing simultaneous in situ measurements made by Juno and remote observations by Hisaki spacecraft (Kita et al., 2016) find that the auroral response is delayed by almost one Jovian rotation period. On the other hand, both Cassini and Juno had opportunities for simultaneous measurements of the solar wind and the auroral intensity, and find a positive correlation.

We note that the origin of the Jovian aurora itself remains an active topic of research. Magnetic field signatures corresponding to field-aligned currents have been seen in the Juno magnetometer data near periapsis (Kotsiaros et al., 2019), along with inverted-V electron distributions (Mauk, Haggerty, Jaskulek, et al., 2017), which originate from discrete acceleration due to large electrostatic potentials. These observations support the theory of corotation-enforcement currents, but Bonfond, Yao, and Grodent (2020) challenge this idea based on recent observations. Field-aligned currents relating to the auroral regions are filamentary and weak (Kotsiaros et al., 2019). Juno's polar trajectory allowed it to sample magnetic field lines which are connected to the auroral regions, and energetic particle observations at these locations have been inconclusive. While field-aligned electron beams have been observed, there are also occasions with bi-directional electron beams or a broader pitch-angle distribution, which adds uncertainty to the hypothesis that the Jovian aurora is directly a product of field aligned currents (Mauk et al., 2018).

1.6 Primary findings

Using our MHD model, we show that an increase in solar wind dynamic pressure decreases the strength of currents in the ionosphere on the dayside (Chapter 3). Assuming that the Jovian auroral brightness is directly linked to the strength of ionospheric currents, this implies that

the Jovian aurora would dim in response to a forward shock in the solar wind. Using the model, we also demonstrate that magnetic reconnection occurs in the Jovian magnetosphere and produces open flux in the polar regions of the planet (Chapter 4). We show that magnetic reconnection may cause changes in magnetic topology of the magnetosphere such that these polar regions can connect to reconnection products in the Jovian magnetotail. In Chapter 5, we use the MHD model to study the dynamics of the Jovian current sheet, which we find is sensitive to changes in the solar wind dynamic pressure. Rather than suppressing the current sheet oscillations, increasing solar wind dynamic pressure decreases the wave-speeds in the magnetosphere, which makes the current sheet more wavy. Together, our results illustrate the complicated nature of the solar-wind-magnetosphere interaction at Jupiter. Lastly, we complement our modeling work by exploring the signatures of magnetic reconnection in the Juno magnetometer data collected in the Jovian magnetotail (Chapter 6). We show that magnetic reconnection in the Jovian magnetotail can occur on very small scales, despite the differences in large-scale magnetospheric dynamics when compared to Earth.

Chapter 2

Model Description

2.1 Introduction

Compared to the size of planetary magnetospheres, in situ coverage by spacecraft is sparse and only provides information about the immediate surroundings. In the past, when in-situ spacecraft were lesser in number, a global understanding of magnetospheric processes was limited to theoretical models, which used various assumptions to simplify the problem statement. After the development of faster computers, it became possible to simulate the magnetosphere by solving the magnetohydrodynamic equations in a large, three-dimensional domain using finite-difference or finite-volume methods (Leboeuf, Tajima, Kennel, & Dawson, 1978; Walker & Ogino, 1989; Ashour-Abdalla & Dutton, 1985).

These global magnetospheric models were crucial to understanding the terrestrial magnetosphere from first-principles. However, they did not account for various phenomena which operate outside the fluid approximation, e.g. the ring current (Fok, Moore, & Delcourt, 1999), magnetic reconnection (Birn et al., 2001) etc. Since the early models, global models of the magnetosphere have been improved tremendously and increased in complexity.

*Parts of this chapter were published in - Sarkango, Y., Jia, X., & Toth, G. (2019). Global MHD simulations of the response of Jupiter's magnetosphere and ionosphere to changes in the solar wind and IMF. Journal of Geophysical Research: Space Physics, 124.

Goodman (1995) proposed a technique to simulate the magnetosphere-ionosphere coupling by connecting the magnetospheric inner boundary with a Poisson solver for the electrostatic potential in the ionosphere. The Michigan Space Weather Modeling Framework (SWMF) coupled the magnetospheric finite-volume solver to dedicated models of the ring current (De Zeeuw et al., 2004). Improvements were made to simulate and understand the interactions between different particle species, instead of relying on a single-fluid (Glocer et al., 2009; Wiltberger, Lotko, Lyon, Damiano, & Merkin, 2010). Meng, Tóth, Liemohn, Gombosi, and Runov (2012) extended the Michigan model by allowing for different plasma pressures along the directions parallel and perpendicular to the field lines.

More recently, there has been increased interest to include kinetic-scale physics within the fluid magnetohydrodynamic models. Existing MHD models, although computationally efficient, cannot accurately predict the effect of magnetic reconnection on the plasma and the magnetosphere. On the other hand, particle-in-cell (PIC) models (e.g. Markidis & Lapenta, 2011 and references therein), which are computationally expensive, have been found to simulate the kinetic processes well. The PIC method involves tracking the influence of the electromagnetic field (due to external or internal sources) on a collection of 'particles', whose motion is modified due to the Lorentz force. Recent models have sought to combine the two approaches by embedding a smaller PIC region within a larger domain, where kinetic physics is considered to be important (Daldorff et al., 2014). An alternative approach is to use higher-order moments of the Vlasov equation (L. Wang, Hakim, Bhattacharjee, & Germaschewski, 2015), which also accounts for the missing physics in ideal MHD; the latter being derived using 3-moments .

Many attempts have been made to model Jupiter's magnetosphere, also trending towards an increasing degree of complexity. The first attempt was by Miyoshi and Kusano (1997), followed by the MHD model of Ogino, Walker, and Kivelson (1998), which was used in multiple studies to model the Jovian bow shock and magnetopause (Joy et al., 2002) and to study magnetospheric currents and the solar wind-magnetosphere interaction. Walker, Ogino, and Kivelson (2001) and Fukazawa, Ogino, and Walker (2006) improved upon the model of Ogino et al. (1998) and investigated the dynamics of the magnetosphere such as the location, frequency of occurrence and characteristics of tail reconnection and plasmoid

formation (Fukazawa, Ogino, & Walker, 2010). Moriguchi, Nakamizo, Tanaka, Obara, and Shimazu (2008) studied magnetospheric currents using their global MHD model. Chané, Saur, and Poedts (2013) developed an MHD model and used it to study the influence of mass loading due to Io on the magnetosphere. In subsequent studies (Chané, Saur, Keppens, & Poedts, 2017; Chané, Palmaerts, & Radioti, 2018), they investigated the response of the magnetosphere to changes in the solar wind (specifically increases in solar wind dynamic pressure) and its influence on field-aligned currents in the ionosphere. Recently, Y. Wang, Guo, Tang, Li, and Wang (2018) and Zhang et al. (2018) have also developed an MHD model for Jupiter's magnetosphere.

Owing to its large size and fast wave-speeds in the inner regions, modeling Jupiter's magnetosphere is computationally challenging. Due to this reason, previous models had placed their inner boundary well beyond the orbit of Io, where mass loading is expected to occur. To account for the mass loading contribution, they had either employed a fixed boundary condition at the inner boundary, or changed the location of the Io torus altogether. For the same reason, all models of the Jupiter system, including the one discussed in this Chapter, solve the ideal MHD equations (with or without relativistic terms) without the aforementioned techniques used for the terrestrial system. One exception is the recent model by Zhang et al. (2018), which uses two ion species - H^+ and O^+ to represent the population from the solar wind and from Io, respectively and is the first multi-fluid model of the Jovian system.

In this chapter we introduce a new MHD model for Jupiter's magnetosphere based on the BATSRUS MHD code (Powell, Roe, Linde, Gombosi, & De Zeeuw, 1999; Gombosi et al., 2002), which is coupled to the Ridley ionosphere electrodynamics solver (Ridley, Gombosi, & DeZeeuw, 2004). Unlike previous MHD models, our model includes mass loading due to Io in a self-consistent manner at the right location.

2.1.1 The BATSRUS MHD model

We use the Block-Adaptive Roe-type Solar wind Tree Upwind Scheme (BATSRUS) magneto-hydrodynamic (MHD) solver to model Jupiter's magnetosphere in a self-consistent manner. BATSRUS uses a finite-volume approach and can be used as a component in the larger

Space Weather Modeling Framework (SWMF) (Tóth et al., 2012), developed at the University of Michigan, which is a collection of models used in conjunction to simulate various space plasma phenomena.

Over the years, BATSRUS has developed into an industry standard for simulating the space environment, especially in global magnetohydrodynamic modeling of planetary magnetospheres and has been used to simulate the magnetospheres of Earth, Mercury, Saturn (Jia et al., 2012) and Jupiter (Hansen, 2001), and also those of exoplanets. In this work, we use BATSRUS to solve the single-fluid, ideal, semi-relativistic MHD equations, repeated below from Gombosi et al. (2002) in the conservative form.

$$\frac{\partial \mathbf{W}}{\partial t} + (\nabla \cdot \mathbf{F})^T = \mathbf{S} \tag{2.1}$$

$$\mathbf{W} = \begin{bmatrix} \rho \\ \rho\mathbf{u} + \frac{1}{c^2}\mathbf{S}_A \\ \mathbf{B} \\ \frac{1}{2}\rho u^2 + \frac{p}{\gamma - 1} + e_A \end{bmatrix} \tag{2.2}$$

$$\mathbf{F} = \begin{bmatrix} \rho\mathbf{u} \\ \rho\mathbf{u}\mathbf{u} + p\mathbf{I} + \mathbf{P}_A \\ \mathbf{u}\mathbf{B} - \mathbf{B}\mathbf{u} \\ \left(\frac{1}{2}\rho u^2 + \frac{\gamma p}{\gamma - 1}\right)\mathbf{u} + \mathbf{S}_A \end{bmatrix}^T \tag{2.3}$$

Where $\mathbf{W}$ is the state vector and $\mathbf{F}$ is the flux diad, comprising of the primitive variables - mass density ρ, plasma velocity $\mathbf{u}$, magnetic field intensity $\mathbf{B}$ and thermal pressure p. Note that in ideal MHD, the electric field is defined to be $\mathbf{E} = -\mathbf{u} \times \mathbf{B}$ (also called the motional electric field). The source terms ($\mathbf{S}$) on the right hand side will be discussed in a later section. $\mathbf{S}_A$, e_A, and $\mathbf{P}_A$ are the Poynting vector, electromagnetic energy density and electromagnetic

pressure tensor.

$$\mathbf{S}_A = \frac{1}{\mu_0}\mathbf{E} \times \mathbf{B} \tag{2.4}$$

$$e_A = \frac{1}{2\mu_0}\left(B^2 + \frac{1}{c^2}E^2\right) \tag{2.5}$$

$$\mathbf{P}_A = e_A\mathbf{I} - \frac{\mathbf{BB}}{\mu_0} - \frac{1}{\mu_0 c^2}\mathbf{EE} \tag{2.6}$$

The semi-relativistic equations are derived from the full relativistic MHD equations (Gombosi et al., 2002) by keeping the relativistic treatment of the electromagnetic terms while assuming that the plasma flow itself is non-relativistic. The use of semi-relativistic or fully relativistic MHD equations is crucial to accurately simulate Jupiter's magnetosphere since the Alfven speeds near the polar regions of the planet approach the speed of light due to the strong planetary magnetic field. This is a major limitation on numerical models, as the Courant–Friedrichs–Lewy criteria specifies that the simulation time step in time-accurate simulations using explicit time-stepping be lower than that determined roughly by the ratio of the grid spacing and the maximum wave speed in the system. Typically, the maximum wave-speed in the system is further limited to a fraction of the speed of light, also called the Boris correction (Tóth, Meng, Gombosi, & Ridley, 2011). In our simulations the Boris correction factor is chosen to be either 0.1 or 1 (no Boris correction), depending on the problem. A detailed description of the implementation for BATSRUS can be found in the literature (Gombosi et al., 2002; Tóth et al., 2012).

Our MHD model for Jupiter's magnetosphere utilizes the Space Weather Modeling Framework (SWMF) developed at the University of Michigan (Tóth et al., 2012) and is an extension of the model used by (Hansen, 2001). Two modules of the SWMF are used — a magnetospheric solver that employs BATSRUS (Gombosi et al., 2002; Powell et al., 1999), and a Poisson solver for the ionospheric electrodynamics (Ridley et al., 2004), and the two modules are two-way coupled through the SWMF. The planetary magnetic field currently used in our model is a dipole with an equatorial surface field strength of 428000 nT, and the rotation period of the planet is set to be 10 hours. While we initially set the magnetic axis to the aligned with the rotation axis, in Chapter 5 we also present the results from simulations

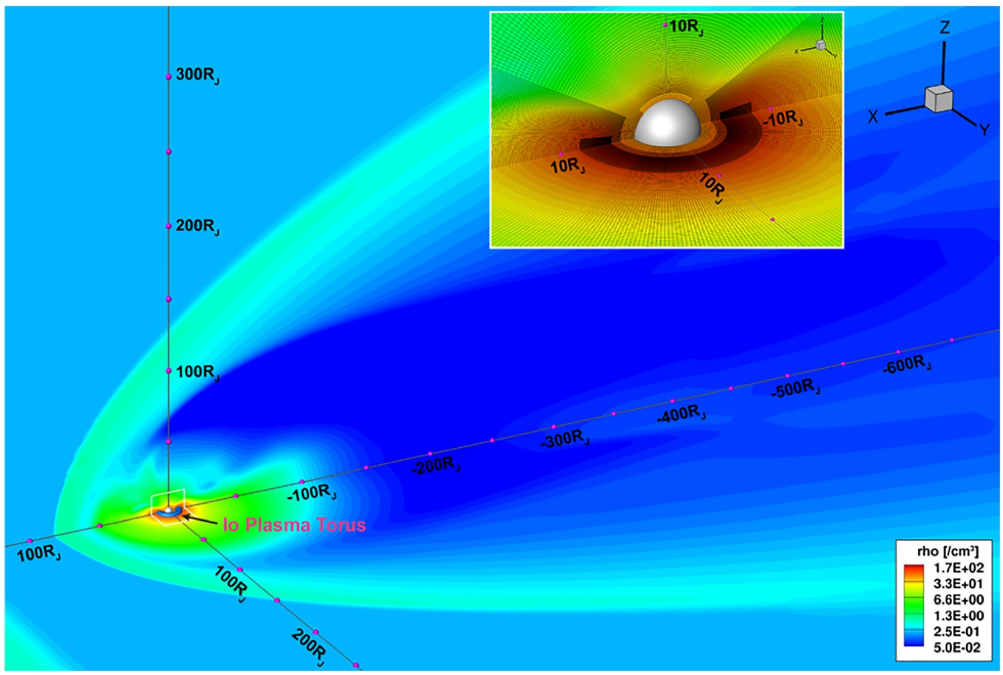

Figure 2.1: A global view of Jupiter's magnetosphere as modeled by BATSRUS. Plasma density contours are shown in the $z = 0$ and $y = 0$ plane. The inset shows the regions close to the planet, where various grid refinements can be seen. The Io torus is located at a radial distance of 6 R_J from the planet.

using a non-axisymmetric internal field, which represents more realistically the situation as observed at Jupiter.

Our three-dimensional magnetospheric simulation domain spans a spherical region of 1800 R_J centered at Jupiter, along with a planar cut at $X = 192$ R_J that serves as the upstream boundary (Figure 2.1). The radial spacing between the grid cells increases in a logarithmic manner allowing for finer cells placed in regions close to the planet. The simulation domain is subdivided into a number of blocks (Powell et al., 1999), which can be refined independently to obtain the desired grid resolution in regions of interest, such as the equatorial magnetosphere, the magnetopause boundary, and the magnetotail. Although BATSRUS allows for physics criteria-based adaptive grid refinements (Tóth et al., 2012), in our simulations the refinements are prescribed initially and are fixed. The spherical inner boundary of our simulation domain is located at 2.5 R_J, which then allows us to include the Io plasma torus centered at ∼5.9 R_J, which is the appropriate location. We specifically chose to refine a torus-like region near Io's orbit for accurately modeling the mass loading

processes occurring in the Io plasma torus. The smallest radial grid spacing is $\sim$0.06 R_J, which is present in the Io plasma torus. Figure 2.1 shows our simulation grid with contours of simulated plasma density shown in the background for context. The relatively coarse grids near the polar regions of the planet were chosen to allow for larger time steps in order to increase the speed of the simulation, as these regions contain strong magnetic fields and thus high wave speeds as well as small grid cells due to the convergence of the spherical grid near the Z axis.

All MHD variables at the upstream boundary at $X = 192\ R_J$ are prescribed on account of the super-Alfvenic and supersonic solar wind flow, whereas floating boundary conditions that set zero gradients for all MHD variations are applied at the outer boundary in the downstream direction (located at -1800 R_J). At the inner boundary at 2.5 R_J, we fixed the plasma density at 50 amu/cm^3 and set the magnetic field and plasma pressure to *float* i.e. take on values similar to the nearest MHD cell. Using the electrostatic potential calculated by the ionosphere electrodynamics Poisson solver (discussed later), we calculate the electric field ($\mathbf{E}$) at the inner boundary. The $\mathbf{E} \times \mathbf{B}$ velocity thus obtained is added to the corotation velocity ($\mathbf{u_c} = -\omega \times \mathbf{r}$) at the inner boundary.

The fluxes at cell interfaces used in the finite-volume method are calculated using a second-order accurate implementation of Linde's HLL scheme (Linde, 2002). To achieve computational speeds feasible for running long-duration simulations, we employ a hybrid time-stepping scheme. Explicit time-stepping methods are subject to the Courant-Friedrichs-Lewy criterion that imposes a stringent constraint on the allowable time step, which may become rather small in regions of high wave speeds, such as the polar region near the planet. Implicit time-stepping schemes are unconditionally stable and therefore allow larger time steps but involve matrix inversion, which can be computationally expensive for large systems. To combine the strengths of these two methods, we use an "explicit/implicit" hybrid time-stepping algorithm developed by (Tóth, De Zeeuw, Gombosi, & Powell, 2006). Since our domain is divided into grid blocks, with each block containing $6 \times 8 \times 8$ cells, this algorithm allows for each block to be solved using either explicit or implicit time stepping for a prescribed value of the computational time step. Blocks in which all cells abide by the CFL criterion defined for the time step are solved using explicit time stepping. In total,

our finite-volume grid contains approximately 19 million cells, and with a 20-s time step our global model can achieve almost real-time performance using ∼2000 cores on NASA's supercomputer Pleiades or the Frontera supercomputer at the University of Texas.

2.1.2 The Ridley Ionosphere Electrodynamics solver

The IE solver operates under an electrostatic assumption and solves for the electrostatic potential on a spherical surface of radius $R_1 = 1$ R_J using the Poisson equation (Ridley et al., 2004).

$$j_R(R_1) = [\nabla_\perp \cdot (\mathbf{\Sigma} \cdot \nabla\psi)]_{r=R_1} \tag{2.7}$$

Where j_R is the current density in the radial direction, ψ is the electrostatic potential on the surface and $\mathbf{\Sigma}$ is the height-integrated conductance tensor which, in a local cartesian coordinate system where Z in the direction of the magnetic field, takes the form

$$\mathbf{\Sigma}' = \begin{bmatrix} \Sigma_P & -\Sigma_H & 0 \\ \Sigma_H & \Sigma_P & 0 \\ 0 & 0 & \Sigma_0 \end{bmatrix} \tag{2.8}$$

With Σ_H, Σ_P and Σ_0 being the Hall, Pedersen and Alfven conductance respectively. The conductance is derived from the respective conductivity by integrating along the radial (height) direction (Goodman, 1995).

$$\Sigma_i = \int_{r_1}^{r_2} \sigma_i \, dr \tag{2.9}$$

The IE solver uses a finite-differencing method to construct the linear system which is solved using iterative methods separately for the northern and southern hemispheres.

Two-way coupling between BATSRUS and the IE solver is achieved in the following manner. Field-aligned currents from the magnetosphere are collected at a prescribed radial distance of 3 R_J ($R_J = 71492$ km is Jupiter's mean radius at 1 bar pressure) and are then mapped to the surface of the planet assuming that the magnetic field between 1 and 3 R_J is dipolar. At the surface, a Poisson solver is used to solve Ohm's law for a given distribution of

ionospheric conductance. In the present work, we assume a uniform Pedersen conductance of either 0.05 S or 0.1 S, which is on the lower end of previous estimates (0.1–10 S by Strobel & Atreya, 1983; Nichols & Cowley, 2003 and 0.47 S by Gérard et al., 2021) and set the Hall conductance to 0. The perturbation electric field obtained from the IE module is added to the co-rotational electric field, and the total electric field is then used to prescribe the plasma velocity at the inner boundary of the MHD domain at 2.5 R_J. A detailed discussion of how this coupling is achieved is given by Ridley et al. (2004) in the context of the terrestrial magnetosphere and by Jia et al. (2012) and Jia and Kivelson (2012) in application to Saturn's magnetosphere.

2.1.3 Mass loading sources terms

In order to accurately model Jupiter's magnetosphere, it is necessary to include the contribution of plasma by its moons, especially Io. Io provides the largest internal source of plasma to Jupiter's magnetosphere, estimated to add ∼250 kg/s to 1 ton/s of plasma (Bagenal & Delamere, 2011). In our model, we include contributions due to ionization and charge-exchange in the form of source terms in the mass, momentum, and energy equations. Dissociative recombination is a minor process and, therefore, neglected in the present simulations. We use a prescribed neutral torus centered at Io's orbital radius of 5.9 R_J according to the following form. The neutral distribution used for the Io torus is a modified form of the one obtained by Schreier, Eviatar, and Vasyliunas (1998) and an exponential falloff with latitude is considered. We prescribe the following expression to calculate the neutral number density (n_n [cm^{-3}]) at a spatial location defined in terms of cylindrical coordinates ($r_{xy} = \sqrt{x^2 + y^2}\ R_J$).

$$n_n\left(r_{xy}, z\right) = n_{n_0} \exp\left(\frac{-z^2}{H_s^2}\right) \times \begin{cases} 60 \exp\left(\frac{r_{xy}-5.71}{0.2067}\right), & r_{xy} < 5.71 \\ 60 \exp\left(\frac{-r_{xy}+5.685}{0.1912}\right), & 5.71 \leq r_{xy} < 5.875 \\ 19.9 \exp\left(\frac{-r_{xy}+5.9455}{0.0531 r_{xy}+0.5586}\right), & r_{xy} >= 5.875 \end{cases} \tag{2.10}$$

Where the scale height is chosen to be $H_s = r_{xy} \tan^{-1} 2.5°$. New ions are produced from the above neutral distribution by multiplying with a constant ionization rate and collision

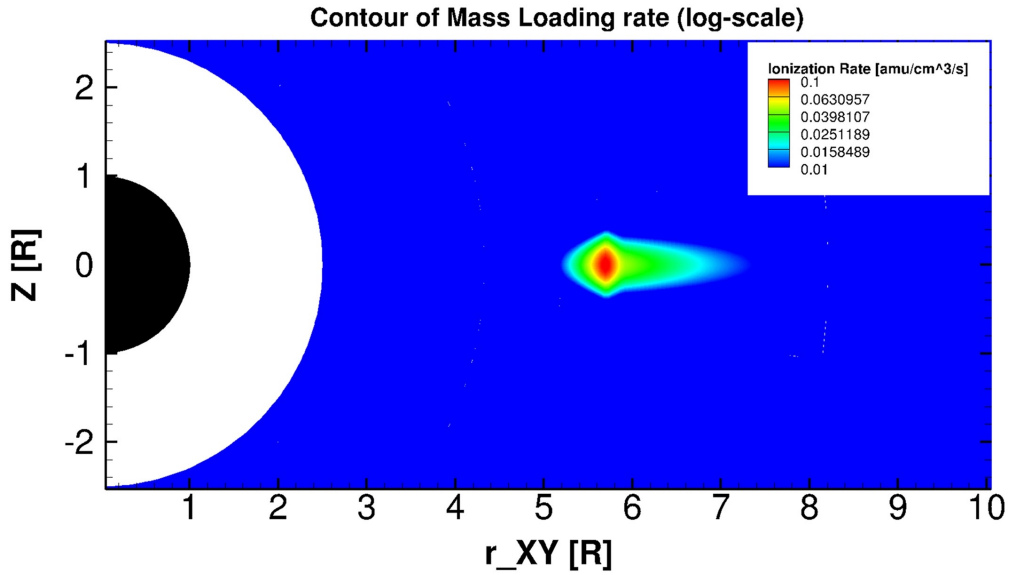

Figure 2.2: Contours of the mass loading source $\dot{\rho}$ in the meridional plane. The inner boundary is at 2.5 R_J and the gap region between the magnetosphere and ionosphere is shown in white.

cross section based on the following expression for the net plasma production rate per unit volume (units of kg m^{-3} s^{-1}):

$$\dot{\rho} = 16 m_p n_n C_i \tag{2.11}$$

Here C_i is the ionization rate (specified to 10^{-4} s^{-1} in our simulations) and 16 amu is taken to be the average mass of the heavy ions present in Jupiter's magnetosphere. Figure 2.2 shows the contours of the ionization source ($\dot{\rho}$) in the plane perpendicular to the equator. With this information, we construct the source term **S** for the mass continuity, momentum, total energy and thermal energy equations (Hansen, 2001; Gombosi, De Zeeuw, Häberli, & Powell, 1996):

$$S_\rho = \dot{\rho} - \alpha\rho \tag{2.12}$$

$$S_{\rho U_x} = (\dot{\rho} - C_x)\, u_{nx} - (C_x + \alpha)\, \rho u_x \tag{2.13}$$

$$S_{\rho U_y} = (\dot{\rho} - C_x)\, u_{ny} - (C_x + \alpha)\, \rho u_y \tag{2.14}$$

$$S_{\rho U_z} = -(C_x + \alpha)\, \rho u_z \tag{2.15}$$

$$S_E = \frac{1}{2}(\dot{\rho} + C_x\rho)\, u_n^2 - \frac{1}{2}\rho u^2 (C_x - \alpha) - \frac{3}{2}\alpha p + \frac{3}{2} C_x p \tag{2.16}$$

$$S_p = \frac{1}{2}(\dot{\rho} + C_x\rho)\, |\mathbf{u} - \mathbf{u}_n|^2 - \frac{3}{2}\alpha p \tag{2.17}$$

Where $C_x = \dot{\rho} - n_n \sigma\, |\mathbf{u} - \mathbf{u}_n|$ is the charge exchange rate, $\mathbf{u}_n$ is the Keplerian velocity of the neutral particles orbiting Jupiter, and α is the recombination rate, which is set to 0 in our current work. As described above, the ion production rate in our simulation is a controlled parameter depending on the neutral profile, ionization rate, and collision cross section. In the present work, we set the total ion production rate of $\sim$1 ton/s. It is important to note that our approach of modeling the Io plasma torus is very different from those adopted by the previous Jupiter global MHD models. For instance, the Miyoshi and Kusano (1997) MHD model had its inner boundary at 30 R_J. The inner boundary of the MHD model by Ogino et al. (1998) and Fukazawa, Ogino, and Walker (2005); Fukazawa et al. (2006, 2010) lied at 15 R_J, while the Moriguchi et al. (2008) model had its inner boundary at 8 R_J. The recent MHD model by Chané et al. (2013, 2017) used an extended ionospheric region spanning from 4.5 to 8.5 R_J and placed the Io torus at an unrealistic location of 10 R_J. In their recent model, Y. Wang et al. (2018) also chose to place the Io torus at 10 R_J for the same reasons. Our model is the first global MHD model which models mass loading due to Io in a self-consistent manner at the right location.

The above mass loading parameters were chosen based on ad-hoc assumptions to provide an equivalent mass loading rate of 1 ton/s. In practice, other neutral profiles can also be used, but regions with high plasma density gradients, such as the Io plasma torus usually have higher rates of numerical diffusion, which can diffuse the initially prescribed density distribution.

2.2 Magnetospheric configuration

To create the magnetosphere, we use steady solar wind conditions with a southward (negative B_Z) IMF (values are given in column 1 of Table 1) to minimize reconnection at the start of the simulation. We speed up the creation of the magnetosphere by using local time stepping (Tóth et al., 2012) for 50000 iterations and then switch to time-accurate mode for 150 hr to produce a quasi-steady state magnetosphere. All simulations presented in this paper have been started either from this point or a later time step. Because of the large system size and long time scales involved in Jupiter's global magnetosphere, it is necessary to use the procedure described above in order to ensure that simulation results shown and discussed here are not from a period dominated by the initial transients.

2.3 Comparisons with in-situ data

To validate our global simulation model, we first present a set of comparisons of our MHD model results with available empirical models and in situ measurements. Figure 2.3 shows a snapshot of the magnetospheric configuration in the equatorial (XY) plane extracted from the simulation using fixed nominal solar wind conditions and a southward IMF (Run 1 in Table 1) after it has reached quasi-steady state. Results are presented in a Jupiter-centered Cartesian coordinate system, where X points toward the Sun, Z is the magnetic and rotational axis (since dipole tilt is ignored in this simulation), and Y completes the right-handed coordinate system. The colors show contours of plasma density in logarithmic scale. The magenta points in the equatorial plane are the extracted equatorial footprints of the last closed field lines, which, on the dayside, correspond to the magnetopause in our model. The bow shock in our model can be readily identified as the separatrix between the unperturbed solar wind and the magnetosheath containing high-density plasmas. Also plotted are the 25% and 75% probability curves from the (Joy et al., 2002) magnetopause and bow shock models assuming the same upstream solar wind pressure as used in our simulation. The comparison shows that the modeled magnetopause and bow shock fall well within the ranges predicted by the Joy et al. (2002) empirical model. It is, however, worth noting that while the modeled

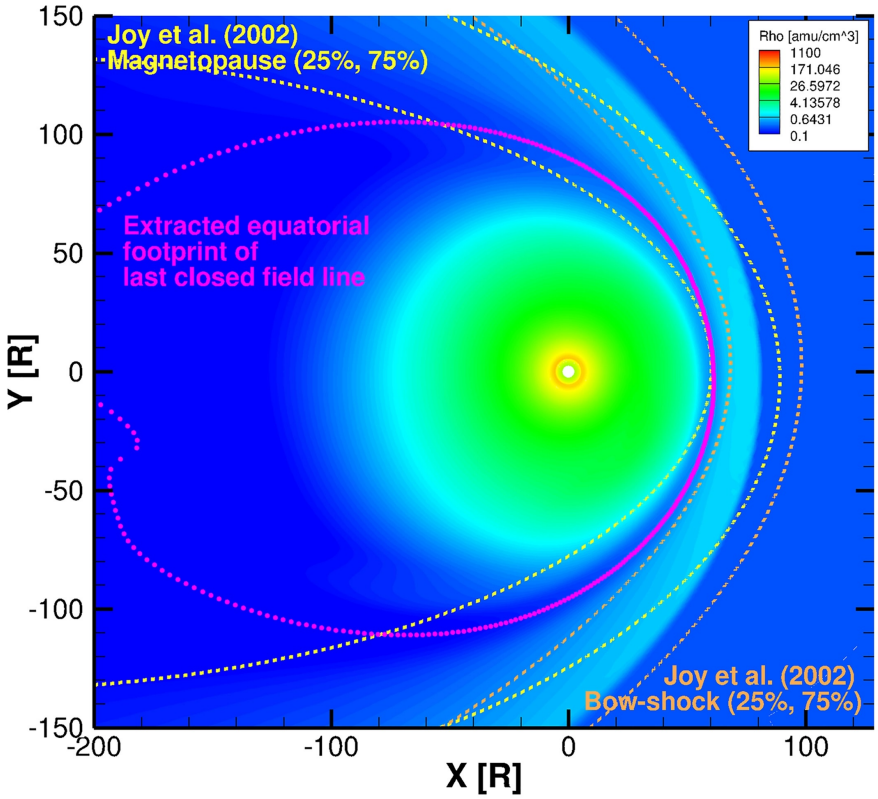

Figure 2.3: Contours of plasma density in the equatorial plane in the MHD simulation. The dashed lines represent the magnetopause and bow-shock locations from the probabilistic model of Joy et al. (2002). The magenta points represent the location of the last closed field line, which corresponds to the magnetopause location on the dayside.

magnetospheric boundaries, in general, have a good agreement with observations, the size of the magnetosphere is slightly underestimated, due in part to absence of energetic particle pressure in our MHD model.

As another step in our model validation, we compare in Figure 2.4 the radial distribution of simulated plasma parameters with available in situ observations. In analyzing our simulation output, it became clear to us that the magnetosphere exhibits strong local time asymmetries and temporal variabilities. Therefore, in order to obtain a fair comparison with satellite data, which were collected in different local time sectors and in different magnetospheric states, we extracted simulation outputs in different local time meridians (LT = 0, 6, 12, and 18) and also from different time steps that cover both the southward (Run 1) and spiral IMF (Run 3) cases. Figure 2.4a shows the time-averaged radial profiles of the simulated plasma density in the central plasma sheet (blue/cyan curves), in comparison with a compilation of density profiles obtained from previous missions (adapted from Bagenal and Delamere (2011)). The density in the inner magnetosphere (inside $\sim$10 R_J) are significantly underestimated in our simulation, whereas it matches the observations in the middle and outer magnetosphere (>10 R_J) generally well. Several factors may contribute to the discrepancy seen in the inner magnetosphere. For instance, the grid resolution in the torus region, albeit relatively fine, may not be high enough to resolve the small scale height associated with the torus. Moreover, plasma pressure is assumed to be isotropic in our ideal MHD model, but anisotropies in plasma pressure may develop in regions where ion pickup occurs, for example, in the torus. Pressure anisotropies ($p_\perp > p_\parallel$) would cause the plasma to be more confined to the centrifugal equator (e.g., as discussed by Dougherty et al. (2017)). However, because of the isotropic pressure assumption in our current ideal MHD model, the modeled plasma sheet in the inner magnetosphere is thicker than observed, which contributes to the underpredicted densities near the equator as shown in Figure 2.4a.

Figure 2.4c shows a comparison of our modeled plasma pressure with the Galileo Plasma Science (PLS) measurements (Frank et al., 2002). Again, our model predicts lower pressures than observed in the inner magnetosphere, because of the lower densities discussed above. Nevertheless, the modeled pressure has a satisfactory agreement with the observations in the middle and outer magnetosphere ($>\sim 15R_J$). Figure 2.4d compares our modeled plasma

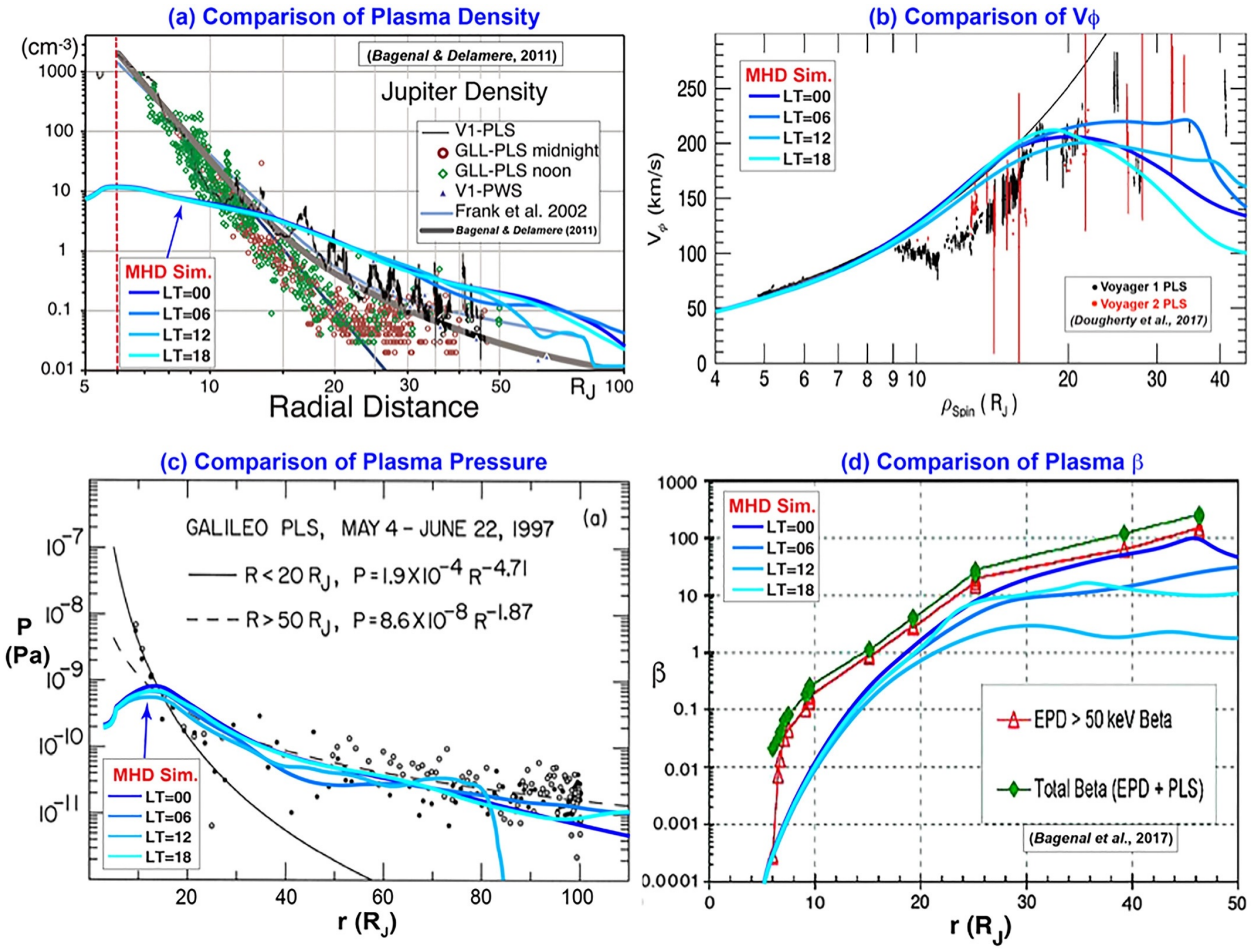

Figure 2.4: Comparisons of the plasma parameters between our global MHD model and observations. In each panel, there are four traces extracted from the MHD model representing the radial profiles at four different local times (LT = 00, 06, 12, 18). (a) Plasma density. The compilation of density profiles based on Voyager and Galileo measurements is adapted from Bagenal and Delamere (2011). (b) Plasma azimuthal velocity (V_ϕ). Voyager 1 and Voyager 2 PLS data are shown as black and red dots (with error bars; adapted from Dougherty et al., 2017). The black curve shows the rigid corotation speed for reference. (c) Plasma thermal pressure. The circles show the plasma pressures measured by Galileo PLS, while the black solid and dashed curves show fits to the data (adapted from Frank et al., 2002). (d) Plasma β. The red symbols and lines show the β that only includes Galileo EPD-measured energetic particle pressure contribution, whereas the green symbols and lines show the total β when both EPD and PLS measured pressures are included (adapted from Mauk et al., 2004).

β with Galileo observations (Mauk et al., 2004). The observations show that the plasma $\beta < 1$ in the inner magnetosphere and $\beta > 1$ in the middle/outer magnetosphere, and it crosses unity around 15 R_J. Our model results show a very similar general trend, although our modeled plasma β tends to be lower than the observations due to the underestimation of density and absence of energetic particle pressure. However, in the middle and outer magnetosphere, our simulated β appears to have a good agreement with the observations, especially in the nightside region. Our model also suggests that there is a considerable variability in the plasma β among different local time sectors (largest near the midnight sector and smallest near noon sector), which is important to consider when it comes to model-data comparison.

Figure 2.4b presents a validation of the plasma azimuthal velocity. The radial profile of the azimuthal velocity provides important constraints on models of plasma transport and magnetosphere-ionosphere coupling, as demonstrated by a number of previous studies (S. W. Cowley & Bunce, 2001; Hill, 1979, 1980; Nichols, 2011; Nichols & Cowley, 2004; Pontius, 1997). The observations show that the plasma flow starts to deviate significantly from rigid corotation around 20 R_J, where the corotation enforcement currents start to develop (S. W. Cowley & Bunce, 2001; Hill, 2001). In comparison, our modeled flow profiles show a very similar behavior in that the corotation breakdown occurs at about 15–20 R_J, in general agreement with the observations. The simulated azimuthal flows in all local time sectors are subcorotating outside of 20 R_J, with a strong dependence on local time varying between 150 and 210 km/s at $\sim$30 R_J, which may account for the relatively large scattering of the measured flow velocities in this region. One feature in the observations that is not captured by our model is the deviation of the plasma flow from rigid corotation between 9 and 15 R_J. Plasma subcororation in this region so deep inside the magnetosphere was not predicted in the previous theoretical and numerical models. The physical cause of this behavior remains unidentified at present, and requires further investigation.

In addition to the plasma parameters, we also compare our simulated magnetic field with observations. As an example, Figure 2.5 presents a comparison of the magnetic field component normal to the current sheet (B_N) to the data collected by previous missions, including Pioneer, Voyager, Ulysses, and Galileo (Vogt et al., 2011). This data set was

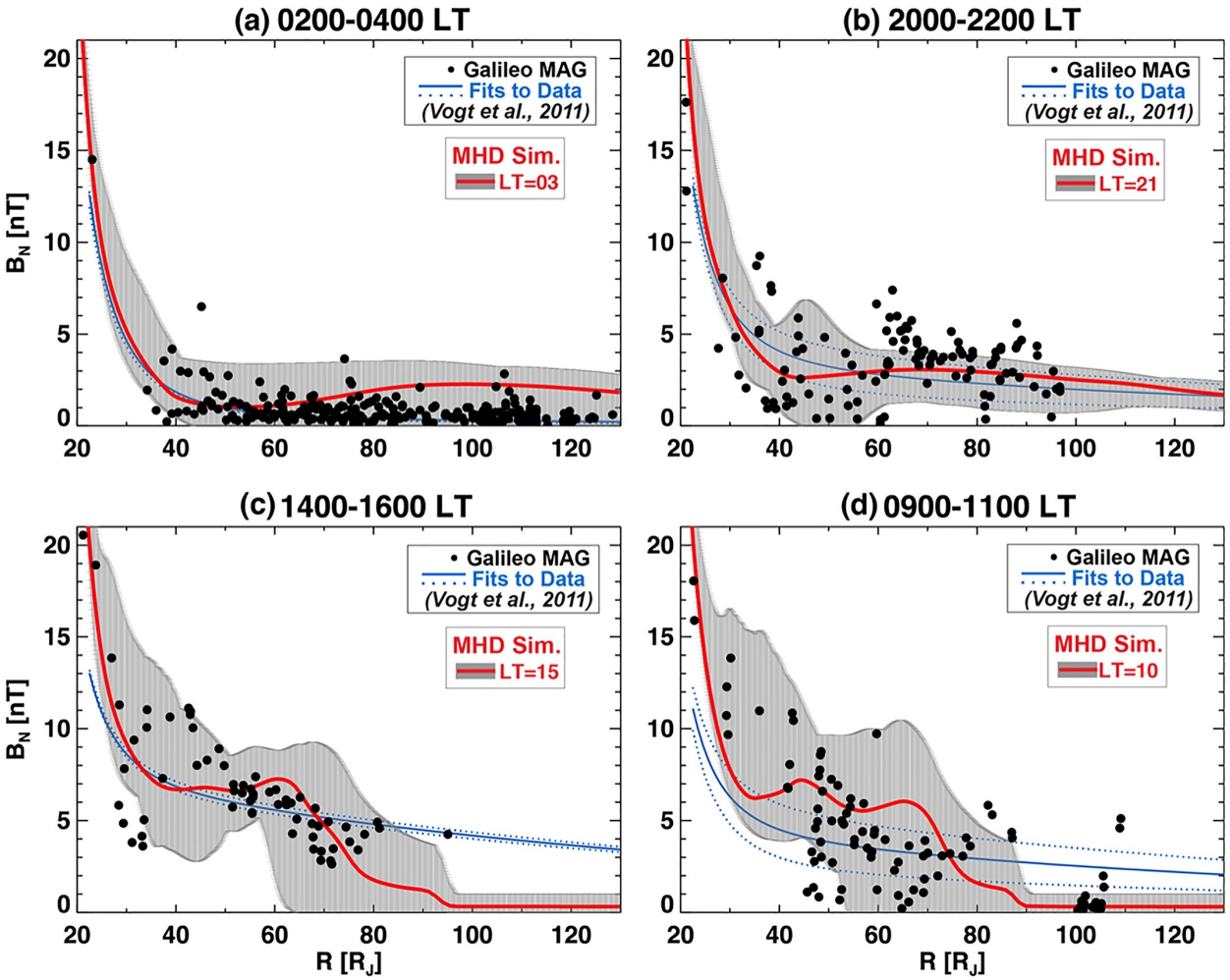

Figure 2.5: In each panel, the black dots show observations of the magnetic field component (B_N) normal to the current sheet, and the blue solid and dashed lines show fits to the data (adapted from Vogt et al., 2011). The red line in each panel represents the average radial profile of B_N output from our magnetohydrodynamic (MHD) simulation in the same local time sector as the data were collected, and the grey bars in the background show the range of values seen at different simulation times in our global model. (Figures adapted from Vogt et al., 2011)

the basis of the magnetic field model (fits to the data shown as blue curves in the figure) developed by (Vogt et al., 2011) that allows to map regions in the magnetosphere to the ionosphere. The observational data were shown in different local time bins; thus, we extracted our model results from the same local time sectors correspondingly. Since there are time-varying structures formed in our simulation even under steady upstream conditions, we show both the time-averaged radial profiles and the range of B_N seen in our simulation. Overall, our model result follows the trends of the B_N variation quite well in all local time sectors compared. Comparing the ranges of our modeled B_N with the data also shows that much of the scattering in the data could potentially be attributed to temporal variations of the magnetosphere and/or changes due to external conditions. Moreover, our model captures very well the observed local time asymmetry in B_N (weak on the dawnside and strong on the duskside), indicative of the different thicknesses of the current sheet between dawn and dusk that have been identified previously (Khurana & Schwarzl, 2005; Kivelson & Khurana, 2002).

2.4 Limitations of the model

We note that the global simulations presented here are based on an ideal MHD model, which does not capture non-ideal MHD processes, such as energy-dependent particle drifts, temperature anisotropy, and kinetic physics involved in magnetic reconnection. While no simulation can fully model the complexity of a planetary magnetosphere, extensive prior work has demonstrated that MHD models generally can provide a reasonably good representation of the global structure of a planetary magnetosphere whose size is much larger than the characteristic ion spatial scales, which is the case for Jupiter. This is true, because while magnetic reconnection occurs due to numerical resistivity in the model, it generally occurs at the right location where the current sheets carry strong currents (numerically represented by a jump in the magnetic field) and approximately with the correct reconnection rate that is some fraction ($\sim$0.1) of the Alfven speed (the numerical diffusion term is proportional with the local maximum wave speed); therefore, the global solution is expected to be approximately right. The main goal of this study is to investigate the large-scale response of

Jupiter's coupled magnetosphere-ionosphere system to solar wind drivers, for which an MHD model is a suitable tool.

2.5 Summary

We have developed a new MHD model for Jupiter's magnetosphere using the BATSRUS MHD code. To validate the model, we compared the modeled density, velocity, thermal pressure, magnetic field, and plasma β extracted from multiple time steps and from simulation runs with different external conditions with available in situ observations and found generally good agreements. In particular, while our model under-predicts the plasma density (and pressure) in the inner magnetosphere ($< 10R_J$) due to potential reasons of grid resolution and/or the assumption of isotropic pressure in ideal MHD, our model results match very well the statistical results from observations outside of 10 R_J in terms of plasma density, azimuthal velocity, and the magnetic field. Further, our model also captures the dawn-dusk asymmetries in the thickness of the current sheet (Khurana & Schwarzl, 2005; Vogt et al., 2011) as observed by the Galileo spacecraft, that is, thicker current sheet on the dusk-side compared to dawn. The locations of the magnetopause and bow shock in our model are also generally consistent with the predictions by the empirical models of (Joy et al., 2002), although our simulated magnetopause is slightly smaller in size due to the lack of energetic particles in the MHD model.

Chapter 3

Influence of the Solar-wind on Jupiter's Ionospheric Currents

3.1 Introduction

The gas giants, Jupiter and Saturn, both possess a strong internal magnetic field like Earth, but the relatively fast planetary rotation and the presence of significant internal sources of plasma lead to vastly different magnetospheric configurations and dynamics compared to the terrestrial magnetosphere (Khurana et al., 2004; Krupp et al., 2004). The internal sources of plasma at the giant planets are supplied predominantly by their moons, Io at Jupiter (Bolton et al., 2015) and Enceladus at Saturn (Blanc et al., 2015). In particular at Jupiter, through ionization of its volcanically erupted neutral particles, Io supplies heavy ions at a rate of ∼250–1,000 kg/s to the magnetosphere (Bagenal & Delamere, 2011). This leads to a high-density plasma sheet that is forced to corotate with the planet to large radial extents (∼20–30 R_J) by the corotation enforcement current system composed of radial currents in the equatorial plane, field-aligned currents that couple the magnetosphere to the ionosphere

*Parts of this chapter were published in - Sarkango, Y., Jia, X., & Toth, G. (2019). Global MHD simulations of the response of Jupiter's magnetosphere and ionosphere to changes in the solar wind and IMF. Journal of Geophysical Research: Space Physics, 124.

and Pedersen currents in the ionosphere (S. W. Cowley & Bunce, 2003, 2001; Hill, 1979, 1980, 2001; Vasyliunas, 1983). In studying the complex spatial form and temporal variability of Jovian aurora, it is typically subdivided into three components—main emission (oval), polar emissions, and equatorward emissions. The main oval of the Jovian aurora is thought to be at the location in the ionosphere where upward field-aligned currents associated with the corotation enforcement current system are present (S. W. Cowley & Bunce, 2001; Hill, 2001; Southwood & Kivelson, 2001). Theoretical models have predicted that a compression of the magnetosphere due to an increase in solar wind dynamic pressure would lead to a reduction of the main auroral oval intensity on the dayside (S. W. Cowley & Bunce, 2003; S. W. Cowley, Nichols, & Andrews, 2007; Southwood & Kivelson, 2001). Subcorotating plasma in the dayside equatorial magnetosphere would speed up in the azimuthal direction as the magnetosphere is compressed due to conservation of angular momentum, thereby decreasing the strength of the corotation enforcement current at this location, which in turn would dim the Jovian main aurora. Using a global magnetohydrodynamic (MHD) model, Chané et al. (2017) found that while the nightside/flank currents in the ionosphere are enhanced due to a simulated forward shock, the dayside currents are weakened, which is consistent with the previous theoretical prediction.

Although the Jovian ultraviolet (UV) aurora is well structured and always present, remote observations made by the Hubble Space Telescope (HST) and Hisaki/EXCEED observations of the Jovian UV aurora have also shown that its intensity is highly variable and is often correlated with the dynamic pressure of the upstream solar wind (Clarke et al., 2009; Kimura et al., 2015, 2018; Kita et al., 2016; Nichols et al., 2007, 2017). Due to lack of a dedicated solar wind monitor at Jupiter, identifying the correlation between changes in the auroral emissions and upstream parameters typically requires a numerical model, typically a 1-D MHD model (Tao, Kataoka, Fukunishi, Takahashi, & Yokoyama, 2005; Zieger & Hansen, 2008), to propagate the solar wind from 1 AU to Jupiter's orbit, which is subject to timing errors due to assumptions made in the model and the orbital geometry/alignment of Jupiter relative to available solar wind monitors at 1 AU. Exceptions to this situation include Cassini's flyby of Jupiter and Juno's approach orbit, during which in situ measurements of the solar wind and remote observations of the Jovian aurora could be made simultaneously (Gurnett et

al., 2002; Nichols et al., 2007, 2017). Gurnett et al. (2002) report an event where Cassini observed an interplanetary shock a few hours prior to a large increase in UV emission intensity from Jupiter. Recently, (Nichols et al., 2017) report observations made by HST during Juno's approach to Jupiter, during which the Juno spacecraft detected a large increase in solar wind dynamic pressure (Wilson et al., 2018), which resulted in intensification of the main emission in UV, observed by both HST and the Hisaki spacecraft (Kimura et al., 2017).

Intensities of the polar emissions are comparable to those of the main emission (Grodent, Clarke, Waite, et al., 2003); however, unlike the main emission, they do not have a steady morphology and are highly variable. UV observations made by HST have shown that the polar aurora contains highly dynamic regions with different repeating patterns such as "swirls" (in the swirl-region), "arcs," and "patches" (in the dusk active region) and occasional "filaments" (Bonfond et al., 2017; Grodent, 2015; Grodent, Clarke, Waite, et al., 2003; Nichols, Clarke, Gérard, & Grodent, 2009). Due to the complex rotationally driven dynamics of the Jovian magnetosphere (Vasyliunas, 1983), it is unclear how much open flux is typically present in the Jovian polar regions, and which features of the polar aurorae map to open field lines in the solar wind as opposed to processes in the outer magnetosphere or magnetotail (S. W. Cowley & Bunce, 2003). Some models argue that Jupiter's magnetosphere is largely closed (McComas & Bagenal, 2007), since the reconnected field lines may undergo successive reconnection during the time it takes to travel through the magnetosphere, while other studies predict that Jupiter's magnetosphere does contain appreciable amount of open flux (S. W. Cowley et al., 2008; Masters, 2017; Vogt et al., 2011) and that the Dungey cycle (Dungey, 1961) and the Vasyliunas cycle coexist to influence the structure and dynamics of Jupiter's magnetosphere.

Using the MHD model (Chapter 2), we investigate in detail the time-dependent global response of the Jovian magnetosphere to different types of solar wind disturbances, such as interplanetary shocks and the rotation of the interplanetary magnetic field (IMF). We analyze the response of the corotation enforcement current system to these upstream changes, to ultimately understand how the Jovian UV aurora may respond to changes in the upstream solar wind.

	Run1	Run2	Run3	Run4
Duration (hours)	400	100	150	100
$\mathbf{n}$ (cm^{-3})	0.2	0.5463	0.2	0.5463
$\mathbf{B}$ (nT)	$(0, 0, -1)$	$(0, 0, -2.82)$	$(0, 1, 0)$	(0, 2.82, 0)
$-u_x$ (km/s)	400	532.47	400	532.47
p_d (nPa)	0.053	0.258	0.053	0.258

Table 3.1: The solar wind and IMF properties used in this study. The solar wind flows in the $-X$ direction. The last row highlights the solar wind dynamic pressure. For Runs 3 and 4, the IMF is oriented toward the Y direction, which is typical for Jupiter's orbit.

3.2 Methodology

After creating the quasi-steady state magnetosphere using a purely southward IMF, we continue the simulation in time-accurate mode and perform four simulation runs using the following sets of upstream input (Table 3.1).

- Run 1: No change—continued run with fixed southward B_Z and steady solar wind
- Run 2: Introduce a dynamic pressure enhancement (forward shock) under southward IMF
- Run 3: Turn the IMF from a purely southward (B_Z) to Parker-spiral like ($B_Y > 0$).
- Run 4: Introduce a dynamic pressure enhancement (forward shock) under Parker spiral IMF

Two configurations of the magnetosphere were first created: Run 1 for a closed magnetosphere with a parallel/southward IMF and Run 3 for an open magnetosphere with a Parker spiral IMF. After the completion of Runs 1 and 3, upstream solar wind conditions were changed to simulate a dynamic pressure enhancement similar to that expected for an interplanetary forward shock (Runs 2 and 4). Solar wind plasma properties and magnetic field magnitude between Runs 1 and 3 were kept the same, that is, same mass density, velocity, and thus dynamic pressure. Likewise, the plasma properties and magnetic field magnitude of the shocked solar wind in Runs 2 and 4 were kept the same, with the only difference being the IMF clock angle. We designed these simulations specifically for understanding the

influence of the solar wind dynamic pressure enhancement on Jupiter's magnetosphere under two different states: a closed magnetosphere with minimal impact from dayside reconnection and an open magnetosphere with dayside reconnection expected between the Parker spiral like IMF and the magnetospheric field.

3.2.1 Calculating the net ionospheric current

The ionospheric Ohm's law solver used in our model adopts a spherical grid discretized at specific intervals in latitude and local time, where each point can be identified by the indices j and i, respectively. For a given simulation time n, we first calculate the net outward current (units of amperes) for a particular local time bin i as,

$$I_1^n(\phi)_i \approx \sum_{j=1}^{N_\theta} \left(\frac{|J_R| + J_R}{2} \right)_{i,j} \Delta s_{i,j} \tag{3.1}$$

In this equation $J_{R_{i,j}}$ the radial current density at location (i, j) and $\Delta s_{i,j}$ is the area of the spherical rectangle formed by the points $(i + 1/2, j)$, $(i - 1/2, j)$, $(i, j + 1/2)$, and $(i, j - 1/2)$. We then sum I_1 over all local times to obtain the net outward current (units of amperes) in one hemisphere at a particular time n as -

$$I_{net}^n = \sum_{i}^{N_\phi} I_1^n(\phi)_i \tag{3.2}$$

Here N_ϕ and N_θ are the number of grid cells in the azimuthal and meridional directions, respectively. In our simulations $N_\phi = 361$ and $N_\theta = 181$ for each hemisphere. The quantity I_{net} represents the net outward current from one hemisphere.

3.3 Results: Magnetospheric response

In Figure 3.1 we show the response of the magnetosphere from these four runs. Plotted in the left and right columns are contours of plasma mass density (log scale) in the meridional plane and equatorial plane, respectively, along with the equatorial footprints of the last closed field lines. In the meridional ($Y = 0$) plane, we also superimpose magnetic field lines in white

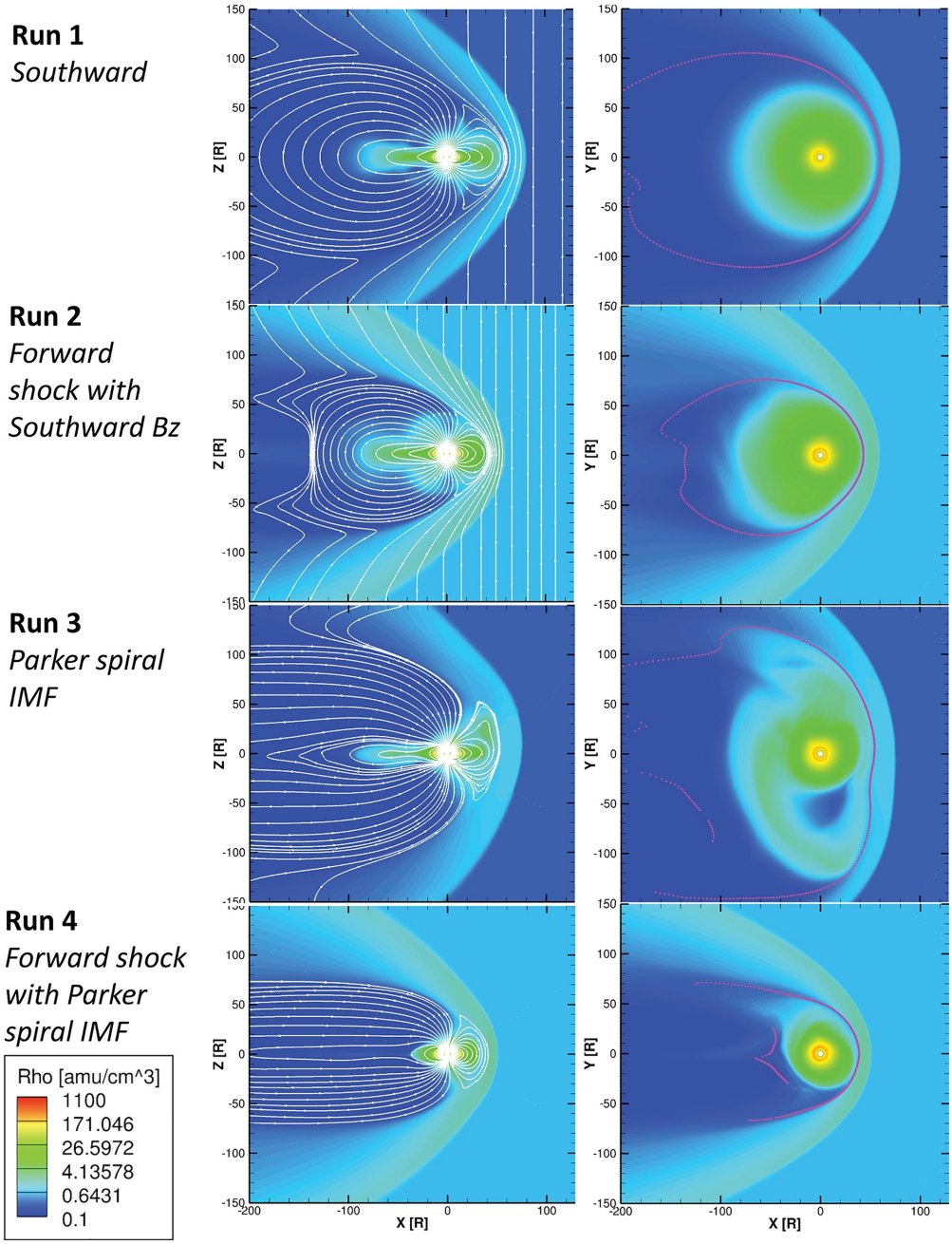

Figure 3.1: The magnetospheric response to various solar wind conditions. Shown in the left column are plasma density contours in the noon-midnight meridian (XZ plane) with superimposed magnetic field lines in white. The right column shows the plasma density contours in the equatorial (XY) plane. The magneta dots are the identified equatorial crossings of the last closed field lines.

that illustrate the disk-like configuration in the inner and middle magnetosphere, which is indicative of the presence of a strong current sheet and departure of the magnetospheric field from dipolar configuration, which is qualitatively consistent with in situ magnetic field measurements (Khurana, 2001).

3.3.1 Magnetospheric response to IMF rotation (Run 3: From southward B_Z to spiral IMF with $B_Y > 0$)

When the IMF is turned from parallel to a spiral configuration, the magnetic shear across the dayside magnetopause increases such that magnetic reconnection occurs at the dayside magnetopause in the simulation resulting in the twisted dayside magnetic field lines as shown Figure 3.1, row 3. On the nightside, the equatorial footprints of the last closed field lines provide an indication for the location of the reconnection X-line, and we find that after turning the IMF to the Parker-spiral configuration, the tail X-line moves planetward. The tail X-line location also exhibits a dawn-dusk asymmetry, being located further from the planet on the duskside and closer to the planet on the dawnside, consistent with that inferred from observations (Vogt et al., 2010, 2014; Woch et al., 2002). In addition to the planetward shift of the tail X-line, turning the IMF also adds open magnetic flux to the magnetotail lobes, which will be discussed in later chapters. As open field lines are added to the tail lobes, the tail magnetic field becomes more stretched with a strong B_X component, in contrast to the dipolar configuration under parallel IMF conditions (Run 1 as shown in row 1 of Figure 3.1).

3.3.2 Magnetospheric response to dynamic pressure enhancement (Runs 2 and 4)

The forward shock introduced in Runs 2 and 4 corresponds to a dynamic pressure enhancement of a factor of $\sim$5 (from 0.053 to 0.258 nPa) with the plasma properties upstream and downstream of the shock taken such that the Rankine-Hugoniot shock relations are satisfied. For Run 2 where the IMF is maintained in the parallel orientation that results in a closed magnetosphere, compression by the introduced forward shock causes the bow shock to move

from ∼80 to ∼60 R_J at the subsolar point, whereas the subsolar magnetopause moves from ∼60 to ∼40 R_J. In the case of an open magnetosphere (Run 4 where the IMF is in the spiral configuration), the bow shock moves from ∼75 to ∼50 R_J, whereas the magnetopause moves planetward from ∼50 to ∼40 R_J at the subsolar point in response to the shock of the same magnitude as in Run 2. The compression due to the forward shock shrinks the magnetosphere in all directions, including the lobes and magnetospheric flanks. In both cases of the closed and open magnetosphere, the last closed field lines move planetward on the nightside. Run 4 shows the location of the X-line for the shocked Parker-spiral IMF, and it lies between 50 and 70 R_J near midnight. Near the magnetopause flanks, the last closed field lines lie at a distance of 100 R_J from the planet. This creates a peculiar configuration of the magnetotail where the closed field lines extend to larger distances on the flanks than in the midnight sector, similar to that predicted for Saturn by (Jia et al., 2012).

In Figure 3.2, we show the contours of plasma angular velocity about the Z axis in the meridional and equatorial plane at different times corresponding to Run 2. The angular velocity is normalized to that of the planet, i.e. $\Omega/\Omega_J = 1$ imply that the plasma is fully corotating with the planet. Also shown are the contours of current density in the ionosphere at the corresponding times. Under steady solar wind conditions, the plasma in the inner and middle magnetosphere is seen to corotate with planet until 20 to 30 R_J, when it starts to lag the planetary rotation. This behaviour is seen throughout the field lines mapping these radial locations. The polar regions of the planet, however, do not show any preference for corotation.

After a forward shock is introduced in the solar wind, the profiles of corotation velocity are perturbed. Initially, within a ∼5 hour period, the shock shrinks the corotating region on the dayside. After ∼ 10 hours, after the passage of the shock, the angular velocity at the dayside outer magnetosphere increases, and regions which were previously sub-corotating are now seen to fully corotate. This transient increase in plasma angular velocity on the dayside subsides after additional time has passed. Correspondingly, as the magnetosphere is compressed, the current density in the ionosphere decreases on the dayside. The reduction in currents is not immediate, but occurs after a delay corresponding to the time when the strongly corotating region forms behind the dayside magnetopause. Both features in the

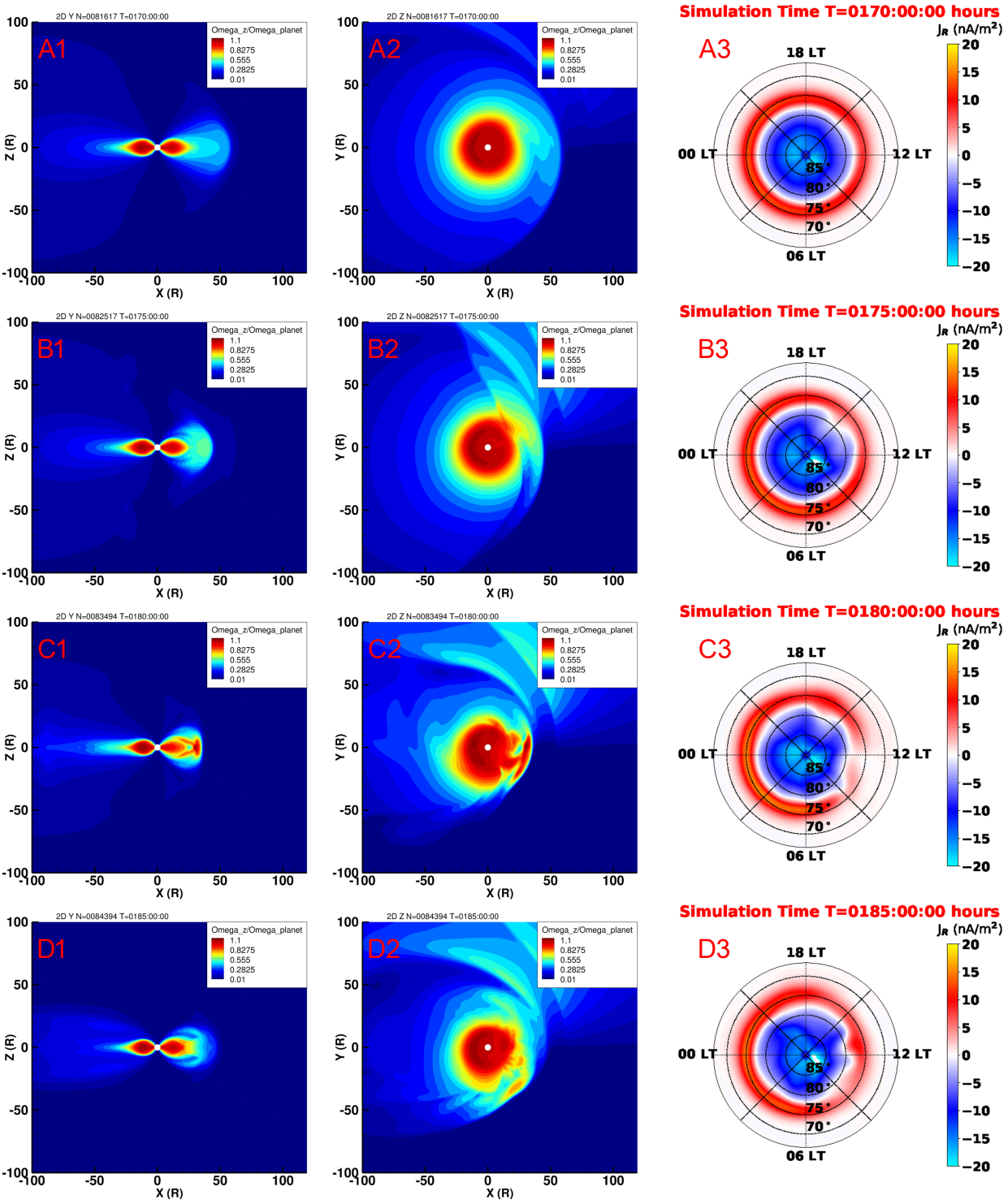

Figure 3.2: Contours of $\Omega_z/\Omega_{\text{Jupiter}}$ in the equatorial and meridional plane for Run 2 during a solar wind driven compression of the magnetosphere. The rightmost column shows the corresponding current density in the ionosphere.

magnetosphere and ionosphere are seen at $\sim$ 10 LT, as the field exhibits the least bend-back at these locations.

A similar behaviour was seen during Run 4, as shown in Figure 3.3. In this case as well, the corotation velocity of the plasma was seen to increase after the solar wind driven compression. However, unlike in the previous case, a large solar wind dynamic pressure causes reconnection to occur in the magnetotail, which generates faster return flows which increase the corotation velocity at the edges of the corotating region at around 03-05 local time. As in the case of Run 2, the response of the ionosphere and magnetosphere is seen several hours after the passage of the shock.

3.4 Results: Ionospheric response

Figure 3.4 shows the response of the ionosphere to different changes in the upstream conditions. The left column presents snapshots from each run showing the contours of the current density parallel to the magnetic field ($J_{\parallel}$). For the northern hemisphere shown here, positive values indicate outward currents and negative values indicate inward currents. The main feature of the current distribution is the circumpolar ring of outward currents centered at $\sim$ 75° latitude. Inside of (or poleward of) the ring are downward field-aligned currents. The upward and downward currents are connected through the horizontal Pedersen currents in the ionosphere, and these currents together make up the corotation enforcement current system.

The parameter I_1 is plotted as a function of local time in column 2 of Figure 3.4. Each thin line represents the nth time of the simulation with a spacing of 0.5 hr. Thick blue or red lines represent the average value of I_1 at a particular local time before and after changing the upstream conditions, respectively. As can be seen in column 2, the parameter I_1 is useful for revealing the local time-dependent response of the outward currents, which are thought to be related to the emission intensity of Jupiter's main auroral oval.

I_{net} is plotted as a function of simulation time in Figure 3.4, column 3. The red vertical dashed line represents the time when the upstream perturbation reaches the subsolar bow shock. Blue curves in column 3 represent the trend expected if there was no change in

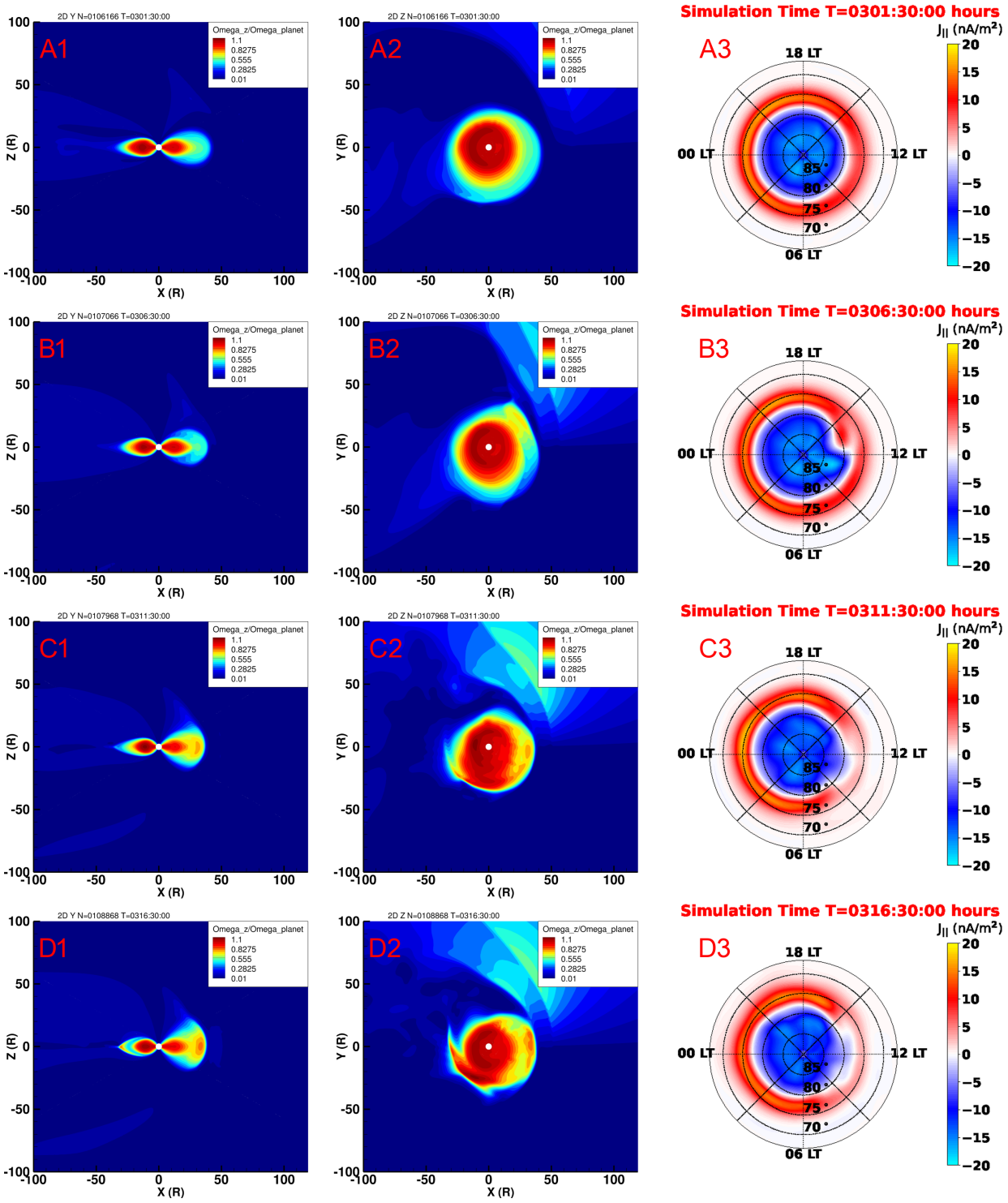

Figure 3.3: Contours of $\Omega_z/\Omega_{\text{Jupiter}}$ in the equatorial and meridional plane for Run 4 during a solar wind driven compression of the magnetosphere. The rightmost column shows the corresponding current density in the ionosphere.

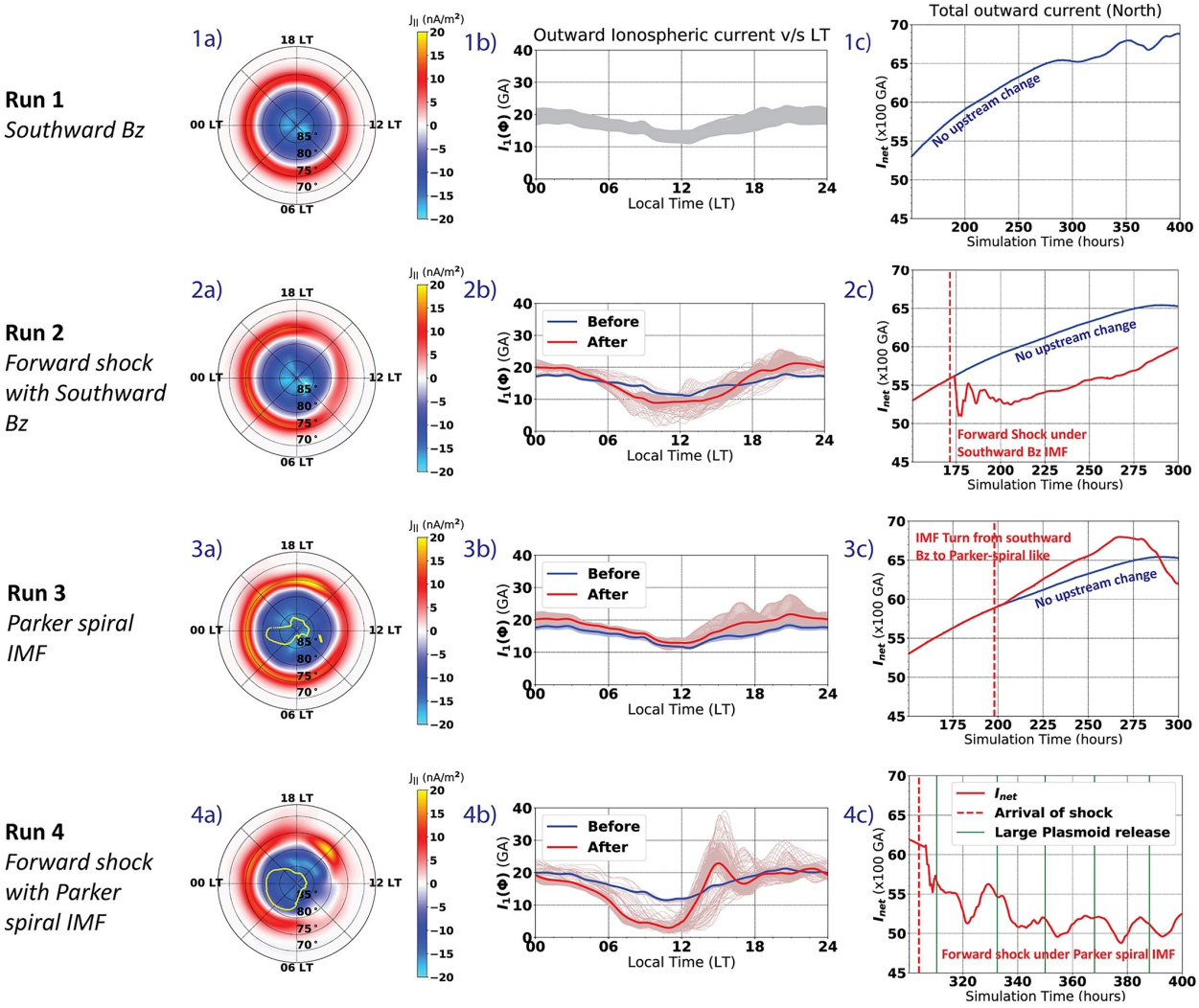

Figure 3.4: Ionospheric response. Each row represents the ionospheric response to the four runs. The first column shows contours of radial current density at the ionosphere with positive values representing outward current. Yellow points are the extracted footprints at the open-closed field line boundaries. In column 2 we show the latitude integrated outward current in the ionosphere as a function of local time. Each curve represents an instance in our simulation, with blue lines representing times before the upstream perturbation reaches the bow shock and red lines representing times after. In column 3 we show the total integrated outward current for all latitudes and local times as a function of simulation time. The blue curves in column 3 represent the variation of total outward current as a function of time for the closed magnetosphere under steady upstream conditions. The red curves represent the same quantity for the particular test case.

upstream conditions (same the blue curve in Figure 3.4-1c).

3.4.1 Ionospheric response - Run 1 (Fixed upstream with parallel IMF)

For the ∼400-hr duration of Run 1 (Figures 3.4-1a to 1c), the magnetosphere remains largely closed due to the southward B_Z IMF imposed at the upstream boundary. Figure 3.4-1b shows that there is a persistent day-night asymmetry present in the field-aligned current distribution with outward currents stronger on the nightside than on the dayside. Figure 3.4-1c also shows that the net outward current is steadily increasing with time (and at all local times/longitudes), despite the upstream conditions being constant. Initially, the rate of increase of the currents is almost linear, but with time the growth rate decreases and eventually the currents are seen to decrease. We believe that the growing trend of currents (with time scales of tens of hours), in the absence of any change in external conditions, is due to internal factors. As the magnetosphere builds more mass due to mass loading in the Io plasma torus, more torque is required from the ionosphere in order to force the magnetospheric plasma to corotate with the planet. Alternatively, consistent mass loading would increase the bend back of the magnetic field lines, which would increase magnetic field strength in the high-latitude regions thereby increasing $J_{\|}$ in the ionosphere. Hence, prolonged mass loading in the absence of mass loss mechanisms, such as plasmoid release, would require an increase in the corotation enforcement currents. Indeed, we see that the ionospheric currents decrease only when a plasmoid is released (at around t = 350 hr), suggesting that with the release of mass to the magnetotail, the net strength of the corotation enforcement circuit is reduced. For comparisons with other runs, the curve showing the expected trend of the total current (i.e., Figure 3.4-1c) is included in all sub-figures in the last column.

3.4.2 Ionospheric response - Run 3 (Turning of the IMF to $B_Y > 0$)

In Run 3, the upstream plasma properties are kept the same as in Run 1, and a tangential discontinuity is introduced in the solar wind across which the IMF is rotated from southward to the Parker-spiral configuration (with $B_Y > 0$). As shown in Figure 3.4-3a, reconnection at the magnetopause produces open magnetic field lines, and the open-closed field line boundary (OCB; marked in yellow lines) starts to expand equatorward. At the time shown in this plot, which is roughly 75 hr after the IMF turning, the region of open field lines extends about a few degrees from the pole and the OCB lies at least 5° poleward of the main oval of outward currents. Similar to that in Run 1 (Figure 3.4-1b), the outward currents in this run (Run 3) are stronger on the nightside than on the dayside (Figure 3.4-3b) and a continuously increasing trend is seen for the net outward current (Figure 3.4-3c). The red dashed line in Figure 3.4-3c marks the time when the discontinuity reaches the subsolar bow shock, and we can see that the rate of increase of currents (shown by the red line) deviates from the curve expected if there were no change in the upstream conditions (shown in blue). Note that the only upstream change introduced in this run is the change in IMF clock angle. Therefore, the comparison between Run 1 and Run 3 indicates that a change in IMF orientation can have significant influences on the large-scale current systems. The increasing trend of current, which now has a larger slope, eventually changes to a decreasing trend after the release of a plasmoid at $t = 270$ hr, consistent with the behavior seen in Run 1.

3.4.3 Ionospheric response - Runs 2 and 4 (Dynamic pressure enhancement)

In comparison to an IMF rotation, the response of the ionosphere to a forward shock that increase the dynamic pressure in the solar wind, is more dramatic. In Runs 2 and 4, we have introduced a dynamic pressure enhancement (a factor of 5 larger than the background). First, we examine Run 2—that is, dynamic pressure enhancement under a closed magnetosphere (3.4-2a to 2c). In all our simulation runs, we find the nightside currents to be stronger than

the dayside, and it can be seen from Figure 3.4-2b that the introduction of a forward shock makes this asymmetry more pronounced; that is, the nightside currents get stronger whereas the dayside currents get weaker. Similar enhancement of the day-night asymmetry has also been seen in the MHD model of (Chané et al., 2017). Apart from the overall response, there are also noticeable local time-dependent responses: Transient peaks in the outward current appear at specific local times. Our simulation predicts a minor enhancement on the nightside (10–20% increase in total currents) and a large decrease in current on the dayside (between 10% and 60%). As a result, the net outward current (I_{net}) sharply decreases after the impingement of the shock. After 50 hours, the system recovers and an increasing trend of the net outward current is seen again.

Our findings are consistent with previously published theoretical models (S. W. Cowley & Bunce, 2003; S. W. Cowley et al., 2007; Southwood & Kivelson, 2001), which have predicted that a dynamic pressure enhancement, and subsequent compression of the magnetosphere, would lead to an increase in azimuthal velocity of the plasma as it conserves angular momentum. In theory, this should decrease the strength of the corotation enforcement current system on the dayside. Consistent with this prediction, we find an increase in angular velocity inside the magnetosphere on the dayside after the shock compression, which leads to much reduced outward field-aligned currents in the dayside ionosphere.

A similar behavior was also found for Run 4—that is, dynamic pressure enhancement with a Parker spiral IMF (3.4-4a to 4c). Due to the increase of magnetic flux reconnecting on the dayside and the release of plasmoids on the nightside (which serves to close previously opened tail lobes), we find a prominent region of open field lines in the polar region. We also find a very strong response of the ionospheric currents, with dayside currents drastically decreasing in strength (by 50–60%), whereas the nightside currents appear almost unaffected (Figure 3.4-4b). Consequently, the net outward current also decreases sharply after the dynamic pressure enhancement at $t = 310$ hours. A key difference between Figure 3.4-4c and 3.4-1c,2c, and 3c is that the time history of the total outward current did not recover back to the increasing trend after the dynamic pressure enhancement. This may be due to very frequent plasmoid releases in the magnetosphere after the shock compression. As seen in Runs 1 and 3, a decrease in the net outward current is well correlated with times at which a

plasmoid is released. It is also noteworthy that the response of the ionosphere to the forward shock was stronger in Run 4 (open magnetosphere) than in Run 2 (closed magnetosphere). Apart from the IMF orientation, there is another difference between Runs 2 and 4: the phase of the magnetosphere in the Vasyliunas cycle. While Run 4 was started 30 hr after the release of a large plasmoid, Run 2 was initiated at a time when the magnetosphere was still in the process of accumulating mass with no prior plasmoid release. It is possible that the differences in the strength of the response may be due in part to the differences in the internal state of the magnetosphere, that is, depleted versus filled magnetosphere, rather than just the orientation of the external IMF. Clearly more work is needed to conclusively separate the internal and external influences.

3.5 Discussion

Under steady solar wind conditions, and in the absence of magnetic reconnection (Run 1), certain features were observed consistently in the magnetosphere and ionosphere, which are discussed first. Continuous mass loading due to Io increases plasma density in the inner and middle magnetosphere, which led to a more stretched magnetodisc. Simultaneously, the outward currents in the ionosphere were seen to increase at all local times. The increase in ionospheric current density was halted only after the release of a plasmoid in the magnetotail, which decreased the magnetic stresses in the magnetotail lobes. Our results suggest that the loading and unloading of magnetic flux tubes corresponding to the Vasyliunas cycle, can also modify the currents in the ionosphere, and thus the brightness of the Jovian aurora.

Another feature seen in all simulations is the relative weakness of outward currents in the ionosphere at noon (12 LT). Observations of the Jovian aurora have shown that it is weakest between 08-13 LT, also referred to as the 'discontinuity' region. This local-time asymmetry in the ionospheric-currents has also been observed in the model by Chané et al. (2013), who proposed that it was due to strong plasma corotation in the dayside, where magnetic field lines have the least 'bend-back', resulting in weaker currents. This is also seen in our model, for e.g. in Figure 3.2-1b, which shows that the corotation velocity near the magnetopause at $x = 50\ R_J$ is larger than at $x = -50\ R_J$ in the magnetotail.

Next we shall discuss the results of Run 3, where we turned the interplanetary magnetic field and that increases the magnetic shear at the magnetopause. This facilitated dayside magnetic reconnection and created open flux in the polar cap. However, like before, the currents in the ionosphere continued to strengthen, supporting the previous hypothesis that the increase in ionospheric currents was due to the internal Vasyliunas cycle. The turn in the IMF created open flux in the polar cap, which was eventually closed at the X-line located on the nightside. The return flow from the X-line interacted with the corotating plasma flow and created a vortex in the magnetosphere on the dusk-side. A similar vortex was also seen by Fukazawa et al. (2006) in their model. The vortex was also associated with an increase in ionospheric currents near 18 LT (dusk) and was responsible for the rate of increase of currents in Figure 3.4-3c. Eventually, the ionospheric currents are seen to decrease after a large plasmoid was released in the magnetotail.

The strongest influence to the magnetosphere and ionosphere was seen for Runs 2 and 4, when the solar wind dynamic pressure was increased abruptly in the form of a forward shock. Certain features are consistent between both runs, which differ in their magnetospheric configuration; Run 2 represents a closed magnetosphere, whereas in Run 4 the magnetosphere is open, which allows for magnetic reconnection to occur more strongly on the dayside due to strong solar wind driving. In both cases, the dynamic pressure enhancement was seen to increase the corotation velocity in the dayside, which decreased the strength of the corotation enforcement current system. However, while the largest decrease in currents was seen at 12 LT for Run 2 (closed), the corresponding reduction in Run 4 was much stronger and occurred at roughly 10 LT. In both cases, the response to the magnetosphere and ionosphere was not immediate. The increase in corotation velocity in the magnetosphere (Figure 3.2) occurred many hours after the passage of the shock.

Our model results support the predictions made by theoretical models (S. W. Cowley & Bunce, 2003; S. W. Cowley et al., 2007; Southwood & Kivelson, 2001) that solar-wind driven compression should decrease the strength of the corotation enforcement current system. However, observations of the Jovian aurora has hinted at a positive correlation between solar wind dynamic pressure and auroral power. The model of Chané et al. (2013) also predicts a positive correlation, although they note that the model takes several Jovian rotations to

reach the new state, which can be explained by the tendency of ionospheric currents to naturally increase due to the Vasyliunas cycle. Contradicting observations of the Jovian aurora by the Hisaki spacecraft, supported by simultaenous observations in the solar wind by Juno, have shown that there is a large delay between the observed dynamic pressure increase and the resulting intensification of the aurora (Kita et al., 2019). The same study also found intervals with high solar wind dynamic pressure when no corresponding increase in auroral power was observed.

It has been generally assumed that the Jovian aurora is produced due to field-aligned currents in the polar region. However, recent in situ observations made by the Juno spacecraft have shown that auroral dynamics are more complex. Particularly, Mauk, Haggerty, Paranicas, et al. (2017) showed that 'inverted-V' electron distributions, which are produced due to discrete acceleration within field-aligned potential drops, exist in Jupiter's auroral regions. At the same time, they note that the the planet-ward energy flux contribution of the broadband electron distributions is comparable and often higher than that for the discretely accelerated electrons (Mauk et al., 2018, 2020). These observations suggest that stochastic acceleration of electrons may play a more important role in generating the observed UV emissions at Jupiter. This is further supported by the study of Pan et al. (2021), who found a correlation between auroral power and ULF wave inferred using the Juno magnetic field observations, and by Tetrick et al. (2017), who observed whistler waves within the polar cap, which they suggest may be responsible for electron acceleration (Elliott et al., 2018). These recent observations suggest that the generation mechanisms for the Jovian aurora are complex and may not directly correspond to the intensity of field-aligned currents, unlike what has always been assumed in the literature. However, field-aligned potentials may still play an important role in determining where wave-particle interactions are likely to occur.

3.6 Summary

After creating a quasi-steady state magnetosphere in the simulation, we introduced various types of changes in the upstream solar wind and IMF, such as an IMF rotation and a dynamic pressure enhancement under southward IMF and Parker spiral IMF conditions. We found

that changing the IMF orientation from a southward (parallel) to Parker-spiral like IMF created open flux in the magnetosphere and thereby modified the large-scale magnetospheric configuration, but it alone had little effect on the corotation enforcement current system. However, in the cases where a forward shock is introduced in the solar wind, it had a significant impact on the global magnetosphere-ionosphere system. In particular, all of our simulations showed that there is an apparent asymmetry in the field-aligned current intensity in the ionosphere between the dayside and the nightside, with more intense currents on the nightside. This day-night asymmetry is further enhanced by the compression of the magnetosphere by a forward shock. In the simulation where a shock is introduced under Parker-spiral IMF conditions (Run 4), a region of intense field-aligned currents is present in the afternoon local time sector (16 LT; 3.4-4a and 4b), which magnetically maps to a region in the middle magnetosphere containing vortical plasma flows created due to the interaction between the return flow from tail reconnection with the corotating plasma. Although the ionospheric currents respond to the forward shock in both simulations (Runs 2 and 4), the magnitude of the response is significantly different. In general, when the magnetosphere contains more open flux (Run 4) due to dayside reconnection, the response of the ionosphere is stronger. It should be noted that while these two runs use the same solar wind parameters with the only difference being the IMF orientation used, the magnetospheric states prior to the shock impact are quite different, which may contribute in part to the differences seen in the simulated response. Future work is needed in order to isolate these two effects, that is, preconditioning of the magnetosphere and the influence of the IMF orientation.

Overall, our simulations clearly show that a solar wind driven compression of the magnetosphere increases the corotation velocity of plasma on the dayside, which reduces the strength of currents in the ionosphere. These results support previous theoretical models. However, recent observations by the Juno spacecraft have shown that the Jovian aurora is as likely to correspond to broadband particle acceleration, which suggests that the aurora may not be a direct result of the corotation enforcement field aligned current system and that wave-particle interactions may play an important role. These high-frequency phenomena cannot be captured within the MHD model, however, they likely occur in regions with large field-aligned potentials, which may drive plasma instabilities.

In the present study we have assumed that Jupiter's internal magnetic field is an axisymmetric dipole. However, recent observations by Juno have revealed significant north-south asymmetries in the internal magnetic field (J. E. Connerney et al., 2018) due to the presence of large higher order moments. How the complex internal magnetic field influences the magnetosphere and its interaction with the ionosphere and the solar wind remains an outstanding question that needs to be addressed in future work.

Chapter 4

Magnetic Reconnection in the Jupiter MHD Model

4.1 Introduction

The terrestrial magnetosphere is sensitive to changes in the solar wind and interplanetary magnetic field (Sibeck, Lopez, & Roelof, 1991; McPherron, Weygand, & Hsu, 2008). Solar wind dynamic pressure can increase the magnetic stresses in the magnetotail, which increases the frequency of magnetospheric substorms (Kokubun, McPherron, & Russell, 1977; Newell & Liou, 2011; Newell et al., 2016). Dayside magnetic reconnection, which typically occurs due to an anti-parallel (southward) IMF at the magnetopause, creates open field lines on the dayside and facilitates entry of solar wind plasma into the magnetosphere (e.g. Phan et al., 2000). This can occur during long periods with southward IMF, or as a result of transient features in the solar wind such as coronal mass ejections, whose interiors are comprised of helical magnetic field lines and dense plasma and which travel through the interplanetary medium at supersonic speeds, often creating strong shocks at their travelling front (Webb

*Parts of this chapter were published in - Sarkango, Y., Jia, X., & Toth, G. (2019). Global MHD simulations of the response of Jupiter's magnetosphere and ionosphere to changes in the solar wind and IMF. Journal of Geophysical Research: Space Physics, 124.

& Howard, 2012). Magnetic reconnection perturbs the terrestrial magnetosphere in various ways, e.g. by loading the magnetotail and facilitating magnetospheric substorms (Morley & Freeman, 2007), which can lead to auroral phenomena on the nightside (Elphinstone, Murphree, & Cogger, 1996), or via geomagnetic storms, which alter the ring current and produce large-scale geomagnetic disturbances (Gonzalez et al., 1994). Magnetic reconnection in the terrestrial system occurs via the opening of flux on the dayside and closure of magnetic flux on the nightside (Dungey, 1961). This cycle of flux circulation (also called the Dungey cycle), also influences plasma flow in the magnetosphere and high-latitude ionosphere, both of which respond to changes in the solar wind dynamic pressure or IMF orientation, which alters the characteristics of magnetic reconnection and thus the Dungey cycle, as discussed in Chapter 1.

However, considerable debate exists in the community regarding the importance of dayside magnetic reconnection in Jupiter's magnetosphere. Unlike the terrestrial magnetosphere, the strong internal magnetic field and presence of internal sources of plasma lead to a very different magnetospheric configuration at Jupiter.

One argument made against dayside magnetic reconnection highlights the improbable timescales for the Dungey cycle. At Earth, a newly reconnected field line on the dayside, which is frozen-in to the solar wind plasma at its other end, is transported tailward at the solar wind speed of $\sim$ 400 km/s. Hence, it will take approximately $\sim$300 s or 5 minutes to travel a distance of $\sim 20R_E$ (1 R_E = 6378 km is the radius of the Earth). On the other hand, at Jupiter, a field line opened on the dayside magnetopause would have to travel a distance of $\sim 200R_J$ to reach the magnetotail, which would take $\sim$ 10 hours, comparable to the rotation period for Jupiter. Moreover, it has been argued that field lines which have reached the magnetotail may take an even longer time to reach the equatorial regions where tail reconnection is likely to occur (McComas & Bagenal, 2007).

The two commonly used counter-arguments propose that Dungey cycle timescales may be considerably shorter. This could be possible if the flux circulation occurs in a localized region on the dusk side instead of over the entire magnetosphere like at Earth. Moreover, another hypothesis is that it is not necessary for the field line to fully diffuse toward the equator, as plasmoid release due to the Vasyliunas cycle may also induce reconnection to

spread to the open tail lobes (S. W. Cowley et al., 2008).

In-situ observations have shown that magnetic reconnection occurs in the Jovian magnetotail and produces plasmoids. This has been seen via north-south reversals of the magnetic field (Vogt et al., 2010, 2014, 2020) or in the form of bursts of energetic particles with a radial velocity (Woch et al., 2002; Kronberg et al., 2007, 2008). The timescales associated with the loading and unloading of the magnetotail (Vasyliunas cycle) has been estimated to be on the order of 2 to 3 days (or 5 to 7 Jovian rotations) (Woch et al., 2002; Vogt et al., 2010).

Finally, this work is also motivated by observations made by the Hubble Space Telescope of Jupiter's polar regions. The polar UV aurorae are highly dynamic, and vary on timescales much shorter than the main oval. Whether these polar regions of the planet connect to distant regions in the Jovian magnetotail via closed field lines, or to the solar wind via open field lines, remains an open question.

In this work, we simulate the Jovian magnetosphere using our MHD model to answer the following questions,

1. Does magnetic reconnection occur on the dayside magnetopause at Jupiter and create open flux in the magnetosphere?

2. Does Jupiter have a persistent polar cap of open field lines?

3. If so, where and how does flux closure occur in the magnetosphere?

Answers to these long-standing questions are crucial to understand the dynamics of the Jovian magnetosphere and to understand the relative contribution of the externally driven Dungey cycle and the internally-driven Vasyliunas cycle. Knowledge of the magnetic topology in the Jovian magnetosphere supports in situ measurements by the Juno spacecraft, and also remote observations of the Jovian UV aurora by the Hubble Space Telescope. As we will demonstrate, global MHD modeling provides a global context to the in situ data, and complements the observations made by HST, which lack context about the external solar wind and IMF, as well as internal magnetospheric configurations.

4.2 Methodology

The MHD simulations presented in Chapter 3 were also used in this study. We will primarily be discussing Runs 2 and 4 (see Table 3.1), which use a Parker-spiral IMF (magnetic field in the Y direction), as typically expected at Jupiter's orbit. In such situations, the magnetic shear between the IMF and the magnetospheric field at the nose of the magnetopause is 90°. The techniques used to analyze the simulation data as described in this section.

4.2.1 Identification of the dayside magnetopause surface

The magnetopause is the surface separating the magnetospheric field from the interplanetary magnetic field. It is a current-carrying discontinuity, and can be identified in MHD simulations as a local peak in the current density (J). It can also be identified by detecting the increase in density due to the density gradient between the outer magnetosphere and the magnetosheath. In our study, we use magnetic field topology to identify the magnetopause, as this definition is more robust. In our case, the dayside magnetopause is the surface which separates closed magnetic field lines of the magnetosphere from the open field lines in the solar wind. This method is unambiguous on the dayside, but cannot be used for higher latitudes or the magnetotail, which also contain open field lines, but are present inside the magnetosphere.

A hemispherical surface is created on the dayside at locations $(r = r_i, \theta_i, \phi_i)$ in spherical coordinates. From each point i of the surface, a radial line segment is created to the point $(r = r_o, \theta_i, \phi_i)$, which lies well beyond the dayside bow shock and hence contains solar wind field lines. A field line is traced from the midpoint of these two locations (r_m), and its connectivity is inferred by examining whether its two footprints are traced to the planet (closed) or to the solar wind (open). If the field line is closed, r_m is chosen as the new inner point ($r_i := r_m$), else r_m is specified as the outer point ($r_o := r_m$). This binary search algorithm is repeated until $r_o - r_i < 2R_J$. The resulting midpoint is the location for the magnetopause. The whole process is repeated for each point on the initially hemispherical surface, which produces a new surface for the magnetopause as shown in Figure 4.1.

4.2.2 Classification of a magnetic field line

Magnetic field lines in the MHD model can only have one of the following properties. Each type is assigned a value in the form of a 'status' variable. The field line can be,

- Connected at both ends with the IMF (external field lines or 'disconnected', status=0).
- Connected to the northern hemisphere of the planet, with the other end connecting to the IMF (open field lines, type N, status=1).
- Connected to the southern hemisphere of the planet, with the other end connecting to the IMF (open field lines, type S, status=2).
- Connected at both ends with the planet (closed field lines, status=3)

Most field lines in the inner and middle magnetosphere are closed (status=3). The type N and S field lines map to the northern or southern polar cap and are created due to dayside magnetic reconnection.

4.2.3 Calculation of the open flux in the polar cap

In order to estimate the open flux in the polar cap, we must first identify the regions in the northern and southern hemispheres which map to open field lines. This is achieved by creating a spherical surface close to the inner boundary of the MHD simulation domain and tracing field lines at each point of the surface. Points which map to closed field lines are identified, and their corresponding locations at 1 R_J are estimated by using a dipole approximation (due to the existence of a gap between 1 R_J and the inner boundary at 2.5 R_J). For an axially aligned dipole field, two points located on the same field line at locations (r_1, θ_1) and (r_2, θ_2) are related as,

$$\frac{r_1}{r_2} = \frac{\sin^2 \theta_1}{\sin^2 \theta_2} \tag{4.1}$$

The mapping to a sphere at $r = 1R_J$ is not necessary to calculate the open flux as the magnetic flux is conserved between the two locations, but it is useful for future comparisons

with the ionosphere currents. After the location have been mapped to a sphere with radius $r = 1R_J$, a grid of spherical rectangles is constructed and the magnetic flux through each rectangle corresponding to open field lines is estimated using the dipole field approximation. In this case, for a spherical rectangle of angular widths $\Delta\theta$ and $\Delta\phi$, centered at (θ_i, ϕ_i), the magnetic flux due to a axially aligned dipole field with moment M at a spherical surface with radius r can be calculated analytically -

$$\Delta\Phi_i = \iint \mathbf{B}\cdot\mathbf{n}\,dS = \iint B_r dS = \frac{M}{r}\cos(\Delta\phi)\left[\sin^2\left(\theta_i + \frac{\Delta\theta}{2}\right) - \sin^2\left(\theta_i - \frac{\Delta\theta}{2}\right)\right] \quad (4.2)$$

The resulting open flux in the polar cap can be calculated by summing up the contributions due to all regions corresponding to open field lines,

$$\Phi_{\text{open}} = \sum \Phi_i \,(\text{status}_i \neq 3) \quad (4.3)$$

4.2.4 Calculation of the reconnection rate

The rate of change of open flux in the polar cap equals the difference in the reconnection rates on the dayside versus that due to Dungey cycle flux closure on the nightside (Milan, Provan, & Hubert, 2007). If no reconnection is observed on the nightside ($\dot{R}_{\text{nightside}} = 0$), then the dayside reconnection rate can be inferred using the rate of change of the open magnetic flux.

$$\frac{d\Phi_{\text{open}}}{dt} = \dot{R}_{\text{dayside}} - \dot{R}_{\text{nightside}} \quad (4.4)$$

4.3 Results

4.3.1 Reconnection on the dayside for Parker-spiral IMF

For the Parker-spiral IMF configuration used in our simulation, reconnection is found to occur primarily on the magnetopause at relatively high latitudes (at $\sim 50°$) latitude) where

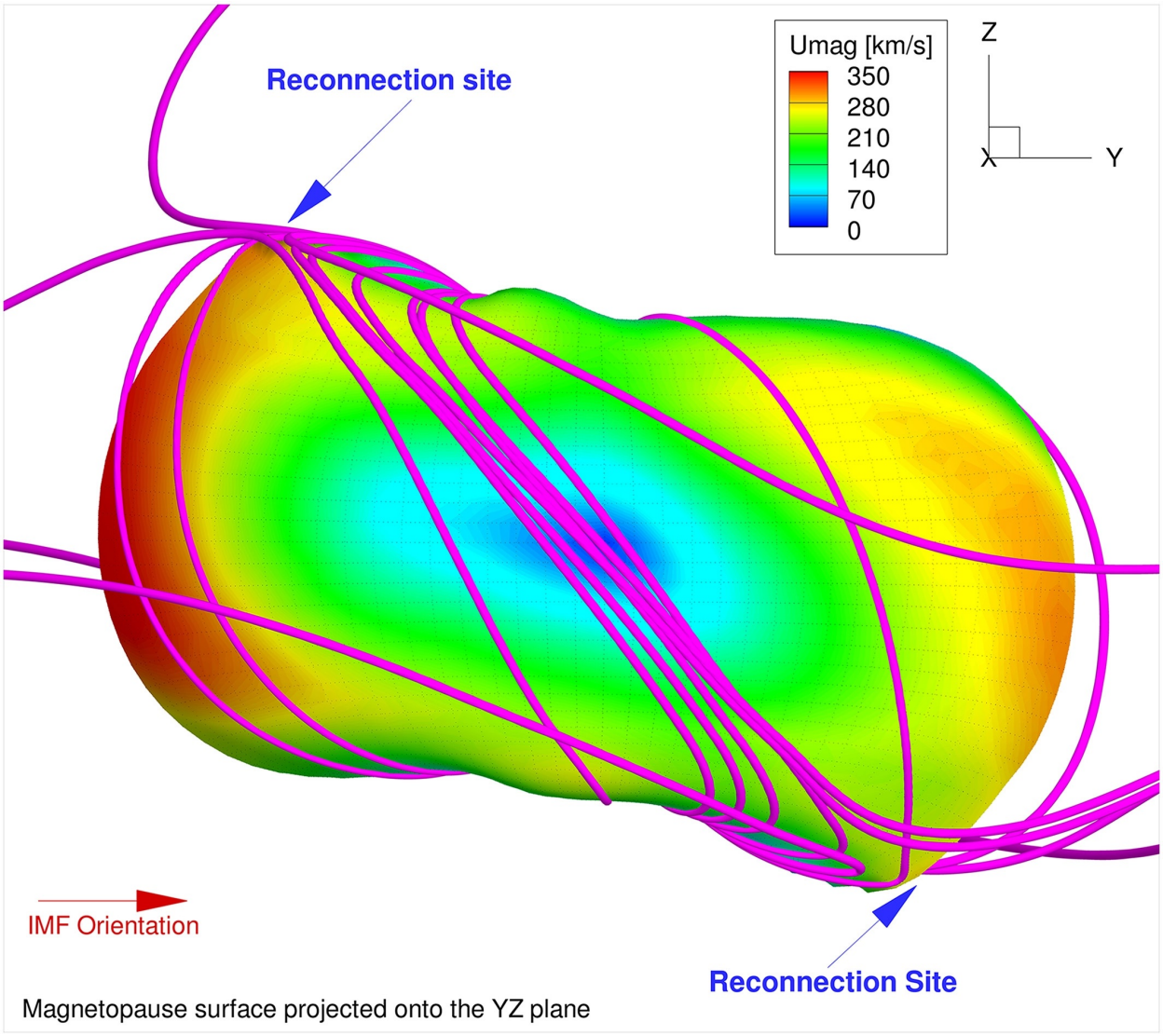

Figure 4.1: The 3D magnetopause surface extracted from our model for the Parker-spiral IMF case. The surface is coloured in contours of plasma speed. Magnetic field lines are shown as magneta tubes. Magnetic reconnection is seen to occur on the mid-latitude dawnside in the northern hemisphere and in the mid-latitude duskside in the southern hemisphere; locations where maximum magnetic shear is expected between the internal field and the IMF.

the strongest magnetic shear is present. Figure 4.1 shows a snapshot of the simulated magnetopause surface extracted from Run 4. The magnetopause surface is determined by identifying the separatrix between magnetospheric and magnetosheath field lines based on 3-D field line tracing. The color contours on the magnetopause surface represent plasma flow speeds, and sample field lines are superimposed to show the magnetic topology. As shown, under the spiral IMF configuration with positive By, we find that reconnection takes place mainly in two quadrants in the YZ plane: in the northern hemisphere on the dawnside and in the southern hemisphere on the duskside. The reconnection geometry is consistent with the prediction by the analytical model of (Masters, 2017) for the same IMF configuration.

4.3.2 Plasmoid release and variation of open magnetic flux

In all simulations listed in Table 3.1, tail reconnection occurs and produces plasmoids. For instance, a large plasmoid can be seen in Figure 3.1, row 3 in the form of a high-density region between 00 and 06 LT. After initially being created at a radial distance of ∼50–70 R_J on the dawnside, the plasmoid is seen to grow and move tailward, eventually escaping the magnetosphere and lost to the solar wind. In Run 4, a vortex structure is created in the magnetosphere on the duskside at around 40 R_J radial distance from the planet (not shown). The vortex is formed subsequent to a large reconnection event in the magnetotail and it strengthens as it moves sunward, eventually reaching the postnoon sector. The vortex is made of corotating and anticorotating flows and produces a strong ionospheric response in the postnoon sector (Figures 3.4-4a and 4b near 16 LT). We believe that this vortex and the subsequent localized bright spot in $J_{\parallel}$ observed near 16 LT in the ionosphere are due to the interaction of return flow from the duskward tail reconnection site with the corotating magnetospheric plasma and has also previously been observed by (Fukazawa et al., 2006) using their MHD model.

In Figure 3.4 the yellow points superimposed onto the contour plots correspond to the OCB identified in our simulations. For each latitudinal and longitudinal position in the ionosphere, we trace 3-D magnetic field lines from a sphere at 3 R_J to identify any transition between open and closed field lines. If a transition is found, its location on a 1 R_J sphere is determined by using a dipole field line tracing, which is then plotted in Figure 4.2. Even

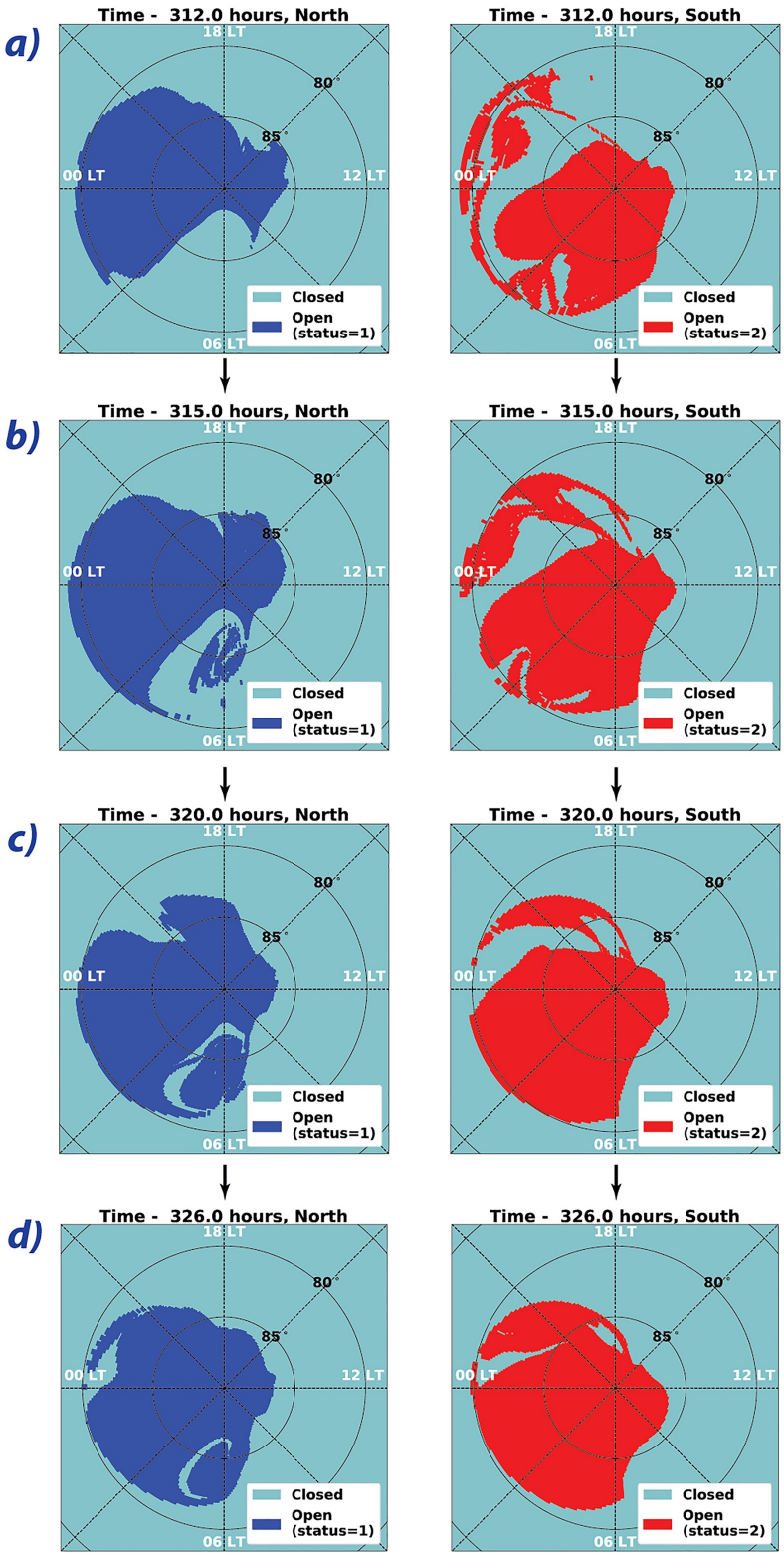

Figure 4.2: The regions of open flux in the northern and southern regions of the planet ($r = 1R_J$) at different times showing the consequence of plasmoid release on magnetic topology. Note the asymmetry between the two hemispheres.

with 1° resolution in both latitude and longitude, our tracing algorithm does not find any such transition during times when the IMF is southward, which is consistent with the picture that the magnetosphere is largely closed under such external conditions. In contrast, under a Parker spiral IMF, the OCB increases in size with time and can reach a latitude of $\sim 80°$ on the nightside under strong solar wind driving (column 4). While the size of the OCB tends to vary depending on the upstream conditions, for the various upstream conditions examined in our simulations it is always located poleward (by at least a few degrees) of the main oval of upward field-aligned currents arising from corotation breakdown, which lies at $\sim 75°$ latitude.

For further analysis we divide the magnetic field lines extracted from our MHD model into four categories, denoted by the "status" variable (Table 2). A status value of 0 represents a closed field line with both ends connected to the planet. A status value of 1 or 2 implies an open field line with one footprint in the northern or southern hemisphere, respectively, while a status value of 3 refers to those field lines with both ends in the solar wind, which we call disconnected field lines. Figure 4.2 shows the status of field lines seeded from the northern and southern ionosphere, whereas Figure 4.4 shows the status of field lines seeded from the equatorial plane in the magnetosphere.

4.3.3 Magnetic topology associated with plasmoid release

In Figure 4.2, we show the status maps of the northern and southern hemispheres on a 1 R_J sphere, at different times during the sequence of a plasmoid release. For both hemispheres, the cyan regions contain field lines that are closed (status = 0). For the northern hemisphere panels, the dark blue regions contain open field lines (status = 1) that magnetically map to the solar wind. For the southern hemisphere panels, the red regions indicate open field lines (status = 2) that map to the solar wind. It is immediately clear from Figure 4.2 that these status maps are not north-south symmetric, with stark differences in the topology between the two hemispheres.

Two plasmoids are observed in the magnetosphere during the times shown in Figure 4.2: a relatively small size plasmoid on the duskside and a much larger plasmoid near dawn. When the plasmoids are initially formed, they contain predominantly closed flux. This is

consistent with the idea that plasmoids form due to the Vasyliunas cycle are created on closed field lines. As the plasmoids move tailward, they grow in size and create a region of closed flux inside the polar cap. The large plasmoid in the dawn sector of the magnetosphere can be identified by its status signature on the dawnside in the form of a large region of closed flux, whereas the smaller plasmoid in the dusk sector also creates a similar region of closed flux in the duskward polar cap. With time, the plasmoids grow in size and interact with the surrounding plasma and magnetic field, which creates rather complicated magnetic field structures that contain intertwined open and closed field lines (Figure 4.2b). As the plasmoids move further down the magnetotail, they continue to grow in size and the status signatures associated with plasmoids move toward midnight (previously at dawn and dusk) and the high-latitude region in the ionosphere starts to be filled with open field lines. With time, the ratio of open field lines to closed field lines in the plasmoid footprint increases in both the northern and southern hemispheres. As a result, the tail plasmoids, when mapped magnetically to the ionosphere, correspond to a stripe-like structure.

Observations of the polar aurorae of Jupiter show various intriguing features such as arcs and filaments (Grodent, Clarke, Waite, et al., 2003; McComas & Bagenal, 2007; Nichols et al., 2009) that have been suggested to be linked to dynamic processes in the solar wind and magnetotail. Our simulation results show that the polar regions of the planet, which are often assumed to lie on open field lines, may magnetically connect to distant regions in the magnetotail associated with a plasmoid. While our MHD simulation does not directly model the kinetic physics of particle energization associated with reconnection, the magnetic topology associated with plasmoid release and propagation through the tail region as seen in our simulation suggests that energization associated with tail plasmoid release may provide a plausible explanation for the observed arc-like or filament-like aurora structures.

In Figure 4.3, we show the three-dimensional magnetic field lines associated with the tail plasmoid along with the plasma density contours in the equatorial plane. Orange field lines are closed field lines, whereas black field lines are "disconnected" field lines with both ends in the solar wind. It can be seen that although the plasmoid is generated on closed field lines, it is surrounded by open field lines as it moves tailward. The inset in Figure 4.3 shows the corresponding ionospheric status map in a similar format as Figure 4.2. Since this plasmoid

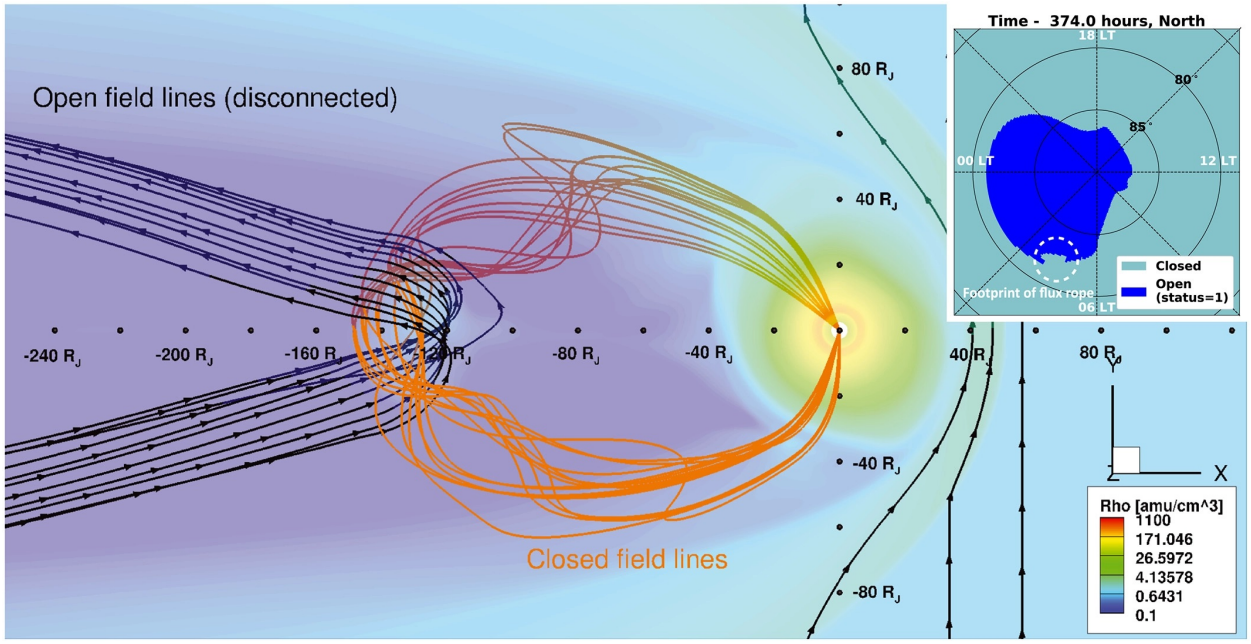

Figure 4.3: 3D magnetic field lines threading a plasmoid are shown. Orange field lines are closed, however they are constrained by open field lines which have both ends in the solar wind. The corresponding topology map at this particular simulation time is shown in the inset, where the footprint of the flux rope has been marked.

is noticeably smaller, it has a smaller, but consistent, status signature in the form of a region of closed flux in the polar cap on the nightside.

4.3.4 Open flux in the magnetosphere

To complement the analysis of the status of field lines shown in the previous sections, we repeated the same procedure of tracing field lines starting in the equatorial plane of the magnetosphere. The corresponding magnetospheric status maps are shown in Figure 4.4 for two different types of plasmoids that we will call Type 1 and Type 2, respectively. The left column shows a plasmoid of Type 1, which is a large plasmoid released on the dawnside, whereas the right column shows a plasmoid of Type 2, which is released near midnight. Both plasmoids have some common features, namely, they both originate from closed field lines. After release, the Type 1 plasmoid severely distorts the magnetic topology of the magnetotail. Upon close examination, one can see regions of closed field lines interspersed within large regions of open field lines. The Type 2 plasmoid, on the other hand, has a

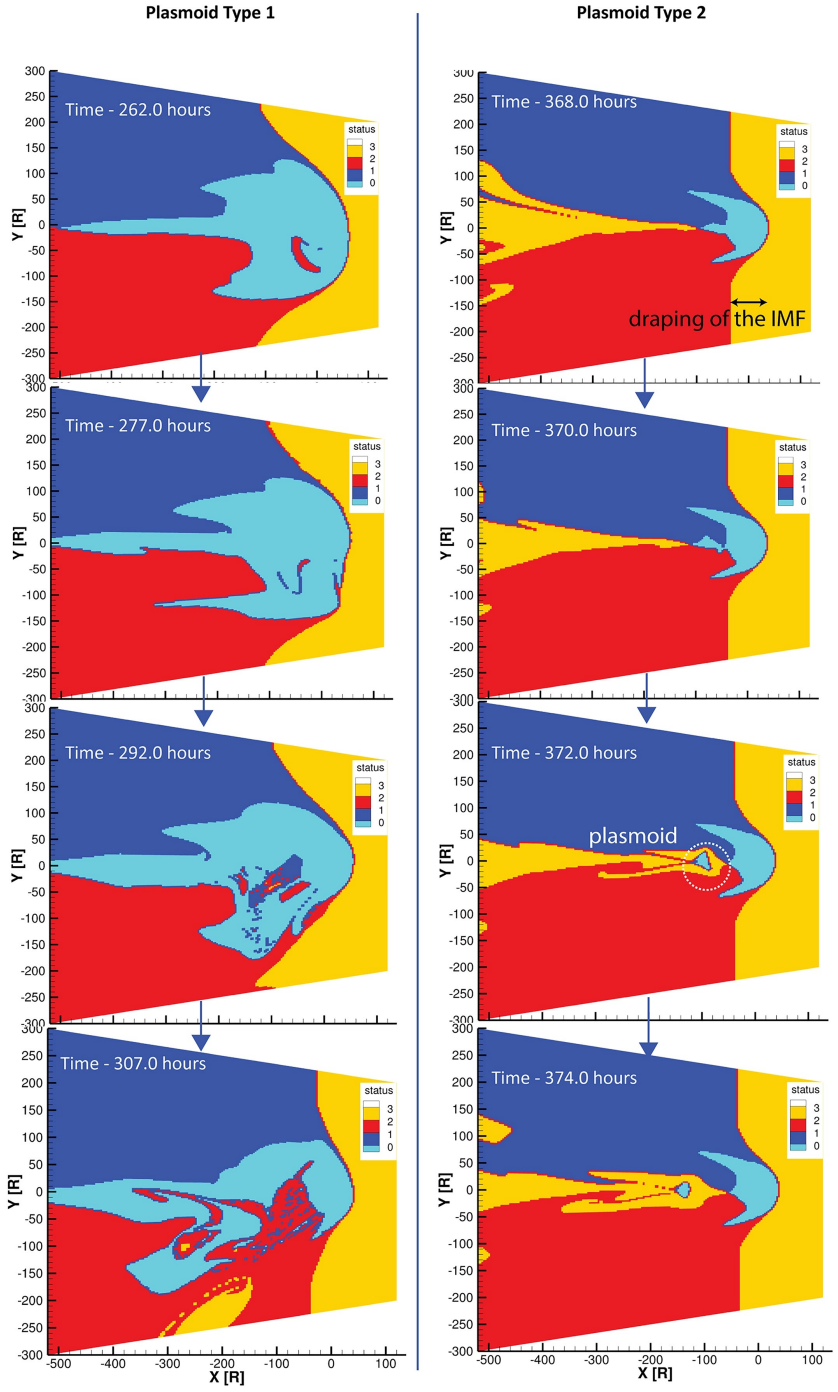

Figure 4.4: Topology maps of the magnetosphere during different stages of plasmoid release. On the left are the large Type-1 plasmoids, where the right column shows the progression of a relatively small Type-2 plasmoids. Both plasmoids originate within closed field lines and get surrounded by open field lines as they travel tailward.

cleaner topological fallout. After being detached as a "blob" of closed flux, the Type 2 plasmoid is surrounded by disconnected field lines (status = 3, both ends in the solar wind) even though it is located deep inside the magnetosphere. With time, the Type 2 plasmoid moves tailward and the region of closed flux associated with the plasmoid decreases in size. However, the region of disconnected flux in the magnetotail expands after the release of a Type 2 plasmoid.

Another feature which can be recognized in Figure 4.4 is the stark separation between dayside disconnected field lines and the open (status = 1 and 2) field lines on the dawn and dusk flanks, as can be identified through the vertical demarcation at $x = -40R_J$ in column 2. We traced 3-D magnetic field lines which suggest that this vertical demarcation is linked to the draping of the IMF around the magnetopause. That field lines in the magnetosheath drape around the magnetopause has been discussed in detail for Earth and Saturn (Crooker et al., 1985; Sulaiman, Masters, Dougherty, & Jia, 2014; Sulaiman et al., 2017) and is expected to be more pronounced at Jupiter due to the large polar flattening of the magnetosphere (Erkaev, Farrugia, & Biernat, 1996; Farrugia, Biernat, & Erkaev, 1998; Slavin, Smith, Spreiter, & Stahara, 1985). While our model does predict the draping of the IMF around Jupiter's magnetopause, the degree of polar flattening in our model is lower than previous predictions ($\epsilon = \sim 0.3$, expected to be ~ 0.8 according to Slavin et al., 1985).

4.3.5 Rate of change of open flux in the magnetosphere

After identifying the status of each point on the 1 R_J sphere for multiple times in our simulations, we integrate the open magnetic flux within the open field region in the northern hemisphere of the planet. Figure 4.5a shows the variation of this calculated open flux in our model as a function of simulation time for Parker-spiral IMF (purely B_Y) but different solar wind dynamic pressures. The black points show the open flux calculated in our simulation, while the dashed red vertical line marks the time when the introduced forward shock arrives at the bow shock. To reveal potential correlation between plasmoid release and open flux variations, we overlay solid lines in this figure to mark the times when plasmoid release occurs in the simulation. We identify plasmoids in the model based mainly on the B_Z component (the normal component to the tail current sheet). A bipolar variation of B_Z in the equatorial

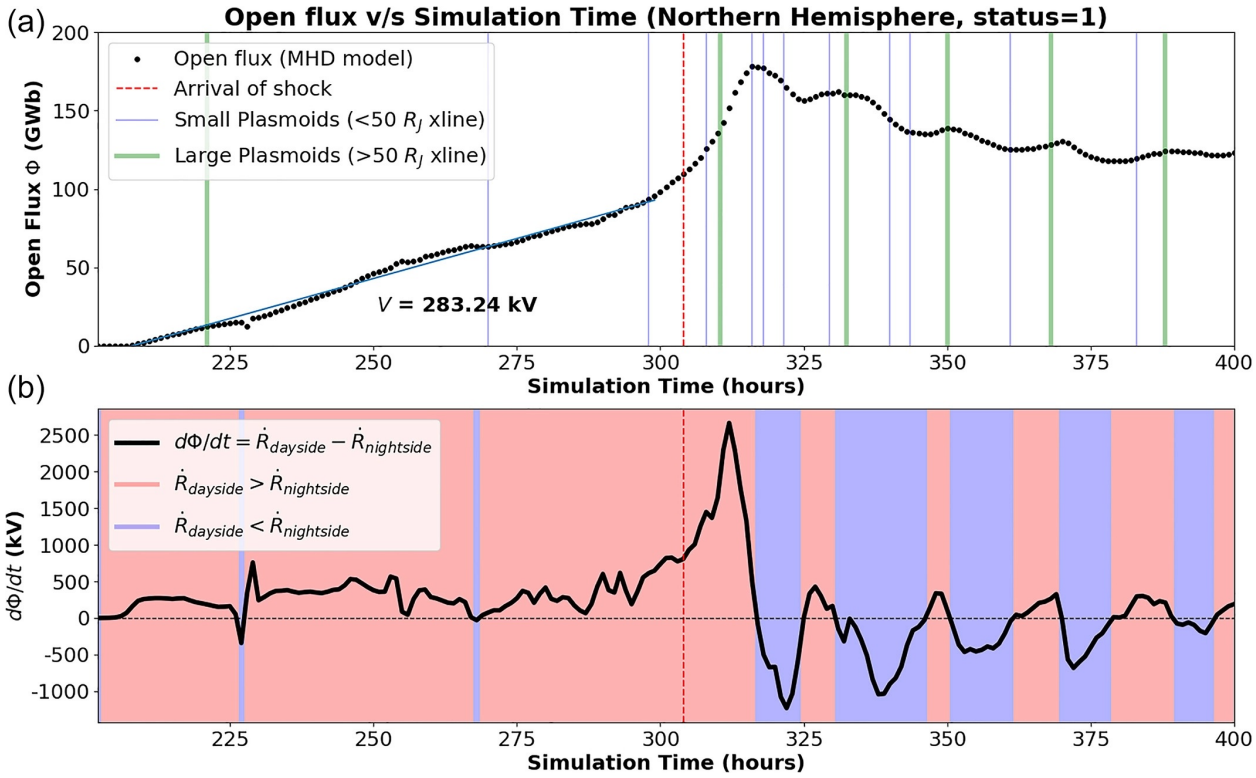

Figure 4.5: Variation of open flux in the MHD simulation, along with the rate of change. Periods of positive rate of change of flux indicate times when dayside reconnection is dominant, whereas those with negative change indicate times when nightside reconnection is active. Alternating periods of negative and positive change signify repetitive plasmoid release.

plane is an indication that a reconnection event has occurred in the magnetotail. Typically, plasmoids generated in our model tend to grow in size as they move tailward. Therefore, we further divide the identified plasmoids into two groups based on their maximum size in the cross-tail direction (Y direction): large plasmoids which have a cross-tail width larger than 50 R_J at their maximum extent and small plasmoids whose maximum width is $< 50R_J$. Green thick lines and thin blue lines represent the times when large and small plasmoids are released, respectively.

Prior to the shock arrival at $t = 302$ hr, the IMF along with the solar wind parameters remain fixed. During this interval, the open flux in our model gradually builds up due to the magnetopause reconnection. At around $t = 223$ hr (marked by the solid green vertical line), a relatively large plasmoid with a cross-tail width exceeding 50 R_J forms in the magnetotail that closes some of the open flux stored in the tail lobes, which can be seen as the change of slope in the time history of the open flux. During this period, there are also a couple of smaller-scale plasmoids (with cross-tail width $< 50R_J$) formed, as marked by the solid blue vertical lines in Figure 4.2. After the shock arrival at $t = 302$ hr, the rate at which the open flux is added to the polar cap increases due to the enhanced solar wind convectional electric field associated with the shock. About 25 hr after the shock impact, a large-size plasmoid is formed and released in the tail that results in a significant reduction of the open flux. After the impingement of the shock, the compressed magnetosphere experiences frequent plasmoid release, both large and small. Compared to the situation seen in the simulation during the nominal solar wind conditions where plasmoid release occurs every 20 to 50 hr, the occurrence rate is significantly higher in the compressed case, which is of the order of one plasmoid every few hours. A similar behavior has been seen in the MHD model of Saturn by (Jia et al., 2012) who found more frequent plasmoid releases during periods of stronger solar wind driving.

The time variation of the open flux provides a useful measure of how the magnetosphere responds globally to the solar wind driving and internal dynamics. As discussed above, dayside reconnection would add open flux to the polar cap whereas tail reconnection would potentially close open flux stored in the tail lobes. Therefore, the time rate of change of the open flux can be used to quantify the global reconnection efficiency, which depends on the

difference in the reconnection rates between the dayside magnetopause reconnection and the tail reconnection. At the beginning of the simulation, in the absence of tail reconnection, we find that the open flux increases at a rate of ∼284 kV, which corresponds approximately to the global reconnection rate under the solar wind conditions listed in Table 3.1, column 2.

In Figure 4.5b, we show the calculated rate of change of open flux in the northern hemisphere (status = 1), that is, $d\Phi/dt$ as a function of simulation time. After the shock is introduced in the simulation, the rate of increase of open flux increases, corresponding to a peak global reconnection potential of ∼2 MV. This increase in the reconnection rate on the dayside is primarily due to enhanced solar wind speed and increased IMF strength due to compression and hence the convectional electric field behind the shock. At later times, the open flux in our simulation is found to decrease and increase periodically at a period of ∼20 hr, highlighting the competing influence of magnetopause reconnection (which serves to open magnetic flux) and nightside reconnection (which decreases the net open magnetic flux). Closer examination reveals that the decreases in open flux are also correlated with the release of large plasmoids. Walker and Jia (2016) report on simulations of the Jovian magnetosphere performed by Fukazawa et al. (2006) and also found quasi-periodic increase and decrease in open flux with a similar period of ∼20–30 hr.

In discussing Figure 4.2 we noted that the release of plasmoids creates a region of open flux in the polar cap, which may seem contradictory to these findings. However, it must also be noted that the overall size of the polar cap also depends on many other factors, such as the difference between reconnection rate on the dayside versus the nightside. Figure 4.4 clearly demonstrates that plasmoid release increases the amount of disconnected flux in the magnetosphere. Since the disconnected field lines, by definition, cannot magnetically map to the northern hemisphere, they are not accounted for in our calculation for net open flux which is done on a 1 R_J sphere for Jupiter (thereby only considering status = 1 type field lines). Figure 4.4 also shows that with the increase of disconnected flux in the magnetotail, the amount of connected open flux (i.e., status = 1 and 2) decreases. This would decrease the overall size of the polar cap, which would lead to decreased status = 1 flux. The overall shrinking of the polar cap can also be seen in Figure 4.2.

As time progresses the dayside and nightside reconnection rates seem to approach steady

state, which can be seen in Figure 4.5b where fluctuations in $d\Phi/dt$ decrease with time. For the compressed magnetosphere, at the end of our simulation (t = 400 hr) the total open flux amounts to $\sim$ 120 GWb. It is interesting to note that the creation of open flux is largely due to the reconnection on the magnetopause, and the result that the net open flux seems to reach a steady state implies that flux closure on the nightside or elsewhere is happening in a manner expected by the terrestrial-like Dungey cycle. Although we have not yet identified any preferential spatial location where flux closure is consistently occurring, it is clear that both Vasyliunas cycle reconnection (detachment of plasmoids on closed field lines) and Dungey cycle-type flux closure contribute to the circulation of magnetic flux in Jupiter's magnetosphere.

Plasmoids generated in Jupiter's magnetotail may be a result of a near-planet like flux closure event attributed to the Dungey cycle or a result of centrifugal stresses exerted on the corotating plasma, that is, the Vasyliunas cycle, both of which may cause reconnection onset on closed field lines. When the IMF is southward (Run 1), absence of dayside magnetopause reconnection would essentially shut off the Dungey cycle. However, plasmoids are still observed in this case (not shown), and they are a direct product of the Vasyliunas cycle. In this case the plasmoid, once generated, is constrained by the surrounding closed field lines, and "escapes" through the magnetopause. In contrast, when the IMF is in the Parker-spiral configuration, dayside magnetopause reconnection would add open field to the tail lobes. In this scenario, plasmoids generated due to a tail reconnection event may induce closure of open flux in the tail lobes (S. W. Cowley et al., 2008) regardless of the original cause of reconnection onset. The lobe reconnection-produced field lines, which are carried by fast-moving reconnection jets moving behind the plasmoids, would facilitate the escape of plasmoids down tail. These findings from our Jupiter simulations are similar to those reported for global simulations of Saturn's magnetosphere (Jia et al., 2012).

As noted earlier, the global simulation presented here is based on an ideal MHD model, in which no kinetic physics is included to describe reconnection. However, reconnection does occur in MHD simulations, which is facilitated by numerical resistivity. It is interesting to compare the global reconnection rate and the resultant amount of open flux in our MHD model with prior estimates based on observations and analytical models. For instance,

Masters (2017) presented an analytical method to estimate the total reconnection potential at Jupiter's magnetopause under different solar wind conditions, and he predicted a dayside reconnection potential ranging between 200 and 1,000 kV. The reconnection potentials estimated in our simulations are in general agreement with the Masters model results. Further, based on auroral observations and magnetic field modeling, Nichols, Cowley, and McComas (2006); Vogt et al. (2011) estimated the typical amount of open flux present in Jupiter's magnetosphere, and their results give a range of 300–700 GWb. The maximum amount of open flux seen in our simulations is about 175 GWb, which is slightly lower than previous estimates and could be related to our use of an ideal axisymmetric dipole for the planetary magnetic field.

4.4 Summary

Our simulations show that magnetic reconnection on the dayside magnetopause at Jupiter creates open flux in the polar caps. The open field lines are magnetically connected to the polar regions of the planet and occupy a relatively small area poleward of the main auroral oval.

Plasmoid release in the tail has long been suggested to be an important means of plasma transport, and signatures of plasmoids have indeed been found in various in situ observations in Jupiter's magnetotail. Our global simulations also show plasmoid formation and release due to reconnection in the magnetotail. The majority of plasmoids seen in our simulations appear to form initially on closed magnetic field lines, consistent with the picture proposed by Vasyliunas (1983). While differing in size, all the plasmoids produced in the simulations develop a complex magnetic topology as they evolve and propagate downtail. As an example, we have shown the time evolution of two plasmoids with different sizes and their mapping to the polar ionosphere. Our magnetic mapping results support the previous hypothesis that the complex morphology of tail plasmoids may be responsible for creating puzzling auroral features such as arcs and filaments (Grodent, Clarke, Waite, et al., 2003; McComas & Bagenal, 2007; Nichols et al., 2009).

As a quantitative measure of the influence of the external driver on the global magne-

tospheric configuration, we have identified the OCB throughout our simulations by tracing 3D magnetic field lines. We have also calculated the total amount of open flux within the magnetosphere and examine the time evolution of the open flux in response to the changes imposed on the upstream parameters. For southward IMF, the magnetosphere has little to no open flux, as expected. As the IMF orientation is changed to a more realistic Parker spiral configuration, open magnetic flux starts to be added to the magnetosphere due to the dayside magnetopause reconnection and as such the OCB in the ionosphere starts to expand in size moving equatorward. In all the simulations present here, the OCB is found to be always located poleward by at least a few degrees of the main oval of upward field-aligned currents associated with corotation breakdown. The total amount of open flux is found to peak around 200 GWb for typical Parker-spiral IMF conditions, which is about a factor of 2 smaller than previously published estimates (Vogt et al., 2011). There is a clear correlation between the reduction of open flux and the release of plasmoids in the tail, whose occurrence frequency appears to be affected by the solar wind convectional electric field with more frequent release under stronger driving. Based on the time rate of change of the open magnetic flux, we estimate the average potential drop associated with the dayside reconnection under nominal solar wind conditions to be approximately 280 kV, which is about a factor of 2 lower than previous estimates (Masters, 2017).

Our simulations also show that the frequency at which plasmoids are released in the magnetotail increases due to higher solar wind dynamic pressure, and are more frequently observed in a situation when the magnetosphere contains open field lines. These results support the hypothesis that the Dungey cycle reconnection occurs in the Jovian magnetotail, but it is not limited to certain regions in the exterior of the magnetosphere and can occur as a result of the internally driven Vasyliunas cycle reconnection, if the field lines which constrain the plasmoids are open to the interplanetary magnetic field. In such cases, plasmoid release induces reconnection in the tail lobe field diffusing toward the Vasyliunas X-line, thus accomplishing flux closure.

Chapter 5

Influence of the Solar-wind on Jupiter's Current Sheet Morphology

5.1 Introduction

Ionization of Iogenic neutrals adds ∼1 ton/s of mass to the inner magnetosphere of Jupiter, which increases the content of the corotating flux tubes (Bagenal & Delamere, 2011). Strong centrifugal forces in the equatorial regions of the Jovian magnetosphere stretch these flux tubes in the radial direction, which leads to the formation of a disk-like current sheet at all longitudes (Khurana et al., 2004) and distorts the magnetic field from the 'dipolar' configuration. However, the Jovian current sheet is not static, and its location changes as a function of radial distance and SIII longitude due to various dynamical processes in the magnetosphere. The first such process which modifies the equatorial current sheet was discussed in Chapter 4, where we studied the implications of a thin current sheet which is unstable to the tearing instability. The resulting multiple X-line reconnection creates O-lines and flux ropes on the ion-inertial scale, which can coalesce to form large plasmoids; much like what has been seen at the terrestrial magnetopause and magnetotail (Akhavan-Tafti et al., 2020; Eastwood et al., 2005).

The second mechanism which perturbs the current sheet is related to the asymmetries in the planetary magnetic field. Early studies of the Jovian magnetosphere, either through the

detection of radio emissions (Carr & Gulkis, 1969) or in situ spacecraft flybys (E. J. Smith et al., 1974), had shown that the internal field of the planet could be better described as a dipole which is tilted with respect to the spin axis. The tilted dipole field rotates at the planetary rotation period and introduces a ∼10 hour periodicity in the magnetosphere. Magnetic field observations made by Pioneer 10 (E. J. Smith et al., 1974) clearly show this 10-hour periodicity in the form of a 'square-wave' signal in the radial component of the magnetic field. These findings were later confirmed by Pioneer 11 (E. J. Smith et al., 1975), Voyager 1 and Voyager 2 (Behannon et al., 1981), Galileo (Khurana, 1992; Khurana & Schwarzl, 2005) and the Juno spacecraft (see e.g. Figure 5.2). With the introduction of dedicated orbiters, namely Galileo and Juno, more sophisticated models of Jupiter's internal field were developed using spherical harmonics. The VIP4 model was obtained by fitting magnetic field observations from Galileo and uses fourth order harmonics (J. E. Connerney, Acuña, Ness, & Satoh, 1998), whereas the more recent JRM09 field model (J. E. Connerney et al., 2018) uses the magnetic field data obtained from Juno's close perijove passes and uses 10th order harmonics. The models show that the Jovian magnetic field is not dipolar and the higher order harmonics have a substantial contribution near the planet. Figure 5.1 shows the contours of magnetic field magnitude on the 1 bar surface of Jupiter as per the JRM09 magnetic field model.

Another mechanism which temporarily modifies the structure of the current sheet is in the form of perturbations with frequencies smaller than that of the planet's rotation. One such transient perturbation relates to times when multiple current sheet crossings are observed within an interval of roughly 1 to 2 hours. This phenomena is termed as 'magnetotail flapping' and is also seen to occur in the terrestrial and Kronian magnetosphere (Volwerk et al., 2013). Other transient perturbations which occur on timescales of a few minutes have also been in Saturn's magnetosphere (Martin & Arridge, 2017).

Many empirical models have been put forward to account for the variation of the Jovian current sheet due to the non-axisymmetric internal field (see e.g Khurana & Schwarzl, 2005 and references therein). Each model has a different set of parameters which are varied to minimize the error between the modeled current sheet location and that seen in situ by the relevant spacecraft. Although they can be used to infer the location of the current

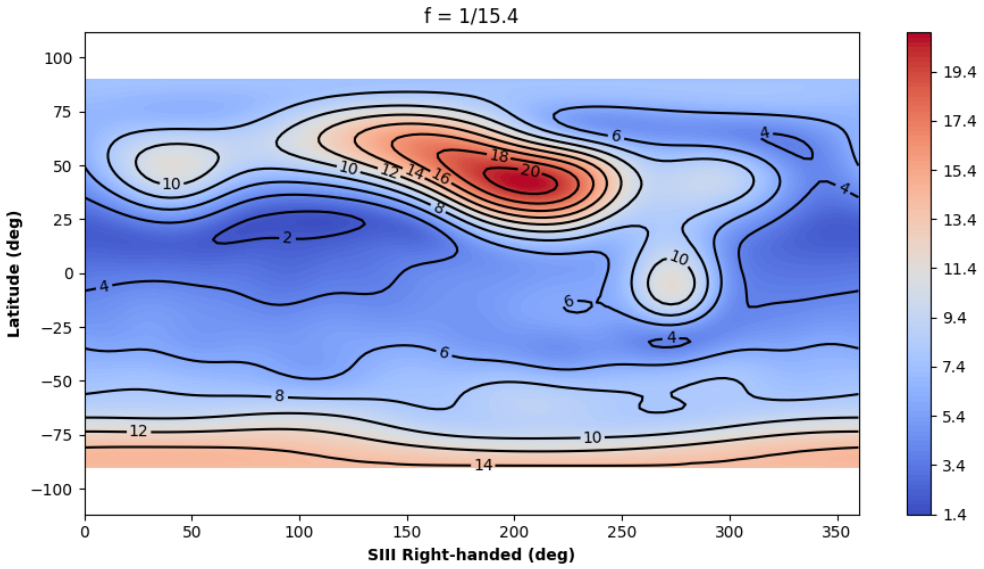

Figure 5.1: Contours of the magnetic field strength (in Gauss) on a representative flattened ellipsoid surface of Jupiter as per the JRM09 magnetic field model. The System III longitude system is a left-handed planetocentric coordinate system often used in studies of the Jovian system. In this system, the planetary magnetic field is constant (J. E. Connerney et al., 2018).

sheet, these empirical models do not provide any information about its strength. On the other hand, models have also been developed to estimate the current sheet strength and its contribution to the distortion of the planetary field (e.g. J. E. P. Connerney, Acuña, & Ness, 1981; Pensionerov, Alexeev, Belenkaya, Connerney, & Cowley, 2019), but these models are typically limited to the inner and middle magnetosphere and ignore the effects of finite-wave propagation speed and hinging.

After the flybys of Voyager 1 and 2, it was discovered that the current sheet crossings associated with a North-to-South rotation of the field were delayed compared to those associated with a South-to-North rotation of the field (Behannon et al., 1981). This led to the development of the concept called magnetotail 'hinging', which proposed that instead of following the magnetic dipole equator at large radial distances, the maximum extent of the current sheet was limited to certain heights in the z direction. An example of current sheet hinging is shown in Figure 5.3, where two current sheets are shown with and without the hinging parameter. In a highly hinged current sheet, a spacecraft located above the $z = 0$

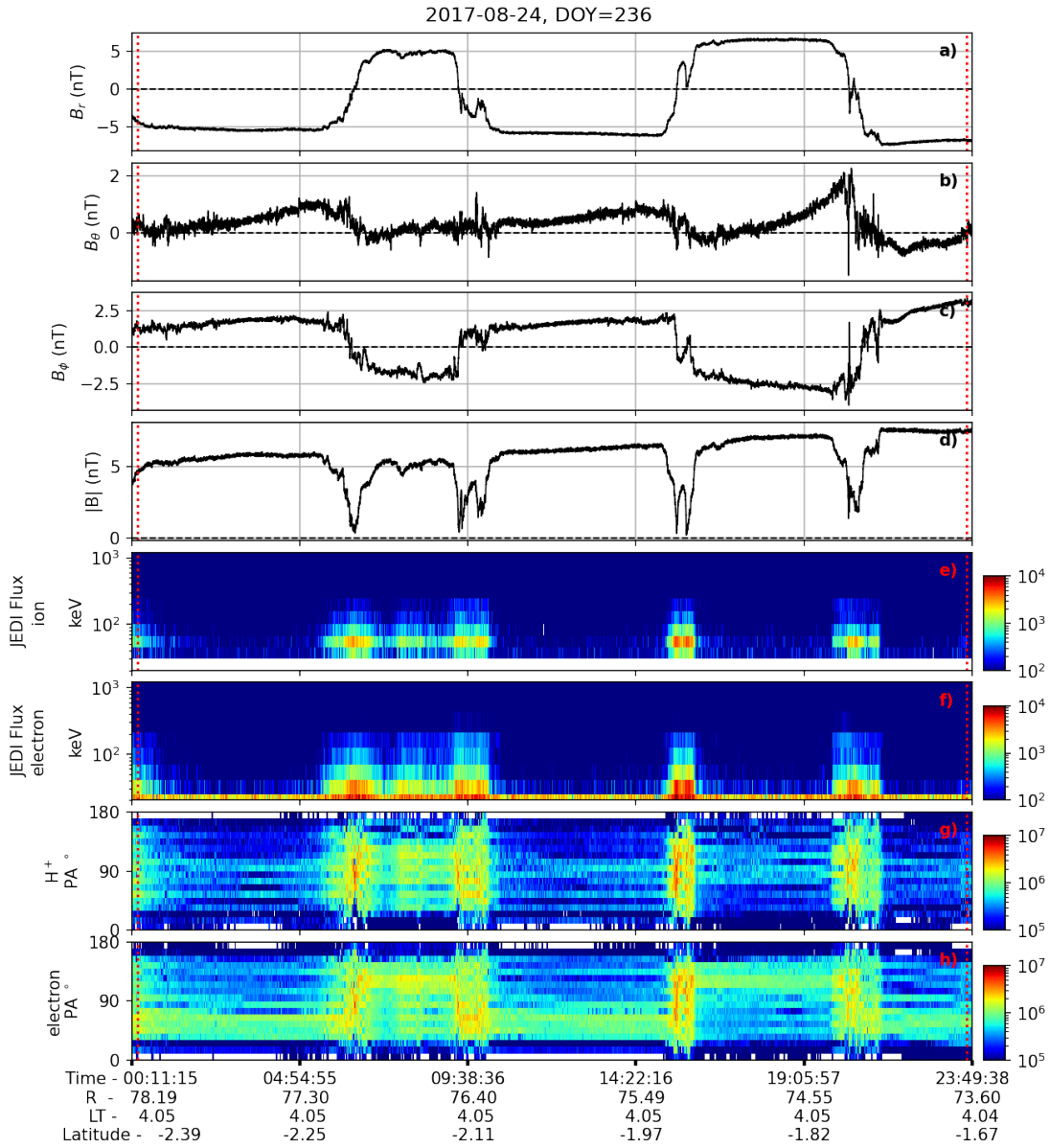

Figure 5.2: Magnetic field and energetic particle (JEDI) measurements taken by the Juno spacecraft in the JSS coordinate system (B_r, B_θ, B_ϕ, $|B|$). Juno crosses the current sheet and plasma sheet twice every rotation period, as seen in the multiple reversals of B_r accompanied with an intensification of particle fluxes separated by roughly $\sim$5 hours. Note the different temporal separation for north-to-south versus south-to-north crossings.

plane would spend a majority of its time either in the northern lobe or the southern lobe. In Figure 5.2, we show an example of a period when Juno is located predominantly in southern magnetotail lobe (where $B_r < 0$), and spends less time in the northern magnetotail lobe ($B_r > 0$) due to the hinging of the current sheet.

The current sheet models were modified to include the hinging phenomena, based on heuristic arguments that hinging was a product of Jupiter's magnetospheric interaction with the solar wind and the formation of a magnetotail. Behannon et al. (1981) showed that the inclusion of current sheet hinging decreased the RMS error between the modeled current sheet and the in situ data, with which it was originally fitted, compared to models which did not include hinging. Tao et al. (2005) showed intervals in the Galileo magnetometer data where the square-wave corresponding to the periodic current sheet was not seen, which they suggested corresponds to intervals of high solar wind dynamic pressure which increased magnetic pressure in the magnetotail lobes and suppressed the oscillations of the current sheet.

In the following sections a description of various empirical models used to fit the in situ observations is provided.

5.1.1 Axial models of the current sheet

Initial models assumed that the Jovian current sheet would be located in a plane corresponding to the magnetic equator of Jupiter, which would rotate at the planetary rotation period. The expected z location of the current sheet at a given radial location in cylindrical coordinates (ρ, ϕ) could then be described simply as (Van Allen et al., 1974; Goertz, 1976),

$$z = -\rho \tan \theta_d \cos (\phi - \phi_d) \tag{5.1}$$

Where θ_d is the tilt of the assumed planetary dipole field with respect to the rotation axis and ϕ_d provides the azimuthal location of the magnetic North pole. The rigid tilted plane model was found to be inaccurate at large distances, and the model was modified to limit the z excursions of the current sheet at large radial distances. The first *hinged* current sheet models (E. J. Smith et al., 1974; Hill, Dessler, & Michel, 1974) added a condition to

limit these excursions beyond $\rho > a$, where a was chosen as the hinging distance and was the only free parameter.

$$z = \begin{cases} -\rho \tan\theta_d \cos\left(\phi - \phi_d\right), & \text{for } \rho \leq a \\ -a \tan\theta_d \cos\left(\phi - \phi_d\right), & \text{for } \rho > a \end{cases} \tag{5.2}$$

Or alternatively, using a tanh function,

$$z = -a \tanh\left(\frac{\rho}{a}\right) \tan\theta_d \cos\left(\phi - \phi_d\right) \tag{5.3}$$

An improvement was suggested by Kivelson et al. (1978) in the form of a phase delay to the current sheet location, proportional to the distance from the wave source and has the following functional form,

$$\phi' = \phi_d - \frac{\Omega\left(\rho - \rho_0\right)}{U} \tag{5.4}$$

Where Ω is the angular velocity of Jupiter, U is the speed at which the wave travels and ρ_0 serves as the radial distance where the current sheet ceases to follow the rotating plane, beyond which all locations perceive a delay in the arrival of the current sheet. The expected current sheet location in the Kivelson et al. (1978) model is then given by,

$$z = \begin{cases} -\rho \tan\theta_d \cos\left(\phi - \phi_d\right), & \text{for } \rho < \rho_0 \\ -\rho \tan\theta_d \cos\left(\phi - \phi'\right), & \text{for } \rho \geq \rho_0 \end{cases} \tag{5.5}$$

Eviatar and Ershkovich (1976) introduced a similar model but limited the latitudinal extent of the oscillation beyond $\rho \geq \rho_0$,

$$z = \begin{cases} -\rho \tan\theta_d \cos\left(\phi - \phi_d\right), & \text{for } \rho < \rho_0 \\ -a \tan\theta_d \cos\left(\phi - \phi'\right), & \text{for } \rho \geq \rho_0 \end{cases} \tag{5.6}$$

Lastly, Behannon et al. (1981) introduced another axial model which includes the effects of wave propagation and current sheet hinging (Equation 11 in Behannon et al. (1981)).

However, they assumed that the wave starts propagating from the origin i.e. $\rho_0 = 0$.

$$z = -a \tanh\left(\frac{\rho}{a}\right) \tan\theta_d \cos\left(\phi - \phi_d + \frac{\Omega\rho}{U}\right) \tag{5.7}$$

5.1.2 Non-axial models of the current sheet

Axial models were found to fit the data poorly at large distances in the magnetotail, and it was suggested that the interaction of the magnetosphere with the solar wind may lead to a formation of a magnetotail, where the current sheet would take the form of a rocking plane instead of a rotating disk. However, the rocking plane model did not accurately represent the current sheet near the planet. Behannon et al. (1981) suggested a hybrid model which followed the magnetic equator close to the planet and took the form of a rocking plane at large distances (also called the Rocking Plane/Rotating Disk model or RP/RD).

$$\phi' = \phi_d - \frac{\Omega\,(x-a)}{U} \tag{5.8}$$

$$z = x\,\mathrm{sech}\left(\frac{x}{a}\right)\cos\left(\phi - \phi'\right) + y\sin\left(\phi - \phi'\right) \tag{5.9}$$

Note that the above model follows a rotating disk near the planet where $\phi' = \phi_d$. The wave starts propagating at distance a at a fixed speed U, which are the two free parameters for this model. Khurana (1992) extended the previous models by prescribing a variation in the wave propagation speed with radial distance as follows,

$$v(\rho) = v_0 \coth\left(\frac{\rho}{\rho_0}\right) \tag{5.10}$$

which leads to the following expressions for the phase delay and the current sheet location,

$$\phi' = \phi_d - \Omega\int\frac{d\rho}{v(\rho)} = \phi_d - \frac{\Omega\rho}{v_0}\ln\cosh\left(\frac{\rho}{\rho_0}\right) \tag{5.11}$$

$$z = -\rho\tan\theta_d \cdot \frac{x_0}{x}\tanh\left(\frac{x}{x_0}\right)\cos\left(\phi - \phi'\right) \tag{5.12}$$

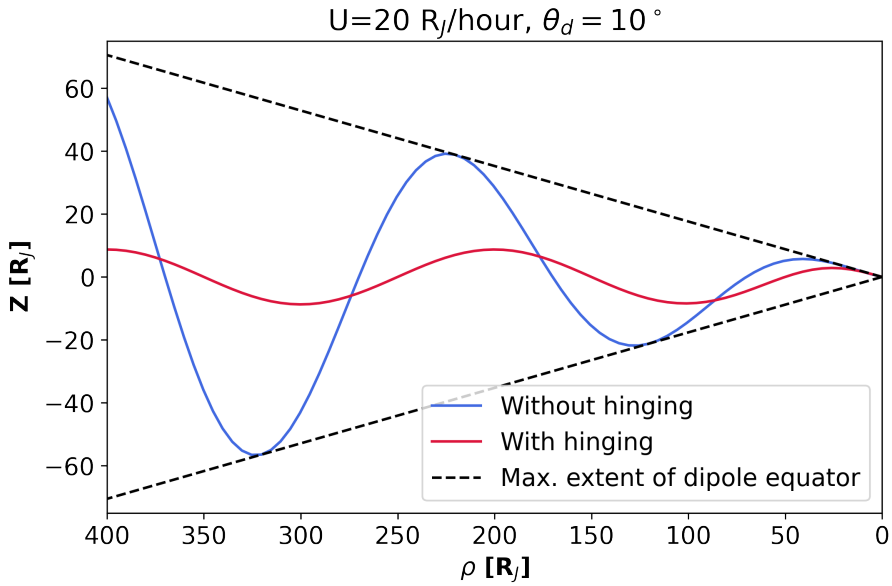

Figure 5.3: Exaggerated examples of the Jovian current sheet locations for two different models. The Kivelson et al. (1978) model does not account for hinging of the current sheet and hence has larger excursions with increasing distance from the planet. The Behannon et al. (1981) model includes current sheet hinging, which limits the oscillations beyond a certain radial distance.

The Khurana (1992) model has three parameters (v_0, ρ_0, x_0) representing the asymptotic wave propagation speed, radial location of outflow, and the hinging point along the X-axis to account for the interaction with the solar wind. Khurana and Schwarzl (2005) updated the model to account for local time asymmetries and solar wind angle of attack, but the generalization increased the number of parameters in the model.

5.1.3 Objective of this study

In Chapter 3 we showed that the Jovian magnetosphere, which was previously assumed to be insensitive to changes in the upstream parameters, does respond to changes in the solar wind dynamic pressure and the interplanetary magnetic field in the form of changes to the magnetospheric configuration and strength of currents in the ionosphere. In this chapter, we discuss the influence of the solar wind dynamic pressure on the Jovian current sheet. Specifically, we seek to answer the following questions,

- Does solar wind dynamic pressure increase or decrease the hinging distance of the

current sheet?

- Does solar wind dynamic pressure change the speed at which the current sheet wave propagates outward from the planet?

- What are the differences in the response of a magnetosphere to a forward shock in the solar wind when using an idealized versus a tilted dipole for the internal field?

In the absence of global in situ coverage, global MHD modeling is the only tool that can support or argue against heuristic arguments on which many Jovian current sheet models as based. In situ measurements of the Jovian magnetotail are rare, and existing empirical models of the current sheet have been seen to agree well only during intervals of data during which they were originally fitted. An understanding of the Jovian current sheet oscillations is crucial to study other dynamics in the magnetotail, such as magnetic reconnection, dipolarizations and magnetotail flapping, which occur on shorter timescales within the dynamic magnetotail.

5.2 Methodology

5.2.1 MHD simulations with a tilted dipole

To simulate the modulation of the Jovian current sheet, we modify the internal magnetic field of Jupiter to take the form of a dipole which is tilted 10° with respect to the spin axis and which rotates around it at the planetary rotation period (10 hours). The simulations are performed in the Jupiter-Sun Equatorial coordinate system (JSE), where the rotation is enforced about the z axis. In this system, the magnetic poles of the planet trace a circular path around the geographic pole.

In the simulations shown in Chapters 3 and 4, we used a spherical grid. Through our tests, we found that a spherical grid is not ideal when simulating a time-varying magnetosphere, where density and magnetic structures frequently cross the polar regions of the planet where grid cells are small and have a large aspect ratio for a spherical grid. To avoid this problem, we use a cartesian grid in the simulations performed for the present study. Like

Run	B nT	u km/s	ρ amu/cm^3	T K	$p_d = \rho u^2$ nPa
1	0.31	322.04	0.062	4.3E2	0.011
2	1.00	400.00	0.200	2.0E5	0.053
3	2.82	532.46	0.564	8.8E5	0.267

Table 5.1: Solar wind magnetic field strength, speed, density, temperature and dynamic pressure used in the present study. The variables are prescribed at the upstream boundary of the simulation at $X = 192\ R_J$. The interplanetary magnetic field is oriented along the negative Z direction.

the previous version, we use the mesh-refinement capability of the BATSRUS MHD code to successively refine regions of interest, such as the Io torus and the low-latitude middle and outer magnetosphere where the current sheets oscillations take place. The cartesian grid contains roughly 19 million cells, with the lowest grid resolution of 0.125 R_J present near the planet and the Io torus.

Different upstream conditions are introduced to evaluate the response of the current sheet to varying solar wind dynamic pressure. The properties of the solar wind used for the three runs are tabulated in Table 5.1. The solar wind dynamic pressure increases by a factor of 5 between each run.

5.2.2 Estimating the current sheet parameters within the MHD model

The current sheet can be identified as the locus of points in the closed magnetosphere region where $B_r = 0$. Its location in our model varies with radial distance and dipole phase. A direct comparison between the current sheet location in the MHD model and the various empirical functions shows a poor fit, as small differences in phase can lead to large differences in the final current sheet location. Moreover, the empirical models have been observed to perform well only for the in situ data to which they were originally fitted (Khurana, 1992; Behannon et al., 1981). For a more accurate comparison, we use the functional form for the various empirical models to find the set of parameters e.g. hinging distance, wave propagation speed, etc. which reproduce best the output seen in the MHD simulations. Then, we compare the parameters obtained by fitting the in situ data, to those obtained by

fitting the MHD simulation results.

We consider three empirical models that incorporate different physics and assume different functional forms as described above.

1. The Kivelson et al. (1978) model described by Equation 5.5 with two parameters - U and ρ_0, corresponding to the speed of wave propagation and the radial location where the current sheet wave starts to propagate.

2. The Behannon et al. (1981) model described by Equation 5.7 with two parameters - U and a_0, corresponding to the speed of wave propagation and the radial location where hinging is introduced.

3. The Khurana (1992) model described by Equation 5.12 with three parameters - v_0, x_0 and ρ_0, corresponding to the asymptotic speed of wave propagation, the characteristic hinging distance in the x direction and the radial location where the wave outflow commences.

The location of the current sheet is extracted in the noon-midnight meridian (00 LT) by identifying the locus of points located between $x = [-100, -4]R_J$ and $z = [-30, 30]R_J$ where $B_r = 0$. A current sheet model is then fitted to the extracted current sheet height $z_{\rm MHD}$ at a given radial location ρ by finding the set of parameters $\boldsymbol{\theta}$ that minimizes the square of the residual $\mathcal{R}$, which is normalized to the standard deviation of the current sheet location in the MHD model ($z_{\rm MHD}$),

$$\mathcal{R} = \frac{1}{\sigma(z_{\rm MHD})} \sum_{i}^{N} \left[z_{\rm MHD}(\rho) - z_{\rm fit}(\rho, \boldsymbol{\theta}) \right]_i^2 \tag{5.13}$$

The Levenberg-Marquardt iterative algorithm (Newville & Stensitzki, 2018; Levenberg, 1944) is used to perform the non-linear minimization for all models. We repeat the above procedure for all simulation data files separated by an interval of 30 minutes, giving us 200 data points within a 100 hour interval for each model. Although we limit our analysis to regions in the $y = 0$ plane and for $x < -4R_J$ (i.e., the nightside magnetotail), we effectively sample different phases of the current sheet due to the rotation of the dipole within each 10-hour rotation cycle. Times when a good fit to the MHD output cannot be obtained are

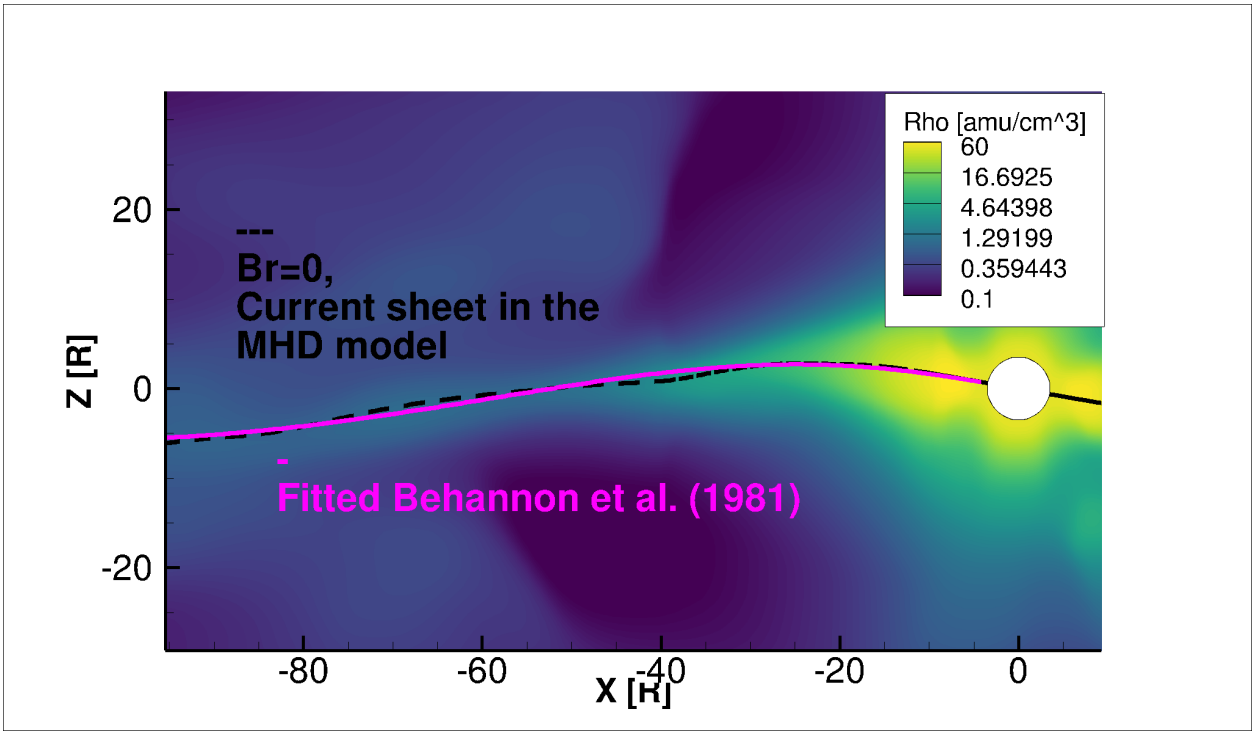

Figure 5.4: An example of the current sheet extracted from the MHD model by identified the contour line where $B_r = 0$ (dashed black curve), along with the fitted current sheet using the Behannon et al. (1981) form (magenta).

identified by evaluating the magnitude of model uncertainties and comparing them to the parameter values, and are subsequently discarded.

Figure 5.4 shows the result of fitting the Behannon et al. (1981) model for the current sheet to that observed at that instance in the MHD simulations. In this instance, the wave velocity U and the hinging distance a_0 are estimated to be 20.8 R_J/hour (413.0 km/s) and 32.4 R_J, respectively.

5.3 Results

We investigate the response of the current sheet parameters to the solar wind dynamic pressure by introducing three different upstream cases which are described in Table 1.

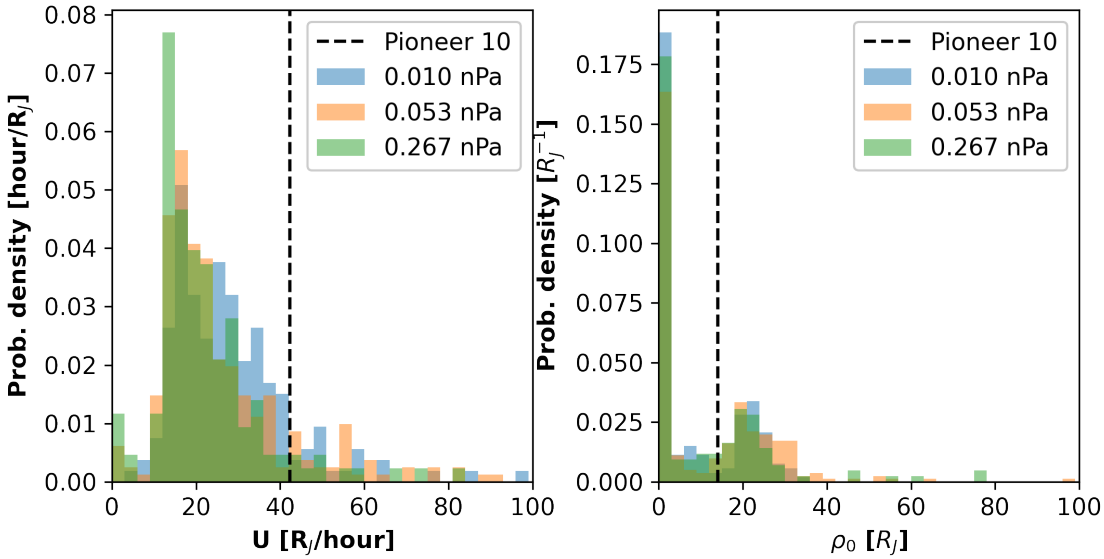

Figure 5.5: Histograms of the parameters used to fit the Kivelson et al. (1978) model form to the current sheet in the MHD model. Different colors represent the different solar wind dynamic pressures.

p_{dyn} nPa	N	mean(U) R_J/hour	median(U) R_J/hour	mean(ρ_0) R_J	median(ρ_0) R_J
0.010	177	28.06	25.83	8.14	0.00
0.053	270	25.57	20.94	12.15	3.74
0.267	143	22.17	18.93	10.88	0.00

Table 5.2: Statistics of the fits to the Kivelson et al. (1978) model shown in the histograms in Figure 5.5. N is the total number of good fits in each case.

5.3.1 The Kivelson et al. (1978) form

Fitting Equation 5.5 to the current sheet extracted from the simulation yield two parameters - the wave propagation speed U and the radial location where wave propagation begins ρ_0. The parameters which fit best the simulation results are plotted in a histogram in Figure 5.5 for the three dynamic pressures and their properties are shown in Table 5.2. The number of simulation times for which a good fit is obtained varies between the different runs. For a meaningful comparison, we show the probability density instead of the total number of events in each bin (i.e. in our case the area under each histogram sums to unity).

The histograms for the wave propagation speed show a range of possible values, from $\sim$10 R_J/hour (198.6 km/s) to $\sim 60R_J$/hour (1191.5 km/s), though the distribution is skewed to lower values. With increasing dynamic pressure, the distribution shifts more to lower values, indicating that the wave propagation speed is lower during intervals when the solar wind dynamic pressure is high. This can also be seen in Table 5.2, where higher solar wind dynamic pressure is seen to decrease the mean and median value of U, from $\sim$ 28.06 R_J/hour (557.24 km/s) to $\sim$ 22.17 R_J/hour (440.27 km/s). Also shown in Figure 5.5 is the U value obtained by Kivelson et al. (1978) by fitting the Pioneer 10 data, which is 42.29 R_J/hour or 840 km/s. The velocity in our simulations is roughly a factor of 2 less than these results, which could be due to different magnetospheric or external conditions.

On the other hand, the distribution of ρ_0 in the MHD model overwhelmingly favours low values and is insensitive to change in the solar wind dynamic pressure. Low ρ_0 values imply that the current sheet wave begins propagating at a finite speed very close to the planet. The mean and median values of ρ_0 as shown in table 5.2 are $\sim$ 10 R_J and $\sim$ 0 R_J, respectively, indicating that although there are some outliers, majority of the fits for low and high solar wind dynamic pressure favour near-zero values for ρ_0. A moderate increase is seen for the intermediate case of 0.05 nPa, where the mean and median values increase to 12.74 R_J and 3.74 R_J, respectively. Although our model predominantly favours near-zero values of ρ_0, all histograms show a small peak near $20R_J$. In comparison, the Pioneer 10 observations (shown in black dashed lines in Figure 5.5) estimate this outflow to begin from a distance of $\sim$ 14 R_J (Kivelson et al., 1978).

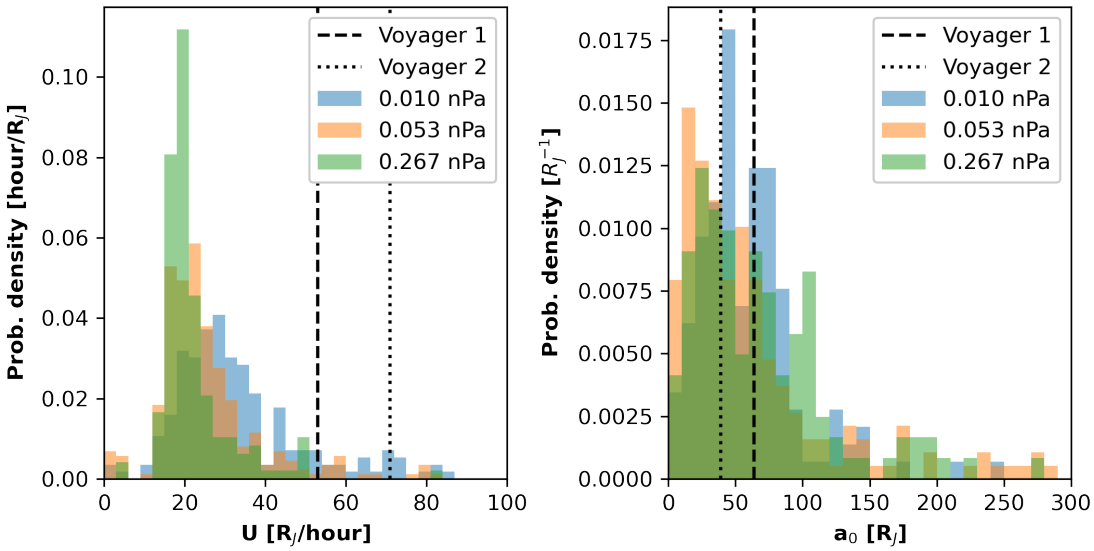

Figure 5.6: Histograms of the parameters used to fit the Behannon et al. (1981) model form to the current sheet in the MHD model. Different colors represent the different solar wind dynamic pressures.

p_{dyn} nPa	N	mean(U) R_J/hour	median(U) R_J/hour	mean(a_0) R_J	median(a_0) R_J
0.01	188	33.04	29.41	2410.45	68.67
0.05	290	25.45	22.28	3411.81	78.19
0.27	161	22.22	19.62	1986.96	75.19

Table 5.3: Statistics of the fits to the Behannon et al. (1981) model shown in the histograms in Figure 5.6. N is the total number of good fits in each case.

5.3.2 The Behannon et al. (1981) form

This model described by Equation 5.7 contains two parameters - the wave propagation speed U and the distance a_0 beyond which the current sheet is *hinged*, i.e. the radial location beyond which its maximum extent in the z direction is limited. As before, we show the normalized histograms of these parameters in Figure 5.6.

Similar to the result obtained when using the Kivelson et al. (1978) form, the propagation speed of the current sheet wave varies between 15 to 50 R_J/hour. For lower solar wind dynamic pressure (0.010 nPa), the mean of the distribution is located at 33.04 R_J/hour (656.13 km/s) and shift to lower values for higher solar wind dynamic pressure to 22.22

R_J/hour (441.26 km/s). The median values of U also decrease with increasing solar wind dynamic pressure from 29.41 to 19.62 R_J/hour. Histograms for U for the three different cases clearly show the shift to lower values as the dynamic pressure of the solar wind is increased (Figure 5.6). For comparison, the fits from the Voyager 1 and 2 flybys estimate the wave speed to be 53 and 71 R_J/hour (or 1052.52 and 1409.98 km/s), respectively, which is roughly 2 to 3 times the values obtained from our simulations. Note that the previous study by Kivelson et al. (1978), which used data from the the Pioneer 10 flyby estimated U to be roughly 840 km/s, which is lower than the Voyager results.

The hinging parameter a_0 also exhibits large variations, with most values ranging between 0 to 100 R_J, although there are some outliers with values $> 1000R_J$. In this case, large values of a_0 would indicate that the current sheet hinges at large radial distances. There is a large discrepancy between the mean and median values, the former ranging between 1986.96 R_J to 3411.81 R_J and the latter ranging between $68.67R_J$ to $78.19R_J$ for the three runs. Large values of a_0 are not unrealistic, as they represent the extreme case of a not-hinged current sheet when $a_0 \to \infty$. The calculation for average a_0 may be biased toward these larger outliers, but the relatively reasonable values of the mean of the distribution show that the majority of fits favour hinging distances around ~ 70 R_J. The corresponding values from the Voyager 1 and 2 flybys also result in similar values of 64 R_J and 39 R_J, respectively. Unlike the case for U, no clear relation is seen between the solar wind dynamic pressure and the properties of the a_0 distribution. As the solar wind dynamic pressure is increased from 0.01 to 0.05 nPa, the mean and median a_0 increase from 2410.45 R_J and 68.67 R_J to 3411.81 R_J and 78.19 R_J, but then decrease as the dynamic pressure is increased further to 0.27 nPa to 1986.96 R_J and 75.19 R_J. No clear shift towards larger or smaller values is seen in the histograms for a_0 between the three runs.

5.3.3 The Khurana (1992) form

The model described by Equation 5.12 contains three parameters - the asymptotic wave propagation speed v_0, the radial location where the current sheet wave starts to propagate ρ_0, and the characteristic hinging distance in the x-direction, x_0. Histograms of these parameters, which best fit the results from different times in the MHD simulation are shown

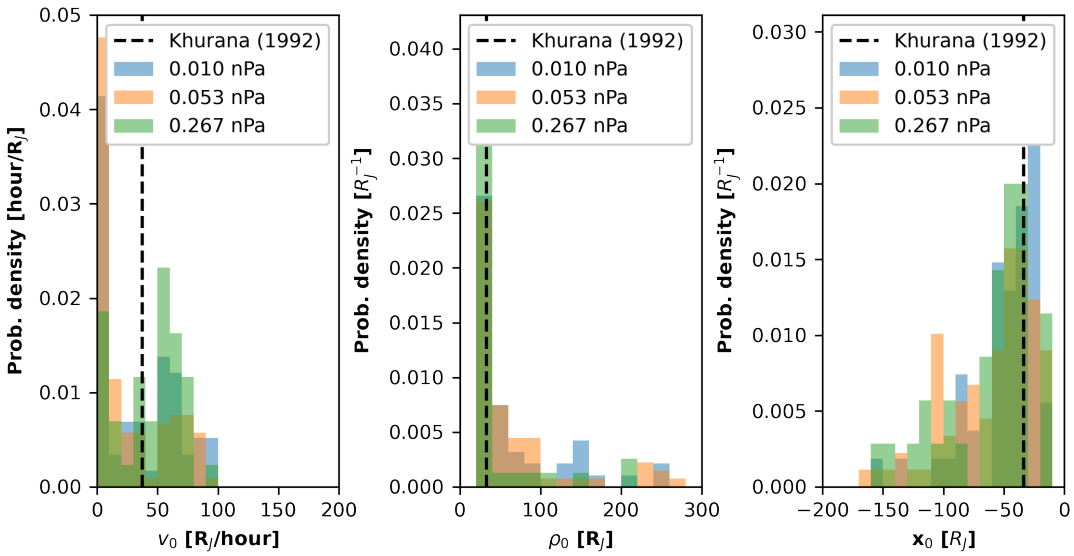

Figure 5.7: Histograms of the parameters used to fit the Khurana (1992) model form to the current sheet in the MHD model. Different colors represent the different solar wind dynamic pressures.

p_{dyn} nPa	N	mean(v_0) R_J/hour	median(v_0) R_J/hour	mean(ρ_0) R_J	median(ρ_0) R_J	mean(x_0) R_J	median(x_0) R_J
0.01	58	34.08	28.90	137.03	52.62	-43.97	-36.49
0.05	105	26.16	12.09	210.03	87.48	-199.34	-49.41
0.27	43	43.25	50.84	78.23	22.10	-101.96	-46.13

Table 5.4: Statistics of the fits to the Khurana (1992) model shown in the histograms in Figure 5.7. N is the total number of good fits in each case.

in Figure 5.7. Since this model has three parameters, the least-squares minimization is less robust at finding the global minima, which could explain the different behaviour as compared to the other models.

Unlike the previous two models, the asymptotic wave propagation speed v_0 does not show a preference and ranges between 0 to 100 R_J/hour. Unlike the previous models, which show a clear correlation between increasing solar wind dynamic pressure and decreasing wave speed, no correlation was seen in this model. The average speed for different solar wind dynamic pressures were found to be 34.08 R_J/hour (676.79 km/s), 26.16 R_J/hour (519.50 km/s) and 43.25 R_J/hour (858.89 km/s), which is close to the value obtained by Khurana (1992) of 37.4 R_J/hour (742.7 km/s).

As seen in the Kivelson et al. (1978) model case, this model too favours low values of ρ_0, which can be seen in the histogram for all three dynamic pressure cases showing a strong peak at ~ 30 R_J, however, there are more outliers in this case as shown in the higher values of the average compared to the median, which are 52.62 R_J, 87.48 R_J and 22.10 R_J for the three dynamic pressure cases, respectively. In comparison, Khurana (1992) obtain a value of 33.2 R_J, which matches well with the peak of the distribution.

The hinging distance x_0 shows a similar range as for the Behannon et al. (1981) model, with the key difference being that x_0 is shown as negative values (as x is negative in the magnetotail), whereas a_0 is applied to all longitudes and is a radial coordinate. The histogram of x_0 shows a preference for distances closer to the planet, but is spread over between -10 to -170 R_J in the magnetotail. The mean of the distribution of the three solar wind dynamic pressure cases are -43.97 R_J, -199.34 R_J and -101.96 R_J, respectively, whereas the median ranges from -36.49 R_J, -49.41 R_J and -46.13 R_J. These values match well the result by Khurana (1992), who found x_0 to be -33.5 R_J. There is considerable overlap between the histograms in all three cases, and no clear correlation can be identified between the value of x_0 and solar wind dynamic pressure.

Overall, the Khurana (1992) gives values which are reasonable, but the different behaviour of v_0 compared to the previous models hints that the minimization process was less robust when the number of parameters to fit was increased. In all cases discussed above, the considerable spread in the hinging parameter (a_0 for the Behannon et al., 1981 case and

x_0 for the Khurana, 1992 case), and its insensitivity to the solar wind dynamic pressure, compared to the relatively less spread in the wave propagation speed (U and v_0) suggests that the wave speed plays a more important role in determining the current sheet structure.

5.3.4 Changes in plasma parameters due to solar wind driven compression

In Figures 5.8-5.14, we show contours of different plasma parameters such as mass density, temperature, magnetic field strength, and the Alfven, sound and magnetosonic speeds to understand how solar wind dynamic pressure influences wave speeds in the magnetosphere. All figures are split into two columns; the left column shows the YZ plane (dawn-dusk meridian) whereas the right column shows the XZ plane (noon-midnight meridian). The current sheet (where $B_r = 0$) is highlighted in each figure as a white line. Different rows represent the three different solar wind dynamic pressures in increasing order as shown in Table 5.1. All plots were made at a time when the magnetic moment of the dipole was entirely in the XZ plane and pointed sunward.

Figure 5.8 shows the contours of plasma density ρ_m in units of amu/cm^3. As expected, the magnetosphere is compressed and reduces in size as the solar wind dynamic pressure is increased, which can be seen by identifying the bow shock and magnetopause regions as two discontinuities characterized by sharp density gradients. The density also increases drastically in the magnetosheath, but also increases in the other regions of the magnetosphere, including its deep interior (panel F). Note particularly the magnetotail lobe regions surrounding the current sheet (white curve), which have a density of ~ 0.1 amu/cm^3 for the 0.011 nPa case and which increases to > 2 amu/cm^3 for the 0.267 nPa solar wind dynamic pressure case.

One can also see the different behaviour of the current sheet in panels D, E and F of Figure 5.8 (solid white curve). For the 0.011 nPa case, the current sheet oscillations appear more gradual, and a minima and maxima are separated by $\sim$ 200 R_J. In constrast, for the 0.267 nPa case, the current sheet oscillates more strongly, with a maxima and minima separation (or the effective half-wavelength) of only about 50 R_J. In panel F, at around

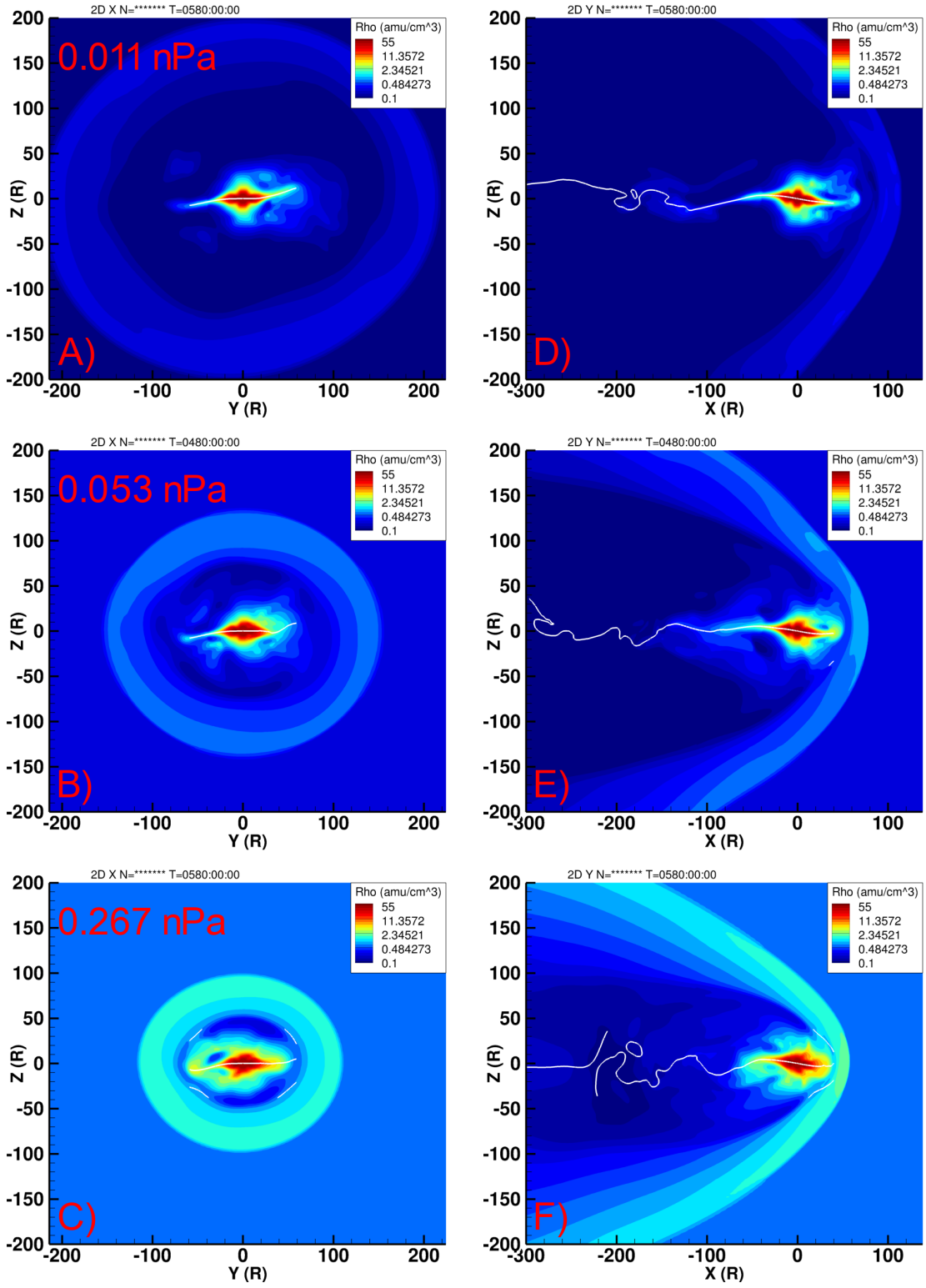

Figure 5.8: Plasma mass density contours in the $x = 0$ (YZ) plane (A-C) and in the $y = 0$ (XZ) plane (D-F) for different solar wind dynamic pressures. The current sheet is highlighted as a solid white curve.

$x = -200\ R_J$ the oscillations of the current sheet break into disjoint curves, which are a result of plasmoid generation due to magnetic reconnection.

In Figure 5.9, we show the contours of plasma temperature $T = p/nk_B$ in eV, assuming an ion mass of 16 amu. The choice for ion mass has no bearing on our overall result except a scaling of the temperature calculated using the ideal gas approximation and was chosen since most plasma inside the Jovian magnetosphere is composed of heavy ions, sulphur and oxygen. The absolute value of temperature in this analysis is not as crucial as the relative change.

As expected, a larger solar wind dynamic pressure creates a stronger bow shock and increases the temperature in the magnetosheath regions. However, we also find that despite an increase in density (as seen in Figure 5.8), the plasma temperature in the magnetotail increases by almost two orders of magnitude between the case of 0.011 nPa and 0.267 nPa, from 100 eV to ∼5000 eV, for e.g. at $x = -200\ R_J$. This increase in plasma temperature is also seen in the magnetotail lobes (panels D, E and F), which we discussed previously as having increased in density by a factor of 10 to 20 due to the solar wind compression.

In Figure 5.10, we show contours of the magnetic field strength in nT. Unlike the previous cases for density and temperature, the magnetic field does not exhibit drastic changes due to the solar wind compression. However, an increase in field strength can be seen in panels D, E and F in the magnetotail lobes, e.g. at $x = -100\ R_J$ and $z = -50\ R_J$ from 3.2 nT to 4.3 nT and 4.1 nT, respectively; likely due to the increased magnetic pressure in the lobes to balance the higher solar wind dynamic pressure outside the magnetopause.

Knowing the magnetic field strength and plasma density, we can calculate the Alfven speeds in the MHD simulation. Its contours are shown in Figure 5.11 in units of km/s. The smallest Alfven speed in the magnetotail are found at the current sheet, where the magnetic field is weak. The results from our MHD simulation clearly show that Alfven speeds in the magnetotail lobes, surrounding the current sheet, reduce due to a solar wind compression. For example, at the same location at $x = -100\ R_J$ and $z = -50\ R_J$, the Alfven speed reduces from $\sim$ 422 km/s to $\sim$ 205 km/s as the solar wind dynamic pressure is increased from 0.011 nPa to 0.267 nPa. The region of high Alfven speed, highlighted via red contours, is seen to shrink with increased solar wind dynamic pressure. This counter-intuitive result

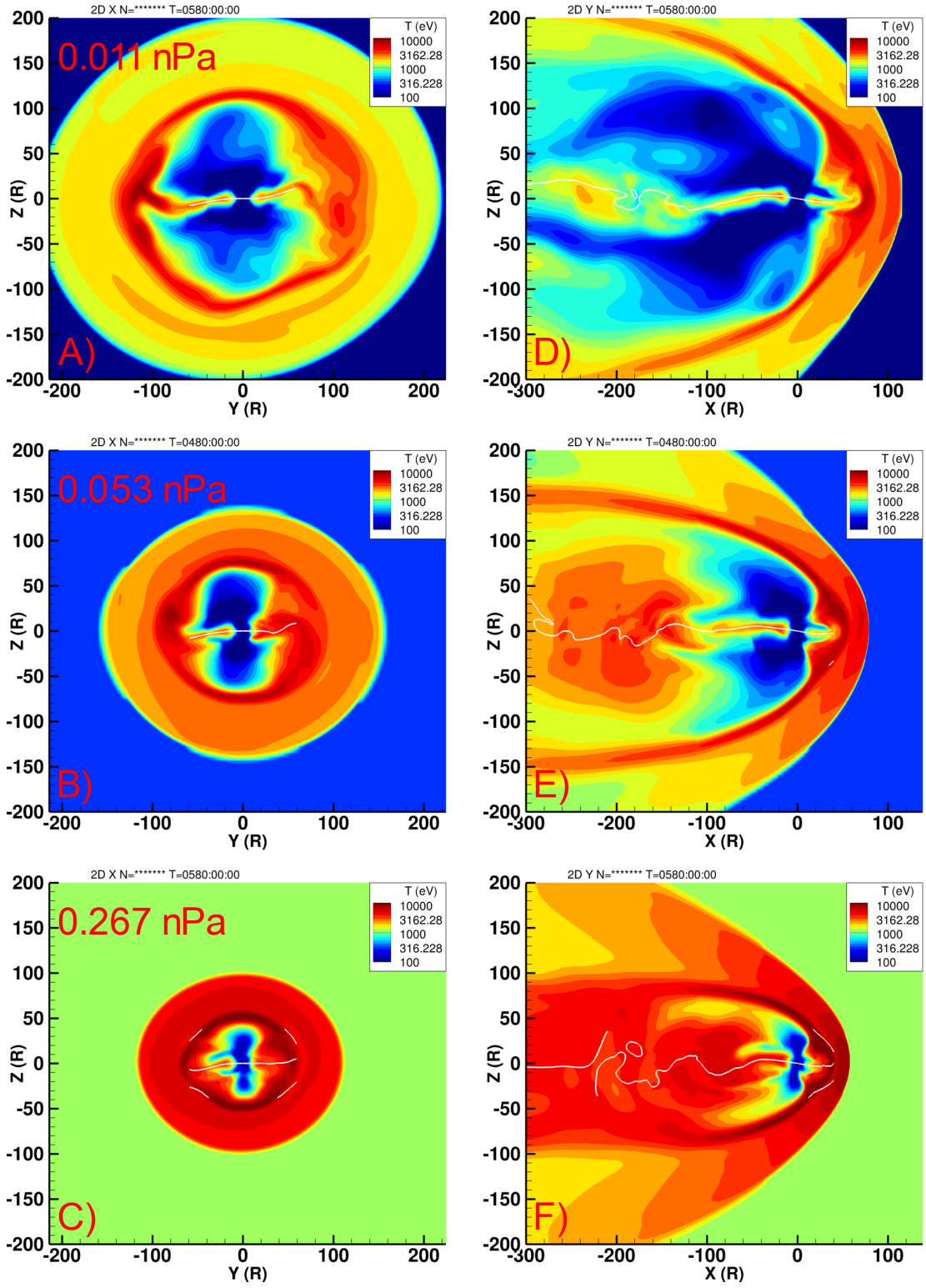

Figure 5.9: Contours of plasma temperature in the $x = 0$ (YZ) plane (A-C) and in the $y = 0$ (XZ) plane (D-F) for different solar wind dynamic pressures. The current sheet is highlighted as a solid white curve.

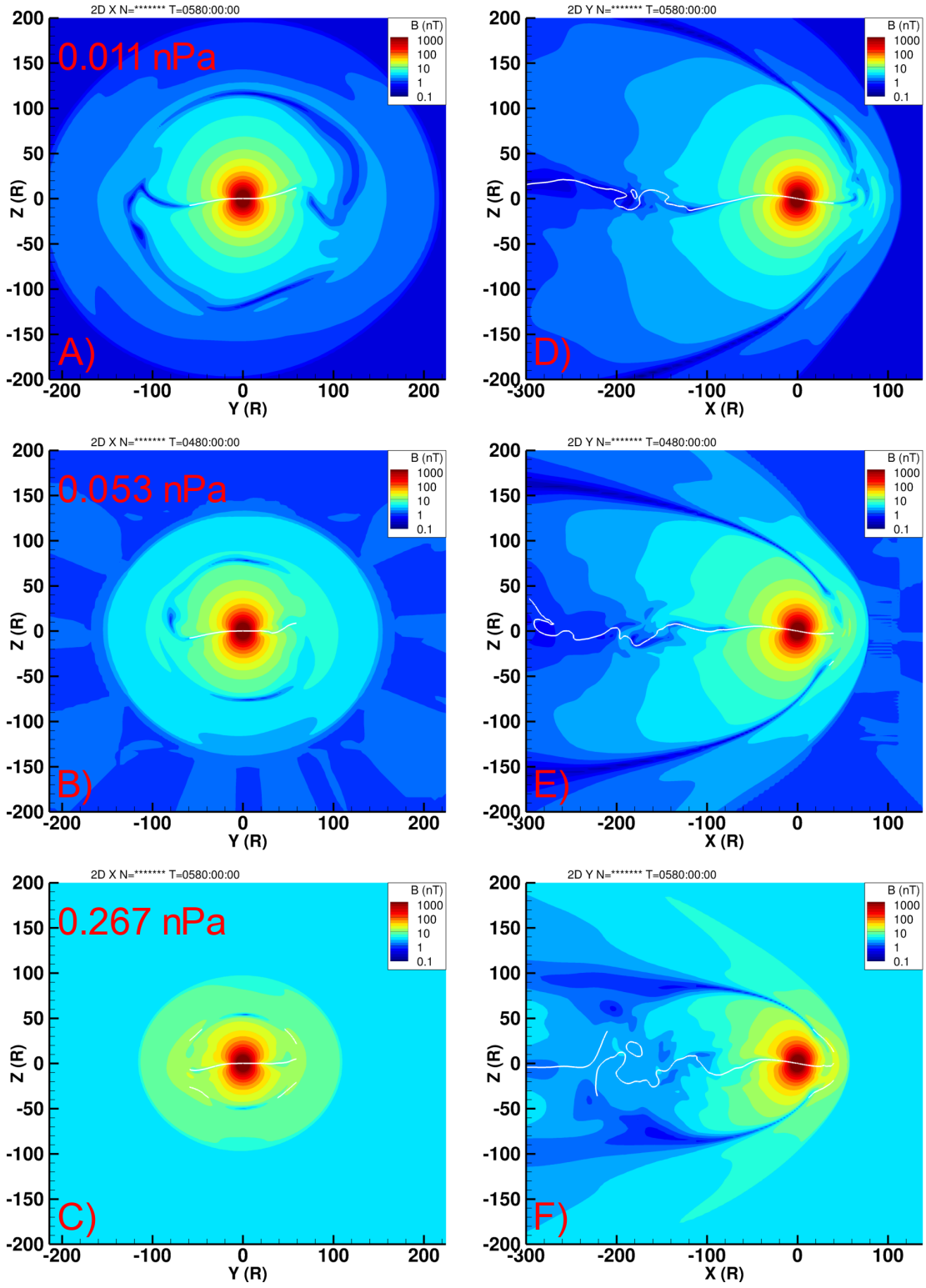

Figure 5.10: Magnetic field strength contours in the $x = 0$ (YZ) plane (A-C) and in the $y = 0$ (XZ) plane (D-F) for different solar wind dynamic pressures. The current sheet is highlighted as a solid white curve.

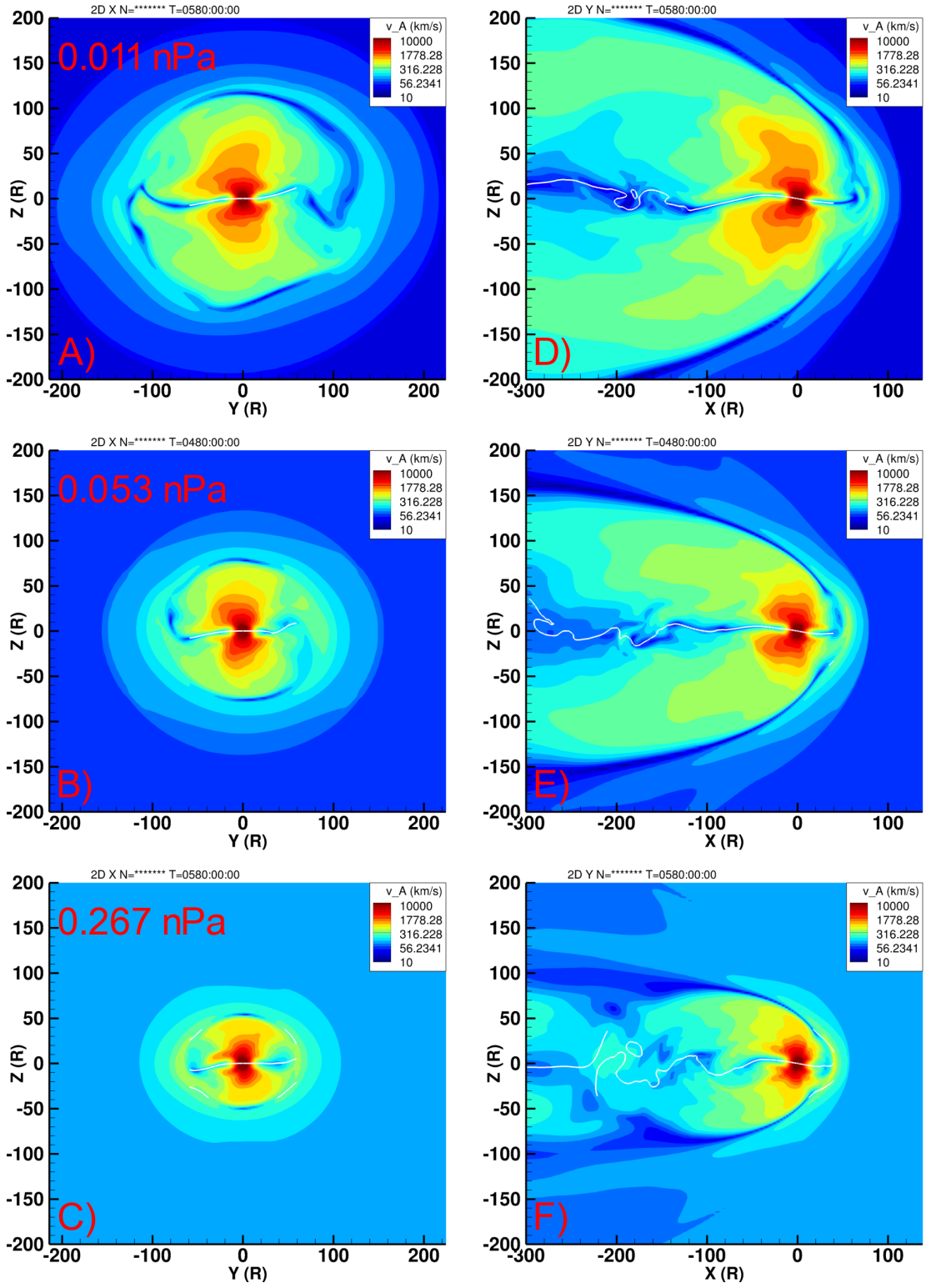

Figure 5.11: Alfven speed contours in the $x = 0$ (YZ) plane (A-C) and in the $y = 0$ (XZ) plane (D-F) for different solar wind dynamic pressures. The current sheet is highlighted as a solid white curve.

can be explained by the relative changes in B and ρ; the increase in plasma density during the 0.267 nPa case is much larger than the corresponding increase in magnetic field strength in the magnetotail lobes.

The sound speed can also be calculated from the model using the plasma pressure and density, and its contours are shown in Figure 5.12. Unlike the Alfven speed, which is smallest at the current sheet, the sound speed inside the current sheet and associated plasma sheet is seen to be greater than in the surrounding magnetotail lobes. Increasing solar wind dynamic pressure increases the sound speed in all regions of the magnetosphere, which is expected as it is closely related to the plasma temperature, which we discussed increased by two orders of magnitude between the 0.011 nPa and 0.267 nPa case (Figure 5.9).

The Alfven speed in the magnetotail is seen to decrease with increasing solar wind dynamic pressure (Figure 5.11), whereas the sound speed is seen to increase (Figure 5.12), and this diverging behaviour needs to be further investigated. In Figure 5.13, we show the contours of the ratio of the Alfven speed to the sound speed. In the majority of the inner and middle magnetosphere, the Alfven speeds are high and are larger than the sound speed by 1 to 2 orders of magnitude. However, this characteristic of the magnetosphere changes for higher solar wind dynamic pressures. Panels D, E and F of Figure 5.13 clearly show that with increasing solar wind dynamic pressure, the ratio of the Alfven speed to the sound speed decreases in all regions of the magnetosphere. Some regions in the outer magnetosphere which were previously dominated by the Alfven speed ($v_A/v_S \approx 20$) for the 0.011 nPa case now have sound speeds comparable to the Alfven speed ($v_A/v_S \approx 1$) for the 0.267 nPa case, e.g. at $x = 100\ R_J$ and $z = -50\ R_J$.

The fastest wave mode in the ideal MHD system is the fast magnetosonic mode, whose speed can be calculated using the Alfven and sound speeds ($v_{\rm ms} = \sqrt{v_A^2 + v_S^2}$). The magnetosonic mode would represent the fastest means by which a location in the distant magnetotail would perceive a change in the orientation of the dipole, and hence is crucial to understanding the oscillations of the current sheet. The contours of $v_{\rm ms}$ are shown in Figure 5.14, which can now be understood based on the changes in the individual components i.e. the Alfven speed and the sound speed, and ultimately the basic plasma properties such as density, temperature and magnetic field strength.

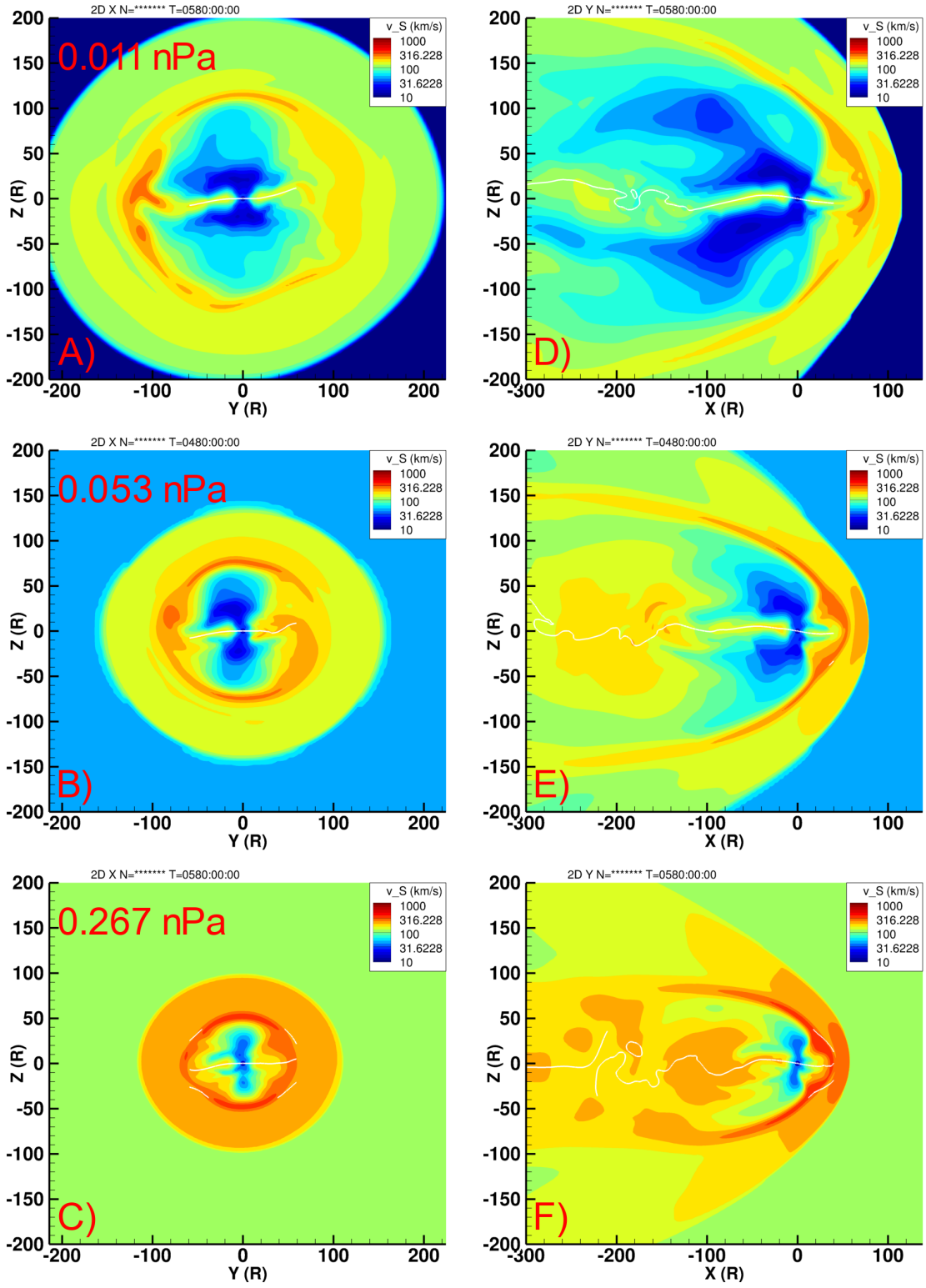

Figure 5.12: Contours of the sound speed in the $x = 0$ (YZ) plane (A-C) and in the $y = 0$ (XZ) plane (D-F) for different solar wind dynamic pressures. The current sheet is highlighted as a solid white curve.

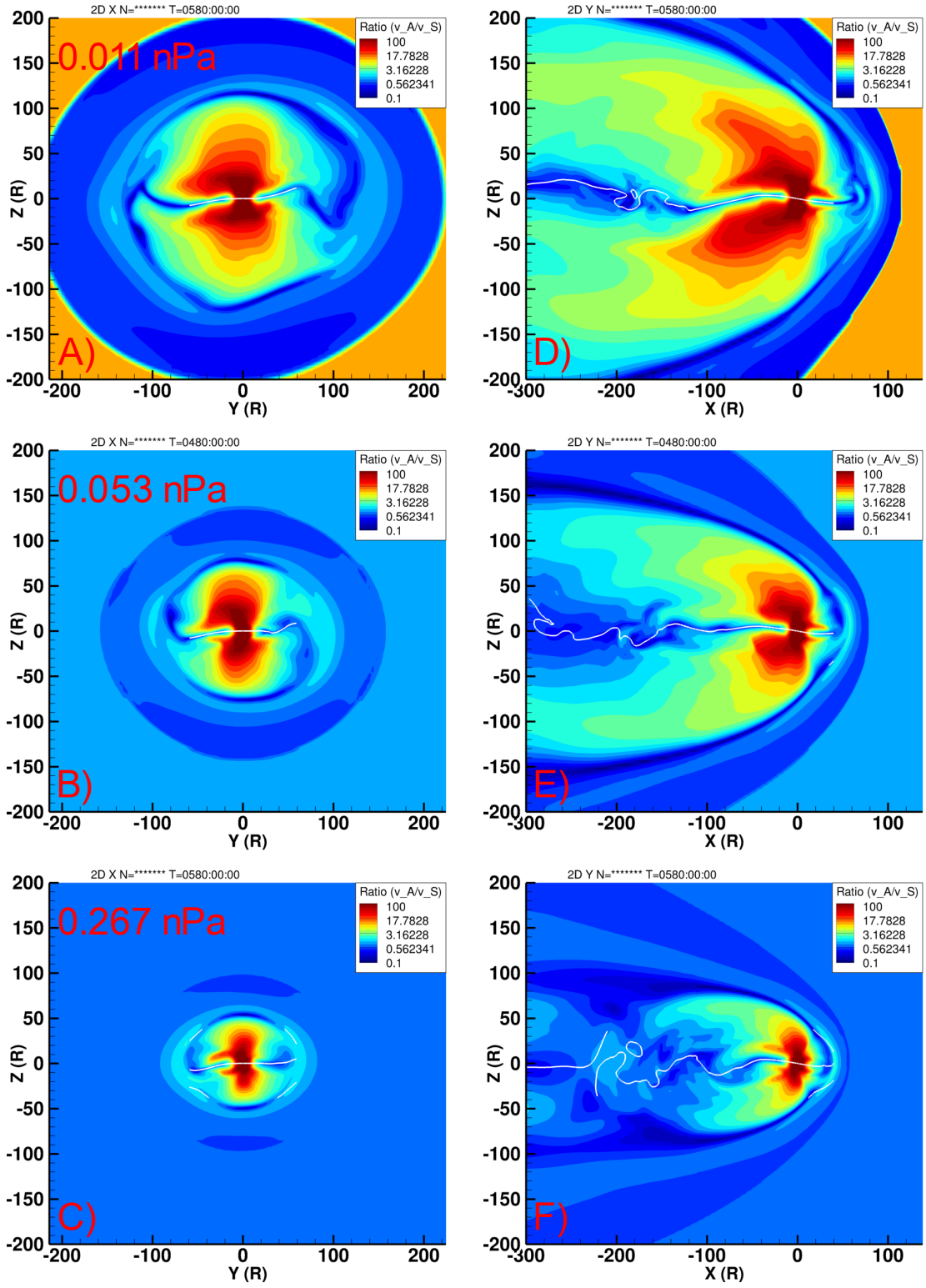

Figure 5.13: Contours of the ratio of the Alfven speed to the sound speed in the $x = 0$ (YZ) plane (A-C) and in the $y = 0$ (XZ) plane (D-F) for different solar wind dynamic pressures. The current sheet is highlighted as a solid white curve.

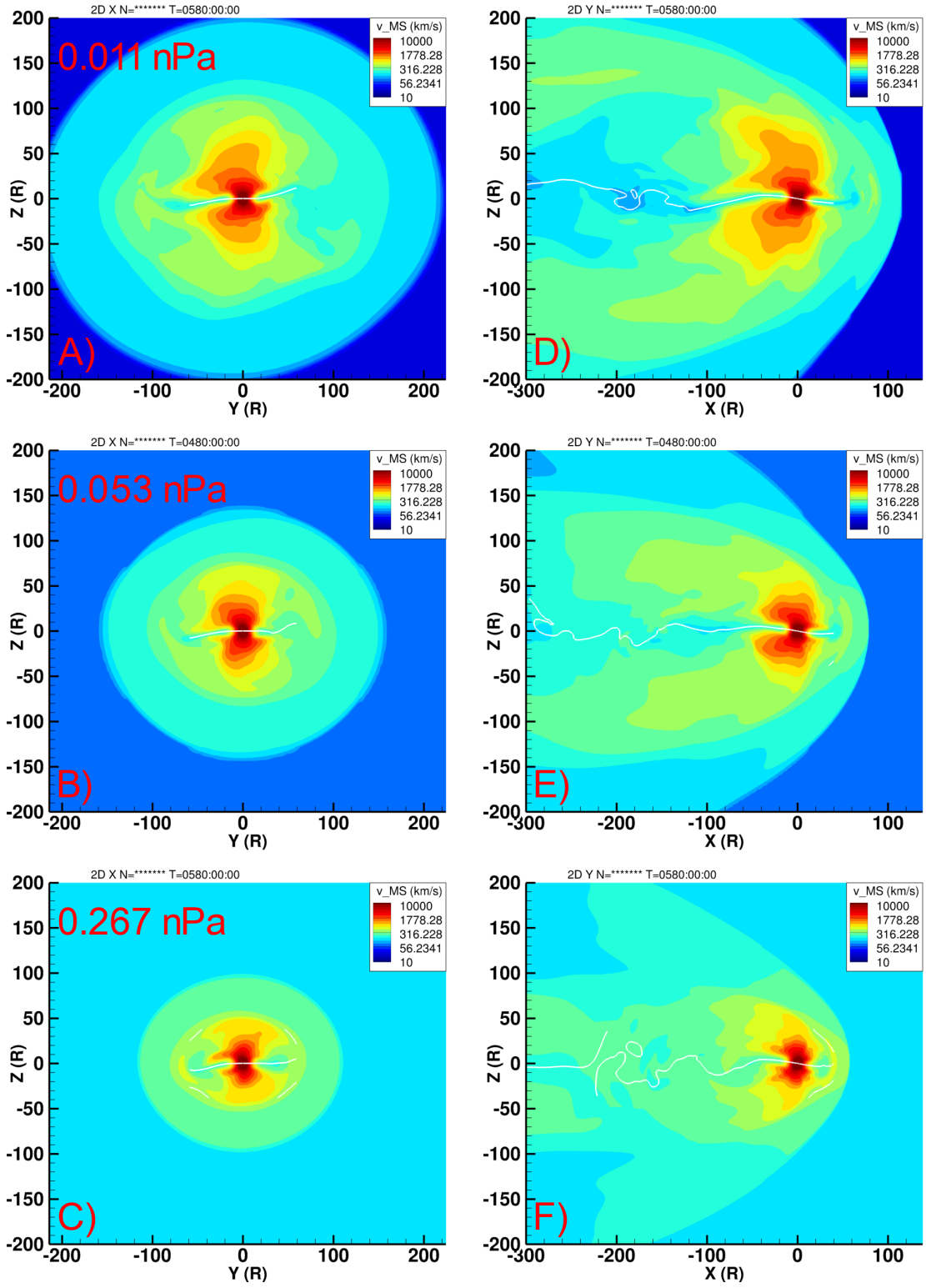

Figure 5.14: Contours of the magnetosonic speed in the $x = 0$ (YZ) plane (A-C) and in the $y = 0$ (XZ) plane (D-F) for different solar wind dynamic pressures. The current sheet is highlighted as a solid white curve.

Note that the wave speeds for semi-relativistic MHD do not have closed form expressions, so in these calculations we apply a simple correction to the conventional wave speeds as $v := \gamma v$ where $\gamma = 1/\sqrt{1 + v^2/c^2}$, and assume that regions in the middle magnetosphere and beyond have wave speeds much smaller than the speed of light and can be analyzed using the conventional expressions for the Alfven and sound speed. The maximum contour line shown in Figures 5.11 and 5.14 (deep red) is 10000 km/s which is still only 3% of the speed of light and occupies a small region located at $r < 15\ R_J$ in the polar regions of the planet.

The contours of the magnetosonic speed are similar to those observed for the Alfven speed, which is not surprising as the Alfven speed is much larger than the sound speed in the inner and middle magnetosphere. Like the Alfven speed, it is smallest near the oscillating current sheet and increases in regions with large magnetic field strength i.e. the magnetotail lobes and the near-planet regions. Increasing solar wind dynamic pressure from 0.011 to 0.053 nPa and ultimately to 0.267 nPa, is seen to decrease the magnetosonic speed at all locations in the magnetotail, including at the regions where the sound speed exceeds the Alfven speed. For example, at $x = -100\ R_J$ and $z = -50\ R_J$, the magnetosonic speed decreases from 422.67 km/s to 340.26 km/s and 283.23 km/s respectively for the three different cases.

A comparison of plasma properties at a fixed location in the magnetotail is shown in Table 5.5. In the next section we will discuss the implications of these results and their influence on the current sheet parameters obtained in the previous sections.

5.4 Discussion

Figures 5.5 and 5.6 show that the speed of the current sheet wave, which propagates outward from the planet, decreases as the solar wind dynamic pressure is increased. This is also seen physically in panels D, E and F or Figure 5.8, which show that the during periods of high solar wind dynamic pressure (0.267 nPa), the current sheet is more *wavy* than for periods during low solar wind dynamic pressure (0.011 nPa). At the same time, the degree of hinging, inferred by the maximum extent of the current sheet in the positive and negative z directions, remains roughly the same. However, the simple constant value for U is a construct for the given form of the empirical models, and in reality the current sheet oscillations are a result

Solar-wind Dynamic Pressure $p_d = (\rho u^2)_{sw}$ (nPa)	**0.011**	**0.053**	**0.267**
Density ρ (amu/cm^3)	0.028	0.089	0.196
Magnetic Field Strength B (nT)	3.242	4.346	4.149
Temperature T (eV)	48.57	1520.57	3937.7
Alfven Speed v_A (km/s)	422.11	317.88	205.14
Sound Speed v_S (km/s)	21.69	121.35	195.29
Magnetosonic Speed v_{MS} (km/s)	422.67	340.26	283.23
Ratio of Alfven to Sound Speed (v_A/v_S)	19.46	2.61	1.05

Table 5.5: Plasma properties at a point located at $x = -100R_J$, $y = 0$ and $z = -50R_J$ in the magnetotail at the simulation times shown in Figures 5.8-5.14.

of the interaction of many large scale MHD waves which originate from the planet due to the time-varying internal field. Nevertheless, the decreasing value of U suggests that wave speeds in the magnetosphere are affected due to the solar wind compression.

In Figure 5.8, we showed that during periods of high solar wind dynamic pressure, the density in the magnetosphere increases by a factor of 10 to 20, which reduces the Alfven speeds in the magnetotail lobes (Figure 5.11) despite a slight increase in the magnetic field strength (Figure 5.10) due to the solar wind driven compression. This behaviour is replicated in the fast mode speed (Figure 5.14), as the Alfven speeds in magnetotail are usually much larger than the sound speed (Figure 5.12).

Based on these findings, we suggests that an increase in solar wind dynamic pressure, which has always been commonly assumed to increase the magnetic stress in the magnetotail lobes and hence the Alfven speed, may reduce the wave speeds for the Alfven and the fast mode. This could have a direct implication on the wavy-ness of the current sheet, as lower values of U would decrease the effective wavelength of the up-down oscillations.

No correlation is seen between the hinging distance and solar wind dynamic pressure, and the model fits show a broad distribution of possible values (Figures 5.6 and 5.7).

5.5 Summary

The non-axisymmetric internal magnetic field of Jupiter introduces a 10-hour periodicity to the magnetosphere, which has been observed in the form of periodic current sheet crossings by in-situ spacecraft. Various empirical models have been constructed to describe the oscillating

motion of the current sheet, focusing mainly on three parameters - the speed at which the current sheet wave propagates from the planet, the source location for the wave, and the distance beyond which the current sheet is hinged, i.e. its excursions in the z-directions do not fully follow the dipole equator but are limited to smaller z values. These models were the first to suggest that solar wind dynamic pressure was directly responsible for the hinging of the current sheet; a phenomena that limits the current sheet oscillations at large radial distances.

Using time-accurate simulations of the Jovian magnetosphere that include the 10° dipole tilt of Jupiter's internal dipole relative to its rotation axis, we have investigated the influence of solar wind dynamic pressure on the oscillations of the tail current sheet by systematically introducing different upstream conditions. As the current sheet location is sensitive to small differences in dipole phase and other wave properties, we do not compare the current sheet location directly with the previously published empirical models, which have been seen to represent the current sheet well only during intervals for which they were originally fitted. Instead, we use the functional form of the empirical models and fit them to the current sheet locations extracted from the MHD simulation, which allows us to extract the hidden parameters such as the wave speed and hinging distance in our model.

We find that despite large changes in the solar wind dynamic pressure (from 0.011 nPa to 0.267 nPa), the hinging distance in the MHD simulation does not exhibit a clear trend toward increasing or decreasing values.

On the other hand, the speed of the current sheet wave clearly decreases during periods of large solar wind dynamic pressure, which increases the wavy nature of the current sheet. This result is counter-intuitive, as it was expected that during periods of compression, the stressed magnetotail would have large Alfven speeds, which would facilitate the travel of MHD waves from the planet. However, our results show that due to the increase in plasma density inside the magnetosphere during a solar wind driven compression, the Alfven speed and the magnetosonic speed decrease in most regions of the magnetotail. This decrease in wavespeed, we argue, would reduce the wavelength of the current sheet oscillations.

Chapter 6

Magnetic Reconnection Observed by Juno

6.1 Introduction

Magnetic reconnection in the magnetotail results in the formation of helical or loop-like magnetic structures called plasmoids, which contain strong plasma pressure gradients that maximize along the central axis and balance the magnetic forces directed inward (Hones et al., 1984; Kivelson & Khurana, 1995; Slavin et al., 1989). However, a subset of plasmoids, called "flux-ropes", lack strong pressure gradients in their interior, and the magnetic force of the outer wraps is balanced by the strong axial core field present at their center (Moldwin & Hughes, 1991; Sibeck et al., 1984). Flux ropes in which magnetic stresses are completely self-balancing are referred to as "force-free" as $\mathbf{J} \times \mathbf{B} = \nabla p = 0$. These force-free flux ropes correspond to the minimum energy state for a plasmoid that all such structures will evolve toward with increasing time (Priest, 2013; Taylor, 1974). Plasmoids which lack a core field and possess weak magnetic fields at their center compared to their surroundings are termed

*Parts of this chapter were published in - Sarkango, Y., Slavin, J. A., Jia, X., DiBraccio, G. A., Gershman, D. J., Connerney, J. E. P., Kurth W. S., & Hospodarsky G. B. (2021). Juno observations of ion-inertial scale flux ropes in the Jovian magnetotail. Geophysical Research Letters, 48, e2020GL089721

"O-lines".

Decades of in situ observations in the terrestrial magnetosphere, together with kinetic simulations (Drake, Swisdak, Che, & Shay, 2006; Drake, Swisdak, Schoeffler, et al., 2006), have revealed that magnetic flux ropes in the night-side plasma sheet can range in size from order 1 to 10 Earth radii (Ieda et al., 1998; Slavin, Owen, Kuznetsova, & Hesse, 1995) to below the local ion inertial length, which is typically on the order of hundreds of km (Eastwood et al., 2016; Sun et al., 2019). The latter are produced due to simultaneous magnetic reconnection occurring at multiple X-lines due to the tearing instability acting on a current sheet that has thinned to between the ion- and electron-inertial length scales (Daughton et al., 2011; Drake, Swisdak, Che, & Shay, 2006; Lapenta, Markidis, Goldman, & Newman, 2015). A similar dichotomy in flux rope size is seen at Mercury (DiBraccio et al., 2015; Slavin et al., 2009; Zhong et al., 2019), whose magnetosphere is closest to that of Earth with tail reconnection being driven by a Dungey-type (Dungey, 1961) magnetic flux transfer cycles, but also possesses differences related to its proximity to the Sun and its lack of an ionosphere. Small-scale flux ropes play an important role in energizing electrons and ions, which can undergo both, adiabatic acceleration due to the evolving flux rope structure (Drake, Swisdak, Schoeffler, et al., 2006; Le, Karimabadi, Egedal, Roytershteyn, & Daughton, 2012; Zhong et al., 2019) and nonadiabatic acceleration due to electromagnetic turbulence (Kronberg et al., 2019).

Plasmoids and flux ropes have also been observed at Jupiter (Kronberg et al., 2007, 2008; Russell, Khurana, Kivelson, & Huddleston, 2000; Vogt et al., 2010, 2014; Woch et al., 2002), Saturn (Jackman, Slavin, & Cowley, 2011), and Uranus (DiBraccio & Gershman, 2019). Especially for Jupiter, Dungey-cycle reconnection is considered to play a minor role (S. W. Cowley et al., 2008; McComas et al., 2007) and plasmoid release is facilitated primarily by the centrifugal force associated with mass loading and the energization of fresh plasma. Closed field lines on the Jovian nightside stretch freely, thinning the equatorial current sheet and in the process initiating reconnection and the release of plasmoids down the magnetotail (S. W. H. Cowley, Nichols, & Jackman, 2015; Kivelson & Southwood, 2005; Vasyliunas, 1983). However, single-spacecraft measurements cannot provide reliable estimates on the three-dimensional structures of the Jovian plasmoids. Despite the limitations,

it was estimated that plasmoids with diameters between 2 and 20 R_J and cross-tail width between 40 and 70 R_J (Vogt et al., 2014) could only account for a loss of ∼30-210 kg/s, which is significantly less than the production at Io, estimated to be between 250 and 1000 kg/s. This discrepancy could be a result of the underestimation of the size of the event (S. W. H. Cowley et al., 2015) or indicate a different loss mechanism altogether-either a diffusive "drizzle" across weak magnetotail field lines or recurring release of small plasmoids (Bagenal, 2007; Kivelson & Southwood, 2005).

Plasmoids and flux ropes observed so far in the Jovian magnetosphere have been fairly large. The mean duration of the observed plasmoids and flux ropes observed by the Galileo spacecraft at Jupiter was determined by (Vogt et al., 2014) to be 6.8 min and by (Kronberg et al., 2008) to be between 10 and 20 min (The two studies use different definitions for the duration of a plasmoid event). (Vogt et al., 2014) estimated the average diameter of the plasmoid to be ∼2.6 R_J (where 1 R_J = 71492 km) or 1.85×10^5 km, though they note that because of single-point measurement limitations, these plasmoid sizes could be larger. Assuming that the equatorial plasma density at a distance of 90 R_J downtail is ~ 0.01 cm^{-3} (Bagenal & Delamere, 2011) and that the plasma is made up of mostly S^+, S^{++}, O^+, and H^+ ions (Kim et al., 2020), we can approximate a mass of 16 amu for the average singly charged ion and estimate an ion inertial length ($d_i = c/\omega_{pi}$, where $\omega_{pi} = \sqrt{e^2 Z^2 n_i/\epsilon_0 m_i}$ is the ion plasma frequency) of $\sim 10^4$ km, which is at least an order of magnitude smaller than the diameter of the plasmoids seen by Galileo. Considering that the Galileo magnetometer had a cadence of a few seconds per vector, it would have been difficult to detect sub-ion scale flux ropes or O-lines, whose in situ signatures would last only a few seconds.

The dichotomy seen at the other planets and in simulations of reconnecting fields leads to a natural question of whether ion-scale flux ropes exist in the Jovian magnetotail and if they can be identified using the high-resolution capabilities of the Juno instrument suite. Recent plasmoid observations by the Juno spacecraft reported by (Vogt et al., 2020) have corroborated the Galileo observations, in that large plasmoids lasting several minutes on average were observed. In this work, we extend upon previous Galileo and Juno investigations and discuss our search for ion-inertial scale flux ropes in the Jovian magnetotail. We show examples of promising candidates in the form of magnetic field, waves and energetic particle

observations, and construct of survey of ion-inertial scale events to compare with previously published work.

6.2 Methodology

We use high-resolution magnetometer data in the Jupiter De-Spun Sun (JSS) coordinate system. The Z axis for the JSS system is aligned with Jupiter's north pole, X points toward the sun and Y completes the right-handed coordinate system. Also used are the corresponding magnetic field components in the spherical polar JSS system (B_r, B_θ, B_ϕ) referring to the radial, co-latitudinal and azimuthal directions. The Juno Magnetometer investigation measures the magnetic field strength and direction ambient to the spacecraft using boom-mounted fluxgate magnetometers (J. E. Connerney et al., 2017) and measures at rates of 16–64 vectors/second. These high cadence rates are significantly greater than what was returned by the Galileo magnetometer (between 24 and 60 s per vector, e.g., Vogt et al., 2010, 2020) and they allow us to study smaller scale structures durations down to ∼100 ms. We also use data from the Juno Waves instrument (Kurth et al., 2017), which measures the fluctuations in the electric field between 50 and 40 MHz and in the magnetic field from 50 and 20 kHz. We use the low frequency cutoff for the continuum radiation to infer the electron density (Barnhart et al., 2009).

The magnetic field observations are also supported by plasma observations made by the JEDI energetic particle detector (Mauk, Haggerty, Jaskulek, et al., 2017), which measures fluxes of the electrons in the energy range between 25 keV to 1 MeV, protons in the range of 10 keV to 2 MeV and oxygen and sulphur ions in the range of 45 keV to 10 MeV. Three JEDI instruments are located on the Juno spacecraft. Each instrument contains 6 solid-state detectors (SSDs), which measure the flux and can provide an estimate of the particle travel direction. The Juno spacecraft's primary mission was to understand the near-planet polar regions, and hence, JEDI data rates for the outer magnetosphere are lower to accommodate data transfers during this portion of the Juno orbit (Mauk, Haggerty, Jaskulek, et al., 2017).

Juno orbits Jupiter in a highly elliptical trajectory, with each perijove pass separated by ∼53 days. However, Juno spent a reasonable amount of time in the equatorial region (Figure

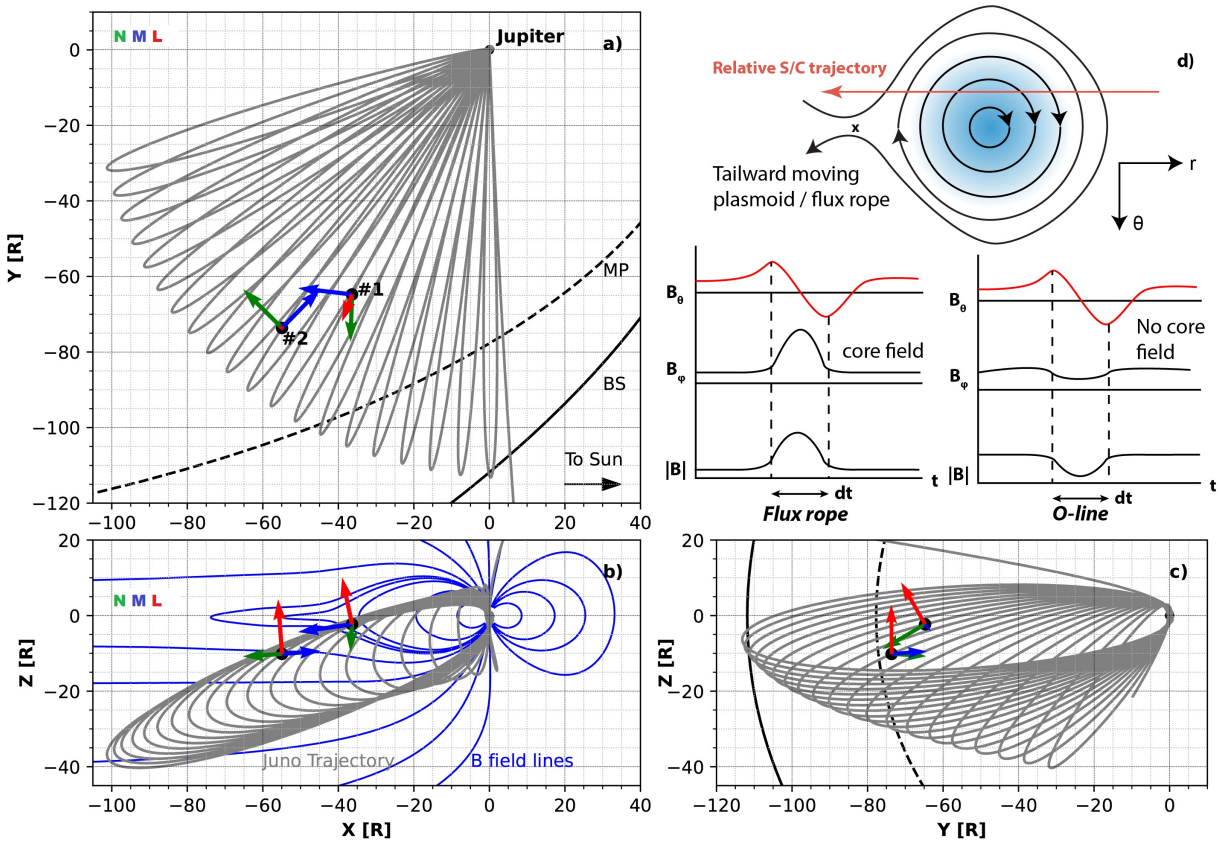

Figure 6.1: The trajectory of the Juno spacecraft in the Jupiter system is shown in panels a, b, and c. Superimposed on panel b are magnetic field lines extracted from the MHD simulation described in previous chapters. The location for two flux rope events are identified and the directions of minimum, intermediate and maximum variance are highlighted via arrows. In panel d), we show the expected magnetic signature of a tailward moving O-line versus a flux rope.

6.1), which enabled it to capture multiple current sheet crossings on every inbound pass.

In this study, as in Vogt et al. (2010, 2014), positive values of B_θ indicate a field pointing in the negative Z_{JSS} direction at the equator. In the quiet state with Jupiter's magnetic moment pointing north, the equatorial magnetic field is primarily in the positive B_θ (negative Z_{JSS}, assuming no current sheet tilt) direction. The magnetic signature of a tailward-moving plasmoid passing over a spacecraft near the equatorial plane is primarily observed in the B_θ component as a slight increase and subsequent reversal to negative values (e.g., Figure 6.1d for the signature of a tailward moving plasmoid). As the plasmoid passes over the spacecraft, the return to positive values can either be symmetric, hinting at reconnection occurring in closed field lines, or gradual, indicative of a postplasmoid plasma sheet that is formed when reconnection has progressed to the tail lobes (Jackman et al., 2011; Jia et al., 2012). Conversely, planetward moving plasmoids would exhibit the opposite signature, that is, an increase of B_θ in the negative direction and a reversal to positive values. If the plasmoid possesses a core field, it should typically be identified by a peak in the cross-tail component, either B_y or B_ϕ as well as a corresponding peak in the magnetic field strength which roughly matches the time where the reversal in B_θ is observed. Most plasmoids observed in Jupiter's plasma sheet (e.g., Vogt et al., 2014, 2020) lack an axial core field and are identified as O-lines. This result is similar to what has been observed at Saturn (Jackman et al., 2011) and could be due to large plasma pressure in a high β plasma and their primary role of carrying plasma away from these planets and balancing the plasma derived from their moons (S. W. H. Cowley et al., 2015; Kivelson & Khurana, 1995).

Using the high-resolution Juno data, we searched for bipolar variations in the B_θ component in proximity to current sheet crossings to identify flux rope signatures which are roughly 1 min or less in duration. Current sheet crossings (identified by a reversal in B_r) are observed only during the planet bound phase of Juno's trajectory with a periodicity of roughly 10 h, which reduces the search duration. As reported by (Vogt et al., 2020), Juno frequently observed bipolar variations in B_θ close to current sheet crossings. This is more evident in the high-resolution data and we show two promising examples in this study (Figures 6.2-6.4).

6.2.1 Minimum variance analysis

The minimum variance analysis (MVA) can be used to identify the orientation of a flux rope with respect to the magnetotail (Sonnerup & Cahill, 1967). For the given time interval, the covariance matrix $\mathbf{M}^{3\times3}$ is first estimated as,

$$M_{i,j} = \langle B_i B_j \rangle - \langle B_i \rangle \langle B_j \rangle \quad i,j \in \{x,y,z\} \tag{6.1}$$

The eigenvectors of the covariance matrix, $\mathbf{M}$ - $\mathbf{x}_N$, $\mathbf{x}_M$, and $\mathbf{x}_L$ represent the directions of minimum, intermediate and maximum variance, respectively. For magnetic flux ropes, which possess a helical field on the outside and a unidirectional axial field on the inside, the axial direction can be inferred using the eigenvector of intermediate variance ($\mathbf{x}_M$). There are additional criteria required to identify a flux rope using MVA: A bipolar signature in the maximum (B_N) varying component should be present and the eigenvector of the maximum variance should be predominantly in the direction normal to the current sheet. The ratio of maximum to intermediate (λ_L/λ_M) and intermediate to minimum (λ_M/λ_N) eigenvalues must be relatively large (ideally larger than 3 or 4, e.g., Lepping, Jones, & Burlaga, 1990) for the orthogonal coordinate system to be well-defined. A rotation should be observed in the B_M - B_N hodogram. An almost zero B_L indicates that the spacecraft passed close to the center of the flux rope or O-line. For a flux rope, the core field should be seen as an enhancement in the B_M component, whereas for an O-line, a local minimum in the B_M component would be seen.

Recently, Rosa Oliveira, da Silva Oliveira, Ojeda-González, and De La Luz (2020) have put forward a new metric to verify the degeneracy of the eigensystem using a single parameter P and suggest that $P > 4.5$ is sufficient to verify the consistency of the MVA analysis.

$$P = 100 \times \frac{\left(\sqrt{\lambda_L} - \sqrt{\lambda_M}\right)\left(\sqrt{\lambda_M} - \sqrt{\lambda_N}\right)\left(\sqrt{\lambda_L} - \sqrt{\lambda_N}\right)}{\sqrt{\lambda_L^3}} \tag{6.2}$$

6.2.2 Force-free flux rope fitting

Under the force-free assumption, pressure gradients and the $\mathbf{J} \times \mathbf{B}$ force are considered to be negligible. In this case, the Lundquist solutions can be used to model a circular force-free flux rope (Lepping et al., 1990; Slavin et al., 2003) as,

$$B_A = B_0 J_0 (\alpha r) \tag{6.3}$$

$$B_T = B_0 H J_1 (\alpha r) \tag{6.4}$$

Where B_A and B_T are the axial and tangential field components, B_0 is the maximum core field of the flux rope, α is a constant parameter, r is the distance to the center of the flux rope normalized to its radius and J_0 and J_1 are Bessel functions of the first kind. Since the velocity at which the plasmoid moves cannot be estimated without making assumptions, we cannot estimate the radius of the flux rope directly. Instead, we estimate the impact parameter (IP) defined as the ratio of distance to the center of the flux at closest approach to the radius of the flux rope. The parameters B_0, IP, the flux rope orientation (θ_A, ϕ_A) and the handedness H are varied so as to minimize reduced χ^2 defined as (Lepping et al., 1990)

$$\chi_r^2 = \frac{1}{N} \sum_{i=1}^{N} \left[(B_x - B_{x,m})^2 + (B_y - B_{y,m})^2 + (B_z - B_{z,m})^2 \right] \tag{6.5}$$

Where B_m is the modeled field and N is the number of data points in the reconstruction. The intermediate direction provided by MVA is used as the initial guess for the orientation of the flux rope and the minimization is performed in two steps - first using a unit normalized magnetic field with $B_0 = 1$ nT and then with B_0 as a variable parameter to fit the core field strength. A non-linear least squares minimization is used to fit the different parameters (Newville & Stensitzki, 2018).

6.2.3 Automated detection of flux ropes / O-lines

We use an algorithm which detects possible flux ropes and O-lines based on the magnetic field signatures to construct a list of such events and study their properties, such as, frequency and region of occurrence and their duration, which provides an estimate of the size of the plasmoid signature. The algorithm is described below.

In a given magnetometer data file, which typically contains data for the entire day (UTC), we first identify all times corresponding to a reversal in B_θ, either from positive to negative values or vice versa. Out of the selected crossings, those which occur beyond $r = 100R_J$ and local time greater than 05 LT are discarded to prevent contamination due to the magnetopause, where the variability in the magnetic field is quite large. Then, for each B_θ reversal (t_0), the corresponding start (t_s) and stop (t_e) times are determined using the algorithm used by A. W. Smith et al. (2017). This is achieved by identifying all local extrema in B_θ near t_0 within a particular window size (δt_w) and finding the maxima-minima (or minima-maxima) pair that when interpolated using a linear function, maximizes the coefficient of determination (A. W. Smith et al., 2017).

In order to select changes in the field which are prominent with respect to the background conditions, we discard all those events where the change in B_θ is less than 2 nT, or less than the standard deviation of the field for a duration of +/- 5 times the window size, i.e. where $\Delta B_\theta = |B_\theta(t_e) - B_\theta(t_s)| < 5\sigma(B_\theta(\delta t_w))$ or $\Delta B_\theta < 2$ nT. To further improve the quality of selected events, we also discard those times where the excursion in the positive values exceeds that in the negative values by a factor of 2 or more (and vice versa).

The event list is further refined based on the minimum variance analysis, which is applied to each potential event identified using the above criteria. The unit eigenvector of the variance matrix which provides the direction of maximum change in the field ($\mathbf{x}_L$) must have a z-component larger than 0.8. The ratio of the the eigenvalues corresponding to the minimum, intermediate and maximum directions must be larger than 3, i.e. $\lambda_L/\lambda_M > 3$ and $\lambda_M/\lambda_N > 3$. The P parameter (described by Equation 6.2) must be larger than 4.5.

We also specify a condition that the component of the magnetic field showing the least variation (B_L) be less than 2 nT, to capture only those events which pass through the center

of the plasmoid structure. Similarly, we place a similar limit on B_r, which should be less than 3 nT, to prevent contamination due to any process in the magnetotail lobes. The latter condition implies that we only identify events which occur close to the magnetotail current sheet.

6.3 Results - Case studies

6.3.1 Event 1 — Flux Rope DOY 236 2017

On DOY 236, 2017 Juno was located 74.3 R_J away from Jupiter at $\sim$ 04 LT (dawnside magnetotail) when it encountered a flux rope between 20:21:15 and 20:21:37 UTC. B_θ was positive before and after this event, but briefly reversed to negative values during the interval (Figure 6.2). The positive B_θ before and after the bipolar signature is consistent with Juno being in the near-Jupiter plasma sheet where the inward magnetic stress exerted by the stretched, closed magnetic field is balanced by the inward gradient in the plasma pressure. B_r is less than 1 nT during the encounter and B_ϕ increases (in the negative) by $\sim$ nT, which is the core field of the flux rope. The difference between the extrema in B_θ is about 4 nT. The sharp peak in the magnetic field strength, closely aligned with the center of the B_θ reversal, is a characteristic signature of a flux rope. The flux rope is close to the current sheet, as evidenced by the reversal of B_r from positive-to-negative values before and after the event. Although there is both a positive-to-negative and negative-to-positive polarity reversal of B_θ, the core field peak is seen during the negative-to-positive reversal, which hints that the flux rope was traveling planetward.

After performing the MVA, we find a bipolar variation in the B_N (maximum) component and a peak in the B_M (Figure 6.2), which is expected for a flux rope with a core field. The ratio between the intermediate and minimum eigenvalues of the variance matrix is 4.7, whereas the ratio between the maximum and intermediate values is 28.76. Looking at the B_M - B_N hodograms shown in Figure 6.2, we can observe a rotation of the magnetic field. Figure 6.2 also shows the magnetic field components of the modeled force-free flux rope (in blue) in the MVA coordinate system which best fits the data (minimum $\chi_r^2 = 0.13$). The

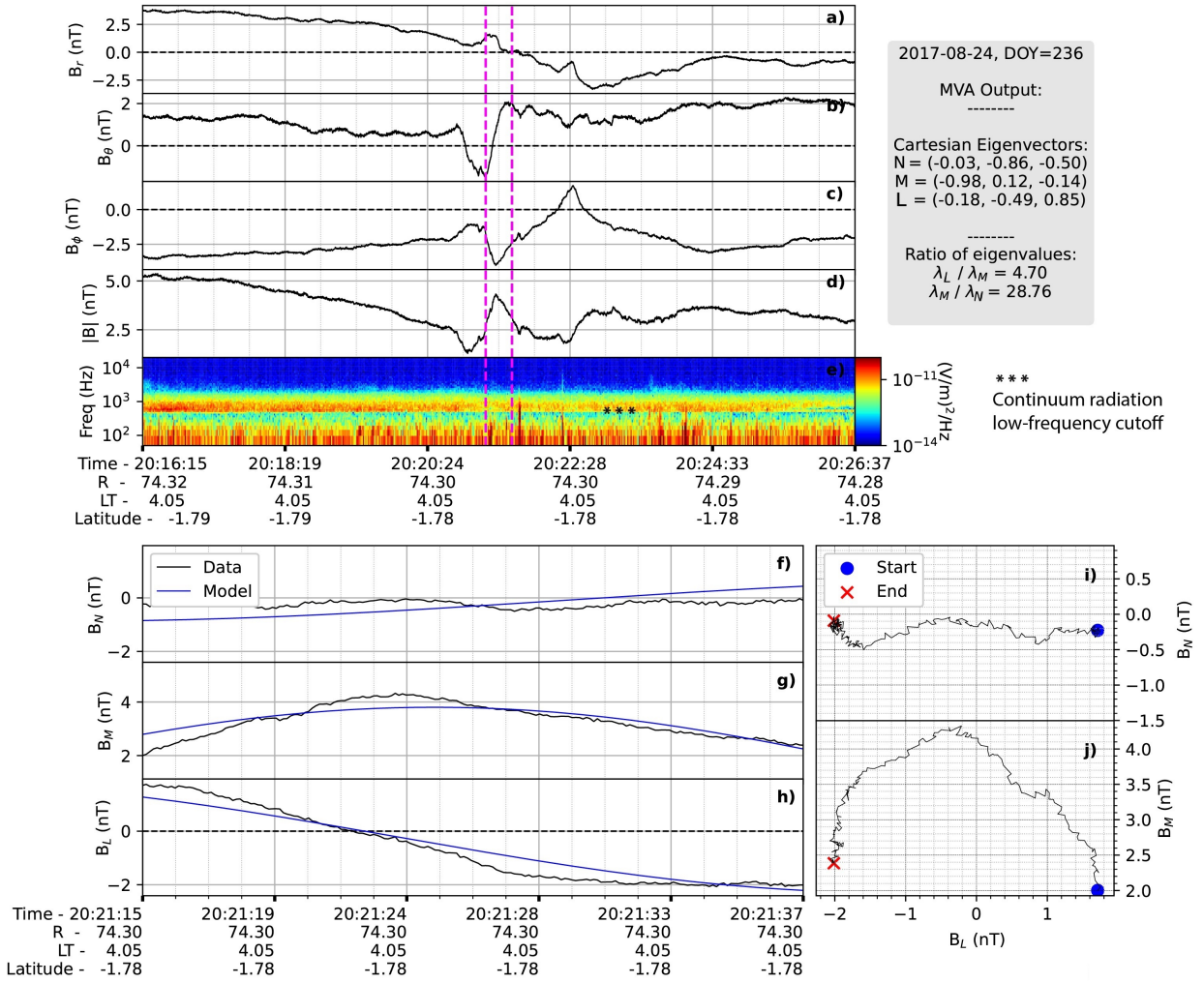

Figure 6.2: Planetward moving flux rope observed by the Juno spacecraft at DOY 236, 2017. Panels a-d show the magnetic field components in the spherical JSS coordinate system, while Panel e shows the spectra for the electric field measured using the Juno Waves instrument for the given time period. The flux rope structure is highlighted within magenta lines. Panels f-h show the result of the minimum variance analysis and force-free flux rope fitting. Panels i-j are hodograms of the different components obtained using MVA.

modeled flux rope has a core field strength of 3.86 nT and an impact parameter of 0.0, which indicates that the spacecraft passed very close to the center of the flux rope structure. This is also supported by the extremely low magnitude of B_L (less than 0.4 nT).

The eigenvectors of the variance matrix in the direction of minimum, intermediate, and maximum variance are (in the Cartesian JSS coordinate system) $\mathbf{x}_N = (-0.03, 0.86, -0.5)$, $\mathbf{x}_M = (-0.98, 0.12, -0.14)$ and $\mathbf{x}_L = (-0.18, -0.49, 0.85)$. Although flux ropes in the terrestrial magnetotail typically have a core field in the Y_{JSS} direction (as provided by $\mathbf{x}_M$), we find that for this event the direction of intermediate variance is in the X_{JSS} direction, which is close to azimuthal direction at the given spacecraft location (Figure 6.1).

In Figure 6.3, we show the measurements taken by JEDI in the 40 minute interval centered at the occurrence of Event 1. Panels e and f show the dynamic spectra of the ion and electron flux for all JEDI detectors and Panels g and h show the pitch angle spectra for the protons and the electrons. An increase in the electron and ion flux is seen after the flux rope event, which could be due to the proximity to the equatorial plasma sheet as inferred from the low values of B_r. The pitch angle for both ions and electrons is close to 90° prior to the flux rope interval, i.e. both species have a preferential motion in the direction perpendicular to the magnetic field. The anisotropy between parallel and perpendicular flux decreases after the flux rope, with more fluxes in the parallel directions.

6.3.2 Event 2 — Flux Rope DOY 338 2017

On DOY 338, 2017 between 01:49:57 and 01:50:59 UTC Juno was located at ∼92 R_J between 03 and 04 LT and observed a reversal in B_θ from positive-to-negative values, indicating a tailward moving flux rope (Figures 3a–3d). Unlike the previous example, the magnetic field magnitude did not peak inside the event interval, despite the presence of an axial core field. The azimuthal field component remained close to zero.

Performing the MVA provides us with additional information (Figures 3f–3h)—the maximum variance is in the Z direction ($\mathbf{x}_L = (-0.07, 0.01, 1.00)$), as expected, whereas the intermediate and minimum variance directions lie in the XZ plane close to the local radial and tangential directions. The component of the magnetic field in the minimum variance direction is close to zero. The intermediate component (B_M) peaks in the middle of the

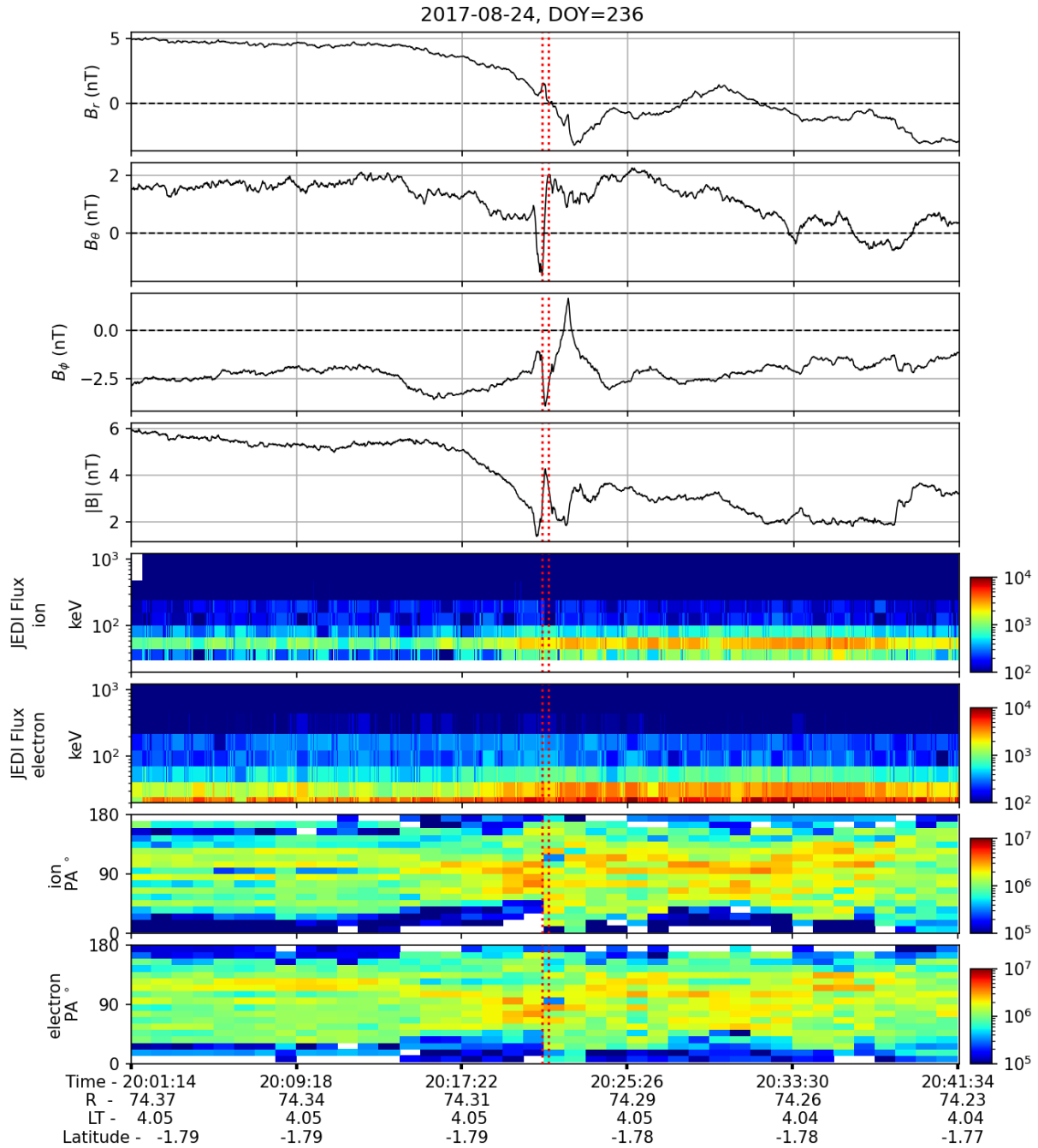

Figure 6.3: The magnetic field observations along with JEDI dynamic spectra for the ions and electrons. The last two rows show the dynamic pitch angle spectra for the protons and electrons respectively.

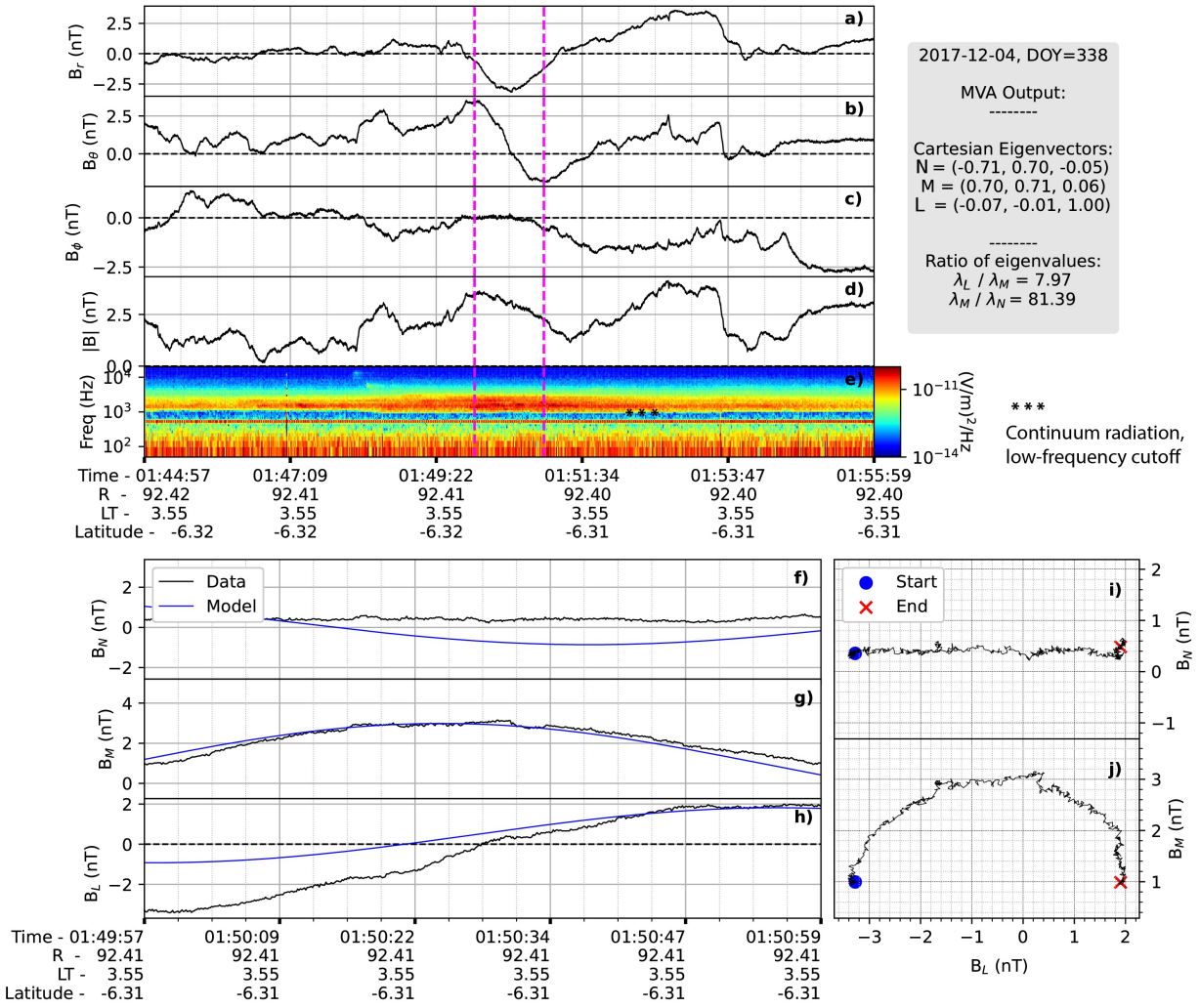

Figure 6.4: Tailward moving flux rope observed by the Juno spacecraft at DOY 338, 2017. Same format as Figure 6.2.

event interval. The B_M - B_N hodograms show a clear rotation of the magnetic field.

The spectra for the electric field as observed by the Waves instrument for Event 2 is shown in Figure 3e. A broadband intensification can be seen between 1 and 3 kHz for the duration of this event. Enhanced fluctuations in the electromagnetic field have been seen inside plasmoid intervals in the past in the terrestrial magnetosphere (Kennel, Coroniti, & Scarf, 1986). Although the continuum radiation is observed during the first event as well, no transient intensification was observed due to the flux rope.

Although Event 1 is an isolated flux rope event during the associated current sheet crossing, that is not true for Event 2. Figure 4 shows the magnetic field observations ∼2 h before and after Event 2. Multiple, alternating B_θ reversals, with peak-to-peak durations of roughly 2-3 min or more were observed prior to the event, and the continuum radiation can be seen throughout the ∼2 h current sheet crossing interval. For context, during the same day (DOY 338, 2017), Vogt et al. (2020) also report two large events observed at times 4:15 and 17:47 UTC.

Data from the JEDI instrument for this interval is sparse and cannot be used for further analysis.

6.3.3 Case studies - Discussion

The duration of the two events discussed in this study, as defined by the time between extrema in B_θ, is roughly 22 and 62 s, respectively. Using the low-frequency cutoff for the continuum radiation, which is roughly between 500 and 600 Hz for Event 1 and ∼1 kHz for Event 2, we estimate the plasma densities (Barnhart et al., 2009) during the intervals in question to be 0.003 and 0.012 cm^{-3}, respectively, which correspond to ion inertial lengths of roughly 16356 (0.23 R_J) and 8178 km (0.11 R_J), assuming an ion mass of 16 amu. Assuming that the plasmoid travel speed is limited by the Alfven speed in the surrounding lobes (S. W. H. Cowley et al., 2015) which are 489 and 220 km/s (which is calculated based on the observed magnetic field strength of 5 and 4.5 nT, respectively and electron density obtained from Waves), the 22 and 62 s duration of the event would correspond to diameters of roughly 10771 km (0.15 R_J or 0.65 d_i) and 13360 km (0.19 R_J or 1.67 d_i), respectively. Kronberg et al. (2008) found that most energetic particle bursts corresponding to plasmoid

events have speeds of roughly 450 km/s, which would provide diameters of 9900 km (0.6 d_i) and 27900 km (3.4 d_i) for the two events respectively, comparable to the local ion inertial length.

After Event 1, when the flux rope has passed over the spacecraft, a reversal in the guide field (B_ϕ) is observed from -4 to 2 nT. This reversal of the out-of-plane component of the magnetic field in close proximity to the reconnection x-line could be due to the quadrupolar Hall magnetic field (Eastwood et al., 2007; Sonnerup & Cahill, 1967), which is formed due to the decoupling of ions and electrons in the ion diffusion region and has been identified by multiple spacecraft in the terrestrial magnetotail (Nagai et al., 2001). We caution however that single-spacecraft measurements are unreliable to conclusively determine whether or not the reversal in B_ϕ is due to the Hall field. Another possible explanation for the reversal could be related to the bend-back of the magnetic field, which has been seen as a correlation between the sign of B_r and B_ϕ. In the present situation, the latter theory is less likely since B_ϕ returns to negative values despite multiple current sheet crossings as seen in B_r.

For Event 2, the MVA analysis shows that Juno is sampling the portion of the flux rope where its axis is almost radial, as determined by the direction of intermediate variance. The ratio of the maximum to intermediate and intermediate to minimum eigenvalues are quite large ($\lambda_L/\lambda_M = 7.97$, $\lambda_M/\lambda_N = 81.31$), indicating that the coordinate system is well-defined. Note that observations of flux ropes in the terrestrial magnetotail have shown that many flux ropes are tilted in the plane of the current sheet (Slavin et al., 2003). However, $|\mathbf{B}|$ does not peak at the center of the interval and the best fit force-free flux rope does not fit the data well ($\chi_r^2 = 5.9$), although the modeled field in the B_M component looks reasonable, and a bipolar signature is observed in the B_N component. While conventionally flux ropes in the terrestrial magnetotail are seen to possess a strong core field, this has not been the case for the giant planet magnetospheres. Plasmoids observed at Jupiter and Saturn usually possess a weak magnetic field at their core, which is likely due to large plasma β. The force-free model is based on the assumption that pressure gradients inside and surrounding the flux rope are negligible, which may not be the case for this event. Another possible explanation is that this is a flux rope in the early stages of formation and has not yet reached the minimum energy force-free state.

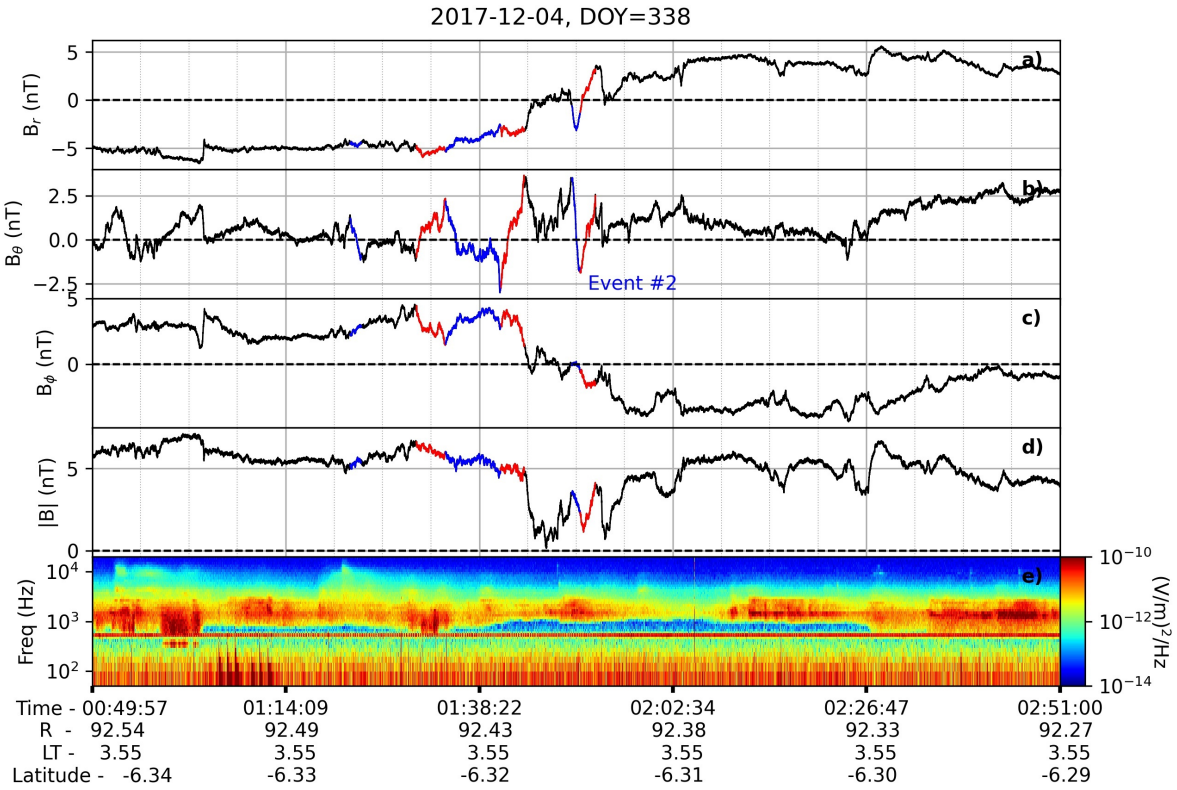

Figure 6.5: Multiple reversals in B_θ seen approximately 1 hour prior to Event #2 (the last positive to negative crossing highlighted in blue).)

Multiple alternating B_θ reversals, with peak-to-peak durations of roughly 2-3 min or more were observed prior to Event 2 (6.5, shown in red and blue). There is no clear increase in the axial magnetic field strength inside these events, which indicates that these north-south reversals correspond to magnetic O-lines. These observations of recurring north-south reversals are similar to those expected for sequentially released plasmoids from a reconnection X-line due to current sheet instabilities, though single-point measurements are not definitive.

Both events are observed in the dawnside magnetotail, where plasma density is relatively low and the Dungey-cycle flux closure is expected to occur (S. W. Cowley, Bunce, Stallard, & Miller, 2003). However, without context of the global magnetosphere, it is not possible to determine whether the reconnection events discussed here were a product of the Dungey or Vasyliunas cycles. Note that both Dungey and Vasyliunas cycle plasmoid release can be initiated by reconnection initially within closed field lines, as proposed by theoretical models (S. W. Cowley et al., 2008) and seen in global simulations (Sarkango, Jia, & Toth, 2019).

6.4 Results - Survey of flux ropes and O-lines

In this section, we discuss the results of the survey of plasmoid events detected using the automated algorithm described previously.

6.4.1 Duration

The algorithm detected 89 flux ropes between DOY 75, 2017 and DOY 301, 2019 which fulfilled all the criteria specified in section 6.2.3. A histogram of their 'peak-to-peak' duration, i.e. the separation between two extrema in B_θ, is shown in Figure 6.6. The upper limit for an event was selected to be 300 s, as we focus on studying on the small scale structures. The lower limit was specified to 10 s to get sufficient data points within the event interval. Most of the events identified by the algorithm have a duration less than 150 s, with a mean of 65.67 s and median value of 47 s. 16 events were identified with durations between 20 and 30 s.

In Figure 6.7, we show the relative scale of these events with the local ion inertial length. For this, we assume that the plasma density can be approximated using the empirical rela-

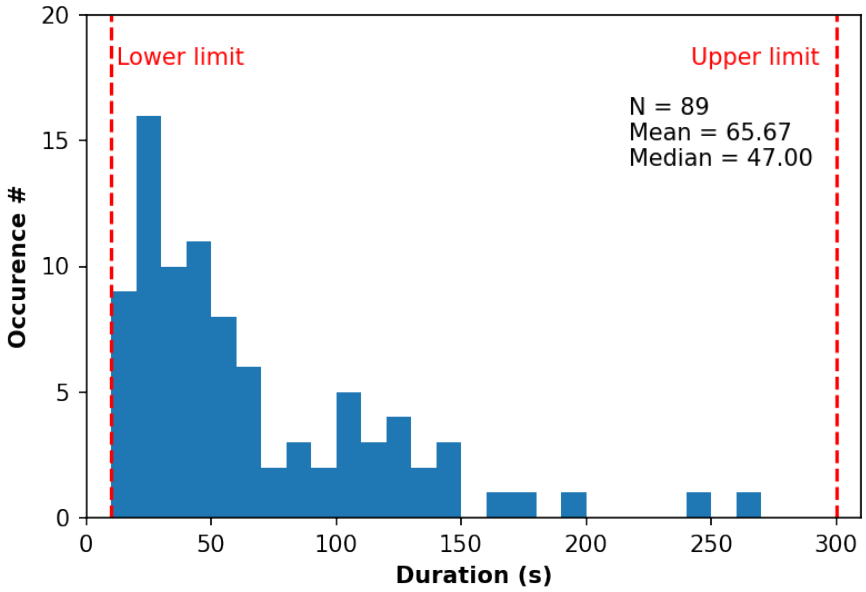

Figure 6.6: Histogram of the peak-to-peak durations of the plasmoid events identified using the automated algorithm.

tionship provided by Bagenal and Delamere (2011). The velocity of each event is assumed to be the Alfven speed during the interaction, for which we use the assumed plasma density based on the empirical profile and the average field strength observed by Juno +/- 5 minutes preceding, within and succeeding the plasmoid signature. This allows us to calculate the diameters of the identified plasmoids (panel c).

$$D = \Delta x + |v\Delta t| \tag{6.6}$$

Where D is the plasmoid diameter, Δx is the distance travelled by the spacecraft during interval Δt and v is the Alfven speed in the surroundings, which is also assumed to be the speed at which the plasmoid was travelling. Also plotted is the curve for the predicted ion-inertial length d_i (in black), based on the same density profile.

There is a considerable spread in the plasmoid diameters, ranging from 10^3 km to 5×10^4 km, but in most cases they are within an order of magnitude of the local ion inertial length. The mean and median diameters are 10342.77 and 7233.10 km, respectively, which are roughly 0.7-0.9 times the ion inertial length, which is between 7000 to 9000 km within

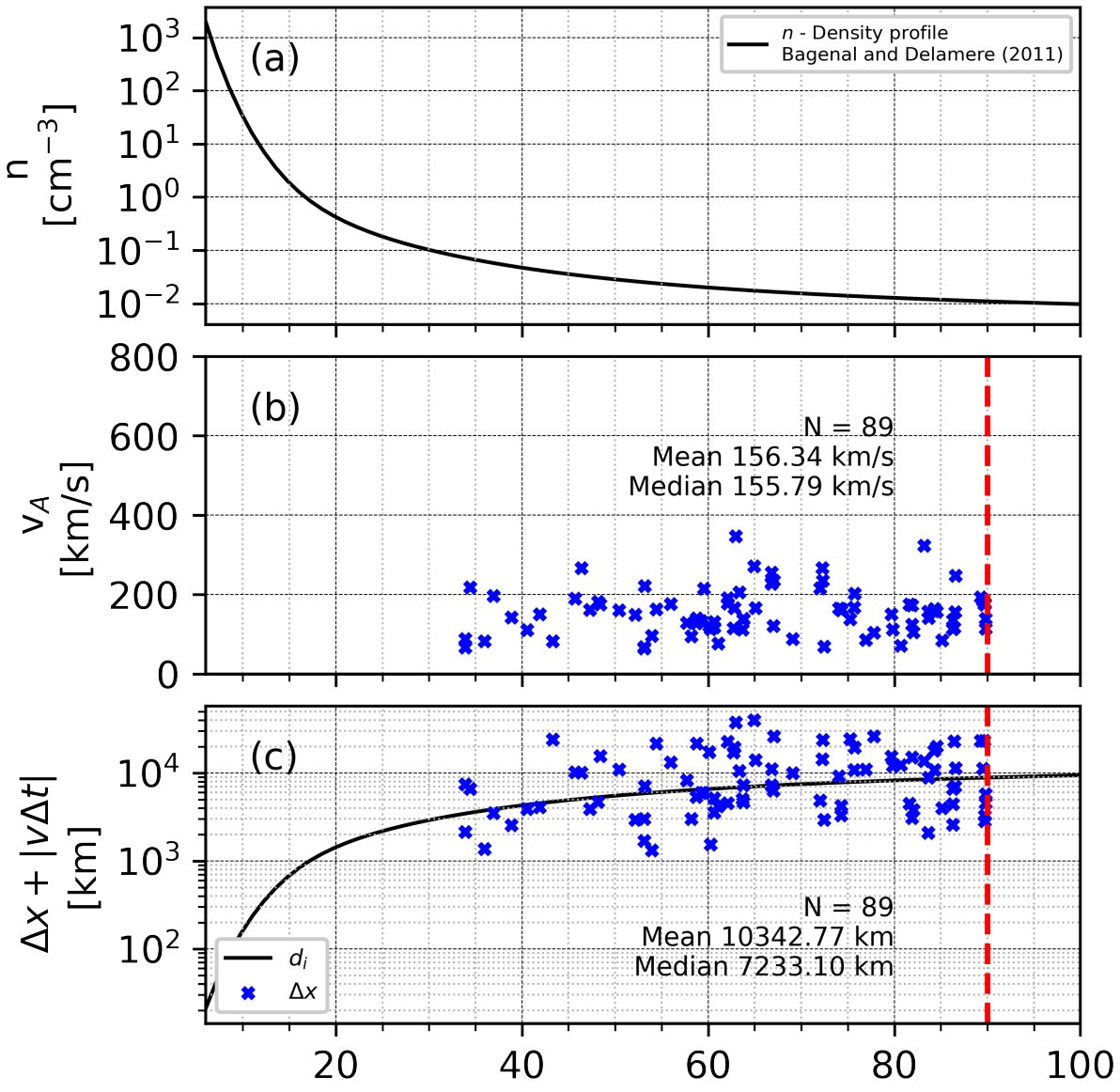

Figure 6.7: a) The empirical density profile by (Bagenal & Delamere, 2011). b) The Alfven speed during a period +/- 5 minutes preceeding and succeeding the plasmoid interval. c) Comparison of the calculated plasmoid diameters for each event with the expected ion inertial length at the corresponding radial location.

60 to 80 R_J. No event was detected beyond 90 R_J, as this is close to the specified outer limit in the algorithm to prevent the detection of B_θ reversals associated with fluctuations in the magnetosheath.

6.4.2 Location and core field direction

In Figure 6.8, we show the location of the events identified by the algorithm, superimposed on Juno's trajectory. The majority of events, except two outliers, were identified during the planetbound phase of Juno's trajectory, where z values are relatively low and the spacecraft is more likely to encounter the oscillating current sheet. Events with a positive-to-negative reversal in B_θ were assumed to correspond to plasmoids with a tail-ward or radial motion, whereas the opposite applies for planet-ward moving plasmoids. Inferring plasmoid travel directions based on their magnetic field signatures has some limitations, as observations in the terrestrial magnetosphere have shown through combined plasma and magnetic field measurements that the above assumptions are not always correct.

In this analysis we assumed that the magnetic field signatures for tail-ward and planet-ward moving flux ropes are consistent with the picture drawn in Figure 6.1. We found that the majority of events located at radial distances $r > 60R_J$ in the dawnside magnetotail (03-04 LT) had a preference for tailward motion, whereas events which were located closer to the planet at $\sim 40R_J$ near midnight were more likely to correspond to negative-to-positive reversals, indicating a preference for planet-ward motion in this region.

For further analysis, we separate events into two categories - flux ropes and O-lines. Those plasmoid events during which the median value of intermediate component in the minimum variance analysis is larger than the value during the starting and ending epochs of the interval (in absolute magnitude), are identified as flux rope events. We chose to select flux rope events based on the intermediate component and not the total field magnitude as we often found plasmoid intervals which show a strong core field signature which does not translate into a peak in magnetic field strength due to the near-zero values of the maximally varying component (B_N) near the center of the flux rope, which opposes the increase due to the core field.

In Figures 6.9 and 6.10, we show the eigenvectors obtained via the minimum variance

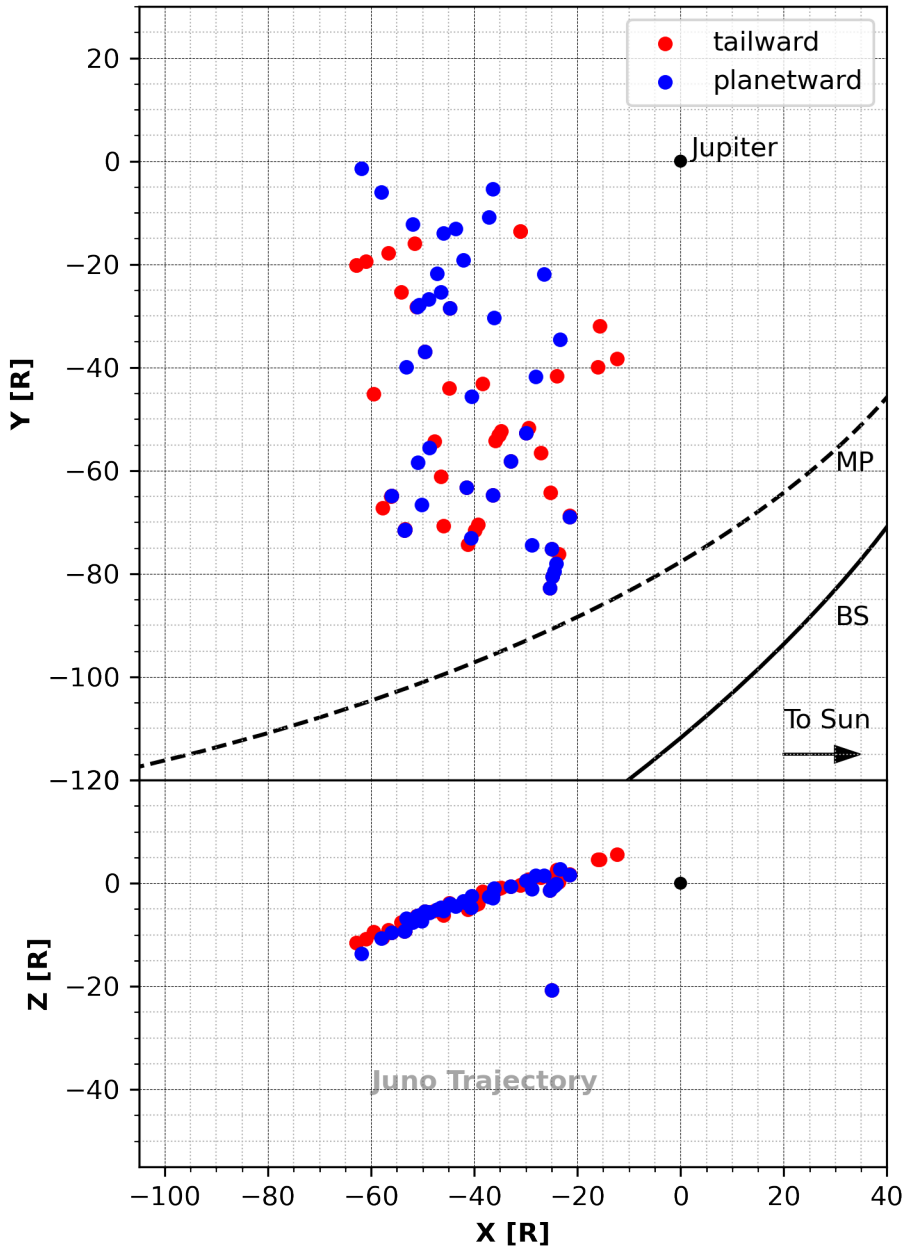

Figure 6.8: Location of all plasmoid events identified by the algorithm (with durations less than 300 s) superimposed on Juno's trajectory. Tail-ward moving events (colored in red) correspond to a reversal from positive to negative B_θ, whereas planet-ward events (colored in blue) correspond to a reversal from negative to positive values.

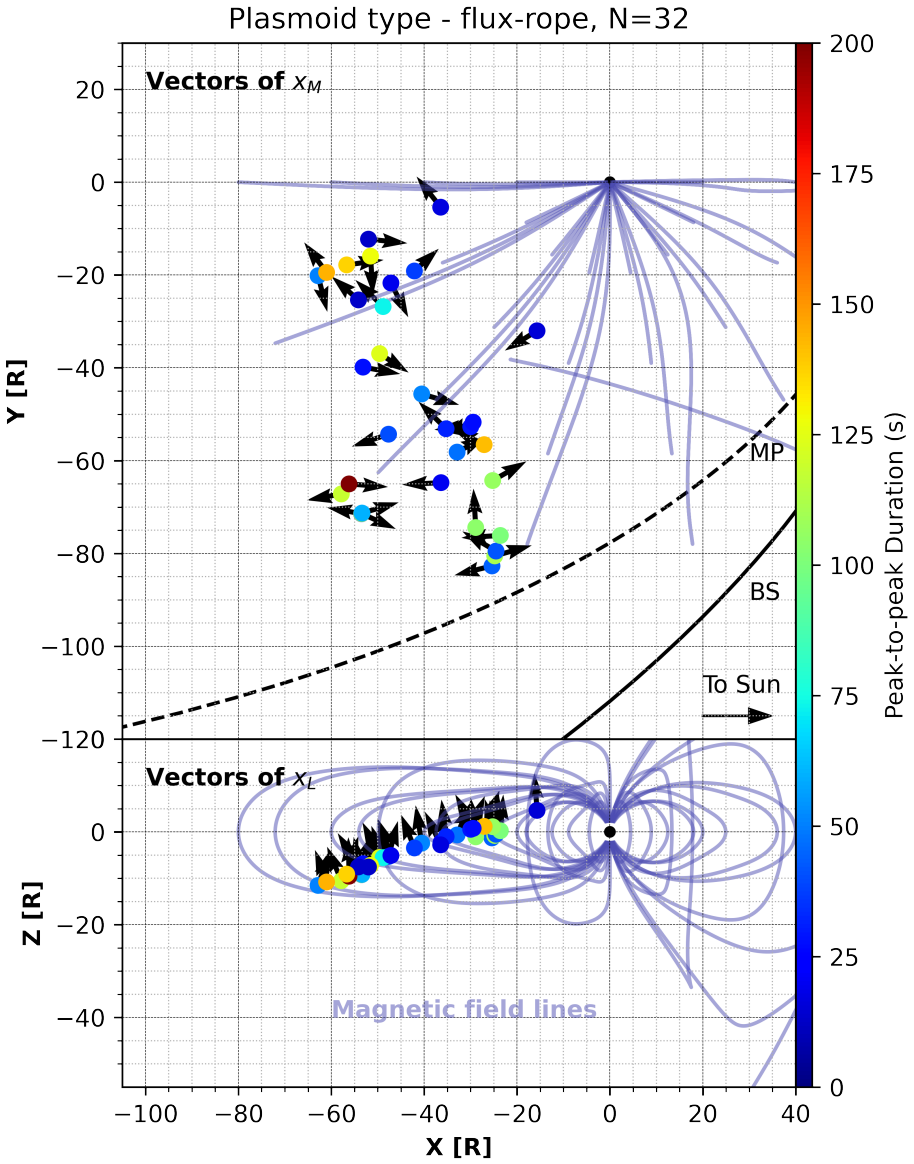

Figure 6.9: Location of flux-ropes identified by the algorithm colored by the peak-to-peak duration. Also plotted in the top and bottom panels are the eigenvectors corresponding to the directions of intermediate ($\mathbf{x}_M$) and maximum variance ($\mathbf{x}_L$) respectively. Also plotted are 3D magnetic field lines from the Sarkango et al., (2019) MHD model. Note that in this particular model the field lines are symmetric about the equatorial plane.

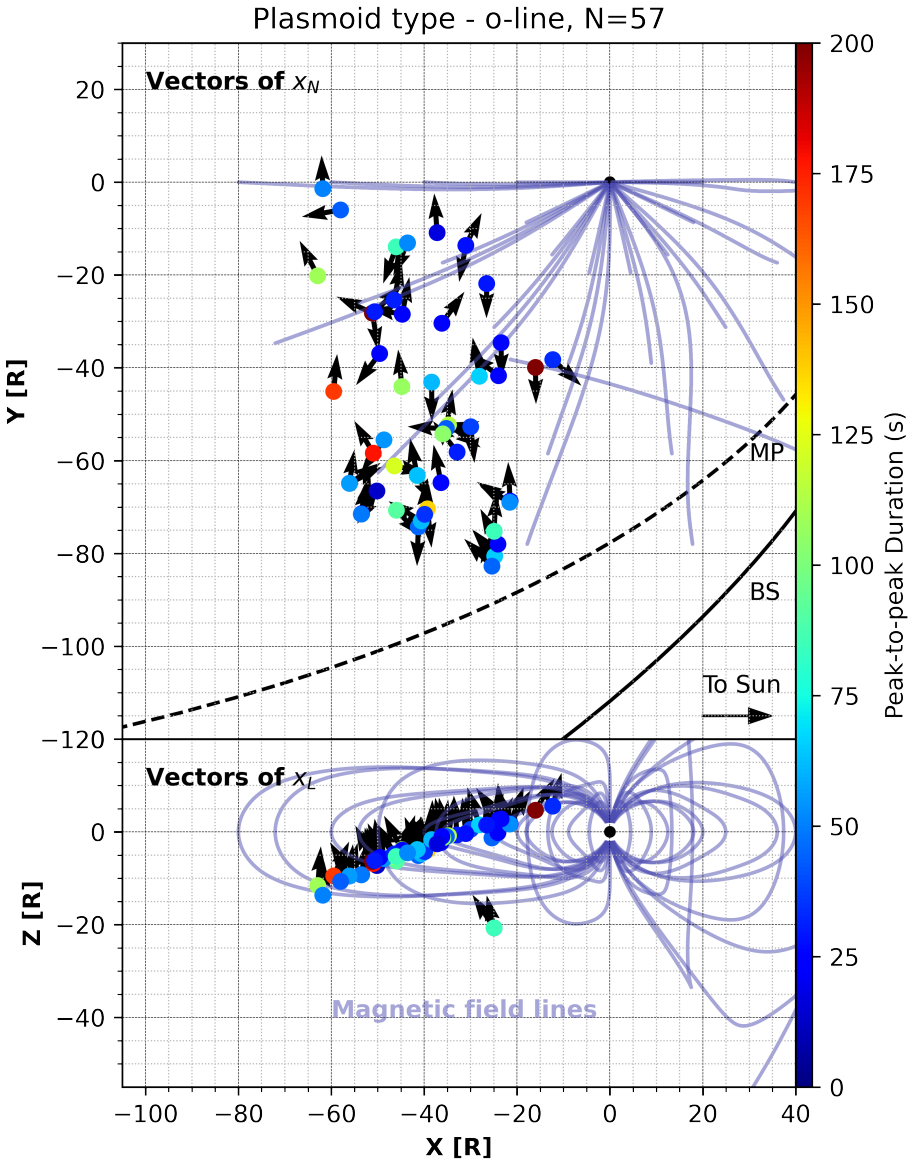

Figure 6.10: Location of o-lines identified by the algorithm colored by the peak-to-peak duration. Also plotted in the top and bottom panels are the eigenvectors corresponding to the directions of minimum ($\mathbf{x}_N$) and maximum ($\mathbf{x}_L$) variance respectively. Also plotted are magnetic field lines from the Sarkango et al., (2019) MHD model.

analysis corresponding to flux-ropes and O-lines. In the case of flux-ropes, we show the directions corresponding to the intermediate variance ($\mathbf{x}_M$), which indicates the direction of the core field. For O-lines, we show the eigenvector corresponding to the minimum variance ($\mathbf{x}_N$). Each data point is colored by the duration of the corresponding event.

Our algorithm identified 33 flux rope events, spanning all local time ranges from 00 (midnight) to 04 LT (dawnside), as shown in Figure 6.9. The core field for the majority of events is skewed in the XY plane. In Figure 6.11-a we show a histogram of the angular offset between the eigenvector of intermediate variance $\mathbf{x}_M$ and the local azimuthal direction. We find that for the majority of events, the angular offset $\Delta\Phi$ is within 45 ° (or larger than 135 °). The least number of events were seen with offsets of $\sim$ 90 °, indicating that most flux ropes have core fields in the azimuthal (or anti-azimuthal) direction.

Out of the 89 identified plasmoid events, 56 did not correspond to an increase in the component of the magnetic field along the intermediate variance direction, and are classified as magnetic o-lines. In the case of O-lines, the direction of the core field corresponds to the smallest eigenvector. Like the flux ropes, o-lines were also identified in a wide range from 04 to 00 LT and between $\sim$ 20 R_J and 60R_J in the magnetotail, as shown in Figure 6.10. The angular offset between the core field the local azimuthal direction is shown in Figure 6.11-b. The majority of o-lines favour large values of $\Delta\Phi$, peaking at $\sim$ 135°, indicating that the o-lines are highly skewed in the XY plane.

6.4.3 Discussion - Survey

As seen in Figure 6.6, most plasmoid events detected by our algorithm within the 10 to 300 s specified range, are small and have a duration less than 150 s. Small-scale flux ropes have been observed to be released more frequently in particle-in-cell simulations, and observations of flux ropes in the solar wind have found that the flux rope sizes obey a power-law like distribution, with the most frequent events being smaller in size. Although our sample size is not that large (N=89), our findings suggest that reconnection does occur in Jupiter's magnetosphere on the small scale and produces small plasmoids relatively frequently. Note that the nature of Juno's orbit implies that small-scale plasmoids, which typically occur in close proximity to the current sheet (which is itself oscillating, see e.g. Chapter 5), can only

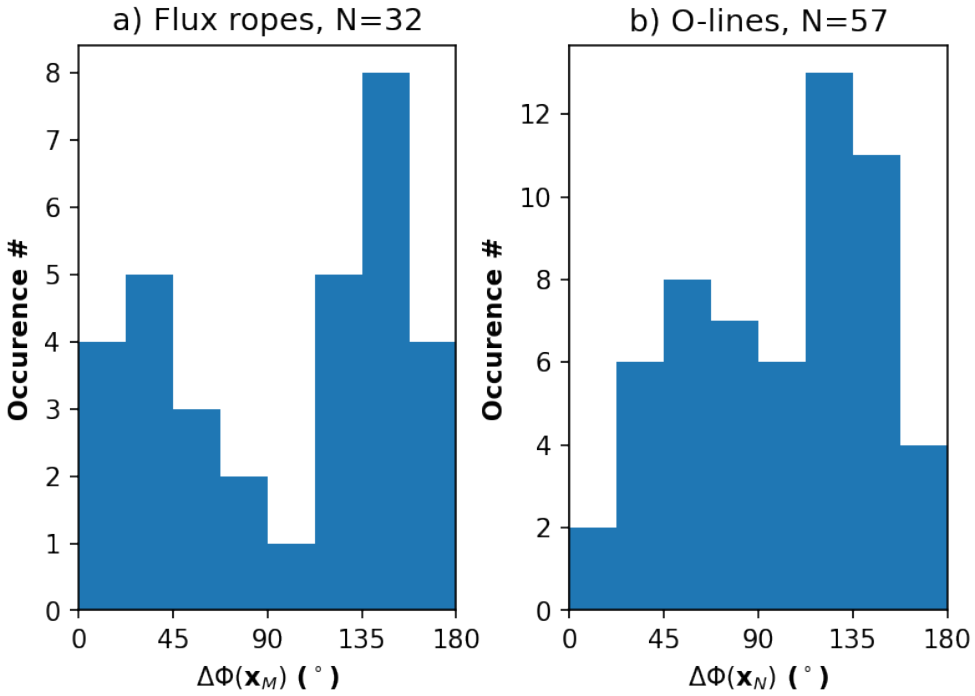

Figure 6.11: Histograms of the angular offset between the eigenvector of intermediate variance $\mathbf{x}_M$ for flux-ropes and eigenvector of minimum variance ($\mathbf{x}_L$) for o-lines, with the local azimuthal direction.

be observed during limited time intervals.

Most of these small-scale events with durations less than 150 s correspond to diameters which are on order of magnitude smaller or larger than the local ion inertial length (Figure 6.7), which is close to the expected dimensions of the oxygen ion-diffusion region. A factor of 2 increase in the Alfven speed (to e.g. 400 km/s) will not have a significant influence on these findings, due to the wide range of sizes, and the occurrence of many events which are smaller than the expected ion inertial length.

Using the minimum variance analysis, we estimated the directions of the core field separately for flux ropes (strong core field) and O-lines (weak core field). Our results suggest that most flux ropes have core fields which are skewed $\sim 45°$ with respect to the azimuthal direction, and are least likely to be in the radial direction, which is expected for a flux rope created due to magnetotail reconnection. However, the axes of the O-lines are found to have a strong preference for larger angles between 90° and 180°, and are least seen in the azimuthal direction.

6.5 Summary

Despite differences in magnetospheric dynamics, reconnection occurs in the Jovian magnetotail and releases plasmoids, much like at Earth and Mercury. However, unlike at the terrestrial planets, where plasmoids (or o-lines) and flux ropes are observed in various sizes, with some at or below the ion inertial length, Jovian plasmoids and flux ropes identified in previous studies were observed to be fairly large, with diameters of several R_J (or an order of magnitude larger than the local ion inertial length) or an in situ magnetic signature that is seen to last 6 min on average (Vogt et al., 2014). Potential ion-scale structures, however, could not have been detected by the Galileo magnetometer, owing to its low temporal resolution of several seconds per vector.

In this study, we report on observations made by the Juno spacecraft of magnetic flux ropes and plasmoids in the Jovian magnetotail, whose diameters were comparable to the local ion inertial length. We show two examples of flux ropes with these small diameters and analyze them using the minimum variance analysis and force-free flux rope modeling. Also

seen preceding one of the events are multiple reversals in the north-south component of the magnetic field, which could be a result of sequential plasmoid release from multiple X-line reconnection.

We developed an algorithm to detect plasmoids in the Jovian magnetotail based on the bipolar variation in B_θ and use it to construct a survey of all plasmoids whose magnetic signatures lasted less than 300 s in the Juno magnetometer data. Our algorithm detected 89 plasmoid events, 33 of which were found to have a core field and were termed flux ropes, whereas 56 events where found to have weak cores and were considered O-lines.

Out of the 89 identified events, most events which were identified by the algorithm had a duration of less than 150 s. The relatively frequent observations of small scale events compared to the larger events ($>$ 150 s) demonstrate that magnetic reconnection occurs in the Jovian magnetotail through the formation of multiple X-lines, which create plasmoids on the ion-inertial scale. This result is supported at Jupiter due to the presence of heavy ions, which increase the relevant length scales.

While the large-scale dynamics of the Jovian magnetosphere may be determined by the relatively large plasmoids reported by earlier investigations, the observations reported in this chapter show that ion-scale flux ropes also exist in the Jovian magnetotail, much like at Earth and Mercury. How these flux ropes influence the mass and energy budget of the magnetosphere remains an open question, for which additional surveys and plasma data are needed to more accurately quantify their distribution, size, mass, and frequency of occurrence. Moreover, the dusk-side magnetotail has not been explored in detail, either by Galileo or Juno. An understanding of reconnection, or lack thereof, in this region is crucial to understanding how Iogenic plasma ultimately escapes the Jovian magnetosphere.

Chapter 7

Summary

In this dissertation, we have used a combination of numerical modeling and data analysis to study the dynamics of the Jovian magnetosphere. The following sections summarize our findings.

7.1 Summary

We used a global magnetohydrodynamics model to simulate the Jovian magnetosphere and its interaction with the upstream solar wind as well as with the Jovian ionosphere.

In Chapter 3, we studied the response of solar wind dynamic pressure enhancements on corotation and corotation-enforcement currents in the ionosphere, which has been suggested to link closely to Jupiter's main aurora. Through systematic numerical experiments, we found that an increase in solar wind dynamic pressure actually decreases the strength of field-aligned currents on the dayside, with minor enhancement on the nightside. By analyzing the magnetospheric response, we proposed that this reduction can be explained by the increase in corotation speed of the magnetospheric plasma near the sub-solar magnetopause. The increase in plasma azimuthal velocity had been proposed by earlier theoretical models to be a consequence of angular-momentum conservation due to the solar wind driven compression of the corotating plasma. Another possible explanation for the increase in azimuthal velocity is due to returning flows from the tail reconnection site, which merge with and accelerate the magnetospheric plasma on the dawnside. Our results support existing theory, but the

MHD model cannot account for high-frequency and kinetic processes such as wave-particle interactions, which recent observations have shown may play an important role.

In Chapter 4, we investigated the role of magnetic reconnection in the Jovian magnetosphere. Unlike the terrestrial magnetosphere, the Jovian magnetosphere was assumed to be insensitive to changes in the solar wind and interplanetary magnetic field. It was believed that magnetic reconnection on the dayside magnetopause, even if it did occur, would not form persistent open field lines, which map to the polar regions of the planet. At the same time, in situ observations have shown that reconnection does occur in the Jovian magnetotail. Moreover, the polar UV aurorae of Jupiter have been observed to be highly dynamic, varying on much shorter time-scales than the main auroral oval.

Using our MHD model, we found that reconnection does occur on the dayside magnetopause at Jupiter, and thus creates open field lines in the polar cap. By tracing magnetic field lines in the magnetosphere, we studied the topology of plasmoids, which are products of magnetotail reconnection. We discovered that plasmoids were created due to internal processes initially within closed field lines. As time progressed, the plasmoids grew in size and escaped the magnetosphere via the magnetotail. By mapping the plasmoids to the ionosphere, we found that plasmoid release creates a region of closed flux inside the previously open polar cap, which gradually refills with open flux as the plasmoid travels to the distant magnetotail. Our results support the hypothesis that the dynamic polar aurora of Jupiter can be related to distant processes in the magnetotail, while at the same time, remaining open to the solar wind.

In Chapter 5, we investigated the role of solar wind dynamic pressure on the morphology of the Jovian current sheet. The magnetotail current sheet at Jupiter oscillates at the planetary rotation period due to the tilt between the magnetic dipole and the rotation axis. It was presumed and supported by empirical models that these magnetotail oscillations were inhibited at distances far from the planet due to the presence of the magnetotail; ultimately a result of the solar wind's interaction with the internal field. By incorporating a more realistic internal field model into our MHD model that includes the 10° dipole tilt, we studied the behaviour of the current sheet under different solar wind dynamic pressures.

We found that increasing solar wind dynamic pressure, rather than inhibiting the oscil-

lations of the current sheet, actually increase its *wavy*-ness by reducing the wavelength of these oscillations. The wavelength is intricately connected to the speed at which these current sheet waves propagate from the planet. Previous models had assumed that an increase in solar wind dynamic pressure would increase the magnetic pressure in the magnetotail lobes, which would inhibit the current sheet oscillations. However, by analyzing our simulations, we showed that an increase in solar wind dynamic also increases plasma density and temperature in the magnetotail. Collectively, these parameters serve to reduce the Alfven and magnetosonic speeds in the magnetotail lobes, contrary to intuition.

In Chapter 6, we study in situ magnetic field and energetic plasma data from the Juno spacecraft to form a holistic picture of reconnection in the Jovian magnetotail. Previous observations and MHD simulations had predicted that plasmoids created via tail reconnection at Jupiter were large and infrequent (with timescales of several days). By using the high-resolution magnetometer data from the Juno spacecraft, we identified several candidates for plasmoids whose in situ signatures last for ~ 1 minute. By using the local Alfven speed and density, we estimated that these durations correspond to plasmoid diameters comparable to the ion inertial length, assuming the dominance of heavy ions such as oxygen and sulfur. The presence of ion inertial scale plasmoids in the Jovian magnetotail suggests that magnetic reconnection proceeds there via current sheet instabilities, similar to observations at Earth and Mercury, despite differences in the initial mechanisms which can cause the current sheet to thin.

7.2 Relevance and Future Work

Our work advances the state of knowledge in Jovian magnetospheric physics and creates new questions that can be future directions for study.

1. The physical mechanism which leads to the brightening of the Jovian aurora roughly 1 rotation period after the solar wind compression remains a mystery. The discrepancy between numerical models and observations of the Jovian main aurora cannot be answered conclusively without a solar wind monitor and multi-spacecraft or high-fidelity propagation of the solar wind from 1 AU to Jupiter's orbit.

2. Recent work has criticized the corotation enforcement current system theory (Bonfond et al., 2020) regarding the formation of the Jovian aurora, yet most MHD models create this current system self-consistently. The physical origin of Jupiter's UV aurora remains a mystery and needs to be investigated on a more fundamental level. Is the aurora produced due to discrete acceleration and precipitation of electrons, or are wave-particle interactions more important?

3. The observations of small-scale reconnection can have large implications on mass loss due to plasmoid release. How frequently does magnetic reconnection occur and what is the contribution of small plasmoids? How does reconnection occur on the dusk-side of the magnetotail?

4. Does Jupiter's magnetosphere contain open flux, and what does that imply about the role of the Dungey cycle in its magnetosphere?

5. Why is the degree of magnetotail hinging insensitive to solar wind dynamic pressure, as seen in the MHD simulations?

Our results illustrate the complexity of the magnetospheric dynamics at Jupiter, which has been the subject of numerous theoretical studies and is subject to speculation due to the sparse in situ measurements. In the absence of sufficient empirical data and global coverage, the task of validation and understanding of various magnetospheric theories falls to numerical models, which can be used to perform numerical experiments, as we have demonstrated. While agreement with the in situ data is encouraging, times when the numerical model disagrees with the in situ observations or the latest theories are also illuminating and should be studied with equal interest. Global MHD models are complicated tools with many free parameters, and numerical experiments like the ones we show are crucial to understand why certain features are seen in the model versus the in situ data and vice versa.

For example, in Chapter 3, we show that sub-corotation of magnetospheric plasma self-consistently creates a circumpolar ring of field-aligned currents, which has also been shown in other MHD models. Despite this, observations of the Jovian aurora has found that in reality, field-aligned currents are weak and filamentary (Kotsiaros et al., 2019). Our results

raise a crucial question - If field-aligned currents are produced self-consistently in the models, and the Jovian aurora is linked to field-aligned currents, why does the aurora brighten in response to solar wind compression when the model results demonstrate otherwise?

Our results also support the observations made by past spacecraft such as Voyager, Pioneer, Galieo, and also data from the existing orbiter, Juno, as shown in Chapters 5 and 6. The Jovian magnetosphere will be visited in the future by multiple spacecraft, namely the Europa Clipper to Europa and the JUICE mission to study Ganymede. The results in this thesis directly contribute to our knowledge of the Jovian environment, which can be relevant to these missions as well.

The results highlighted in Chapter 6 also support recent observations in the solar wind and terrestrial magnetosphere and advance our understanding of magnetic reconnection, a fundamental physical process in all magnetized plasma. The observations of small-scale flux ropes in the Jovian magnetotail leads to a natural question - Does reconnection in all regions of the space environment proceed via current sheet instabilities? Additional observations and advanced numerical simulations are needed to determine the answer.

Lastly, the Jovian magnetosphere is an excellent laboratory for the study of plasma in an environment that is different and complementary to that of the Earth. An improved understanding of the Jovian magnetosphere, which is an extreme magnetospheric environment that can be visited by in-situ spacecraft, is crucial to better understand not only the terrestrial magnetosphere, but also other regions in the space environment such as the solar corona, and also the magnetospheres of pulsars and exoplanets, where rotation plays an important role.

References

Akhavan-Tafti, M., Palmroth, M., Slavin, J. A., Battarbee, M., Ganse, U., Grandin, M., ... Stawarz, J. E. (2020, 7). Comparative Analysis of the Vlasiator Simulations and MMS Observations of Multiple X-Line Reconnection and Flux Transfer Events. *Journal of Geophysical Research: Space Physics*, *125*(7), e2019JA027410. Retrieved from `https://onlinelibrary.wiley.com/doi/10.1029/2019JA027410` doi: 10.1029/2019JA027410

Ashour-Abdalla, M., & Dutton, D. A. (1985). Space Plasma Simulations. In *Space plasma simulations.* Springer Netherlands. doi: 10.1007/978-94-009-5454-0

Bagenal, F. (2007). The magnetosphere of Jupiter: Coupling the equator to the poles. *Journal of Atmospheric and Solar-Terrestrial Physics*. doi: 10.1016/j.jastp.2006.08.012

Bagenal, F. (2013, 1). Planetary magnetospheres. In *Planets, stars and stellar systems: Volume 3: Solar and stellar planetary systems* (pp. 251–307). Springer Netherlands. Retrieved from `https://link.springer.com/referenceworkentry/10.1007/978-94-007-5606-9_6` doi: 10.1007/978-94-007-5606-9{_}6

Bagenal, F., & Delamere, P. A. (2011). Flow of mass and energy in the magnetospheres of Jupiter and Saturn. *Journal of Geophysical Research: Space Physics*. doi: 10.1029/2010JA016294

Barnhart, B. L., Kurth, W. S., Groene, J. B., Faden, J. B., Santolik, O., & Gurnett, D. A. (2009). Electron densities in Jupiter's outer magnetosphere determined from Voyager 1 and 2 plasma wave spectra. *Journal of Geophysical Research: Space Physics*. doi: 10.1029/2009JA014069

Behannon, K. W., Burlaga, L. F., & Ness, N. F. (1981, 9). The Jovian magnetotail and its current sheet. *Journal of Geophysical Research: Space Physics*, *86*(A10), 8385–8401. Retrieved from `http://doi.wiley.com/10.1029/JA086iA10p08385` doi: 10.1029/JA086iA10p08385

Birn, J., Drake, J. F., Shay, M. A., Rogers, B. N., Denton, R. E., Hesse, M., ... Pritchett, P. L. (2001, 3). Geospace Environmental Modeling (GEM) Magnetic Reconnection Challenge. *Journal of Geophysical Research: Space Physics*, *106*(A3), 3715–3719. Retrieved from `http://doi.wiley.com/10.1029/1999JA900449` doi: 10.1029/1999JA900449

Blanc, M., Andrews, D. J., Coates, A. J., Hamilton, D. C., Jackman, C. M., Jia, X., ... Westlake, J. H. (2015). *Saturn Plasma Sources and Associated Transport Processes.* doi: 10.1007/s11214-015-0172-9

Bolton, S. J., Bagenal, F., Blanc, M., Cassidy, T., Chané, E., Jackman, C., ... Waite, H. (2015). *Jupiter's Magnetosphere: Plasma Sources and Transport.* doi: 10.1007/s11214-015-0184-5

Bonfond, B., Gladstone, G. R., Grodent, D., Greathouse, T. K., Versteeg, M. H., Hue, V., ... Kurth, W. S. (2017). Morphology of the UV aurorae Jupiter during Juno's first perijove observations. *Geophysical Research Letters*. doi: 10.1002/2017GL073114

Bonfond, B., Yao, Z., & Grodent, D. (2020, 11). Six Pieces of Evidence Against the Corotation Enforcement Theory to Explain the Main Aurora at Jupiter. *Journal of Geophysical Research: Space Physics*, *125*(11), e2020JA028152. Retrieved from https://onlinelibrary.wiley.com/doi/10.1029/2020JA028152 doi: 10.1029/2020JA028152

Borovsky, J. E., & Denton, M. H. (2006, 7). Differences between CME-driven storms and CIR-driven storms. *Journal of Geophysical Research*, *111*(A7), A07S08. Retrieved from http://doi.wiley.com/10.1029/2005JA011447 doi: 10.1029/2005JA011447

Boudouridis, A. (2005, 5). Enhanced solar wind geoeffectiveness after a sudden increase in dynamic pressure during southward IMF orientation. *Journal of Geophysical Research*, *110*(A5), A05214. Retrieved from http://doi.wiley.com/10.1029/2004JA010704 doi: 10.1029/2004JA010704

Bruno, R., & Carbone, V. (2013, 5). The solar wind as a turbulence laboratory. *Living Reviews in Solar Physics*, *10*(1), 1–208. Retrieved from http://www.livingreviews.org/http://www.iaps.inaf.ithttp://fis.unical.ithttp://creativecommons.org/licenses/by-nc/3.0/de/ doi: 10.12942/lrsp-2013-2

Burch, J. L., Moore, T. E., Torbert, R. B., & Giles, B. L. (2016, 3). *Magnetospheric Multiscale Overview and Science Objectives* (Vol. 199) (No. 1-4). Springer Netherlands. Retrieved from https://link.springer.com/article/10.1007/s11214-015-0164-9 doi: 10.1007/s11214-015-0164-9

Cairns, I. H., & Lyon, J. G. (1996, 10). Magnetic field orientation effects on the standoff distance of Earth's bow shock. *Geophysical Research Letters*, *23*(21), 2883–2886. Retrieved from http://doi.wiley.com/10.1029/96GL02755 doi: 10.1029/96GL02755

Carr, T. D., & Gulkis, S. (1969). The Magnetosphere of Jupiter. *Annual Review of Astronomy and Astrophysics*, *7*(1), 577–618.

Chané, E., Palmaerts, B., & Radioti, A. (2018). Periodic shearing motions in the Jovian magnetosphere causing a localized peak in the main auroral emission close to noon. *Planetary and Space Science*. doi: 10.1016/j.pss.2018.04.023

Chané, E., Saur, J., Keppens, R., & Poedts, S. (2017). How is the Jovian main auroral emission affected by the solar wind? *Journal of Geophysical Research: Space Physics*. doi: 10.1002/2016JA023318

Chané, E., Saur, J., & Poedts, S. (2013). Modeling Jupiter's magnetosphere: Influence of the internal sources. *Journal of Geophysical Research: Space Physics*. doi: 10.1002/jgra.50258

Chen, F. F. (1995). *Introduction to Plasma Physics.* Boston, MA: Springer US. Retrieved from http://link.springer.com/10.1007/978-1-4757-0459-4 doi: 10.1007/978-1-4757-0459-4

Clarke, J. T., Nichols, J., Gérard, J. C., Grodent, D., Hansen, K. C., Kurth, W., ... Cecconi,

B. (2009). *Response of Jupiter's and Saturn's auroral activity to the solar wind.* doi: 10.1029/2008JA013694

Connerney, J. E., Acuña, M. H., Ness, N. F., & Satoh, T. (1998, 6). New models of Jupiter's magnetic field constrained by the Io flux tube footprint. *Journal of Geophysical Research: Space Physics*, *103*(A6), 11929–11939. Retrieved from http://doi.wiley.com/10.1029/97JA03726 doi: 10.1029/97ja03726

Connerney, J. E., Benn, M., Bjarno, J. B., Denver, T., Espley, J., Jorgensen, J. L., ... Smith, E. J. (2017). *The Juno Magnetic Field Investigation.* doi: 10.1007/s11214-017-0334-z

Connerney, J. E., Kotsiaros, S., Oliversen, R. J., Espley, J. R., Joergensen, J. L., Joergensen, P. S., ... Levin, S. M. (2018). A New Model of Jupiter's Magnetic Field From Juno's First Nine Orbits. *Geophysical Research Letters*. doi: 10.1002/2018GL077312

Connerney, J. E. P., Acuña, M. H., & Ness, N. F. (1981, 9). Modeling the Jovian current sheet and inner magnetosphere. *Journal of Geophysical Research: Space Physics*, *86*(A10), 8370–8384. Retrieved from http://doi.wiley.com/10.1029/JA086iA10p08370 doi: 10.1029/JA086iA10p08370

Cowley, S. W., Badman, S. V., Imber, S. M., & Milan, S. E. (2008). *Comment on "Jupiter: A fundamentally different magnetospheric interaction with the solar wind" by D. J. McComas and F. Bagenal* (Vol. 35) (No. 10). doi: 10.1029/2007GL032645

Cowley, S. W., & Bunce, E. J. (2001). Origin of the main auroral oval in Jupiter's coupled magnetosphere-ionosphere system. *Planetary and Space Science*, *49*(10-11), 1067–1088. doi: 10.1016/S0032-0633(00)00167-7

Cowley, S. W., & Bunce, E. J. (2003). Modulation of Jupiter's main auroral oval emissions by solar wind induced expansions and compressions of the magnetosphere. *Planetary and Space Science*. doi: 10.1016/S0032-0633(02)00118-6

Cowley, S. W., Bunce, E. J., Stallard, T. S., & Miller, S. (2003). Jupiter's polar ionospheric flows: Theoretical interpretation. *Geophysical Research Letters*, *30*(5). doi: 10.1029/2002gl016030

Cowley, S. W., Nichols, J. D., & Andrews, D. J. (2007). Modulation of Jupiter's plasma flow, polar currents, and auroral precipitation by solar wind-induced compressions and expansions of the magnetosphere: A simple theoretical model. *Annales Geophysicae*. doi: 10.5194/angeo-25-1433-2007

Cowley, S. W. H., Nichols, J. D., & Jackman, C. M. (2015). Down-tail mass loss by plasmoids in Jupiter's and Saturn's magnetospheres. *Journal of Geophysical Research A: Space Physics*, *120*(8), 6347–6356. doi: 10.1002/2015JA021500

Crooker, N. U., Luhmann, J. G., Russell, C. T., Smith, E. J., Spreiter, J. R., & Stahara, S. S. (1985). Magnetic field draping against the dayside magnetopause. *Journal of Geophysical Research*. doi: 10.1029/ja090ia04p03505

Daldorff, L. K., Tóth, G., Gombosi, T. I., Lapenta, G., Amaya, J., Markidis, S., & Brackbill, J. U. (2014, 7). Two-way coupling of a global Hall magnetohydrodynamics model with a local implicit particle-in-cell model. *Journal of Computational Physics*, *268*, 236–254. doi: 10.1016/j.jcp.2014.03.009

Daughton, W., Roytershteyn, V., Karimabadi, H., Yin, L., Albright, B. J., Bergen, B., & Bowers, K. J. (2011). Role of electron physics in the development of turbulent magnetic reconnection in collisionless plasmas. *Nature Physics*. doi: 10.1038/nphys1965

Denton, M. H., Borovsky, J. E., Skoug, R. M., Thomsen, M. F., Lavraud, B., Henderson,

M. G., ... Liemohn, M. W. (2006, 7). Geomagnetic storms driven by ICME- and CIR-dominated solar wind. *Journal of Geophysical Research*, *111*(A7), A07S07. Retrieved from http://doi.wiley.com/10.1029/2005JA011436 doi: 10.1029/2005JA011436

De Zeeuw, D. L., Sazykin, S., Wolf, R. A., Gombosi, T. I., Ridley, A. J., & Tóth, G. (2004, 12). Coupling of a global MHD code and an inner magnetospheric model: Initial results. *Journal of Geophysical Research: Space Physics*, *109*(A12), A12219. Retrieved from http://doi.wiley.com/10.1029/2003JA010366 doi: 10.1029/2003JA010366

DiBraccio, G. A., & Gershman, D. J. (2019). Voyager 2 constraints on plasmoid-based transport at Uranus. *Geophysical Research Letters*. doi: 10.1029/2019GL083909

DiBraccio, G. A., Slavin, J. A., Imber, S. M., Gershman, D. J., Raines, J. M., Jackman, C. M., ... Solomon, S. C. (2015). MESSENGER observations of flux ropes in Mercury's magnetotail. *Planetary and Space Science*. doi: 10.1016/j.pss.2014.12.016

Dougherty, L. P., Bodisch, K. M., & Bagenal, F. (2017). Survey of Voyager plasma science ions at Jupiter: 2. Heavy ions. *Journal of Geophysical Research: Space Physics*. doi: 10.1002/2017JA024053

Drake, J. F., Swisdak, M., Che, H., & Shay, M. A. (2006). Electron acceleration from contracting magnetic islands during reconnection. *Nature*. doi: 10.1038/nature05116

Drake, J. F., Swisdak, M., Schoeffler, K. M., Rogers, B. N., & Kobayashi, S. (2006). Formation of secondary islands during magnetic reconnection. *Geophysical Research Letters*. doi: 10.1029/2006GL025957

Dungey, J. W. (1961). Interplanetary magnetic field and the auroral zones. *Physical Review Letters*. doi: 10.1103/PhysRevLett.6.47

Eastwood, J. P., Phan, T. D., Cassak, P. A., Gershman, D. J., Haggerty, C., Malakit, K., ... Wang, S. (2016). Ion-scale secondary flux ropes generated by magnetopause reconnection as resolved by MMS. *Geophysical Research Letters*. doi: 10.1002/2016GL068747

Eastwood, J. P., Phan, T. D., Mozer, F. S., Shay, M. A., Fujimoto, M., Retinò, A., ... Dandouras, I. (2007). Multi-point observations of the Hall electromagnetic field and secondary island formation during magnetic reconnecti on. *Journal of Geophysical Research: Space Physics*. doi: 10.1029/2006JA012158

Eastwood, J. P., Sibeck, D. G., Slavin, J. A., Goldstein, M. L., Lavraud, B., Sitnov, M., ... Dandouras, I. (2005, 6). Observations of multiple X-line structure in the Earth's magnetotail current sheet: A Cluster case study. *Geophysical Research Letters*, *32*(11). Retrieved from http://doi.wiley.com/10.1029/2005GL022509 doi: 10.1029/2005GL022509

Elliott, S. S., Gurnett, D. A., Kurth, W. S., Mauk, B. H., Ebert, R. W., Clark, G., ... Bolton, S. J. (2018, 9). The Acceleration of Electrons to High Energies Over the Jovian Polar Cap via Whistler Mode Wave-Particle Interactions. *Journal of Geophysical Research: Space Physics*, *123*(9), 7523–7533. Retrieved from http://doi.wiley.com/10.1029/2018JA025797 doi: 10.1029/2018JA025797

Elphinstone, R. D., Murphree, J. S., & Cogger, L. L. (1996, 5). What is a global auroral substorm? *Reviews of Geophysics*, *34*(2), 169–232. Retrieved from http://doi.wiley.com/10.1029/96RG00483 doi: 10.1029/96RG00483

Erkaev, N. V., Farrugia, C. J., & Biernat, H. K. (1996). Effects on the Jovian magnetosheath arising from solar wind flow around nonaxisymmetric bodies. *Journal of Geophysical Research: Space Physics*. doi: 10.1029/95ja03518

Eviatar, A., & Ershkovich, A. I. (1976, 8). Plasma density in the outer Jovian magnetosphere. *Journal of Geophysical Research*, *81*(22), 4027–4028. Retrieved from https://ui.adsabs.harvard.edu/abs/1976JGR....81.4027E/abstracthttp://doi.wiley.com/10.1029/JA081i022p04027

Farrugia, C. J., Biernat, H. K., & Erkaev, N. V. (1998). The effect of the magnetopause shapes of Jupiter and Saturn on magnetosheath parameters. *Planetary and Space Science*. doi: 10.1016/s0032-0633(97)00225-0

Fok, M.-C., Moore, T. E., & Delcourt, D. C. (1999, 7). Modeling of inner plasma sheet and ring current during substorms. *Journal of Geophysical Research: Space Physics*, *104*(A7), 14557–14569. Retrieved from http://doi.wiley.com/10.1029/1999JA900014 doi: 10.1029/1999JA900014

Frank, L. A., Paterson, W. R., & Khurana, K. K. (2002). Observations of thermal plasmas in Jupiter's magnetotail. *Journal of Geophysical Research: Space Physics*. doi: 10.1029/2001JA000077

Fukazawa, K., Ogino, T., & Walker, R. J. (2005). Dynamics of the Jovian magnetosphere for northward interplanetary magnetic field (IMF). *Geophysical Research Letters*. doi: 10.1029/2004GL021392

Fukazawa, K., Ogino, T., & Walker, R. J. (2006). Configuration and dynamics of the Jovian magnetosphere. *Journal of Geophysical Research: Space Physics*. doi: 10.1029/2006JA011874

Fukazawa, K., Ogino, T., & Walker, R. J. (2010). A simulation study of dynamics in the distant Jovian magnetotail. *Journal of Geophysical Research: Space Physics*. doi: 10.1029/2009JA015228

Gérard, J., Gkouvelis, L., Bonfond, B., Grodent, D., Gladstone, G., Hue, V., ... Giles, R. (2021, 3). Variability and hemispheric symmetry of the Pedersen conductance in the Jovian aurora. *Journal of Geophysical Research: Space Physics*, e2020JA028949. Retrieved from https://onlinelibrary.wiley.com/doi/10.1029/2020JA028949 doi: 10.1029/2020JA028949

Glocer, A., Tóth, G., Ma, Y., Gombosi, T., Zhang, J.-C., & Kistler, L. M. (2009, 12). Multifluid Block-Adaptive-Tree Solar wind Roe-type Upwind Scheme: Magnetospheric composition and dynamics during geomagnetic storms-Initial results. *Journal of Geophysical Research: Space Physics*, *114*(A12), n/a-n/a. Retrieved from http://doi.wiley.com/10.1029/2009JA014418 doi: 10.1029/2009JA014418

Goertz, C. K. (1976, 7). The current sheet in Jupiter's magnetosphere. *Journal of Geophysical Research*, *81*(19), 3368–3372. Retrieved from http://doi.wiley.com/10.1029/JA081i019p03368 doi: 10.1029/JA081i019p03368

Gombosi, T. I. (1998). *Physics of the Space Environment*. Cambridge University Press. Retrieved from https://www-cambridge-org.proxy.lib.umich.edu/core/books/physics-of-the-space-environment/CB472874EC2AB2A0937FB556355948C3 doi: 10.1017/cbo9780511529474

Gombosi, T. I., De Zeeuw, D. L., Häberli, R. M., & Powell, K. G. (1996). Three-dimensional multiscale MHD model of cometary plasma environments. *Journal of Geophysical Research: Space Physics*. doi: 10.1029/96ja01075

Gombosi, T. I., Tóth, G., De Zeeuw, D. L., Hansen, K. C., Kabin, K., & Powell, K. G. (2002, 3). Semirelativistic magnetohydrodynamics and physics-based convergence

acceleration. *Journal of Computational Physics*, *177*(1), 176–205. Retrieved from https://www.sciencedirect.com/science/article/pii/S0021999102970099 doi: 10.1006/jcph.2002.7009

Gonzalez, W. D., Joselyn, J. A., Kamide, Y., Kroehl, H. W., Rostoker, G., Tsurutani, B. T., & Vasyliunas, V. M. (1994, 4). What is a geomagnetic storm? *Journal of Geophysical Research*, *99*(A4), 5771. Retrieved from http://doi.wiley.com/10.1029/93JA02867 doi: 10.1029/93JA02867

Gonzalez, W. D., Parker, E. N., Mozer, F. S., Vasyliūnas, V. M., Pritchett, P. L., Karimabadi, H., ... Koga, D. (2016). Fundamental Concepts Associated with Magnetic Reconnection. In (pp. 1–32). Springer, Cham. Retrieved from https://link-springer-com.proxy.lib.umich.edu/chapter/10.1007/978-3-319-26432-5_1 doi: 10.1007/978-3-319-26432-5{_}1

Goodman, M. L. (1995, 8). A three-dimensional, iterative mapping procedure for the implementation of an ionosphere-magnetosphere anisotropic Ohm's law boundary condition in global magnetohydrodynamic simulations. *Annales Geophysicae*, *13*(8), 843–853. Retrieved from https://link.springer.com/article/10.1007/s00585-995-0843-z doi: 10.1007/s00585-995-0843-z

Grodent, D. (2015). *A Brief Review of Ultraviolet Auroral Emissions on Giant Planets.* doi: 10.1007/s11214-014-0052-8

Grodent, D., Clarke, J. T., Kim, J., Waite, J. H., & Cowley, S. W. (2003, 11). Jupiter's main auroral oval observed with HST-STIS. *Journal of Geophysical Research: Space Physics*, *108*(A11), 1389. Retrieved from http://doi.wiley.com/10.1029/2003JA009921 doi: 10.1029/2003JA009921

Grodent, D., Clarke, J. T., Waite, J. H., Cowley, S. W., Gérard, J. C., & Kim, J. (2003). Jupiter's polar auroral emissions. *Journal of Geophysical Research: Space Physics*. doi: 10.1029/2003JA010017

Gurnett, D. A., Kurth, W. S., Hospodarsky, G. B., Persoon, A. M., Zarka, P., Lecacheux, A., ... Dougherty, M. K. (2002). Control of Jupiter's radio emission and aurorae by the solar wind. *Nature*. doi: 10.1038/415985a

Gustin, J., Cowley, S. W. H., Gérard, J.-C., Gladstone, G. R., Grodent, D., & Clarke, J. T. (2006, 9). Characteristics of Jovian morning bright FUV aurora from Hubble Space Telescope/Space Telescope Imaging Spectrograph imaging and spectral observations. *Journal of Geophysical Research*, *111*(A9), A09220. Retrieved from http://doi.wiley.com/10.1029/2006JA011730 doi: 10.1029/2006JA011730

Hansen, K. C. (2001). MHD simulations of the magnetospheres of Jupiter and Saturn: Application to the Cassini mission. *Ph.D. Thesis*.

Heelis, R. A. (1984, 5). The effects of interplanetary magnetic field orientation on dayside high-latitude ionospheric convection. *Journal of Geophysical Research*, *89*(A5), 2873. Retrieved from http://doi.wiley.com/10.1029/JA089iA05p02873 doi: 10.1029/JA089iA05p02873

Hesse, M., & Cassak, P. A. (2020, 2). Magnetic Reconnection in the Space Sciences: Past, Present, and Future. *Journal of Geophysical Research: Space Physics*, *125*(2), e2018JA025935. Retrieved from https://svs.gsfc.nasa.gov/12239. doi: 10.1029/2018ja025935

Hill, T. W. (1979). Inertial limit on corotation. *Journal of Geophysical Research*. doi:

10.1029/JA084iA11p06554
Hill, T. W. (1980). Corotation lag in Jupiter's magnetosphere: Comparison of observation and theory. *Science*. doi: 10.1126/science.207.4428.301
Hill, T. W. (2001). The Jovian auroral oval. *Journal of Geophysical Research: Space Physics*. doi: 10.1029/2000ja000302
Hill, T. W., Dessler, A. J., & Michel, F. C. (1974, 5). Configuration of the Jovian magnetosphere. *Geophysical Research Letters*, *1*(1), 3–6. Retrieved from http://doi.wiley.com/10.1029/GL001i001p00003 doi: 10.1029/GL001i001p00003
Hones, E. W., Baker, D. N., Bame, S. J., Feldman, W. C., Gosling, J. T., McComas, D. J., ... Tsurutani, B. T. (1984, 1). Structure of the magnetotail at 220 RE and its response to geomagnetic activity. *Geophysical Research Letters*, *11*(1), 5–7. Retrieved from http://doi.wiley.com/10.1029/GL011i001p00005 doi: 10.1029/GL011i001p00005
Hughes, W. J. (2019, 11). The Magnetopause, Magnetotail, and Magnetic Reconnection. In *Introduction to space physics* (pp. 227–287). Cambridge University Press. doi: 10.1017/9781139878296.010
Ieda, A., Machida, S., Mukai, T., Saito, Y., Yamamoto, T., Nishida, A., ... Kokubun, S. (1998). Statistical analysis of the plasmoid evolution with Geotail observations. *Journal of Geophysical Research: Space Physics*. doi: 10.1029/97ja03240
Jackman, C. M., Slavin, J. A., & Cowley, S. W. (2011). *Cassini observations of plasmoid structure and dynamics: Implications for the role of magnetic reconnection in magnetospheric circulation at Saturn.* doi: 10.1029/2011JA016682
Jia, X., Hansen, K. C., Gombosi, T. I., Kivelson, M. G., Tóth, G., Dezeeuw, D. L., & Ridley, A. J. (2012). Magnetospheric configuration and dynamics of Saturn's magnetosphere: A global MHD simulation. *Journal of Geophysical Research: Space Physics*. doi: 10.1029/2012JA017575
Jia, X., & Kivelson, M. G. (2012, 11). Driving Saturn's magnetospheric periodicities from the upper atmosphere/ionosphere: Magnetotail response to dual sources. *Journal of Geophysical Research: Space Physics*, *117*(A11), n/a-n/a. Retrieved from http://doi.wiley.com/10.1029/2012JA018183 doi: 10.1029/2012JA018183
Jia, X., Kivelson, M. G., Khurana, K. K., & Walker, R. J. (2010, 5). Magnetic fields of the satellites of jupiter and saturn. *Space Science Reviews*, *152*(1-4), 271–305. Retrieved from https://link.springer.com/article/10.1007/s11214-009-9507-8 doi: 10.1007/s11214-009-9507-8
Joy, S. P., Kivelson, M. G., Walker, R. J., Khurana, K. K., Russell, C. T., & Ogino, T. (2002). Probabilistic models of the Jovian magnetopause and bow shock locations. *Journal of Geophysical Research: Space Physics*, *107*(A10). doi: 10.1029/2001JA009146
Kennel, C. F., Coroniti, F. V., & Scarf, F. L. (1986). Plasma waves in magnetotail flux ropes. *Journal of Geophysical Research*. doi: 10.1029/ja091ia02p01424
Khurana, K. K. (1992, 5). A generalized hinged-magnetodisc model of Jupiter's nightside current sheet. *Journal of Geophysical Research*, *97*(A5), 6269. Retrieved from http://doi.wiley.com/10.1029/92JA00169 doi: 10.1029/92JA00169
Khurana, K. K. (2001). Influence of solar wind on Jupiter's magnetosphere deduced from currents in the equatorial plane. *Journal of Geophysical Research: Space Physics*. doi: 10.1029/2000ja000352

Khurana, K. K., Jia, X., Kivelson, M. G., Nimmo, F., Schubert, G., & Russell, C. T. (2011, 6). Evidence of a global magma ocean in Io's interior. *Science*, *332*(6034), 1186–1189. Retrieved from www.sciencemag.orgSCIENCEVOLhttp://science.sciencemag.org/ doi: 10.1126/science.1201425

Khurana, K. K., Kivelson, M. G., Vasyliunas, V. M., Krupp, N., Woch, J., Lagg, A., ... Kurth, W. S. (2004). The Configuration of Jupiter's Magnetosphere (Chapter 24). *Jupiter: The Planet, Satellites and Magnetosphere*.

Khurana, K. K., & Schwarzl, H. K. (2005). Global structure of Jupiter's magnetospheric current sheet. *Journal of Geophysical Research: Space Physics*. doi: 10.1029/2004JA010757

Kim, T. K., Ebert, R. W., Valek, P. W., Allegrini, F., McComas, D. J., Bagenal, F., ... Bolton, S. J. (2020). Survey of Ion Properties in Jupiter's Plasma Sheet: Juno JADE-I Observations. *Journal of Geophysical Research: Space Physics*. doi: 10.1029/2019JA027696

Kimura, T., Badman, S. V., Tao, C., Yoshioka, K., Murakami, G., Yamazaki, A., ... Clarke, J. T. (2015). Transient internally driven aurora at Jupiter discovered by Hisaki and the Hubble Space Telescope. *Geophysical Research Letters*. doi: 10.1002/2015GL063272

Kimura, T., Hiraki, Y., Tao, C., Tsuchiya, F., Delamere, P. A., Yoshioka, K., ... Fujimoto, M. (2018). Response of Jupiter's Aurora to Plasma Mass Loading Rate Monitored by the Hisaki Satellite During Volcanic Eruptions at Io. *Journal of Geophysical Research: Space Physics*. doi: 10.1002/2017JA025029

Kimura, T., Nichols, J. D., Gray, R. L., Tao, C., Murakami, G., Yamazaki, A., ... Fujimoto, M. (2017). Transient brightening of Jupiter's aurora observed by the Hisaki satellite and Hubble Space Telescope during approach phase of the Juno spacecraft. *Geophysical Research Letters*. doi: 10.1002/2017GL072912

Kita, H., Kimura, T., Tao, C., Tsuchiya, F., Misawa, H., Sakanoi, T., ... Fujimoto, M. (2016). Characteristics of solar wind control on Jovian UV auroral activity deciphered by long-term Hisaki EXCEED observations: Evidence of preconditioning of the magnetosphere? *Geophysical Research Letters*. doi: 10.1002/2016GL069481

Kita, H., Kimura, T., Tao, C., Tsuchiya, F., Murakami, G., Yamazaki, A., ... Fujimoto, M. (2019, 12). Jovian UV Aurora's Response to the Solar Wind: Hisaki EXCEED and Juno Observations. *Journal of Geophysical Research: Space Physics*, *124*(12), 10209–10218. Retrieved from https://onlinelibrary.wiley.com/doi/abs/10.1029/2019JA026997 doi: 10.1029/2019JA026997

Kivelson, M. G., Coleman, P. J., Froidevaux, L., & Rosenberg, R. L. (1978, 10). A Time Dependent Model of the Jovian Current Sheet. *Journal of Geophysical Research*, *83*(A10), 4823–4829. Retrieved from http://doi.wiley.com/10.1029/JA083iA10p04823 doi: 10.1029/JA083iA10p04823

Kivelson, M. G., & Khurana, K. K. (1995). Models of flux ropes embedded in a harris neutral sheet: Force-free solutions in low and high beta plasmas. *Journal of Geophysical Research*. doi: 10.1029/95ja01548

Kivelson, M. G., & Khurana, K. K. (2002). Properties of the magnetic field in the Jovian magnetotail. *Journal of Geophysical Research: Space Physics*. doi: 10.1029/2001JA000249

Kivelson, M. G., Khurana, K. K., Russell, C. T., Volwerk, M., Walker, R. J., & Zimmer, C. (2000, 8). Galileo magnetometer measurements: A stronger case for a subsurface

ocean at Europa. *Science*, *289*(5483), 1340–1343. Retrieved from http://science.sciencemag.org/ doi: 10.1126/science.289.5483.1340

Kivelson, M. G., Khurana, K. K., Russell, C. T., & Walker, R. J. (1997, 9). Intermittent short-duration magnetic field anomalies in the Io torus: Evidence for plasma interchange? *Geophysical Research Letters*, *24*(17), 2127–2130. Retrieved from http://doi.wiley.com/10.1029/97GL02202 doi: 10.1029/97GL02202

Kivelson, M. G., Khurana, K. K., Russell, C. T., Walker, R. J., Warnecke, J., Coroniti, F. V., ... Schubert, G. (1996, 12). Discovery of Ganymede's magnetic field by the Galileo spacecraft. *Nature*, *384*(6609), 537–541. Retrieved from https://www.nature.com/articles/384537a0 doi: 10.1038/384537a0

Kivelson, M. G., & Southwood, D. J. (2005). Dynamical consequences of two modes of centrifugal instability in Jupiter's outer magnetosphere. *Journal of Geophysical Research: Space Physics*. doi: 10.1029/2005JA011176

Kokubun, S., McPherron, R. L., & Russell, C. T. (1977, 1). Triggering of substorms by solar wind discontinuities. *Journal of Geophysical Research*, *82*(1), 74–86. Retrieved from http://doi.wiley.com/10.1029/JA082i001p00074 doi: 10.1029/JA082i001p00074

Kotsiaros, S., Connerney, J. E., Clark, G., Allegrini, F., Gladstone, G. R., Kurth, W. S., ... Levin, S. M. (2019, 10). *Birkeland currents in Jupiter's magnetosphere observed by the polar-orbiting Juno spacecraft* (Vol. 3) (No. 10). Nature Publishing Group. Retrieved from https://doi.org/10.1038/s41550-019-0819-7 doi: 10.1038/s41550-019-0819-7

Kronberg, E. A., Glassmeier, K. H., Woch, J., Krupp, N., Lagg, A., & Dougherty, M. K. (2007). A possible intrinsic mechanism for the quasi-periodic dynamics of the Jovian magnetosphere. *Journal of Geophysical Research: Space Physics*. doi: 10.1029/2006JA011994

Kronberg, E. A., Grigorenko, E. E., Malykhin, A., Kozak, L., Petrenko, B., Vogt, M. F., ... Masters, A. (2019, 7). Acceleration of Ions in Jovian Plasmoids: Does Turbulence Play a Role? *Journal of Geophysical Research: Space Physics*, *124*(7), 5056–5069. Retrieved from https://onlinelibrary.wiley.com/doi/10.1029/2019JA026553 doi: 10.1029/2019JA026553

Kronberg, E. A., Woch, J., Krupp, N., & Lagg, A. (2008). Mass release process in the Jovian magnetosphere: Statistics on particle burst parameters. *Journal of Geophysical Research: Space Physics*. doi: 10.1029/2008JA013332

Krupp, N. (2016). Comparison of Plasma Sources in Solar System Magnetospheres. In *Space science reviews journal* (pp. 285–295). Springer, New York, NY. Retrieved from https://link.springer.com/chapter/10.1007/978-1-4939-3544-4_8 doi: 10.1007/978-1-4939-3544-4{_}8

Krupp, N., Vytenis, M., Woch, J., Lagg, A., & Krishan, K. (2004). Dynamics of the Jovian Magnetosphere. In *Jupiter: The planet, satellites and magnetosphere.* Cambridge University Press, UK. Retrieved from https://scholar.google.com/scholar_lookup?hl=en&publication_year=2004&pages=617-638&author=N.+Krupp&author=V.+Vasyliunas&author=J.+Woch&author=A.+Lagg&author=K.+Khurana&author=M.+Kivelson&author=B.+H.+Mauk&author=E.+C.+Roelof&author=D.+J.+Williams&author=

Kurth, W. S., Hospodarsky, G. B., Kirchner, D. L., Mokrzycki, B. T., Averkamp, T. F.,

Robison, W. T., ... Zarka, P. (2017). *The Juno Waves Investigation.* doi: 10.1007/s11214-017-0396-y

Lapenta, G., Markidis, S., Goldman, M. V., & Newman, D. L. (2015). Secondary reconnection sites in reconnection-generated flux ropes and reconnection fronts. *Nature Physics*. doi: 10.1038/nphys3406

Le, A., Karimabadi, H., Egedal, J., Roytershteyn, V., & Daughton, W. (2012). Electron energization during magnetic island coalescence. *Physics of Plasmas*. doi: 10.1063/1.4739244

Leboeuf, J. N., Tajima, T., Kennel, C. F., & Dawson, J. M. (1978, 7). Global simulation of the time-dependent magnetosphere. *Geophysical Research Letters*, *5*(7), 609–612. Retrieved from http://doi.wiley.com/10.1029/GL005i007p00609 doi: 10.1029/GL005i007p00609

Lemaire, J. F., Gringauz, K. I., Carpenter, D. L., & Bassolo, V. (1998). *The Earth's Plasmasphere.* Cambridge University Press. Retrieved from https://www-cambridge-org.proxy.lib.umich.edu/core/books/earths-plasmasphere/6D7B1A034B455ED14DA2457432B3A44B doi: 10.1017/cbo9780511600098

Lepping, R. P., Jones, J. A., & Burlaga, L. F. (1990). Magnetic field structure of interplanetary magnetic clouds at 1 AU. *Journal of Geophysical Research*. doi: 10.1029/ja095ia08p11957

Levenberg, K. (1944, 7). A method for the solution of certain non-linear problems in least squares. *Quarterly of Applied Mathematics*, *2*(2), 164–168. Retrieved from https://www.ams.org/qam/1944-02-02/S0033-569X-1944-10666-0/ doi: 10.1090/qam/10666

Linde, T. (2002). A practical, general-purpose, two-state HLL Riemann solver for hyperbolic conservation laws. *International Journal for Numerical Methods in Fluids*. doi: 10.1002/fld.312

Lucek, E. A., Constantinescu, D., Goldstein, M. L., Pickett, J., Pinçon, J. L., Sahraoui, F., ... Walker, S. N. (2005, 6). *The magnetosheath* (Vol. 118) (No. 1-4). Springer. Retrieved from https://link.springer.com/article/10.1007/s11214-005-3825-2 doi: 10.1007/s11214-005-3825-2

Markidis, S., Henri, P., Lapenta, G., Divin, A., Goldman, M. V., Newman, D., & Eriksson, S. (2012). Collisionless magnetic reconnection in a plasmoid chain. *Nonlinear Processes in Geophysics*, *19*(1), 145–153. doi: 10.5194/npg-19-145-2012

Markidis, S., & Lapenta, G. (2011, 8). The energy conserving particle-in-cell method. *Journal of Computational Physics*, *230*(18), 7037–7052. doi: 10.1016/j.jcp.2011.05.033

Martin, C. J., & Arridge, C. S. (2017, 8). Cassini observations of aperiodic waves on Saturn's magnetodisc. *Journal of Geophysical Research: Space Physics*, *122*(8), 8063–8077. Retrieved from http://doi.wiley.com/10.1002/2017JA024293 doi: 10.1002/2017JA024293

Masters, A. (2017). Model-Based Assessments of Magnetic Reconnection and Kelvin-Helmholtz Instability at Jupiter's Magnetopause. *Journal of Geophysical Research: Space Physics*. doi: 10.1002/2017JA024736

Mauk, B. H., Clark, G., Gladstone, G. R., Kotsiaros, S., Adriani, A., Allegrini, F., ... Rymer, A. M. (2020, 3). Energetic Particles and Acceleration Regions Over Jupiter's Polar Cap and Main Aurora: A Broad Overview. *Journal of Geophysical Research: Space Physics*,

125(3), e2019JA027699. Retrieved from https://onlinelibrary.wiley.com/doi/abs/10.1029/2019JA027699 doi: 10.1029/2019JA027699

Mauk, B. H., Haggerty, D. K., Jaskulek, S. E., Schlemm, C. E., Brown, L. E., Cooper, S. A., ... Stokes, M. R. (2017, 11). *The Jupiter Energetic Particle Detector Instrument (JEDI) Investigation for the Juno Mission* (Vol. 213) (No. 1-4). Springer Netherlands. Retrieved from https://link.springer.com/article/10.1007/s11214-013-0025-3 doi: 10.1007/s11214-013-0025-3

Mauk, B. H., Haggerty, D. K., Paranicas, C., Clark, G., Kollmann, P., Rymer, A. M., ... Valek, P. (2017, 9). Discrete and broadband electron acceleration in Jupiter's powerful aurora. *Nature*, *549*(7670), 66–69. Retrieved from https://www.nature.com/articles/nature23648 doi: 10.1038/nature23648

Mauk, B. H., Haggerty, D. K., Paranicas, C., Clark, G., Kollmann, P., Rymer, A. M., ... Valek, P. (2018, 2). Diverse Electron and Ion Acceleration Characteristics Observed Over Jupiter's Main Aurora. *Geophysical Research Letters*, *45*(3), 1277–1285. Retrieved from https://onlinelibrary.wiley.com/doi/abs/10.1002/2017GL076901 doi: 10.1002/2017GL076901

Mauk, B. H., Mitchell, D. G., McEntire, R. W., Paranicas, C. P., Roelof, E. C., Williams, D. J., ... Lagg, A. (2004). Energetic ion characteristics and neutral gas interactions in Jupiter's magnetosphere. *Journal of Geophysical Research: Space Physics*. doi: 10.1029/2003JA010270

McComas, D. J., Allegrini, F., Bagenal, F., Crary, F., Ebert, R. W., Elliott, H., ... Valek, P. (2007). Diverse plasma populations and structures in Jupiter's magnetotail. *Science*. doi: 10.1126/science.1147393

McComas, D. J., & Bagenal, F. (2007). Jupiter: A fundamentally different magnetospheric interaction with the solar wind. *Geophysical Research Letters*. doi: 10.1029/2007GL031078

McPherron, R. L., Weygand, J. M., & Hsu, T. S. (2008, 2). Response of the Earth's magnetosphere to changes in the solar wind. *Journal of Atmospheric and Solar-Terrestrial Physics*, *70*(2-4), 303–315. doi: 10.1016/j.jastp.2007.08.040

Meng, X., Tóth, G., Liemohn, M. W., Gombosi, T. I., & Runov, A. (2012, 8). Pressure anisotropy in global magnetospheric simulations: A magnetohydrodynamics model. *Journal of Geophysical Research: Space Physics*, *117*(A8), n/a-n/a. Retrieved from http://doi.wiley.com/10.1029/2012JA017791 doi: 10.1029/2012JA017791

Milan, S. E., Boakes, P. D., & Hubert, B. (2008, 9). Response of the expanding/contracting polar cap to weak and strong solar wind driving: Implications for substorm onset. *Journal of Geophysical Research: Space Physics*, *113*(A9), n/a-n/a. Retrieved from http://doi.wiley.com/10.1029/2008JA013340 doi: 10.1029/2008JA013340

Milan, S. E., Provan, G., & Hubert, B. (2007, 1). Magnetic flux transport in the Dungey cycle: A survey of dayside and nightside reconnection rates. *Journal of Geophysical Research: Space Physics*, *112*(A1), n/a-n/a. Retrieved from http://doi.wiley.com/10.1029/2006JA011642 doi: 10.1029/2006JA011642

Miyoshi, T., & Kusano, K. (1997). MHD simulation of a rapidly rotating magnetosphere interacting with the external plasma flow. *Geophysical Research Letters*. doi: 10.1029/97GL52739

Moldwin, M. B., & Hughes, W. J. (1991). Plasmoids as magnetic flux ropes. *Journal of*

Geophysical Research: Space Physics. doi: 10.1029/91ja01167

Moriguchi, T., Nakamizo, A., Tanaka, T., Obara, T., & Shimazu, H. (2008). Current systems in the Jovian magnetosphere. *Journal of Geophysical Research: Space Physics*. doi: 10.1029/2007JA012751

Morley, S. K., & Freeman, M. P. (2007, 4). On the association between northward turnings of the interplanetary magnetic field and substorm onsets. *Geophysical Research Letters*, *34*(8). Retrieved from http://doi.wiley.com/10.1029/2006GL028891 doi: 10.1029/2006GL028891

Nagai, T., Shinohara, I., Fujimoto, M., Hoshino, M., Saito, Y., Machida, S., & Mukai, T. (2001). Geotail observations of the Hall current system: Evidence of magnetic reconnection in the magnetotail. *Journal of Geophysical Research: Space Physics*. doi: 10.1029/2001ja900038

Nakamura, R., Baumjohann, W., Asano, Y., Runov, A., Balogh, A., Owen, C. J., ... Rème, H. (2006, 11). Dynamics of thin current sheets associated with magnetotail reconnection. *Journal of Geophysical Research*, *111*(A11), A11206. Retrieved from http://doi.wiley.com/10.1029/2006JA011706 doi: 10.1029/2006JA011706

Ness, N. F., & Wilcox, J. M. (1964, 10). Solar origin of the interplanetary magnetic field. *Physical Review Letters*, *13*(15), 461–464. Retrieved from https://journals.aps.org/prl/abstract/10.1103/PhysRevLett.13.461 doi: 10.1103/PhysRevLett.13.461

Newell, P. T., & Liou, K. (2011, 3). Solar wind driving and substorm triggering. *Journal of Geophysical Research: Space Physics*, *116*(A3), 3229. Retrieved from http://doi.wiley.com/10.1029/2010JA016139 doi: 10.1029/2010JA016139

Newell, P. T., Liou, K., Gjerloev, J. W., Sotirelis, T., Wing, S., & Mitchell, E. J. (2016, 8). Substorm probabilities are best predicted from solar wind speed. *Journal of Atmospheric and Solar-Terrestrial Physics*, *146*, 28–37. doi: 10.1016/j.jastp.2016.04.019

Newville, M., & Stensitzki, T. (2018, 9). Non-Linear Least-Squares Minimization and Curve-Fitting for Python. *Non-Linear Least-Squares Minimization and Curve-Fitting for Python*, 65. Retrieved from http://cars9.uchicago.edu/software/python/lmfit/lmfit.pdf doi: 10.5281/ZENODO.11813

Nichols, J. D. (2011). Magnetosphere-ionosphere coupling in Jupiter's middle magnetosphere: Computations including a self-consistent current sheet magnetic field model. *Journal of Geophysical Research: Space Physics*. doi: 10.1029/2011JA016922

Nichols, J. D., Badman, S. V., Bagenal, F., Bolton, S. J., Bonfond, B., Bunce, E. J., ... Yoshikawa, I. (2017). Response of Jupiter's auroras to conditions in the interplanetary medium as measured by the Hubble Space Telescope and Juno. *Geophysical Research Letters*. doi: 10.1002/2017GL073029

Nichols, J. D., Bunce, E. J., Clarke, J. T., Cowley, S. W., Gérard, J. C., Grodent, D., & Pryor, W. R. (2007). Response of Jupiter's UV auroras to interplanetary conditions as observed by the Hubble Space Telescope during the Cassini flyby campaign. *Journal of Geophysical Research: Space Physics*. doi: 10.1029/2006JA012005

Nichols, J. D., Clarke, J. T., Gérard, J. C., & Grodent, D. (2009). Observations of Jovian polar auroral filaments. *Geophysical Research Letters*. doi: 10.1029/2009GL037578

Nichols, J. D., & Cowley, S. W. (2003). Magnetosphere-ionosphere coupling currents in Jupiter's middle magnetosphere: Dependence on the effective ionospheric Pedersen

conductivity and iogenic plasma mass outflow rate. *Annales Geophysicae*. doi: 10.5194/angeo-21-1419-2003

Nichols, J. D., & Cowley, S. W. (2004). Magnetosphere-ionosphere coupling currents in Jupiter's middle magnetosphere: Effect of precipitation-induced enhancement of the ionospheric Pedersen conductivity. *Annales Geophysicae*. doi: 10.5194/angeo-22-1799-2004

Nichols, J. D., Cowley, S. W. H., & McComas, D. J. (2006, 3). Magnetopause reconnection rate estimates for Jupiter's magnetosphere based on interplanetary measurements at ~5AU. *Annales Geophysicae*, *24*(1), 393–406. Retrieved from `http://www.ann-geophys.net/24/393/2006/` doi: 10.5194/angeo-24-393-2006

Ogino, T., Walker, R. J., & Kivelson, M. G. (1998). A global magnetohydrodynamic simulation of the Jovian magnetosphere. *Journal of Geophysical Research: Space Physics*. doi: 10.1029/97ja02247

Pan, D., Yao, Z., Manners, H., Dunn, W., Bonfond, B., Grodent, D., ... Wei, Y. (2021, 3). Ultralow-Frequency Waves in Driving Jovian Aurorae Revealed by Observations From HST and Juno. *Geophysical Research Letters*, *48*(5), e2020GL091579. Retrieved from `https://onlinelibrary.wiley.com/doi/10.1029/2020GL091579` doi: 10.1029/2020GL091579

Parker, E. N. (1958, 11). Dynamics of the Interplanetary Gas and Magnetic Fields. *The Astrophysical Journal*, *128*, 664. Retrieved from `https://ui.adsabs.harvard.edu/abs/1958ApJ...128..664P/abstract` doi: 10.1086/146579

Pensionerov, I. A., Alexeev, I. I., Belenkaya, E. S., Connerney, J. E. P., & Cowley, S. W. H. (2019, 3). Model of Jupiter's Current Sheet With a Piecewise Current Density. *Journal of Geophysical Research: Space Physics*, *124*(3), 1843–1854. Retrieved from `https://onlinelibrary.wiley.com/doi/abs/10.1029/2018JA026321` doi: 10.1029/2018JA026321

Phan, T. D., Gosling, J. T., Paschmann, G., Pasma, C., Drake, J. F., Øieroset, M., ... Davis, M. S. (2010, 8). The dependence of magnetic reconnection on plasma β and magnetic shear: Evidence from solar wind observations. *Astrophysical Journal Letters*, *719*(2 PART 2), L199. Retrieved from `https://iopscience.iop.org/article/10.1088/2041-8205/719/2/L199https://iopscience.iop.org/article/10.1088/2041-8205/719/2/L199/meta` doi: 10.1088/2041-8205/719/2/L199

Phan, T. D., Kistler, L. M., Klecker, B., Haerendel, G., Paschmann, G., Sonnerup, B. U., ... Reme, H. (2000, 4). Extended magnetic reconnection at the Earth's magnetopause from detection of bi-directional jets. *Nature*, *404*(6780), 848–850. Retrieved from `www.nature.com` doi: 10.1038/35009050

Pontius, D. H. (1997). Radial mass transport and rotational dynamics. *Journal of Geophysical Research A: Space Physics*. doi: 10.1029/97JA00289

Powell, K. G., Roe, P. L., Linde, T. J., Gombosi, T. I., & De Zeeuw, D. L. (1999). A Solution-Adaptive Upwind Scheme for Ideal Magnetohydrodynamics. *Journal of Computational Physics*. doi: 10.1006/jcph.1999.6299

Priest, E. (2013). The Equilibrium of Magnetic Flux Ropes (Tutorial Lecture). *Physics of Magnetic Flux Ropes (eds C.T. Russell, E.R. Priest and L.C. Lee)*. doi: 10.1029/GM058p0001

Priest, E., & Forbes, T. (2000). *Magnetic Reconnection*. Cambridge University Press. Retrieved from https://www.cambridge.org/core/product/identifier/9780511525087/type/book doi: 10.1017/CBO9780511525087

Ridley, A. J., Gombosi, T. I., & DeZeeuw, D. L. (2004, 1). Ionospheric control of the magnetosphere: conductance. *Annales Geophysicae*, *22*(2), 567–584. Retrieved from http://www.ann-geophys.net/22/567/2004/ doi: 10.5194/angeo-22-567-2004

Ripoll, J. F., Claudepierre, S. G., Ukhorskiy, A. Y., Colpitts, C., Li, X., Fennell, J. F., & Crabtree, C. (2020, 5). Particle Dynamics in the Earth's Radiation Belts: Review of Current Research and Open Questions. *Journal of Geophysical Research: Space Physics*, *125*(5), e2019JA026735. Retrieved from https://doi.org/ doi: 10.1029/2019JA026735

Rosa Oliveira, R. A., da Silva Oliveira, M. W., Ojeda-González, A., & De La Luz, V. (2020, 3). New Metric for Minimum Variance Analysis Validation in the Study of Interplanetary Magnetic Clouds. *Solar Physics*, *295*(3), 45. Retrieved from https://doi.org/10.1007/s11207-020-01610-6 doi: 10.1007/s11207-020-01610-6

Russell, C. T. (2005, 4). Interaction of the Galilean Moons with their plasma environments. In *Planetary and space science* (Vol. 53, pp. 473–485). Pergamon. doi: 10.1016/j.pss.2004.05.003

Russell, C. T., & Elphic, R. C. (1978). *Initial ISEE magnetometer results: Magnetopause observations* (Tech. Rep.). Retrieved from https://link.springer.com/content/pdf/10.1007/BF00212619.pdf

Russell, C. T., Khurana, K. K., Kivelson, M. G., & Huddleston, D. E. (2000). Substorms at Jupiter: Galileo observations of transient reconnection in the near tail. *Advances in Space Research*. doi: 10.1016/S0273-1177(00)00084-3

Sarkango, Y., Jia, X., & Toth, G. (2019). Global MHD simulations of the Response of Jupiter's Magnetosphere and Ionosphere to Changes in the Solar Wind and IMF. *Journal of Geophysical Research: Space Physics*. doi: 10.1029/2019ja026787

Schreier, R., Eviatar, A., & Vasyliunas, V. M. (1998). A two-dimensional model of plasma transport and chemistry in the Jovian magnetosphere. *Journal of Geophysical Research E: Planets*. doi: 10.1029/98je00697

Schunk, R., & Nagy, A. (2009). *Ionospheres*. Cambridge University Press. Retrieved from https://www-cambridge-org.proxy.lib.umich.edu/core/books/ionospheres/0C725C779F49AE7DF0C45BF5A350A003 doi: 10.1017/cbo9780511635342

Shue, J.-H., Song, P., Russell, C. T., Steinberg, J. T., Chao, J. K., Zastenker, G., ... Kawano, H. (1998, 8). Magnetopause location under extreme solar wind conditions. *Journal of Geophysical Research: Space Physics*, *103*(A8), 17691–17700. Retrieved from http://doi.wiley.com/10.1029/98JA01103 doi: 10.1029/98JA01103

Sibeck, D. G., Lopez, R. E., & Roelof, E. C. (1991, 4). Solar wind control of the magnetopause shape, location, and motion. *Journal of Geophysical Research*, *96*(A4), 5489. Retrieved from http://doi.wiley.com/10.1029/90JA02464 doi: 10.1029/90JA02464

Sibeck, D. G., Siscoe, G. L., Slavin, J. A., Smith, E. J., Bame, S. J., & Scarf, F. L. (1984). Magnetotail flux ropes. *Geophysical Research Letters*. doi: 10.1029/GL011i010p01090

Slavin, J. A., Acuna, M. H., Anderson, B. J., Baker, D. N., Benna, M., Boardsen, S. A., ... Zurbuchen, T. H. (2009). MESSENGER observations of magnetic reconnection

inmercury's magnetosphere. *Science*. doi: 10.1126/science.1172011

Slavin, J. A., Baker, D. N., Craven, J. D., Elphic, R. C., Fairfield, D. H., Frank, L. A., ... Zwickl, R. D. (1989). CDAW 8 observations of plasmoid signatures in the geomagnetic tail: An assessment. *Journal of Geophysical Research*. doi: 10.1029/ja094ia11p15153

Slavin, J. A., Lepping, R. P., Gjerloev, J., Fairfield, D. H., Hesse, M., Owen, C. J., ... Mukai, T. (2003). Geotail observations of magnetic flux ropes in the plasma sheet. *Journal of Geophysical Research: Space Physics*. doi: 10.1029/2002JA009557

Slavin, J. A., Owen, C. J., Kuznetsova, M. M., & Hesse, M. (1995). ISEE 3 observations of plasmoids with flux rope magnectic topologies. *Geophysical Research Letters*. doi: 10.1029/95GL01977

Slavin, J. A., Smith, E. J., Spreiter, J. R., & Stahara, S. S. (1985). Solar wind flow about the outer planets: Gas dynamic modeling of the Jupiter and Saturn bow shocks. *Journal of Geophysical Research*. doi: 10.1029/ja090ia07p06275

Smith, A. W., Slavin, J. A., Jackman, C. M., Fear, R. C., Poh, G. K., DiBraccio, G. A., ... Trenchi, L. (2017, 1). Automated force-free flux rope identification. *Journal of Geophysical Research: Space Physics*, *122*(1), 780–791. Retrieved from `https://onlinelibrary.wiley.com/doi/abs/10.1002/2016JA022994` doi: 10.1002/2016JA022994

Smith, E. J., Davis, L., Jones, D. E., Coleman, P. J., Colburn, D. S., Dyal, P., ... Frandsen, A. M. A. (1974, 9). The planetary magnetic field and magnetosphere of Jupiter: Pioneer 10. *Journal of Geophysical Research*, *79*(25), 3501–3513. Retrieved from `http://doi.wiley.com/10.1029/JA079i025p03501` doi: 10.1029/JA079i025p03501

Smith, E. J., Davis, L., Jones, D. E., Coleman, P. J., Colburn, D. S., Dyal, P., & Sonett, C. P. (1975, 5). Jupiter's magnetic field, magnetosphere, and interaction with the solar wind: Pioneer 11. *Science*, *188*(4187), 451–455. Retrieved from `http://science.sciencemag.org/` doi: 10.1126/science.188.4187.451

Smyth, W. H. (1992, 8). Neutral cloud distribution in the Jovian system. *Advances in Space Research*, *12*(8), 337–346. doi: 10.1016/0273-1177(92)90408-P

Smyth, W. H., & Marconi, M. L. (2006, 4). Europa's atmosphere, gas tori, and magnetospheric implications. *Icarus*, *181*(2), 510–526. doi: 10.1016/j.icarus.2005.10.019

Sonnerup, B. U., & Cahill, L. J. (1967). Magnetopause structure and attitude from Explorer 12 observations. *Journal of Geophysical Research*. doi: 10.1029/jz072i001p00171

Southwood, D. J., & Kivelson, M. G. (2001). A new perspective concerning the influence of the solar wind on the Jovian magnetosphere. *Journal of Geophysical Research: Space Physics*. doi: 10.1029/2000ja000236

Spreiter, J. R., Summers, A. L., & Alksne, A. Y. (1966, 3). Hydromagnetic flow around the magnetosphere. *Planetary and Space Science*, *14*(3), 223–253. doi: 10.1016/0032-0633(66)90124-3

Strobel, D. F., & Atreya, S. K. (1983). Ionosphere. In A. J. Dessler (Ed.), *Physics of the jovian magnetosphere* (pp. 51–67). Cambridge: Cambridge University Press. Retrieved from `https://www.cambridge.org/core/product/identifier/CBO9780511564574A015/type/book_part` doi: 10.1017/CBO9780511564574.004

Sulaiman, A. H., Jia, X., Achilleos, N., Sergis, N., Gurnett, D. A., & Kurth, W. S. (2017, 9). Large-scale solar wind flow around Saturn's nonaxisymmetric magnetosphere. *Journal of Geophysical Research: Space Physics*, *122*(9), 9198–9206. Retrieved from `http://`

doi.wiley.com/10.1002/2017JA024595 doi: 10.1002/2017JA024595

Sulaiman, A. H., Masters, A., Dougherty, M. K., & Jia, X. (2014). The magnetic structure of Saturn's magnetosheath. *Journal of Geophysical Research: Space Physics*. doi: 10.1002/2014JA020019

Sun, W. J., Slavin, J. A., Tian, A. M., Bai, S. C., Poh, G. K., Akhavan-Tafti, M., ... Burch, J. L. (2019). MMS Study of the Structure of Ion-Scale Flux Ropes in the Earth's Cross-Tail Current Sheet. *Geophysical Research Letters*. doi: 10.1029/2019GL083301

Swisdak, M., Opher, M., Drake, J. F., & Alouani Bibi, F. (2010, 2). The vector direction of the interstellar magnetic field outside the heliosphere. *Astrophysical Journal*, *710*(2), 1769–1775. Retrieved from https://iopscience.iop.org/article/10.1088/0004-637X/710/2/1769https://iopscience.iop.org/article/10.1088/0004-637X/710/2/1769/meta doi: 10.1088/0004-637X/710/2/1769

Swisdak, M., Rogers, B. N., Drake, J. F., & Shay, M. A. (2003, 5). Diamagnetic suppression of component magnetic reconnection at the magnetopause. *Journal of Geophysical Research: Space Physics*, *108*(A5), 1218. Retrieved from http://doi.wiley.com/10.1029/2002JA009726 doi: 10.1029/2002JA009726

Tao, C., Kataoka, R., Fukunishi, H., Takahashi, Y., & Yokoyama, T. (2005). Magnetic field variations in the Jovian magnetotail induced by solar wind dynamic pressure enhancements. *Journal of Geophysical Research: Space Physics*. doi: 10.1029/2004JA010959

Taylor, J. B. (1974). Relaxation of toroidal plasma and generation of reverse magnetic fields. *Physical Review Letters*. doi: 10.1103/PhysRevLett.33.1139

Tetrick, S. S., Gurnett, D. A., Kurth, W. S., Imai, M., Hospodarsky, G. B., Bolton, S. J., ... Mauk, B. H. (2017, 5). Plasma waves in Jupiter's high-latitude regions: Observations from the Juno spacecraft. *Geophysical Research Letters*, *44*(10), 4447–4454. Retrieved from http://doi.wiley.com/10.1002/2017GL073073 doi: 10.1002/2017GL073073

Thorne, R. M., Armstrong, T. P., Stone, S., Williams, D. J., McEntire, R. W., Bolton, S. J., ... Kivelson, M. G. (1997, 9). Galileo evidence for rapid interchange transport in the Io torus. *Geophysical Research Letters*, *24*(17), 2131–2134. Retrieved from http://doi.wiley.com/10.1029/97GL01788 doi: 10.1029/97GL01788

Tóth, G., De Zeeuw, D. L., Gombosi, T. I., & Powell, K. G. (2006, 9). A parallel explicit/implicit time stepping scheme on block-adaptive grids. *Journal of Computational Physics*, *217*(2), 722–758. Retrieved from https://www.sciencedirect.com/science/article/pii/S0021999106000337?via%3Dihub doi: 10.1016/J.JCP.2006.01.029

Tóth, G., Meng, X., Gombosi, T. I., & Ridley, A. J. (2011). Reducing numerical diffusion in magnetospheric simulations. *Journal of Geophysical Research: Space Physics*. doi: 10.1029/2010JA016370

Tóth, G., van der Holst, B., Sokolov, I. V., De Zeeuw, D. L., Gombosi, T. I., Fang, F., ... Opher, M. (2012). Adaptive numerical algorithms in space weather modeling. *Journal of Computational Physics*. doi: 10.1016/j.jcp.2011.02.006

Van Allen, J. A., Baker, D. N., Randall, B. A., Thomsen, M. F., Sentman, D. D., & Flindt, H. R. (1974, 1). Energetic electrons in the magnetosphere of Jupiter. *Science*, *183*(4122), 309–311. Retrieved from http://science.sciencemag.org/ doi: 10.1126/science.183.4122.309

Vasyliunas, V. M. (1975, 2). Theoretical models of magnetic field line merging. *Re-*

views of Geophysics, *13*(1), 303. Retrieved from http://doi.wiley.com/10.1029/RG013i001p00303 doi: 10.1029/RG013i001p00303

Vasyliunas, V. M. (1983). Plasma distribution and flow. In *Physics of the jovian magnetosphere.* doi: 10.1017/cbo9780511564574.013

Vogt, M. F., Connerney, J. E., DiBraccio, G. A., Wilson, R. J., Thomsen, M. F., Ebert, R. W., ... Bolton, S. J. (2020). Magnetotail Reconnection at Jupiter: A Survey of Juno Magnetic Field Observations. *Journal of Geophysical Research: Space Physics*. doi: 10.1029/2019JA027486

Vogt, M. F., Jackman, C. M., Slavin, J. A., Bunce, E. J., Cowley, S. W., Kivelson, M. G., & Khurana, K. K. (2014). Structure and statistical properties of plasmoids in Jupiter's magnetotail. *Journal of Geophysical Research A: Space Physics*. doi: 10.1002/2013JA019393

Vogt, M. F., Kivelson, M. G., Khurana, K. K., Joy, S. P., & Walker, R. J. (2010). Reconnection and flows in the Jovian magnetotail as inferred from magnetometer observations. *Journal of Geophysical Research: Space Physics*. doi: 10.1029/2009JA015098

Vogt, M. F., Kivelson, M. G., Khurana, K. K., Walker, R. J., Bonfond, B., Grodent, D., & Radioti, A. (2011). Improved mapping of Jupiter's auroral features to magnetospheric sources. *Journal of Geophysical Research: Space Physics*. doi: 10.1029/2010JA016148

Volwerk, M., André, N., Arridge, C. S., Jackman, C. M., Jia, X., Milan, S. E., ... Forsyth, C. (2013, 5). Comparative magnetotail flapping: An overview of selected events at Earth, Jupiter and Saturn. *Annales Geophysicae*, *31*(5), 817–883. doi: 10.5194/angeo-31-817-2013

Walker, R. J., & Jia, X. (2016). Simulation Studies of Plasma Transport at Earth, Jupiter and Saturn.. doi: 10.1007/978-3-319-26432-5{_}9

Walker, R. J., & Ogino, T. (1989). Global Magnetohydrodynamic Simulations of the Magnetosphere. *IEEE Transactions on Plasma Science*, *17*(2), 135–149. doi: 10.1109/27.24618

Walker, R. J., Ogino, T., & Kivelson, M. G. (2001). Magnetohydrodynamic simulations of the effects of the solar wind on the Jovian magnetosphere. *Planetary and Space Science*. doi: 10.1016/S0032-0633(00)00145-8

Wang, L., Hakim, A. H., Bhattacharjee, A., & Germaschewski, K. (2015, 1). Comparison of multi-fluid moment models with particle-in-cell simulations of collisionless magnetic reconnection. *Physics of Plasmas*, *22*(1), 012108. Retrieved from http://aip.scitation.org/doi/10.1063/1.4906063 doi: 10.1063/1.4906063

Wang, R., Lu, Q., Nakamura, R., Huang, C., Du, A., Guo, F., ... Wang, S. (2016, 3). Coalescence of magnetic flux ropes in the ion diffusion region of magnetic reconnection. *Nature Physics*, *12*(3), 263–267. Retrieved from www.nature.com/naturephysics doi: 10.1038/nphys3578

Wang, Y., Guo, X., Tang, B., Li, W., & Wang, C. (2018, 7). Modeling the Jovian magnetosphere under an antiparallel interplanetary magnetic field from a global MHD simulation. *Earth and Planetary Physics*, *2*(4), 303–309. Retrieved from http://www.eppcgs.org//article/doi/10.26464/epp2018028?pageType=en doi: 10.26464/epp2018028

Webb, D. F., & Howard, T. A. (2012, 6). Coronal mass ejections: Observations. *Living Reviews in Solar Physics*, *9*(1), 3. Retrieved from http://www.livingreviews.org/

lrsp-2012-3http://www.boulder.swri.edu/~howard/ doi: 10.12942/lrsp-2012-3

Wilson, R. J., Bagenal, F., Valek, P. W., McComas, D. J., Allegrini, F., Ebert, R. W., ... Thomsen, M. F. (2018, 4). Solar Wind Properties During Juno's Approach to Jupiter: Data Analysis and Resulting Plasma Properties Utilizing a 1-D Forward Model. *Journal of Geophysical Research: Space Physics*, *123*(4), 2772–2786. Retrieved from http://doi.wiley.com/10.1002/2017JA024860 doi: 10.1002/2017JA024860

Wiltberger, M., Lotko, W., Lyon, J. G., Damiano, P., & Merkin, V. (2010, 10). Influence of cusp O ¡sup¿+¡/sup¿ outflow on magnetotail dynamics in a multifluid MHD model of the magnetosphere. *Journal of Geophysical Research: Space Physics*, *115*(A10), n/a-n/a. Retrieved from http://doi.wiley.com/10.1029/2010JA015579 doi: 10.1029/2010JA015579

Woch, J., Krupp, N., & Lagg, A. (2002). Particle bursts in the Jovian magnetosphere: Evidence for a near-Jupiter neutral line. *Geophysical Research Letters*. doi: 10.1029/2001GL014080

Yamada, M., Kulsrud, R., & Ji, H. (2010, 3). Magnetic reconnection. *Reviews of Modern Physics*, *82*(1), 603–664. Retrieved from https://journals.aps.org/rmp/abstract/10.1103/RevModPhys.82.603 doi: 10.1103/RevModPhys.82.603

Zhang, B., Delamere, P. A., Ma, X., Burkholder, B., Wiltberger, M., Lyon, J. G., ... Sorathia, K. A. (2018, 1). Asymmetric Kelvin-Helmholtz Instability at Jupiter's Magnetopause Boundary: Implications for Corotation-Dominated Systems. *Geophysical Research Letters*, *45*(1), 56–63. Retrieved from http://doi.wiley.com/10.1002/2017GL076315 doi: 10.1002/2017GL076315

Zhong, J., Zong, Q. G., Wei, Y., Slavin, J. A., Cao, X., Pu, Z. Y., ... Wan, W. X. (2019). MESSENGER Observations of Giant Plasmoids in Mercury's Magnetotail . *The Astrophysical Journal*. doi: 10.3847/2041-8213/ab5650

Zieger, B., & Hansen, K. C. (2008). Statistical validation of a solar wind propagation model from 1 to 10 AU. *Journal of Geophysical Research: Space Physics*. doi: 10.1029/2008JA013046